

Development of a Two-Fault Tolerant Cold Gas Propulsion System and Air Bearing Testbed for Application to a Spacecraft-Inspection CubeSat

By

JOSH WILLIAM DAY
THESIS

Submitted in partial satisfaction of the requirements for the degree of

MASTER OF SCIENCE

in

Mechanical and Aerospace Engineering

in the

OFFICE OF GRADUATE STUDIES

of the

UNIVERSITY OF CALIFORNIA

DAVIS

Approved:

Stephen K. Robinson, Chair

Paul A. Erickson

Sanjay S. Joshi

Committee in Charge

2020

*To my friends and loved ones, both near and far; both past and present. Thank you for
believing in me, especially when I did not.*

CONTENTS

List of Figures	vii
List of Tables	xiv
Abstract	xvi
Acknowledgments	xvii
1 Introduction	1
1.1 Motivation for Remote Inspection of Spacecraft	1
1.2 Notable Incidents in Human Spaceflight	2
1.3 A Review of Relevant Technological Developments	6
1.3.1 Historical Precedence for Inspection-Oriented Missions	7
1.3.2 Adoption of the CubeSat Standard	8
1.3.3 Cold Gas Propulsion Systems	8
1.3.4 3D Printing in Propulsion Systems	10
1.3.5 Fault Tolerance in Propulsion Systems	11
1.4 Summary	13
1.5 Research Objective	14
2 Design Methodology	17
2.1 Mission Overview	18
2.1.1 Safety Considerations	18
2.1.2 Design Reference Mission	18
2.2 Determining ΔV Requirements	20
2.2.1 Clohessy-Wiltshire Model	20
2.2.2 Inclination Change Requirements	22
2.2.3 Station-Keeping Maneuver Requirements	24
2.2.4 End-of-Mission Requirements	28
2.2.5 Summary of ΔV Requirements	30
2.3 Propulsion System Design Considerations	31
2.3.1 Net Thrust and Impulse Requirements	31

2.3.2	Propellant Selection	33
2.3.3	Thruster Configuration	34
2.3.4	Considerations for a Plenum-based Architecture	39
2.4	Nozzle Design and Plenum Sizing	39
2.4.1	In-Space Performance Reqs. and Resultant Design	40
2.4.2	Total Propellant Mass for In-Space Design	42
2.4.3	On-Ground Performance Reqs. and Resultant Design	44
2.4.4	Optimum Nozzle Geometry for On-Ground Testing	47
2.5	Realistic Considerations of Performance	49
2.6	Summary	50
3	Manufacturing and Construction	52
3.1	Air Bearing Testbed	52
3.1.1	Air Bearing Test Platform	53
3.1.2	Air Bearing Table	60
3.2	Converging-Diverging Nozzle	63
3.2.1	Nozzle Design Specifications	63
3.2.2	Nozzle Manufacturing Procedure	66
3.3	Plenum Chamber	67
3.3.1	Design Considerations	67
3.3.2	Assembly Process	70
3.3.3	Manufacturing Challenges	72
3.3.4	Stress Analysis	73
3.3.5	Failure Considerations	76
3.4	Propulsion System Control Board	77
3.5	Wireless Control System	79
3.6	Computer Vision System	81
3.6.1	OpenCV and the ArUco Library	81
3.6.2	Kalman Filtering	83
3.7	Summary	88

4 Thruster Characterization and Full System Testing	89
4.1 Characterization of 3D Printed Plenum Chambers	89
4.2 Characterization of Nozzle Design	91
4.2.1 Steady-State Thrust and Mass Flow Rate	91
4.2.2 Single Plenum Discharge	95
4.3 Full-Scale Two-Stage Thruster Testing	96
4.3.1 Valve Designations	97
4.3.2 Nominal Performance	98
4.3.3 Valve Failure Test Outline	101
4.3.4 One-Fault Failure Modes	102
4.3.5 Two-Fault Failure Modes, Single Thruster Line	107
4.3.6 Two-Fault Failure Modes, Adjacent Thruster Lines	112
4.3.7 Two-Fault Failure Modes, Opposite Thruster Lines	115
4.4 Summary of Results	119
4.4.1 Air Bearing Test Platform	119
4.4.2 Thruster Design and Characterization	120
4.4.3 Wireless Communications Interface	120
4.4.4 Nozzle Design	120
4.4.5 Full-scale Propulsion System Testing	121
4.4.6 Computer Vision and Kalman Filter	122
5 Conclusion and Recommendations	123
5.1 Lessons Learned and Future Recommendations	123
5.1.1 CubeSat Propulsion System	123
5.1.2 3D Printing	124
5.1.3 Air Bearing Table	124
5.1.4 Air Bearing Platform	125
5.2 Conclusion	126
A Hohmann Transfer Review	129

B Isentropic Nozzle Flow Review	132
C Single Plenum Discharge Simulation	136
C.1 Simulation Development	136
C.2 Selection of Appropriate Simulation Time Step	138
D Realistic Considerations of Performance	142
D.1 Limitations of Isentropic Model	142
D.2 Heat Transfer Through Valve	145
D.3 Throat Reynolds Number During Discharge	148
D.4 Estimating Viscous Losses	149
E Off-The-Shelf Component Selection	153
E.1 Pneumatic Component Selection	153
E.2 Regulator Selection	153
E.3 Valve Selection	154
E.4 Fittings and Adapters	156
F PCB Wiring Diagram	159
G Online Resources	161

LIST OF FIGURES

1.1	Missing tile on STS-27 exposing partially-melted plate.	3
1.2	Protruding gap fillers observed during external inspection of Discovery on STS-114.	4
1.3	Orbiter Boom Sensor System being grappled by the SRMS during STS-114. .	4
1.4	Ammonia leak from ISS	5
1.5	A graphical timeline of selected relevant missions and their corresponding technology over the last 25 years, ordered by development date.	6
1.6	AERCam Sprint next to Seeker/Kenobi.	7
1.7	Comparison of CanX-2 and SNAP-1 propulsion systems.	9
1.8	Comparison of MEPSI and Seeker propulsion systems.	10
1.9	Comparison of MarCO and Apollo LM propulsion system schematics. . . .	12
1.10	Schematic of proposed two-fault tolerant propulsion system with fixed-volume plenums between valves. A single valve-plenum assembly is highlighted in red.	15
2.1	ISS dimensions	19
2.2	Orbits of the ISS and inspection CubeSat (not to scale) illustrating a maximum separation of 54.5 meters.	19
2.3	Apparent flight path of the CubeSat during continuous propulsion-assisted station-keeping per the Clohessy-Wiltshire model	25
2.4	Illustration of the relative motion during an inspection task. In the LVLH frame, the Z-axis points down into the page and directly toward Earth, and the target's orbital velocity is along the X-axis.	25
2.5	Clohessy-Wiltshire model showing how required ΔV and burn schedules vary with allowable stray distances from a range of out-of-plane inspection target positions. The selected target position and stray distance are indicated. . . .	26
2.6	In-space thruster configuration.	34
2.7	Thruster configuration for 3 DOF control during on-ground testing.	36

2.8	Simulation results for idealized thruster design wherein all required impulse is imparted in a single discharge. The impulse objective of 118 mN-s is met at 12.5 seconds resulting in an average thrust of 9.4 mN	41
2.9	Simulation results showing the change in specific impulse (I_{sp}) for a single plenum discharge of the in-space design.	43
2.10	Simulation results for target thruster design. The smaller plenum necessitates multiple discharges, while the larger throat diameter makes for a larger net thrust and reduces the overall maneuver time.	47
2.11	Effect of expansion ratio (ϵ) on total impulse during a single plenum discharge for on-ground propulsion system.	48
2.12	Similar impulse vs. expansion ratio exploration for in-space propulsion system in vacuum conditions.	49
3.1	Air bearing test platform pneumatic diagram. CO ₂ is stored at approximately 850 psig in two 9 oz. bottles, then brought down to 25 psig at the in-line regulator before being distributed to three 25 mm flat round air bearings. . .	54
3.2	Two SPHERES air bearing test platforms used for design reference; single-bearing rear profile (view opposite of air bearing pressure regulator) [54] (a), three-bearing triangular base sans CO ₂ supply [55] (b).	54
3.3	Lift-Load curve for New Way 25 mm round flat air bearing. Operating pressure was selected by assuming a 5 kg (49 N) divided evenly over three bearings, which comes out to approximately 16 N each [56].	55
3.4	Initial test build of the air bearing test platform (Rev 1); (a) Underside showing the pneumatic layout and (b) with prototype circuitry for wireless data transmission.	56
3.5	Second revision of the air bearing test platform; (a) CAD mock-up and (b) physical construction.	58
3.6	Third revision of the air bearing test platform; (a) CAD mock-up and (b) initial prototype build.	59
3.7	UC Davis HRVIP glass-topped air bearing table.	62

3.8	0.6 mm throat diameter nozzle schematic (linear dimensions in millimeters). The nozzle features are machined into a COTS M5 brass hex plug.	65
3.9	Snapshot of the nozzle manufacturing process. (a) Drilling the throat using a $\phi = 0.6$ mm drill bit and (b) illustrating the use of a 20° engraving bit with $\phi = 0.1$ mm tip.	66
3.10	Plenum CAD design; Fully assembled (a) and broken-out (b) views.	68
3.11	Single plenum with valves attached at each end via the M5 threaded fitting.	68
3.12	End-on illustration of a plenum half with its threaded fitting showing how a single 60° “clock” of the plenum on the fitting (solid red line) results in an effective 15° “clock” of the flange slots (dashed blue line).	69
3.13	All possible slot positions for a single plenum half (a), two overlapping plenums (shaded region highlights the mating plenum slots which are offset at 7.5°) il- lustrating how a successful mate can be established even at the worst-possible orientation (b).	70
3.14	Plenum epoxy process as demonstrated with an old revision plenum, prior to the inclusion of slotted flange holes. During application (a), and while curing (b).	71
3.15	Plenum tightening pattern (a), and fully assembled and integrated (b).	72
3.16	Summarized results from [70]. Tests were conducted with 0.1, 0.2, and 0.3mm layer thickness samples. Means and standard deviations are plotted for each test angle.	74
3.17	Stress-Strain curve for PLA and other plastics, from [71].	74
3.18	Z-Normal stress distribution over a single plenum hemisphere under 791 kPa (100 psig) internal pressure shown on a scale from a range of 0 to 10,000 kPa. The peak stress value at the flagged point is 6557 kPa.	76
3.19	Propulsion control board schematic (a), bare board (b), with terminals sol- dered (c), and with all components inserted (d).	78
3.20	Top-level architecture diagram for wireless communication system	79

3.21	Three primary control screens of the user interface designed to control unit as a whole, hold selected valves open, and touch-toggle individually valves for debugging.	80
3.22	The ArUco marker detection process. (a) Original image. (b) Local thresholding used for segmentation. (c) Contour detection. (d) Polygonal approximation and removal of irrelevant contours. (e) Perspective projection correction. (f) Bit assignment for each cell within the marker.	82
3.23	The general process of Kalman filtering to produce a state estimate from a combination of sensor data and model predictions, for each time step	83
3.24	Illustration of the Kalman filtering process whereby an <i>a priori</i> state estimate is made then updated with measurements [75].	85
4.1	Plenum pressure testing configuration (a), and aftermath of a failed test (b).	90
4.2	Plenum pressure test configuration with test hardware labeled.	90
4.3	Steady-state thrust test stand with adjustable base.	92
4.4	Inlet pressure and resultant thrust for fixed pressure set points.	92
4.5	Thrust and mass flow rate at measured pressures compared to their respective isentropic models.	93
4.6	Single plenum discharge characterization configuration.	95
4.7	Single plenum discharge compared to isentropic model.	96
4.8	Valve layout and designations used for full test platform assembly (a); completed prototype assembly (b).	97
4.9	Illustration of pure translation-type motion moving left-to-right. Some rotation is induced by imperfections in the air bearing table.	98
4.10	Results from executing two consecutive plenum discharges to produce pure translational motion.	99
4.11	Recorded displacement and resultant estimated states for an A2 failure mode during translation maneuvers.	103
4.12	Recorded displacement and resultant estimated states for an A2 failure mode during rotation maneuvers.	104

4.13 Recorded displacement and resultant estimated states for an A3 failure mode during translation maneuvers.	105
4.14 Recorded displacement and resultant estimated states for an A3 failure mode during rotation maneuvers.	106
4.15 Recorded displacement and resultant estimated states for an A1+A2 failure mode during translation maneuvers.	107
4.16 Recorded displacement and resultant estimated states for an A1+A2 failure mode during rotation maneuvers.	108
4.17 Recorded displacement and resultant estimated states for an A1+A3 failure mode during translation maneuvers. Fuel was depleted prior to conducting a third trial and a bearing crash occurred in Trial 1, indicated by the sudden deceleration at $t = 6$ sec.	109
4.18 Recorded displacement and resultant estimated states for an A1+A3 failure mode during rotation maneuvers.	110
4.19 Recorded displacement and resultant estimated states for an A2+A3 failure mode during translation maneuvers.	111
4.20 Recorded displacement and resultant estimated states for an A2+A3 failure mode during rotation maneuvers.	112
4.21 Recorded displacement and resultant estimated states for an A2+D2 failure mode during translation maneuvers.	113
4.22 Recorded displacement and resultant estimated states for an A2+D3 failure mode during translation maneuvers.	114
4.23 Recorded displacement and resultant estimated states for an A3+D3 failure mode during translation maneuvers.	115
4.24 Recorded displacement and resultant estimated states for an A2+C2 failure mode during rotation maneuvers.	116
4.25 Recorded displacement and resultant estimated states for an A2+C3 failure mode during rotation maneuvers.	117
4.26 Recorded displacement and resultant estimated states for an A3+C3 failure mode during rotation maneuvers.	118

A.1 Depiction of a Hohmann transfer used to reduce the altitude of an object by transferring it from circular orbit A to circular orbit C by means of elliptical orbit B and two separate propulsive burns.	130
B.1 Mach Number - Area relationship defined by Equation B.1 for three gasses	134
B.2 Pressure ratio distribution along the length of a converging-diverging (De Laval) nozzle. The subsonic and supersonic solutions to Equation B.1 are labeled as lines C and D, respectively [76].	135
C.1 Convergence study for an in-space R134a-based system described in Section 2.4.	139
C.2 Convergence study for an on-ground CO ₂ -based system described in Section 2.4.	140
D.1 Plenum pressure and temperature over the course of a single plenum discharge modeled as entirely isentropic, illustrating how the isentropic model does not account for phase change.	143
D.2 Density-energy plot of CO ₂ illustrating the path it takes as a plenum discharges, showing when a phase change begins to take place as the path crosses into the phase coexistence region.	144
D.3 Plenum pressure and temperature over the course of a single plenum discharge modeled using conservation of energy and by tracking when a phase change occurs.	145
D.4 Total CO ₂ flow temperatures upstream and downstream of the valve illustrating the marginal effect of heat transfer on the flow temperature itself.	147
D.5 Total R134a flow temperatures upstream and downstream of the valve illustrating the marginal effect of heat transfer on the flow temperature itself.	148
D.6 Comparison of the throat Reynolds number for CO ₂ and R134a.	149
D.7 Thrust coefficient and estimated viscous losses for CO ₂ -based nozzle used in on-ground testing.	151
D.8 Thrust coefficient and estimated viscous losses for a hypothetical R134a-based nozzle to be used in space.	152

E.1 Regulator style comparison, piston [80] (a), and diaphragm [81] (b).	155
F.1 Wiring diagram for propulsion system control board.	160

LIST OF TABLES

2.1 Orbital parameters used in Clohessy-Wiltshire model	21
2.2 Orbit lifetime for a selection of 3U CubeSats which were placed in similar orbits as is to be expected for this CubeSat mission.	28
2.3 ΔV requirements for complete mission	30
2.4 ΔV requirements for complete mission	30
2.5 Tabulated summary of the geometric properties which define the location and orientation of the four thrusters on the air bearing platform.	38
2.6 Thruster combinations required to affect motion in the listed directions. . . .	38
2.7 Performance requirements to inform nozzle and plenum design for hypothetical in-space propulsion system for a 5 kg object.	40
2.8 Nozzle and plenum geometry to meet in-space performance requirements with one complete plenum discharge.	41
2.9 Performance objectives to determine nozzle and plenum design for on-ground testing.	45
2.10 Nozzle and plenum geometry given the constraints and design choices described.	46
2.11 Performance expectations for a 30 cm ³ plenum completing two discharges. .	46
3.1 Definitions to describe surface quality for air bearing applications.	60
3.2 Nozzle geometry to be manufactured for on-ground testing.	64
3.3 Values used to define the orthotropic mechanical properties of a PLA-based 3D printed plenum.	75
4.1 Summary of conducted tests and expected resultant motion of the air bearing platform.	102
C.1 A sample listing of time steps calculated from Equation C.9 based on the convergence results from Figures C.1 and C.2. Parameters which are varied from their design value are bolded.	141
E.1 Sample valve selection and flow rate comparison to 0.6 mm C-D nozzle. . . .	156

E.2	Fitting types used to assemble the high-pressure side of the air bearing platform's pneumatics, listed here for ease of reproducibility.	157
E.3	Fitting types used to assemble the low-pressure side of the air bearing platform's pneumatics, listed here for ease of reproducibility.	158

ABSTRACT

Development of a Two-Fault Tolerant Cold Gas Propulsion System and Air Bearing Testbed for Application to a Spacecraft-Inspection CubeSat

The design of a cold gas propulsion system intended to demonstrate the feasibility of a two-fault tolerant system architecture is presented. The objective of this design is to protect against a jet fail-on type of malfunction which could endanger a spacecraft or its human occupants in the event of a collision. The design reference mission is a close-proximity external inspection task of an in-flight spacecraft, and we seek to demonstrate continued controllability in the event that up to two separate valve failures occur. Fault-tolerance was achieved by implementing a series of in-line valves and fixed-volume plenums for each thruster to limit the amount of uncontrolled impulse in a valve fail-open scenario. A computer simulation was developed to predict the atypical thrust profile expected in this type of system architecture, and an air bearing-based test platform was constructed to test a 3 degree-of-freedom analog propulsion system prototype. This testbed utilizes computer vision-based position tracking to provide Kalman filter-based estimates of the velocity and acceleration states of the spacecraft analog. A wireless user interface was developed to provide user control of the spacecraft analog, control over individual valve states to simulate valve fail-open failure modes, and to relay pressure and thrust data to validate thruster design. Strong emphasis is placed on utilizing commercially available products, 3D printed pressure vessels, and in-house manufacturing to develop the system in the hopes of disseminating the knowledge gained from this work to aid student teams and other institutions in developing their own satellite testbeds. The results from static testing indicate good agreement with the theory-based simulation predictions, and adverse motion induced by different failure modes was consistently bound to a low level even in two-fault failure scenarios. The most significant adverse motion was induced by two failures which occurred on the same thruster, as well as uncontrolled gravitational forces due to imperfections in the air bearing table. Recommendations are provided for future iterations of the propulsion system and corresponding air bearing testbed.

ACKNOWLEDGMENTS

There exists no reality where I would be at this point without the guidance and support from an uncountable number of people. To that end, I would like to extend my utmost gratitude to the following individuals for their contribution to this project: Chris Lorenzen, for being a sounding board and a ground to reality, and helping me stay on track when I got lost time and time again. Holly Kim, for her help and feedback in the design of our air bearing test bed when this journey began. Nelson Flores, for his help in improving and characterizing the air bearing test bed, and for his role as our machine shop liaison. Adriana Henriquez, for pioneering our computer vision tracking system which proved crucial in the final phase of this project. Rob Hurtado, for his help in designing the propulsion control board and 3D printed plenums, which I would otherwise still be working on to this day.

I also wish to extend my thanks to the rest of my peers in the Human/Robotics/Vehicle Integration and Performance Lab. They questioned everything and made no assumptions, and in doing so raised the standard of excellence for our entire organization. For their support, friendship, and company during the ~ 123.1 US gallons of coffee consumed over the course of this project, I will be eternally grateful.

Thank you as well to all the staff in the College of Engineering who work tirelessly in the background to make things run smoothly. They have been extraordinarily kind and patient, and they provided opportunities for professional growth which I might not have gotten elsewhere.

To Professor Robinson, for his infinite wisdom and endless pool of cringeworthy jokes: thank you for entrusting me with this work. I only regret that I could not do more. Likewise, thank you to my committee members, Professor Erickson and Professor Joshi, who would not let anyone get away with sub-par work.

And lastly, thank you to my family for their unending support. We were raised by patient and loving parents who understand that the path forward is rarely straight and smooth, and who instilled within us the capacity to persist in even the most trying times. Through them, and all of my colleagues, I have learned that I must challenge my preconceptions or else they will challenge me.

Chapter 1

Introduction

1.1 Motivation for Remote Inspection of Spacecraft

Remote external spacecraft inspection is a valuable and necessary tool to promote safe human spaceflight operations. Inspection has supported operations on the Space Shuttle and the International Space Station (ISS) by providing “clearance assessments, anomaly resolution, and leak locating” [1]. In other words, visually confirming no collisions will occur, identifying and resolving external hardware damage or failures, and providing an extra set of eyes outside the spacecraft to visually assess malfunctions or external damage. Additional inspection needs and opportunities still exist in the form of improving leak isolation precision and timeliness, imaging hard to reach areas, and damage assessment. Furthermore, advanced inspection capabilities will be required in support of future missions beyond Low Earth Orbit (LEO) as crews are expected to operate with greater autonomy during long-duration missions. Providing a means for remote robotic inspection can reduce crew Extravehicular Activity (EVA) time and improve awareness of overall spacecraft health.

The UC Davis Human/Robotics/Vehicle Integration and Performance (HRVIP) Lab is designing a semi-autonomous inspection satellite to remotely inspect a spacecraft exterior [2]. This capability would augment existing external inspection ability by providing a means to reach places otherwise unobservable from windows, exterior-mounted cameras, robotic arms, or EVAs. A remote inspector will require a self-contained propulsion system to maneuver into place for an inspection task and subsequently de-orbit or remove itself from vehicle proximity post-mission. To accomplish such a task, the propulsion system of the inspection satellite

must be highly reliable and tolerant to multiple faults such that any two valve failures will not pose even greater danger to the inspection target. The specific failure mode of concern is that of a *jet fail-on* in which a valve that is stuck open will normally apply an unknowable and uncontrollable thrust on the vehicle. This will be addressed by incorporating hardware-based redundancy and fixed volumes between valves to bound the amount of applied impulse and limit the maximum induced adverse motion (i.e. tumbling) of the inspection spacecraft. This thesis will therefore cover the design and subsequent prototyping of a novel two-fault tolerant cold gas propulsion system to be used with a 3-Unit (3U) CubeSat for remote spacecraft inspection.

The following section reviews previous incidents in human spaceflight which either utilized or could have utilized in-flight inspection capabilities. We then review the state-of-the-art in cold gas propulsion, 3D-printed propulsion technology, small form-factor satellites, and fault-tolerance in their design as these categories will be pertinent to the development of the propulsion system presented herein. The term “small satellite” is very broad and can refer to any satellite less than 500 kg in mass [3], so this review will focus on the *nano-* class of small satellites which fall within 1-10 kg and thus include most CubeSats. Some missions are discussed which are not inspection-oriented but still possess technological aspects which would be advantageous to an inspection mission.

1.2 Notable Incidents in Human Spaceflight

The following review will confirm the need for in-space vehicle inspection by reviewing incidents in the past – both major and minor – which would have benefited from semi-autonomous remote inspection capability. This section will illustrate how pivotal this tool could have been in reducing risk, and in some cases saving lives, by showing what events have occurred and extrapolating to what could have been instead if these missions had a remote inspection satellite at their disposal.

Physical damage to the Thermal Protection System (TPS) of the Space Shuttle was a persistent problem throughout the lifetime of the program. As early as 1988, just two missions after the ill-fated STS-51-L Challenger accident, significant damage to the TPS tiles was noted after liftoff of STS-27 Atlantis, likely caused by debris from the right solid

rocket booster. Post-mission inspection revealed over 700 impact sites and one tile completely removed from the forward-right fuselage over the L-band antenna cover – a thick, metal plate holding the antenna in place – shown in Figure 1.1 [4]. It is possible that had a tile been removed in a different location, the resultant heat from reentry could have destroyed the orbiter [5]. The problem was compounded by the fact that remote visual inspection using cameras mounted on the end of the shuttle robotic arm - the Shuttle Remote Manipulator System (SRMS) – was limited by the reach of the arm, which was unable to utilize its end-effector camera to inspect the underside of the TPS tiles. Combined with video restrictions put in place due to the classified nature of their cargo, ground teams were not convinced that the damage was significant enough to warrant cause for concern and instead suggested the damage was just “lights and shadows”.



Figure 1.1: Missing tile location which covered an antenna mounting plate on STS-27. Partial melting of the metal plate indicates that it was exposed to high temperature flow during reentry [6].

In January of 2003, insulating foam debris shook loose from the external tank during the launch of the Space Shuttle Columbia on STS-107 and struck the leading edge of the left wing of the orbiter. As indicated previously, foam strikes were a known event prior to STS-107, but engineers were unaware of the extensive damage this particular strike caused. The strike dislodged critical portions of the reinforced Carbon-Carbon tiles that make up the Shuttle’s

Thermal Protection System (TPS). Upon reentry, the Shuttle's space frame was catastrophically damaged by the impinging hypersonic atmospheric gasses, resulting in a complete loss of the orbiter and its crew. After resuming spaceflight activities, NASA implemented an on-orbit inspection procedure to check the status of the TPS prior to reentry. Inspection was performed by maneuvering the orbiter through a slow "backflip" while observers from the ISS relayed high-resolution photos of the underside to ground control. Additionally, self-inspection capabilities were improved with the addition of the Orbiter Boom Sensory System (OBSS): a grappled extension for the SRMS affixed with a suite of cameras and sensors to inspect different regions of the orbiter (shown in Figure 1.3).

During STS-114, ISS-based inspection of the orbiter revealed protruding tile gap fillers, shown in Figure 1.2, which could have interrupted the nominally smooth boundary layer which forms underneath the orbiter during reentry and destroy it [7]. The protruding gap fillers were fortunately easy to remove by hand during an EVA, but it nevertheless reflected the need to have greater in-flight inspection and repair autonomy.



Figure 1.2: Protruding gap fillers observed during external inspection of Discovery on STS-114 [8].



Figure 1.3: The Orbiter Boom Sensor System being grappled by the SRMS during STS-114. The OBSS was an extension to the SRMS that allows for greater reach during remote inspection tasks [9].

Another example of the need for external inspection technology occurred on May 9th, 2013, when the crew of the ISS reported seeing small white flakes floating away from the station. The source of the leak could not be observed directly as no external camera could be positioned for direct line-of-sight observation of the leak site. The best observation made by the crew was of a visible plume as sunlight refracted through the rapidly dispersing cloud of

ammonia, shown in Figure 1.4. The source of the flakes was later confirmed to be ammonia leaking from part of the station’s cooling system used to regulate the temperature of the solar panels which provide power to the station. The leak was located at the far end of the P6 truss section – one of the furthest points away from the center of the station. An emergency EVA was performed shortly after to fix the problem by replacing a faulty ammonia pump controller box with a spare located in an adjacent compartment [10].



Figure 1.4: Ammonia leak from ISS (Image courtesy of NASA).

While the emergency EVA was successful, this event called attention to the need for astronauts and ground crew to quickly and accurately assess a situation so that they may plan accordingly and minimize the harm to equipment or personnel. Without the ability to deploy any form of autonomous remote inspection tool, the astronauts and the ground crew were forced to rely on piecing together incomplete sources of information before determining a course of action. Such an act can take precious time away from effecting repairs and could potentially result in loss of life or vehicle if the damage were to a more critical system. Moreover, EVAs are high-risk by their very nature, and any work which could be done to limit EVA time would translate directly into reduced risk to astronaut wellbeing.

Prior to the retirement of the Space Shuttle in 2011, the ISS acted as an external inspector to the Shuttle by noting any damage to the orbiter’s TPS tiles typically caused by debris from launch. Likewise, the Shuttle could act as an external inspector for the ISS and note any external damage in areas where cameras might not be able to reach. The mutually beneficial arrangement of having two, free-flying spacecraft in close proximity proved to be an invaluable tool in reducing risk to life and vehicle in human spaceflight. With the Shuttle no longer flying, the ISS has been left alone to self-inspect – a critical task performed in a

limited capacity with a combination of externally-mounted cameras, robotic arms, and EVAs. With future manned missions to the Moon, Mars, and beyond which could see astronauts operate autonomously for years at a time, it is even more important to develop a means for reliable remote inspection of spacecraft exteriors.

1.3 A Review of Relevant Technological Developments

Five specific fields have been identified as the most relevant areas of focus in addressing the lack of free-flying inspection capabilities:

1. Historical precedence for inspection-oriented missions
2. Adoption of the CubeSat standard
3. Utilization of cold gas propulsion
4. Utilization of 3D printing in propulsion systems
5. Implementation of hardware-based fault tolerance for propulsion systems

This review will provide a brief historical summary for each of these five fields in the context of previous developments, specifically focusing on their application to small satellites when possible. Figure 1.5 provides a chronology of when these fields have been addressed in past missions and highlights the lack of hardware-based fault tolerance in the propulsion systems for these designs.

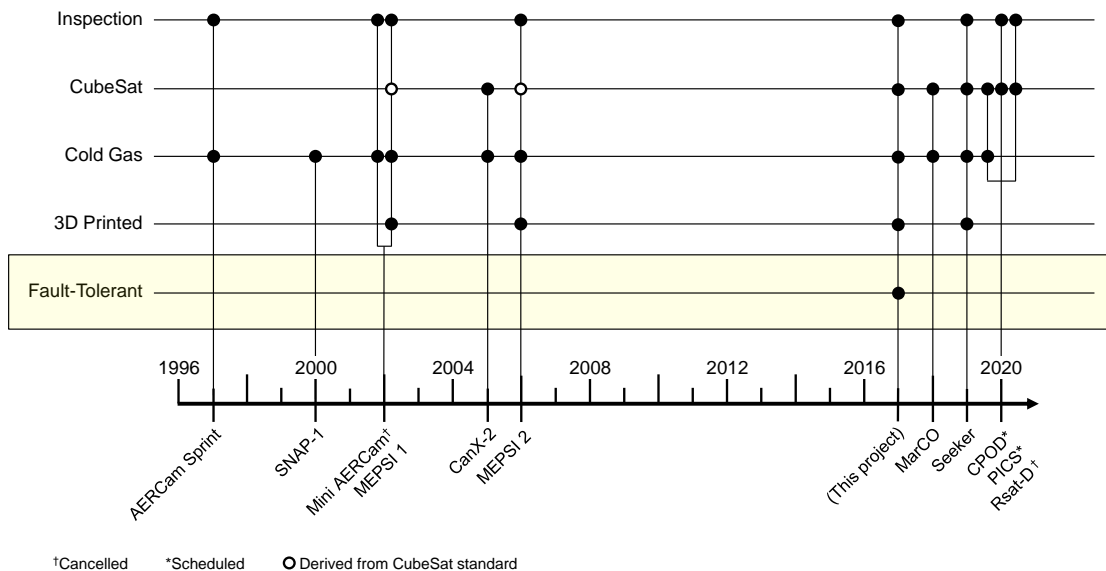


Figure 1.5: A graphical timeline of selected relevant missions and their corresponding technology over the last 25 years, ordered by development date.

1.3.1 Historical Precedence for Inspection-Oriented Missions

NASA performed the first known demonstration of a free-flying inspector in 1997 during the STS-87 shuttle mission with AERCam Sprint [11], shown in Figure 1.6a, and the concept was later revisited in 2005 with the development of Mini-AERCam [12], though this iteration never flew. The Aerospace Corporation developed the Micro Electro-Mechanical Systems-based PicoSat Inspector (MEPSI) series of satellites in 2002 and 2006 to demonstrate key technologies needed for inspection tasks, such as proximity operations and built-in propulsion [13]. MEPSI was the first known in-flight demonstration of additive manufacturing in propulsion systems, having had its propellant storage, gasification volume, and manifold printed stereolithographically in one single piece. Unfortunately, only two of the four planned MEPSI missions were ever flown and the program was subsequently cancelled.

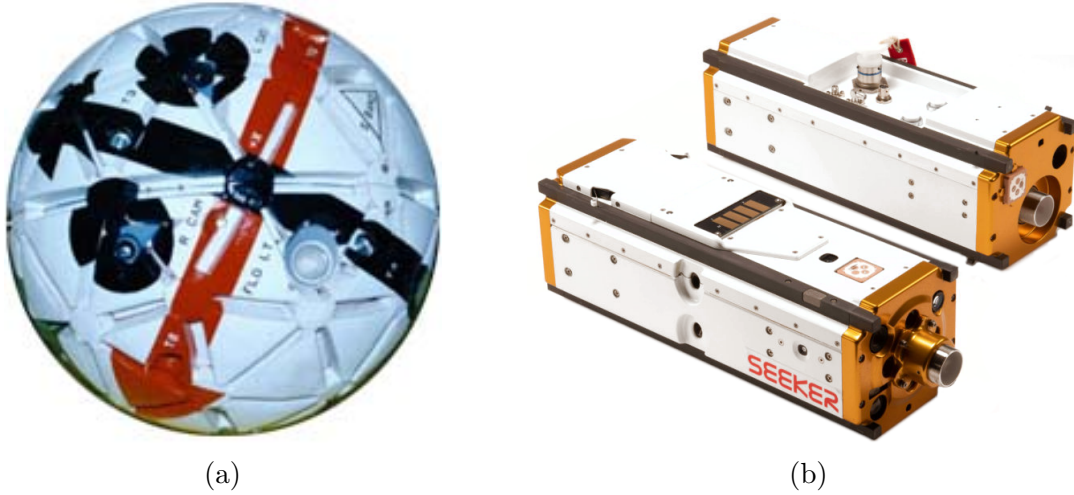


Figure 1.6: The first inspection-oriented free flyer, AERCam Sprint [11] (a) next to the most recent as of 2020, Seeker [14] (b).

No major developments in inspection-type missions occurred until the end of the following decade with the development and launch of NASA’s Seeker CubeSat in 2019 [15], shown in Figure 1.6b. The Seeker mission was intended to demonstrate low-cost in-space inspection capability by drawing on hardware and experience from previous missions. Specifically, it reused propulsion hardware originally developed for Mini-AERCAM and – like MEPSI – utilized additive manufacturing to create a geometrically compact, low-cost manifold and nozzles. Passive inspection capability such as those provided by BYU’s Passive Inspection CubeSat (PICS) benefits from a highly simplified design which can reduce cost and com-

plexity, albeit limiting the application to low-risk targets and missions [16] due to a lack of any attitude or position control system. Some inspector missions have also been designed to include manipulators for grappling and remote repair, shifting the boundary from purely inspection to also include repair [17]. However, none of these missions have been designed to operate in proximity to a high-value target such as the ISS, and none were designed specifically to protect against a jet fail-on which might otherwise endanger the health of the parent spacecraft and its occupants.

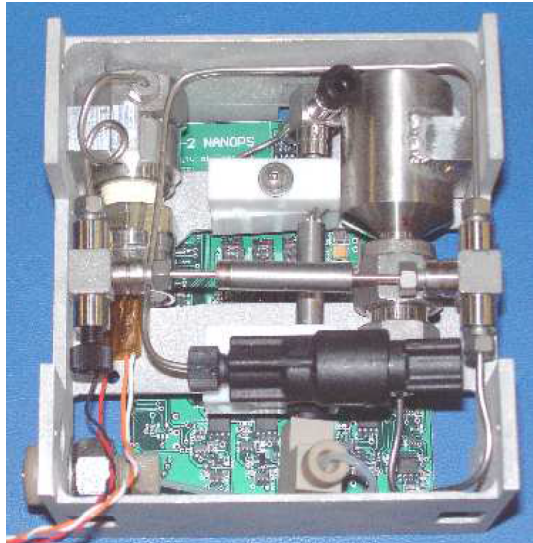
1.3.2 Adoption of the CubeSat Standard

The first modern nanosatellite (one with a mass between 1 and 10 kg, including most CubeSats) didn't launch until 1996 [18]. Miniaturization is a critical path forward in support of remote inspection missions, but many of the enabling technologies have only been available for the last 25 years and only a few nanosatellite missions flew prior to widespread adoption of the CubeSat standard [11, 12, 19]. Starting in 2002 with MEPSI 1, most missions which either demonstrate inspection capabilities or close-proximity operations have conformed to the CubeSat standard [13, 15, 17, 20, 21]. One notable exception to this is NASA/JPL's Mars CubeSat One (MarCO), which holds the honor of becoming the first pair of interplanetary CubeSats when they were launched alongside JPL's InSight Mars Lander in 2018 [22]. The cost reduction benefits of conforming to the CubeSat standard stem from a low capped mass requirement which reduces launch cost, and standardized configurations which allow greater utilization of commercial off-the-shelf (COTS) components. CubeSats deployed from the ISS are stored within the pressurized volume prior to launching, thus providing operators with the opportunity for one final quality control check via the on-board astronauts prior to being deployed [23]. The small and standardized form factor allows for repeatable and reliable deployment from the Japanese Experiment Module (JEM) via the Robotic Manipulator System (JEMRMS) or the NanoRacks CubeSat Deployer [24].

1.3.3 Cold Gas Propulsion Systems

While CubeSats and similarly-sized small satellites have enjoyed nearly two decades of ever-increasing popularity and success as a low-cost platform for university research and technology demonstration, only a small subset have ever flown with any form of propulsion. Out

of 1210 CubeSats launched as of May 2020, only approximately 50 have included any form of propulsion system [25]. Despite the variety of propulsion systems available for CubeSats, cold gas remains the most common, although the exact details of their implementation varies heavily based on the mission parameters, and their configuration can vary greatly, as illustrated in Figure 1.7. Many cold gas systems use two-phase substances as propellant due to their ability to be stored as liquids at relatively low pressures and evaporated into gas (“gasification”) prior to expulsion [13, 19–21, 26]. This evaporation process can rapidly cool the propellant, so propulsion systems utilizing two-phase substances often require integrated heating elements to raise the temperature of the gas back up to a nominal range before being used. Other systems utilize inert gasses, such as nitrogen, which remains in a gaseous state thus avoiding the extremely large temperature drop caused by evaporation, though this presents a greater hazard due to the higher storage pressure [11, 12, 15]. In general, most CubeSat-class cold gas propulsion systems can provide anywhere between 10 mN to 10 N of thrust, with specific impulses (I_{sp}) ranging from 40 to 70 seconds [27]. This is extremely low compared to other small satellite propulsion technologies which can achieve many hundreds to thousands of seconds of I_{sp} , albeit at the cost of reduced net thrust or increased risk.



(a)

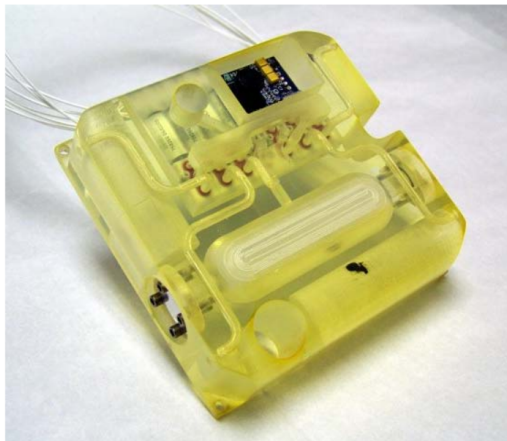


(b)

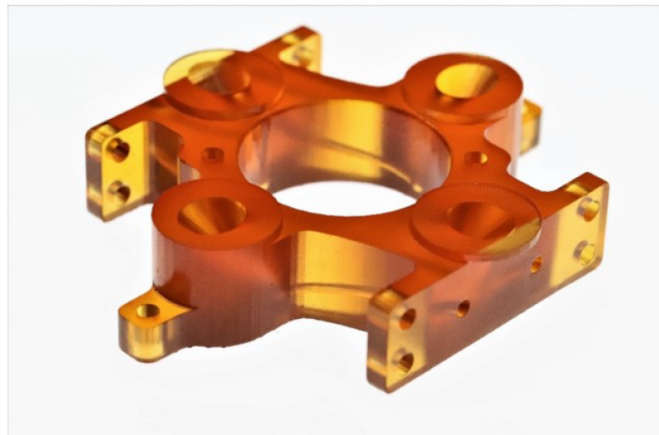
Figure 1.7: Sulphur hexafluoride-based propulsion system for CanX-2 [28] (a) and butane-based propulsion system built by Surrey Satellite Technology using a bent steel tube as the propellant storage [29] (b).

1.3.4 3D Printing in Propulsion Systems

Cold gas propulsion by itself is a very mature technology, but the introduction of the CubeSat standard has challenged engineers to create more compact systems with the same robustness and performance expectations as their larger counterparts. Recent advancements in 3D printing capabilities have allowed complex and compact propulsion manifolds to be integrated into a CubeSat bus [13, 15, 30]. The first known application of 3D printing to form the bulk of a nanosatellite propulsion system was in 2008 by The Aerospace Corporation in the development of the MEPSI series of satellites. The MEPSI project utilized stereolithographic (SLA) 3D printing methods in order to form an airtight and structurally sound pressure vessel made from WaterShed XC 11122 plastic resin, shown in Figure 1.8a. It wasn't until three years later when the Aerojet-Rocketdyne corporation developed an off-the-shelf CubeSat propulsion system using selective laser melting (SLM) 3D printed titanium pressure vessels [31]. 3D printed propulsion systems returned to their resin roots in 2019 for NASA's Seeker propulsion system, which used a proprietary Continuous Liquid Interface Production (CLIP) method to manufacture the propulsion manifold out of Cyanate Ester 221 plastic, as shown in Figure 1.8b.



(a)



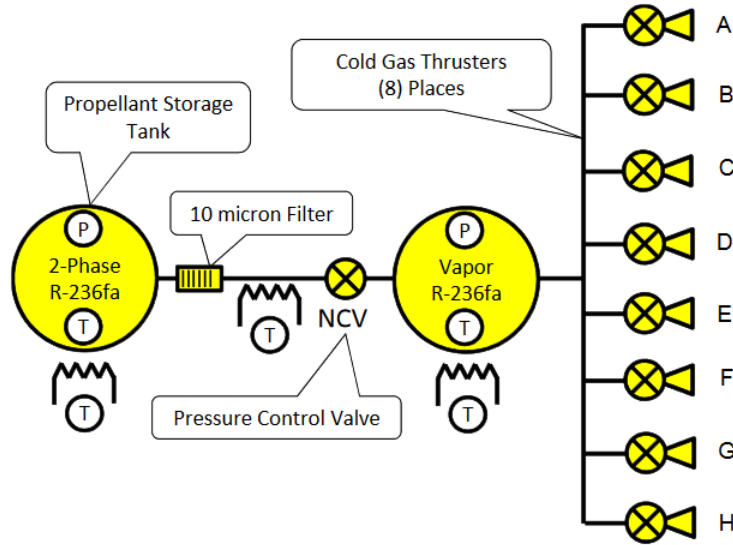
(b)

Figure 1.8: SLA-manufactured resin propulsion system with attached valves for MEPSI [32] (a), thruster manifold and integrated nozzle structure for Seeker [33] (b).

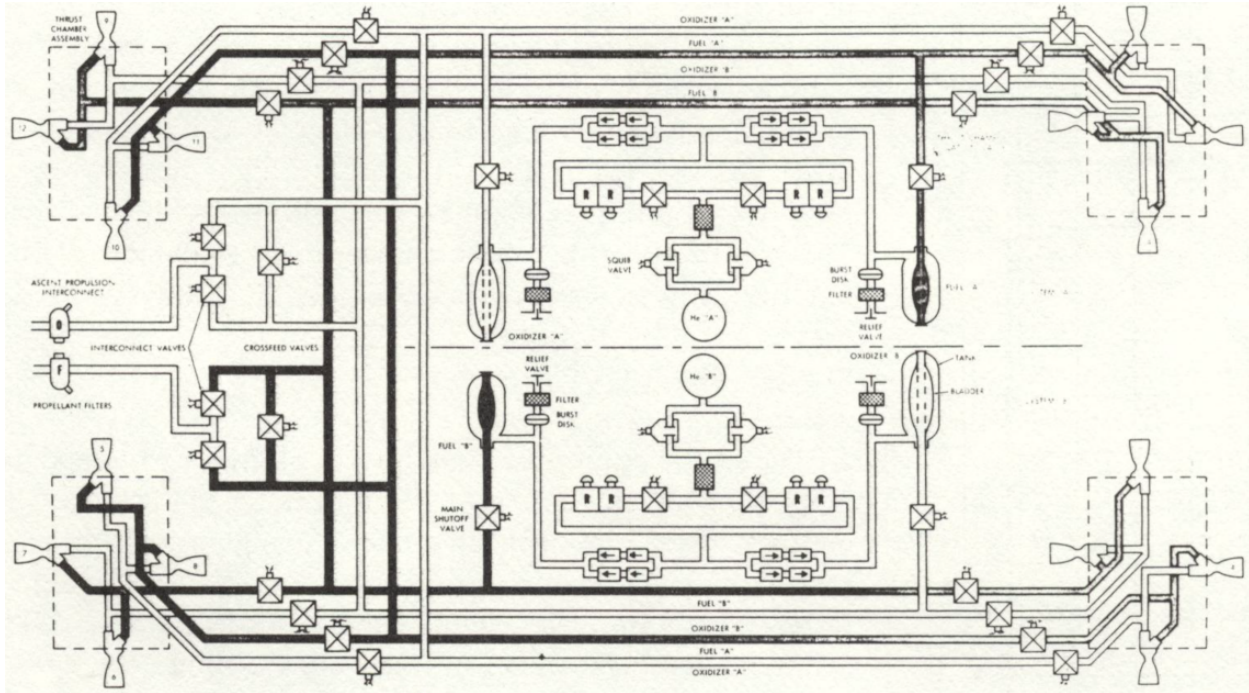
1.3.5 Fault Tolerance in Propulsion Systems

While the prior developments discussed have helped pave the way for robotic free-flying inspection capabilities, the lack of fault-tolerance in the propulsion systems has yet to be addressed. Fault tolerance is necessary to prevent, among other risks, an inadvertent thruster firing (jet fail-on) from imparting unknown and uncontrollable forces on the vehicle which could lead to a hazardous situation. Designing against this potential hazard is paramount for proximity operations (such as an inspection task) since a jet fail-on could result in an uncontrollable tumbling motion and pose a grave collision risk between the inspection vehicle and target. A lack of fault tolerance has on one occasion resulted in life-threatening circumstances which were narrowly resolved only with the competent piloting skills of Astronaut Neil Armstrong during the Gemini VIII mission [34]. In this situation, a thruster valve had remained energized due to an electrical short and subsequently stuck open, causing a jet fail-on failure mode which introduced a steadily increasing and uncontrollable tumble in the spacecraft. It was only by shutting down power to the entire attitude control system and using the reentry thrusters to stabilize the spacecraft was the fault overcome.

Though hardware-level fault tolerance has not been a key feature of most CubeSat propulsion systems, it is heavily used on larger systems and is in fact required by federal law for launch operators [35]. For example, each thruster on the Mars Science Laboratory (MSL) cruise stage propulsion subsystem was one-fault tolerant by integrating dual thruster valves into each propellant line to insure against a valve sticking closed and preventing fuel flow [36]. Larger propulsion systems in the past have been built with entire system-level redundancy, each completely insulated from one another, such as the Apollo Lunar module reaction control system (RCS) [37, 38] and NASA’s Cassini RCS [39]. Figure 1.9 showcases the differences in hardware-based fault tolerance between a small satellite cold gas propulsion system and the Apollo Lunar Module (LM) RCS. Differences in propellant choices will also affect the complexity of the system, and it can be seen in Figure 1.9 that significantly more redundancy exists in the Apollo LM propulsion system compared to MarCO’s propulsion system.



(a)



(b)

Figure 1.9: Comparison of MarCO's relatively simple cold gas propulsion system [40] (a) with the more complicated Apollo LM RCS [38] (b). The Apollo LM architecture utilizes sets of valves in series and parallel to protect against stuck-open and stuck-closed failure modes. Furthermore, the architecture uses entirely redundant pairs of thrusters and feed lines, each pressurized with their own helium source.

1.4 Summary

The prior work outlined above has served to advance the capabilities of CubeSat-compatible technology, inspection-oriented navigation and control, and small satellite cold gas propulsion. Each project has emphasized the development and advancement of one or more of the relevant technologies discussed previously necessary for close-proximity inspection. Of the selected missions which were outlined, only eight were designed with an inspection-oriented task in mind [11–13, 15–17, 20]. Of those eight, only six utilized any form of cold gas propulsion [11–13, 15, 20] – the rest operated entirely passively with the exception of Rsat-D’s parent spacecraft (BRICSat), which would have utilized micro-Cathode Arc Thrusters. Out of those six remaining, four were designed around a CubeSat architecture [13, 15, 20]. Note that, while not strictly CubeSats, the MEPSI missions are considered to be “CubeSat-inspired” and are therefore included in this count. With the exception of CanX-2, those same missions utilized 3D printing technology in the design of their propulsion systems, presumably driven by the compact dimensional requirements of a CubeSat [13, 15].

Based on the design of their respective propulsion systems it is clear that none of the listed missions considered fault-tolerance as part of their design objective, though special consideration should be given to AERCam Sprint as it is the only one to have ever operated in proximity to a high-value target. AERCam Sprint utilized a gaseous nitrogen-based propulsion system derived from the Simplified Aid for EVA Rescue (SAFER) system worn by astronauts during extravehicular activities (EVA). The SAFER system only used one valve per thruster, though manual shutoff of the high-pressure side of the system was possible [41]. Nevertheless, even a single jet fail-on fault would render the entire system unusable since it would depressurize the entire propellant manifold and induce an uncontrollable tumble. While one may argue that this design does constitute “fault tolerance” on the grounds that a single failure would not produce a hazardous event, it is not sufficiently tolerant to allow a mission to proceed in any capacity. Therefore, despite the design feature of a manual shut-off valve, this system is not considered to be fault tolerant in the context of this work.

1.5 Research Objective

The objective of the work presented herein was to design, construct, and test a prototype two-fault tolerant cold gas propulsion system capable of meeting mission performance requirements laid out for a hypothetical inspection task to be performed by a 3U-sized CubeSat estimated to be a mass of 5 kg. This was accomplished by incorporating hardware-based redundancy in a small form factor by taking advantage of the benefits offered by 3D printing to make compact and customizable geometry.

An additional objective was to design and construct a test bed to simulate zero gravity and provide an environment within which to test the prototype two-fault tolerant propulsion system. The test bed utilized planar air bearings to allow three degrees of freedom (DOF) in motion. Building on the knowledge summarized previously, we demonstrate methods for utilizing off-the-shelf components and 3D printing to drive down the cost of both the propulsion system and the experimental testbed. The lessons learned herein can be disseminated to any university, student team, R&D group, or small business so they can use the information to cost-effectively kickstart their own CubeSat program.

The two-fault tolerance objective was met by pursuing a hardware-based approach that physically separates the thruster exit from the propellant source by at least three independent valves. Between each valve sits a fixed volume to house a portion of the propellant, herein referred to as a “plenum”, ready to be expelled. As a consequence of this design, a jet fail-on failure mode – wherein the external-most valve is stuck open and the contents of the plenum are allowed to escape and produce adverse thrust – will produce predictable and bounded motion by virtue of the fact that a known plenum volume will restrict the thruster to imparting a known impulse on the CubeSat.

The proposed propulsion system schematic is shown in Figure 1.10. Characterizing the performance of a plenum-based architecture initially involved a single valve-plenum assembly (outlined in red in Figure 1.10) prototyped and tested. Following this, a 3 degree-of-freedom (DOF) platform was constructed to test a set of four two-fault tolerant thruster lines.

Normally-closed valves are used to ensure that no propellant is lost in the event of a power failure, and three valves in-line ensure safe, continued operation in the unlikely event of two valves in the same line failing open. The jet fail-on mode is considered to pose a greater risk

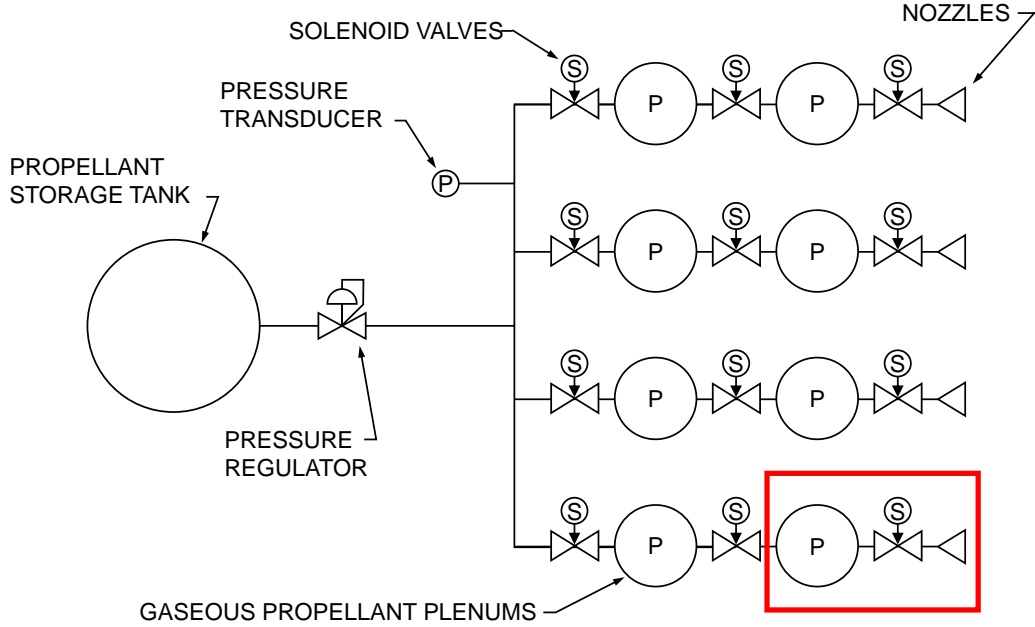


Figure 1.10: Schematic of proposed two-fault tolerant propulsion system with fixed-volume plenums between valves. A single valve-plenum assembly is highlighted in red.

to crew and mission compared to that of a fail-off mode since an uncontrolled propulsive event will introduce kinetic energy into the system and shorten the available response time of the crew. Conversely, a jet fail-off mode, while inconvenient, will still allow partial control of some degrees of freedom and in turn allow the satellite to be removed from the proximity of the inspection target without shortening the available response time. As such, jet fail-off failure modes are considered to be out of scope for this project.

The work outlined herein will begin in Chapter 2 by detailing a design case for an ISS-based inspection task in which an out-of-plane maneuver will be performed to reach the furthest edge of the station. Starting with a brief overview of the governing equations, the design case will lay out all of the individual maneuvers required to achieve this task and tally up the total change in velocity (ΔV) required. Following the summary of performance requirements will be a review of the relevant thermodynamic equations used for modeling and predicting the thrust, mass flow rate, and other performance metrics for a cold gas propulsion system. Propellant choice and thruster layout will be briefly touched upon, after which the thruster requirements necessary to meet the performance objective will be determined. The details of a computer simulation designed to study this specific propulsion architecture will

also be reviewed.

Chapter 3 will walk the reader through the hardware design and manufacturing methods employed for constructing the prototype propulsion system. The design of an air bearing-based test platform will also be covered. Included in this chapter will be a description of a combined computer vision and Kalman filter-based motion tracking system which will be used as an external reference to measure the forces acting on the air bearing test platform.

With the gas-dynamics theory and propulsion system hardware development established, Chapter 4 will detail the testing procedures which take place throughout hardware development. Each subsystem and component subassembly is individually tested before integration, and the results of these tests are summarized. Lastly, the full propulsion assembly will be placed on the air bearing test platform and its motion will be quantified by a computer vision system. A series of valve failures will be induced to simulate all possible combinations of a jet-fail on situation, and the resulting motion and motion-arresting process will be discussed.

Chapter 2

Design Methodology

As discussed in Chapter 1, the objective of this project is to design, build, and test a prototype two-fault tolerant cold gas propulsion system for use on an inspection CubeSat. The two-fault tolerance objective will be met by constructing each individual thruster with a series of interstitial volumes, called “plenums”, separated by normally-closed two-way valves to introduce hardware-based redundancy at a per-thruster level. This chapter will outline a design reference mission (DRM) for the inspection satellite and present the governing equations used to model the orbital mechanics for the DRM. These equations will be used to determine the propulsion system’s performance requirements needed to accomplish the mission, including velocity change (ΔV), thrust, and net impulse. From there, the performance requirements will inform the operating pressure, plenum volume, propellant selection, and nozzle geometry for the propulsion system.

In order to effectively test an analogous system on the ground within the constraints of our test facilities, a modified set of performance requirements specifically for on-ground testing will be outlined along with their in-space counterparts. A Python-based computer simulation which predicts the performance of a single-plenum discharge will be used to estimate plenum volume and nozzle size. Lastly, the simulation will be used to determine an optimum nozzle geometry which will be used to inform the nozzle manufacturing process, covered in Chapter 3.

The thruster performance objectives established in this chapter will be used to design a propulsion system which will be mounted on an air bearing-based test platform, discussed

in greater detail in Chapter 3. This test platform will allow for low friction 3 DOF motion, allowing us to approximate a zero gravity environment suitable for testing. Likewise, the propulsion system developed for on-ground testing will be designed for 3 DOF control of the test platform.

2.1 Mission Overview

2.1.1 Safety Considerations

The satellite’s systems must meet an acceptable level of reliability to ensure that performing the inspection mission will not add more risk than it is trying to mitigate by performing the inspection task. NASA regulations state that systems must be two-fault tolerant in order to operate in proximity to the ISS or other high-value target [42]. This operational requirement is mandated in order to preserve the system assets (which can include crew) and to preserve functionality in the presence of predicted or existing failures [43]. By this token, the propulsion system must be capable of completing the inspection task in the event of one failure and safely aborting the mission in the event of two failures.

The guiding principle behind a plenum-based architecture is that a valve failing in a stuck-open position (“valve fail-on”) will impart a bounded, predictable, and small impulse governed by the plenum volume which can be tightly controlled. Furthermore, introducing a series of two plenums in each thruster serves to preserve the operation of the system in the event of one or two valves failing open. Thus, safety is enhanced not only through redundancy, but also by physically limiting the amount of uncontrolled motion that is attainable in a jet fail-on situation.

2.1.2 Design Reference Mission

Citing the notable incidents in human spaceflight as motivation, we define a hypothetical mission whereby the CubeSat is deployed to inspect an exterior point on the International Space Station (ISS). The “worst-case” would require the CubeSat to inspect the furthest point of the largest dimension of the International Space Station out of the initial orbital plane, thus requiring the greatest expenditure of fuel to change its orbit and reach the target. The ISS’s largest span is along the Integrated Truss Structure—the primary structure upon which solar arrays, radiators, and other equipment is mounted—which measures ap-

proximately 109 meters long and is illustrated in Fig 2.1. Therefore, the satellite's trajectory must be adjusted such that it reaches at least 54.5 meters from the center of mass (C.M.) of the ISS, as illustrated in Fig 2.2. This scenario was chosen because plane-changing maneuvers are the most energetically costly, and therefore establish an upper bound for our performance criterion.

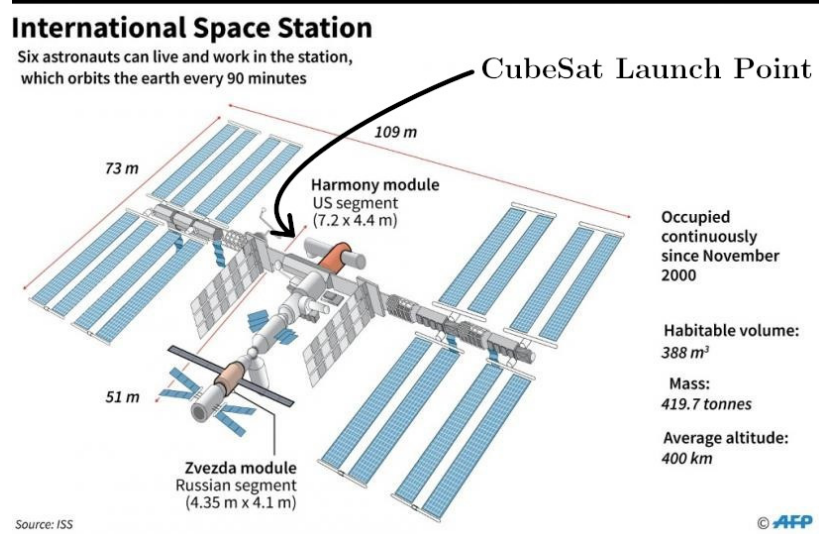


Figure 2.1: ISS dimensions (Image courtesy of Agence France-Presse (AFP) [44])

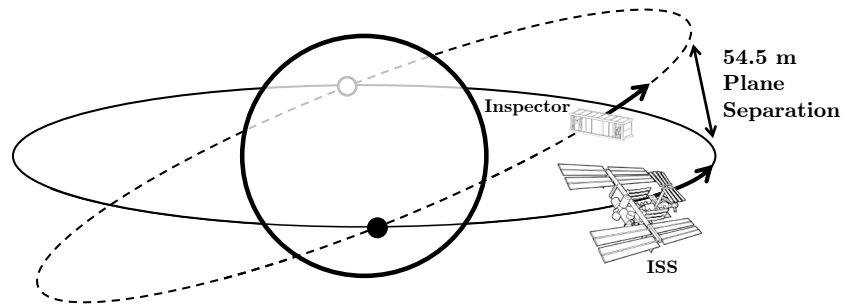


Figure 2.2: Orbits of the ISS and inspection CubeSat (not to scale) illustrating a maximum separation of 54.5 meters.

With the mission objective established, we will introduce the governing equations to model the relative motion between the inspection CubeSat and the ISS in the next section.

2.2 Determining ΔV Requirements

The inspection CubeSat’s orbital motion is modeled using the Clohessy-Wiltshire equations, which describes the relative motion of two bodies orbiting a common gravitational center. This model will be applied to the inspection task outlined previously and used to estimate the ΔV required to reach the hypothetical inspection target. An additional analysis will be performed to estimate how much ΔV will be required to maintain the CubeSat’s position around the inspection target for a variable amount of time. Following this, the ΔV required to deorbit or otherwise remove the CubeSat from the ISS’s proximity at the end of the inspection mission will be calculated. The total ΔV will be tabulated and used to inform net thrust and impulse requirements for the satellite, the details of which are covered in Section 2.3.

2.2.1 Clohessy-Wiltshire Model

The simplest mathematical model of orbital motion is described by Kepler’s laws of planetary motion, and indeed this would theoretically be sufficient for describing the short-term orbital motion of the ISS and the corresponding inspection satellite. However, applying Kepler’s laws to extract the relative motion between two objects presents a number of mathematical challenges owing to the nonlinearity of these equations. Additionally, the large disparity between the orders of magnitude of the distances and masses involved makes solving these equations numerically challenging. A solution to these challenges was derived in 1960 by W.H. Clohessy and R.S. Wiltshire of the Martin Company while developing a guidance system for satellite rendezvous, and is known today as the Clohessy-Wiltshire model [45].

The Clohessy-Wiltshire model summarized by Equation Set 2.1 describes the relative motion between two spacecraft orbiting a common body – a three-body problem, albeit simplified by a number of assumptions. In this model, the initial spacecraft is the “target” and is assumed to be in a perfectly circular orbit around the perfectly spherical common body while the other “chaser” spacecraft can be in either an elliptical or circular orbit. The model assumes both spacecraft are relatively close to one another (a few tens of kilometers), as larger distances will result in greater error due to linearization. The reference frame of the system is affixed to the target spacecraft, and the system of equations themselves are

first-order accurate. The reader should note that the accelerations which appear in the Clohessy-Wiltshire model are due to the target being in a non-inertial frame of reference and are therefore incomplete.

$$\ddot{x} = 3n^2x + 2n\dot{y} \quad (2.1a)$$

$$\ddot{y} = -2n\dot{x} \quad (2.1b)$$

$$\ddot{z} = -n^2z \quad (2.1c)$$

The closed-form solution of the Clohessy-Wiltshire model results in a set of coupled equations for motion in the x - and y -directions and a decoupled equation for motion in the z -direction. As we are only looking in the z -direction (out-of-plane motion) per the DRM objective, we only require the closed-form solution to motion in the z -axis (Equation 2.2).

$$\begin{bmatrix} z(t) \\ \dot{z}(t) \end{bmatrix} = \begin{bmatrix} \cos nt & \frac{1}{n} \sin nt \\ -n \sin nt & \cos nt \end{bmatrix} \begin{bmatrix} z_0 \\ \dot{z}_0 \end{bmatrix} \quad (2.2)$$

The parameter n is the orbital rate of the target body, determined using Equation 2.3, and expressed in units of rad/s.

$$n = \sqrt{\frac{\mu}{a^3}} \quad (2.3)$$

The parameters a and μ are the radius of the target body's circular orbit and the standard gravitational parameter, respectively. The relevant values used in the forthcoming analysis are shown in Table 2.1.

Supplied Values	Earth Radius	6378 km [46]
	ISS Altitude (Average)	409 km [47]
	Standard Gravitational Parameter (μ)	$3.986 \times 10^{14} \text{ m}^3/\text{s}^2$ [48]
Calculated Values	ISS Orbital Radius (a)	$6.787 \times 10^6 \text{ m}$
	ISS Orbital Rate (n)	$1.129 \times 10^{-3} \text{ rad/s}$
	ISS Orbital Period (T)	92.72 min
	ISS Orbital Velocity (V_o)	7663 m/s

Table 2.1: Orbital parameters used in Clohessy-Wiltshire model

Assuming the inspection satellite is a “chaser” in a similarly circular orbit as the target but at a different inclination, the acceleration in the x - and y - directions will be zero and the only apparent motion will take place along the z - direction. As described by Equation 2.1c, acceleration in the z -direction is directly proportional to distance along the same axis. Consequently, a larger acceleration will appear to act on the chaser spacecraft as it moves further out-of-plane from the target, meaning any action taken to change the chaser’s momentum must also overcome a larger relative acceleration. In other words, for a fixed thrust and burn time, the effectiveness of a given applied impulse will be reduced as the chaser moves further away from the target.

The degree to which maneuver time affects impulsive effectiveness can be determined by integrating the Clohessy-Wiltshire equation which governs acceleration in the lateral z - direction. As previously described, any deviation from the orbital plane of the target spacecraft will result in an acceleration appearing to drive the chaser back towards the target. The acceleration is not constant but instead cycles periodically with orbit where maximum acceleration is reached at the two points of furthest separation between the target and chaser spacecraft during one complete revolution. Velocity, being defined as the integral of acceleration, is out of phase by 90° and as such is zero when acceleration is maximum. Likewise, velocity is maximum when acceleration is zero. This occurs when the chaser spacecraft reaches the two points where the orbital paths of the target and chaser spacecraft cross – called the “ascending” and “descending” nodes. In each case, the acceleration vector always points towards the target spacecraft.

2.2.2 Inclination Change Requirements

As stated in Section 2.1.2, the satellite must adjust its orbital inclination such that its trajectory will take it along a path that will just reach the edge of the largest dimension of the ISS in the z -direction. The Integrated Truss Section is the largest structure of the ISS and is 109 meters long (including the extra length of the attached solar panels), so the satellite’s trajectory must place it at 54.5 meters from the C.M. of the ISS. The orientation of the ISS is such that the axis of the Integrated Truss Section lies out of the orbital plane, thus the inspection satellite will be required to change its inclination to reach the aforementioned inspection position. Plane change maneuvers can be very costly in low-Earth orbit (LEO)

since the direction of the orbital velocity vector must be changed, and the amount of ΔV required to change the direction of that vector increases with the initial velocity.

The following assumptions are made in determining the required ΔV for this maneuver:

- The Center of Mass (C.M.) of the ISS lies equidistant from either end of the truss structure
- The inspection CubeSat's initial orbit is identical to the ISS's orbit
- The orbits of both spacecraft are perfectly circular throughout the entire maneuver
- Impulse is applied instantaneously

These assumptions greatly reduce complexity during initial scoping and propellant sizing and are considered reasonable for the time being. Perhaps the largest assumption – and one that will be reexamined when determining thrust duration in Section 2.3.1 – is the assumption of instantaneous impulse. For the time being, we assume that as long as the impulse duration is less than 1% of half the orbital period, it is sufficiently short to be treated as instantaneous.

For a circular orbit, the inclination angle and resultant required ΔV can be calculated using Equation Set 2.4. The inclination angle θ is first determined by Equation 2.4a, which is simply the Law of Cosines applied to our situation. In this equation, the value c represents the maximum separation between our target spacecraft and inspection CubeSat, while the values a and b represent the orbital radii of the two spacecraft which, since we assume circular and equal orbits, are equal to one another. Once the inclination angle is determined, the resultant required ΔV can be determined from Equation 2.4b, where the parameter V_o represents the orbital velocity for a circular orbit.

$$\theta = \cos^{-1} \frac{a^2 + b^2 - c^2}{2ab} \quad (2.4a)$$

$$\Delta V = 2V_o \sin \frac{\theta}{2} \quad (2.4b)$$

For a circular orbit of radius 6787 km (409 km above mean sea level) and an inspection target distance of 54.5 meters, the inspection CubeSat must change its inclination by 0.00046° ($0.0276'$). At an orbital velocity of 7663 m/s, this corresponds to a required ΔV of 0.062 m/s. Upon application of this ΔV , the satellite will reach its intended destination at 1/4

of the orbital period: approximately 23 minutes for an ISS-like orbit. Without any further ΔV applications, the satellite's position will be solely determined by the orbital mechanics described by the Clohessy-Wiltshire equations. It will continue to drift in an oscillating motion from one side of the truss to the other, returning back to its starting position with each orbit.

2.2.3 Station-Keeping Maneuver Requirements

When the CubeSat's orbit is not coplanar with the ISS, there will always be some amount of relative motion between the two vehicles. The magnitude of this relative motion will be dictated by the angular separation between their respective orbits, and the periodicity will be determined by the altitude of their orbits. Once the CubeSat reaches its inspection target, it will immediately begin to drift back toward the ISS, top at the opposite side of the truss, and subsequently begin to drift back again. In the event the CubeSat must remain within a fixed range of the inspection target for a duration longer than orbital mechanics allow for, thrust must be applied along the z -axis to modify the CubeSat's orbit and allow it to remain in proximity to the inspection site. These maneuvers will take place away from the ascending and descending nodes of the co-orbits, at the point of farthest separation between the two orbital paths, necessitating greater fuel expenditure.

Ideally, continuous station-keeping could be attained by applying a constant thrust to negate the apparent restoring force described by Equation 2.1c. In the inertial frame, this thrust would continually change the orientation of the inspection satellite's orbital angular momentum vector (\bar{h}_{sat}). The vector \bar{h}_{sat} would precess about the target's orbital angular momentum vector (\bar{h}_{target}) at a rate equal to the period of the target spacecraft's orbit, and the inclination between the two orbits would remain constant. Tracing the path of the inspection satellite as it orbits the Earth while performing this maneuver would draw a circle parallel to the orbital plane of the target, offset by a distance equal the maximum separation between the two orbits (exaggeratedly shown in Figure 2.3), and not passing through the center of the Earth. Relative to the target spacecraft, the inspection spacecraft would appear to be motionless despite being out of the target spacecraft's orbital plane.

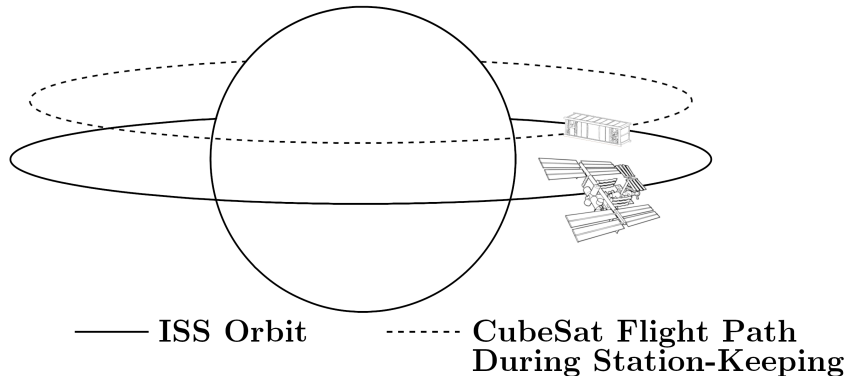


Figure 2.3: Apparent flight path of the CubeSat during continuous propulsion-assisted station-keeping per the Clohessy-Wiltshire model

At a separation of 54.5 meters and using the values supplied in Table 2.1, Equation 2.1c reveals that the satellite will experience a relative acceleration in the z -direction of $6.97 \times 10^{-5} \text{ m/s}^{-2}$. For a 5 kg CubeSat, this equates to $348 \mu\text{N}$ of constant thrust necessary to maintain relative position. Such maneuvering could theoretically be accomplished by an electric propulsion system, but the nature of the cold gas system explored herein makes this constant-thrust maneuver exceedingly difficult to control. Instead, relative position could be maintained within a prescribed window, called a “stray distance”, through the use of timed propulsive bursts from the cold gas system as illustrated by Figure 2.4, drawn with respect to the Local Vertical-Local Horizontal (LVLH) frame.

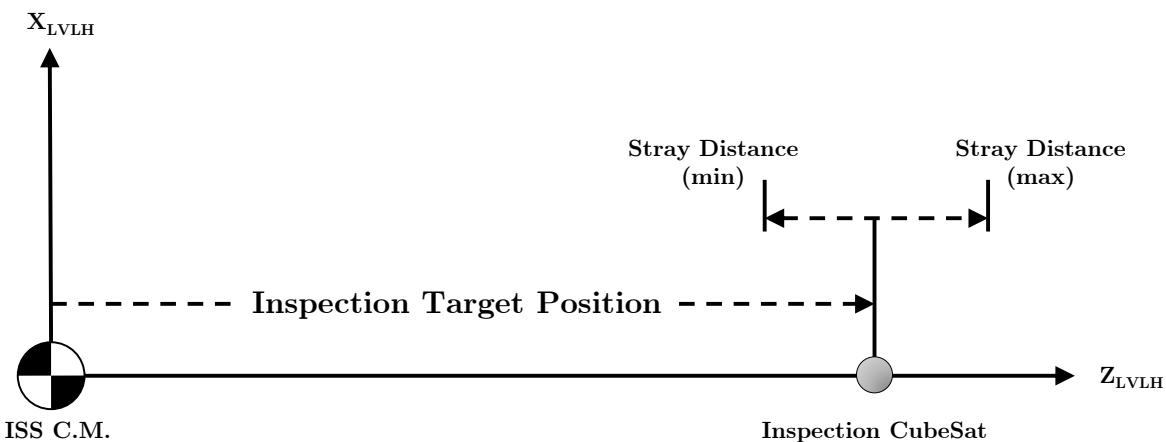


Figure 2.4: Illustration of the relative motion during an inspection task. In the LVLH frame, the Z-axis points down into the page and directly toward Earth, and the target's orbital velocity is along the X-axis.

Without a constant thrust to negate the relative motion between two co-orbiting objects with a non-zero inclination relative to one another, a series of scheduled burns must take place to keep the inspection satellite within range of the inspection target. From an observer on the station, the satellite would first appear to drift back toward the centerline of the station's orbital path until it reaches the edge of its allowed stray distance. At this point, a small propulsive burst would propel the satellite back in the opposite direction with equal speed. The satellite will slowly come to a stop before beginning to drift back toward the station, at which point the process will be repeated. This would result in what might be described as a slow "bouncing" motion.

The details of this periodic bouncing motion will depend both on how far out-of-plane the inspection target is and the allowable stray distance. The Clohessy-Wiltshire model can be used to determine the required ΔV and burn schedule for given target and stray distances. This relationship is illustrated in Figure 2.5 which, in addition to ΔV and burn schedule, also shows what the cumulative ΔV per orbit is required to maintain the prescribed position.

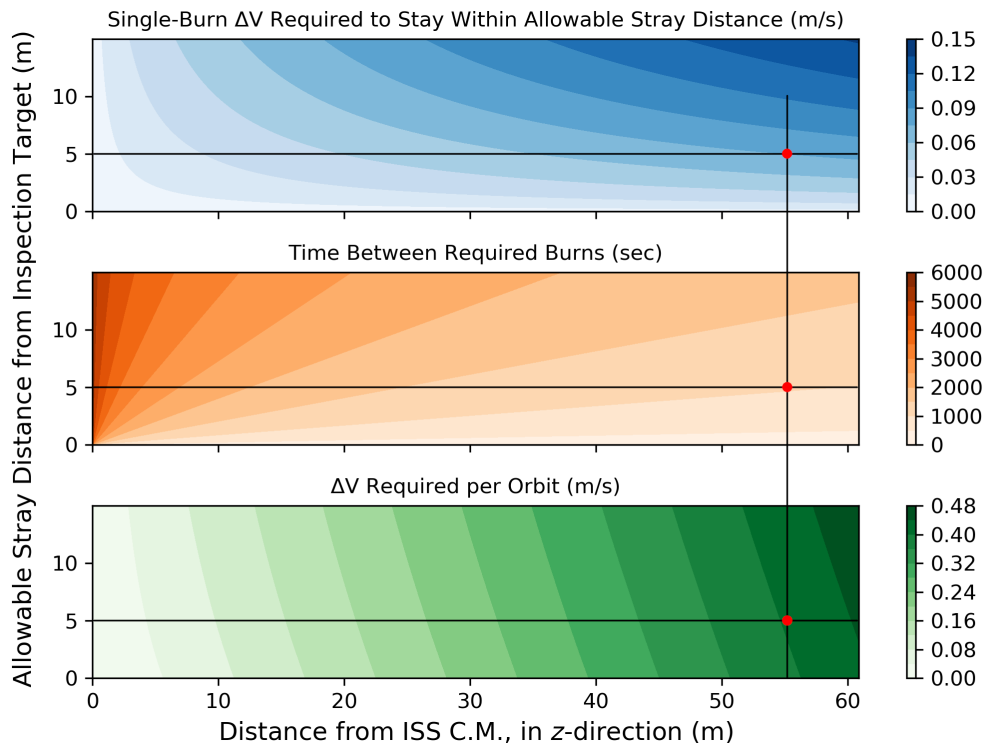


Figure 2.5: Clohessy-Wiltshire model showing how required ΔV and burn schedules vary with allowable stray distances from a range of out-of-plane inspection target positions. The selected target position and stray distance are indicated.

For a range of inspection target positions, the time-of-flight between each edge of the allowable stray distance window is calculated using the closed-form solution to Equation 2.1c. This time-of-flight is then used to determine the velocity at the edge of the stray window, at which point the ΔV required is simply taken to be $-2 \times$ the value, given that the speed must not only be reduced to zero, but entirely reversed in order to remain in the window. Likewise, the time between burns is simply taken to be $2 \times$ the time-of-flight from the max-to-min edges of the allowable stray window. The ΔV required per orbit is determined by dividing the ΔV required to stay within the allowable window by the ratio of the time between burns to the orbital period.

Allowable stray distance from the inspection target will largely be determined by the optics on the inspection CubeSat which, at the time of writing, have not been selected. Note that for a fixed inspection target position, the required cumulative ΔV per orbit is minimized by reducing the stray distance window size. Likewise, the required ΔV per single burn is reduced. The time between burns for even a small stray distance window of ± 1 meter at an inspection target position 54.5 meters out is on the order of many hundreds of seconds. As will be seen further in the development of this propulsion system, that is more than enough time to safely recharge the plenums and prepare for another corrective thrust.

For the time being, we will assume that a stray distance of ± 5 meters is prescribed for an inspection target at a distance of 54.5 meters, meaning that a corrective thrust will occur when the satellite closes in to 50 meters and will drift as far out as 60 meters from the C.M. of the ISS. This assumption fixes our single-burn ΔV requirement to 0.075 m/s, a time between burns of 1000 seconds, and a cumulative ΔV expenditure of 0.400 m/s per orbit.

Note that this requirement will slightly change the initial orbit inclination ΔV requirement. In Section 2.2.2 we used the 54.5 meter distance of the inspection target as the initial plane change requirement. Now that we must take into account an allowable stray distance, the initial plane change requirement must consequently shift out to 5 meters beyond the plane change target – 59.5 meters. At this distance, again using Equation Set 2.4, the required inclination change is a mere 0.00050° ($0.030'$), resulting in a required ΔV of 0.067 m/s – marginally higher than the initial estimate of 0.062 m/s.

Once again, the ΔV estimates determined in this section and prior were for plane change

and out-of-plane maneuvers, which are generally the most costly in terms of propellant consumption. Any inspection target which can be reached in-plane will require less ΔV , so this situation is not discussed herein.

2.2.4 End-of-Mission Requirements

In addition to completing the inspection task, the satellite must also be capable of deorbiting itself in a safe and timely manner, or at the very least removing it from the proximity of the ISS. This requirement is necessary due to increased launch rate of small satellites into low Earth orbit, each of which create potential collision hazards for future missions. The Inter-Agency Space Debris Coordination Committee (IADC) has mandated that all spacecraft be placed in a LEO such that it will decay within 25 years post-launch, or be placed in a graveyard orbit indefinitely post-mission [49].

Significant prior work has been completed on the analysis of CubeSat orbit decay, courtesy of Oltrogge and Leveque from Analytical Graphics, Inc [50]. The analysis presented by them served to support the prediction of the orbital lifetime of the inspection CubeSat which showed that even in the worst-case scenario, the inspection CubeSat's orbit should decay well within the 25-year limit. A sample of similar size and mass CubeSats taken from their analysis has been updated and tabulated in Table 2.2. Note that both missions listed are specifically CubeSats of 3U form factor.

Mission	Mass (g)	Apogee (km)	Perigee (km)	Lifetime (years)
GeneSat-1	5000	420	413	3.64
PharmaSat	4500	466	428	3.24

Table 2.2: Orbit lifetime for a selection of 3U CubeSats which were placed in similar orbits as is to be expected for this CubeSat mission.

This listing shows that the orbits of small spacecraft launched to altitudes like that of the ISS will naturally decay in well under 25 years, although there is certain to be some variability owing to externalities such as atmospheric variations over solar cycles or differing ballistic coefficients. For the purposes of this mission, however, it will still be necessary to move the spacecraft out of range of the ISS post-mission to prevent any possibility of collision in the

future. Collision warnings for the ISS are supported by data from the United States Space Surveillance Network, operated by the United States Strategic Command (USSTRATCOM) [51]. USSTRATCOM analyzes the trajectory of orbital debris and publishes warnings in the event debris is predicted to come in proximity to the ISS. Special perturbation methods are used to screen debris after the initial prediction puts it within a box measuring $\pm 10 \text{ km} \times \pm 40 \text{ km} \times \pm 40 \text{ km}$ ($\pm \Delta r_u \times \pm \Delta r_v \times \pm \Delta r_w$).

The $\{u \ v \ w\}$ frame is defined as such:

- u : Radial position, drawn from the center of the host body to the orbiting body. Variations in u are equivalent to variations in altitude. For circular orbits, this vector lies exactly opposite to the Z_{LVLH} direction illustrated in Figure 2.4.
- w : Angular momentum. This vector is parallel to the cross-track direction Y_{LVLH} in the LVLH frame.
- v : $w \times u$. For a circular orbit, this vector is coincident with the in-track velocity vector X_{LVLH} in Figure 2.4.

Further analysis is performed once the debris is predicted to fall within a box measuring $\pm 2 \text{ km} \times \pm 25 \text{ km} \times \pm 25 \text{ km}$. Finally, hazard avoidance maneuvers are considered when debris is predicted to come within a box-shaped zone centered on the ISS measuring $\pm 0.75 \text{ km} \times \pm 25 \text{ km} \times \pm 25 \text{ km}$. Therefore, the deorbit maneuver must reduce the altitude of the satellite by a minimum of 0.75 km. However, since USSTRATCOM generally flags any object that is predicted to come within 60 km of the ISS, the most desirable deorbit maneuver would reduce the satellite's altitude by at least that same amount.

As discussed, 3U CubeSats of similar altitude can be expected to naturally deorbit well within 25 years, so the only task remaining is to lower the orbit such that it would not present a navigational hazard to the ISS. Table 2.3 lists the total ΔV required for a range post-mission altitude changes assuming the initial and final orbits are circular, determined using *vis-viva* equation for a Hohmann transfer. The details of this process is reviewed in Appendix A.

Target Alt (Circular Orbit, km)	ΔV Required (m/s)
409	0
408.25	0.423
407	1.129
349	34.101

Table 2.3: ΔV requirements for complete mission

As can be seen, the ΔV required to remove the CubeSat from the USSTRATCOM flagging range is significantly larger than any of the on-mission maneuvers previously discussed. Therefore, it is likely that the CubeSat will not contain enough propellant in order to fully meet this objective. For the time being, we will make the deorbit objective to be an altitude reduction of the minimum of 0.75 km, which will require 0.423 m/s of ΔV .

2.2.5 Summary of ΔV Requirements

Tabulating the ΔV requirements from the previous sections, we find that the vast majority of propellant would be needed for deorbiting the inspection satellite, as seen in Table 2.4.

Maneuver	ΔV (m/s)
Single Inclination Change	0.067
Single Orbit Station-Keeping	0.400
End-of-Mission Altitude Change	0.423
Total ΔV Required	0.890

Table 2.4: ΔV requirements for complete mission

The value of 0.890 m/s represents an approximation of how much ΔV is required to complete this specific objective and represents the minimum requirement. This does not include considerations for detumbling and nulling out relative velocity after ejection, maneuvering around structures, inspecting multiple points in one mission, or performing any on-track maneuvers. Moreover, this tally assumes that 100% of the thrust is pointed in the desired direction and that thrust is effected directly through the center of mass of the satellite to produce pure translational motion. Realistically, the configuration of multiple

thrusters around the CubeSat will determine how efficiently thrust is applied and what combination of thrusters must be used in order to produce the desired motion. To that end, a brief exploration of thruster configuration is covered in Section 2.3.3, the results of which will be used to inform the design of each individual thruster.

2.3 Propulsion System Design Considerations

The ΔV requirements calculated in Section 2.2 and tabulated in Table 2.4 will be used to determine net thrust requirements. This will be achieved by determining the net impulse with ΔV and mass and relating this to burn time and thrust. Following a brief overview of propellant selection based on the work of Lorenzen et al. [2], a description of thruster configuration on the CubeSat will be given. Thruster configuration will be used along with thrust and impulse requirements to inform the nozzle and plenum design for a single thruster line. The content of this section relies on the results of a computer program which was developed specifically to model the discharge from a single plenum to determine the time-rate of change of pressure, thrust, impulse, and other relevant properties.

2.3.1 Net Thrust and Impulse Requirements

The net thrust required to sufficiently modify the CubeSat’s orbit and reach the inspection target at the edge of the ISS can be estimated using the classical definitions of momentum and impulse. Momentum (p) is defined as the product of mass and velocity (Equation 2.5a). A force acting on an object changes the momentum of that object which, for an object of constant mass, will result in a change in velocity (Equation 2.5b). Impulse (J) is defined as the integral of force over a time interval, which can also be expressed in terms of mass and velocity (Equation 2.5c) Equating these two definitions of impulse forms a proportional relationship between average force, time, mass, and change in velocity (Equation 2.5d).

m = mass of spacecraft

$$p = mv \quad (2.5a)$$

$$F = \frac{dp}{dt} = m \frac{dV}{dt} \quad (2.5b)$$

$$J = \int_{t_1}^{t_2} F dt = m \int_{V_1}^{V_2} dV \quad (2.5c)$$

$$J = F_{avg} \Delta t = m \Delta V \quad (2.5d)$$

With regards to a spacecraft, the constant mass assumption is only appropriate for incrementally small propulsive events. For long burns that are typical for orbit injection burns or large changes in orbital characteristics, propulsion engineers must utilize the Tsiolkovsky rocket equation, illustrated in Equation 2.6. This equation defines the amount a spacecraft can change its velocity by the exit velocity of the propulsive exhaust (V_e) and the mass of the spacecraft before and after the burn (m_0 and m_f , respectively).

$$\Delta V = V_e \ln \frac{m_0}{m_f} \quad (2.6)$$

As the mass fraction m_0/m_f approaches 1, the change in velocity approaches zero. Furthermore, the non-constant plenum pressure will result in an equally non-constant exit velocity, making the determination of ΔV for a single plenum discharge using Equation 2.6 difficult. Therefore, as an initial approximation, we will assume the spacecraft mass stays constant during the course of a single plenum discharge since the mass of propellant consumed will be significantly smaller than the mass of the CubeSat. This assumption is conservative since, realistically, some mass would be lost and the resultant thrust would produce a larger ΔV than estimated here. However, once the dynamics of a single plenum discharge are better understood, Equation 2.6 can be used to determine the overall propellant mass required for a complete mission by determining the average exit velocity over the course of a single plenum discharge.

Initially, we can utilize Equation 2.5d to determine a required average net thrust (F_{avg}). For a 5.00 kg satellite requiring 0.067 m/s of ΔV as determined in Section 2.2, a total net impulse of 335 mN-s is found to be required. To determine average net thrust, a thrust time must also be known or assumed.

Previously, while determining ΔV requirements, the change in velocity was assumed to be applied instantaneously and thrust time was not considered. Therefore, in order for the ΔV requirements to remain valid, the thrust time must be made sufficiently small so as to be approximately instantaneous.

Because of this, we will choose to limit the total thrust time to no more than 1% of half the orbital period of the ISS in order to maintain an approximately instantaneous impulse. Note that a half-period is selected as the reference rather than a full period due to the fact that the maneuver will see the satellite return to (and continue through) its starting position half-way through a full orbit. For an orbit period of 5563 seconds (92.72 minutes, taken from Table 2.1), it places an upper bound of 28 seconds on the total time allowed to thrust. Consequently, this establishes a required minimum average net average thrust of 12.0 mN over the duration of the maneuver.

In summary, the satellite will require a net average thrust of 12.0 mN acted upon it over a duration of no more than 28 seconds in order to adjust its orbit so as to reach the inspection target. This thrust can be applied either from a single thruster or a combination of thrusters configured such that the sum of their individual thrusts meets or exceeds the net thrust requirement. Section 2.3.3 will discuss the assumed thruster configuration for the satellite and illustrate how the layout and orientation of thrusters around the body of the satellite will determine the thrust and impulse requirements for each individual thruster.

2.3.2 Propellant Selection

Propellant choices are laid out by Lorenzen [2] and are limited largely by safety factors such as storage pressure and toxicity. Specifically, propellant storage pressure must be less than 100 pounds per square inch *absolute* (psia) as a holdover from NASA's requirements for payloads using the space shuttle [52], and propellants must be selected such that they are capable of being scrubbed by the ISS air recycling system in the event of a leak. The assumption for this project is that the final propellant choice will most likely be a low vapor pressure liquid such as R134a, which vaporizes to 82.9 psia at 68°F (572 kPa at 20°C). For on-ground testing, pressure-regulated CO₂ is instead being used as an analogous propellant due to its availability, low cost, and non-toxic properties.

2.3.3 Thruster Configuration

The orientation and configuration of thrusters around the body of the CubeSat will need to be known or assumed in order to appropriately size each individual thruster such that the net thrust requirement is met. For this analysis, the thrusters are configured such that each thruster is placed at the corner of a 1U section in the middle of the satellite and oriented 45° laterally inward and vertically downward, illustrated in Figure 2.6. This configuration was chosen as it allows for independent 6 DOF control while minimizing the number of individual thrusters, thus minimizing mass and reducing complexity. Furthermore, the complete loss functionality on any two separate thrusters will still allow partial control of the CubeSat.

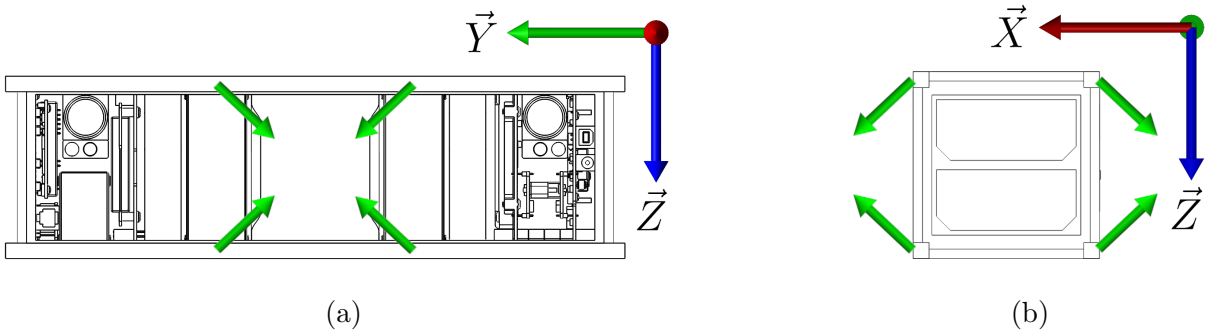


Figure 2.6: Thruster configuration, (a) front view, (b) side view

Thrust components are determined by computing the rotation angles between the satellite reference frame and each individual thruster's reference frame, which is assumed to be oriented such that the X-axis is collinear with the line of thrust. The angles of rotation are defined here as corresponding to a proper Euler $[X' \ Z' \ X'']$ rotation sequence, although we are by no means strictly limited to this order. Only two rotations are required to translate from one frame to the other given that the thruster is axisymmetric.

Taking as example the upper-right thruster in Figure 2.6a, the rotation is performed in two steps: first by rotating $+45^\circ$ about the X-axis to produce the X', Y', Z' reference frame, followed by rotating $+45^\circ$ about the Z' -axis. Propellant would be expelled along the X'' axis, and the corresponding thrust vector would therefore be pointed along the $-X''$ axis.

These two rotation steps are mathematically modeled by Equations 2.7 and 2.8:

$$\begin{bmatrix} X' \\ Y' \\ Z' \end{bmatrix} = \begin{bmatrix} 1 & 0 & 0 \\ 0 & \cos(45) & \sin(45) \\ 0 & -\sin(45) & \cos(45) \end{bmatrix} \begin{bmatrix} X \\ Y \\ Z \end{bmatrix} \quad (2.7)$$

$$\begin{bmatrix} X'' \\ Y'' \\ Z'' \end{bmatrix} = \begin{bmatrix} \cos(45) & \sin(45) & 0 \\ -\sin(45) & \cos(45) & 0 \\ 0 & 0 & 1 \end{bmatrix} \begin{bmatrix} X' \\ Y' \\ Z' \end{bmatrix} \quad (2.8)$$

When Equation 2.7 is substituted into 2.8, they combine and reduce to form Equation 2.9, which represents the conversion from the satellite reference frame X, Y, Z to the upper-right thruster reference frame X'', Y'', Z'' .

$$\begin{bmatrix} X'' \\ Y'' \\ Z'' \end{bmatrix} = \begin{bmatrix} \cos(45) & \sin(45)\cos(45) & \sin^2(45) \\ -\sin(45) & \cos^2(45) & \sin(45)\cos(45) \\ 0 & -\sin(45) & \cos(45) \end{bmatrix} \begin{bmatrix} X \\ Y \\ Z \end{bmatrix} \quad (2.9)$$

Reducing the sine and cosine terms inside the rotation matrix, we get a simplified relationship expressed by Equation 2.10.

$$\begin{bmatrix} X'' \\ Y'' \\ Z'' \end{bmatrix} = \begin{bmatrix} \frac{\sqrt{2}}{2} & \frac{1}{2} & \frac{1}{2} \\ -\frac{\sqrt{2}}{2} & \frac{1}{2} & \frac{1}{2} \\ 0 & -\frac{\sqrt{2}}{2} & \frac{\sqrt{2}}{2} \end{bmatrix} \begin{bmatrix} X \\ Y \\ Z \end{bmatrix} \quad (2.10)$$

By inverting this matrix, we derive a means to directly translate the thrust from the individual thruster into its components in the X, Y, Z frame, expressed by Equation 2.11. This will then be used to determine what portion of the individual thrust contributes to the net thrust of the satellite.

$$\begin{bmatrix} X \\ Y \\ Z \end{bmatrix} = \begin{bmatrix} \frac{\sqrt{2}}{2} & -\frac{\sqrt{2}}{2} & 0 \\ \frac{1}{2} & \frac{1}{2} & -\frac{\sqrt{2}}{2} \\ \frac{1}{2} & \frac{1}{2} & \frac{\sqrt{2}}{2} \end{bmatrix} \begin{bmatrix} X'' \\ Y'' \\ Z'' \end{bmatrix} \quad (2.11)$$

Per Equation 2.11, a thrust $|T|$ in the $-X''$ direction would result in a thrust component $\frac{\sqrt{2}}{2}|T|$ strong in the X direction and $\frac{1}{2}|T|$ strong in the Y and Z directions. Combining all

four thrusters would result in a singular net thrust of magnitude $2\sqrt{2}|T|$ in the X direction, although only two thrusters would be needed for pure translation in the X direction. Four thrusters would be required to translate in the Y and Z directions.

Since the thrust vector is entirely in the X'' direction, Equation 2.11 simplifies down to the following relationship:

$$\begin{bmatrix} X \\ Y \\ Z \end{bmatrix} = \begin{bmatrix} \frac{\sqrt{2}}{2} \\ \frac{1}{2} \\ \frac{1}{2} \end{bmatrix} \begin{bmatrix} X'' \end{bmatrix} \quad (2.12)$$

This relationship will be used later in Section 2.4 to determine the thrust requirements for each individual thruster line.

On-ground testing will be conducted in 3 DOF using an air bearing-based platform, outlined in greater detail in Section 3.1. This platform will have four thrusters in an analogous configuration, shown in Figure 2.7, and labeled ‘A’ through ‘D’ sequentially in a clockwise direction. Each thruster will be oriented at an angle θ in increments of 45° and the corresponding line of thrust will lie along the X' axis for each thruster’s reference frame.

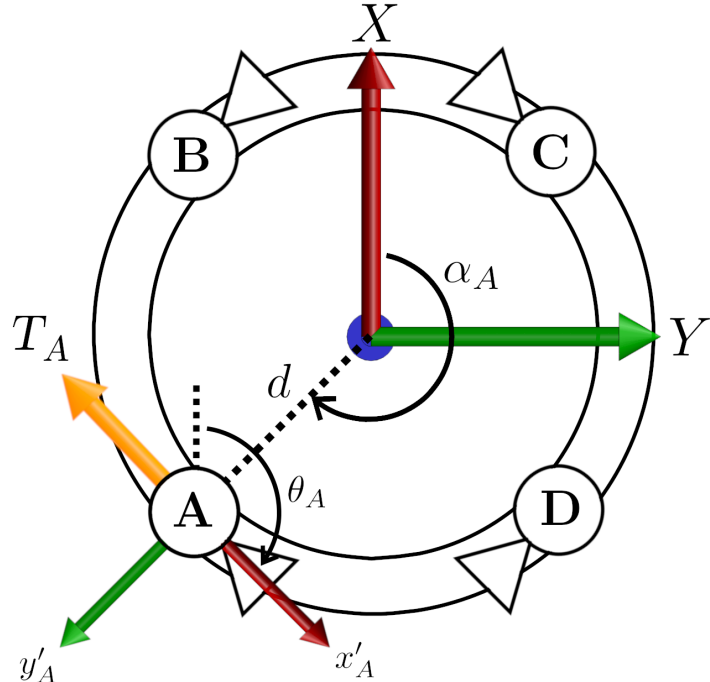


Figure 2.7: Thruster configuration for 3 DOF control during on-ground testing.

The body reference frame is a right-handed coordinate frame located at the geometric center of the platform with the X-axis defining the forward direction, Y-axis defining the starboard direction, and with Z-axis pointing down. Thus, from our overhead perspective, clockwise rotations are defined as positive. Likewise, the position of each thruster in the body frame is governed by a corresponding angle α measured from the body X-axis and distance d measured from the body origin.

Equation 2.13 demonstrates how thrust from A translates into the reference frame of the entire assembly. For simplicity, the Y-axis component of the thruster frame is omitted from the translation since the line of thrust acts entirely along the X-axis of the thruster. The thruster frame X-axis (notated as x') is rotated $\theta_A = 135^\circ$ degrees relative to the body frame X-axis.

$$\begin{bmatrix} X \\ Y \end{bmatrix} = \begin{bmatrix} \cos(\theta_A) \\ -\sin(\theta_A) \end{bmatrix} = \begin{bmatrix} \cos(-135) \\ -\sin(-135) \end{bmatrix} = \begin{bmatrix} -\frac{\sqrt{2}}{2} \\ \frac{\sqrt{2}}{2} \end{bmatrix} \begin{bmatrix} x'_A \end{bmatrix} \quad (2.13)$$

Expanding on this concept, we construct a relationship for the entire propulsion assembly by relating the total resultant forces and moments on the air bearing platform (T_X, T_Y, M_Z) to the forces imparted by each of the four thruster (T_A, T_B, T_C, T_D), as shown in Equation 2.14. The functions \sin and \cos are abbreviated as s and c , respectively, for the sake of compact representation.

$$\begin{bmatrix} T_X \\ T_Y \\ M_Z \end{bmatrix} = \begin{bmatrix} c(\theta_A) & c(\theta_B) & c(\theta_C) & c(\theta_D) \\ -s(\theta_A) & -s(\theta_B) & -s(\theta_C) & -s(\theta_D) \\ d_A s(\theta_A - \alpha_A) & d_B s(\theta_B - \alpha_B) & d_C s(\theta_C - \alpha_C) & d_D s(\theta_D - \alpha_D) \end{bmatrix} \begin{bmatrix} T_A \\ T_B \\ T_C \\ T_D \end{bmatrix} \quad (2.14)$$

The X - and Y -axes are replaced by the net thrust T in said axes, and the resultant moment M about the Z -axis is defined by both the orientation and position of the thruster relative to the body frame. We introduce the angle α and distance d to specify the thruster location in the body frame, also indicated in Figure 2.7. The details of the physical design of the air bearing platform leading to knowledge of the value d are discussed in Section 3.1. Notation for orientation relative to the body frame remains identical.

Given the relationships summarized in Table 2.5, the values in Matrix Equation 2.14 can be filled in and reduced to a simple set, summarized in Matrix Equation 2.15.

Thruster	θ	α	d
A	135°	-135°	0.18 m
B	45°	-45°	0.18 m
C	-45°	45°	0.18 m
D	-135°	135°	0.18 m

Table 2.5: Tabulated summary of the geometric properties which define the location and orientation of the four thrusters on the air bearing platform.

$$\begin{bmatrix} T_X \\ T_Y \\ M_Z \end{bmatrix} \begin{bmatrix} -\frac{\sqrt{2}}{2} & \frac{\sqrt{2}}{2} & \frac{\sqrt{2}}{2} & -\frac{\sqrt{2}}{2} \\ \frac{\sqrt{2}}{2} & \frac{\sqrt{2}}{2} & -\frac{\sqrt{2}}{2} & -\frac{\sqrt{2}}{2} \\ -d & d & -d & d \end{bmatrix} \begin{bmatrix} T_A \\ T_B \\ T_C \\ T_D \end{bmatrix} \quad (2.15)$$

The relationships outlined by Equation 2.15 illustrate the translation between forces imparted by each thruster to the net result on the body. When thrust is known, these equations yield insight into the predicted motion of the test platform for any combination of thruster firings. Assuming equal thrust is directed along the $-x'$ axis for each thruster, the combinations listed in Table 2.6 will be required to impart motion in the listed direction.

Translation	Thruster Combinations
+X	A + D
-X	B + C
+Y	A + B
-Y	C + D
Rotation	Thruster Combinations
+Z	A + C
-Z	B + D

Table 2.6: Thruster combinations required to affect motion in the listed directions.

2.3.4 Considerations for a Plenum-based Architecture

As outlined previously in Section 1.5, the propulsion system explored herein will utilize discrete volumes, or “plenums”, to supply propellant to thrusters. Specifically, each thruster will have its own set of plenums, as illustrated previously in Figure 1.10, to limit the amount of propellant lost in the event of a series of two valve fail-ON failures in a single thruster line. As a consequence of this design choice, the supply pressure for a single plenum discharge will constantly decrease, resulting in a non-constant thrust applied over the thrust duration. This behavior complicates the analysis of this system, necessitating the development of a computational model to more effectively study the time-rate of change of thrust. This program was used to determine the required plenum volume and nozzle size for a single thruster and is discussed in Section 2.4.

Furthermore, it is possible that multiple thruster firings / plenum discharges will be necessary to perform a plane-change maneuver. To that end, the time needed refill the plenum must also be accounted for during the allotted thrusting period. The initial design will assume that a plenum will require an equal amount of time to recharge as it does to discharge. Once again, the effect this consideration will have on the final design is outlined in further detail in 2.4.

2.4 Nozzle Design and Plenum Sizing

This section will lay out the process for determining an appropriate nozzle geometry and plenum size given the requirements listed previously in Section 2.2. Two different designs will be outlined in parallel: an “in-space” design for use on the hypothetical CubeSat, and an analogous “on-ground” design which will be pursued for the remainder of this project. The “on-ground” design will be used to test the plenum-based concept and replicate the desired motion of the inspection CubeSat, within the limitations of the air bearing test bed. Due to size constraints and adverse friction present in the air bearing test bed, the on-ground performance objective was made to have a larger net thrust and shorter discharge time in order to impart an equal amount of ΔV as required of the actual CubeSat.

2.4.1 In-Space Performance Reqs. and Resultant Design

With the theory and performance requirements established, work can begin on designing an appropriate nozzle. The in-space propulsive requirements are listed in Table 2.7 with R134a as the chosen propellant. Taking into account the thruster configuration described in 2.3.3, the net performance can be broken down into performance requirements for each of the four individual thrusters.

In-Space Performance Requirements

Propellant	R134a	
Parameter	Net Performance	Per Thruster
ΔV	0.067 m/s	0.024 m/s
Impulse	335 mN-s	118 mN-s
Maneuver Time	28 sec	28 sec
Average Thrust	12.0 mN	4.24 mN

Table 2.7: Performance requirements to inform nozzle and plenum design for hypothetical in-space propulsion system for a 5 kg object.

Average thrust is related to nozzle design (most dramatically affected by throat diameter) and supply pressure. Likewise, impulse is related to the total plenum volume since, for a given nozzle geometry, a larger plenum will increase the amount of propellant available, thus increasing the discharge time. As described in Section 2.3.4, if the required plenum volume is too large to realistically integrate into the CubeSat, then multiple discharges from a smaller plenum could be performed back-to-back to achieve the same net impulse requirement.

Using the principles of isentropic flow outlined which are in Appendix B, a nozzle-plenum discharge simulation was programmed to explore the design space outlined in Table 2.7. The details of the plenum discharge simulation are outlined in Appendix C. The time-rate of change of the performance characteristics listed in Table 2.7 of a single plenum discharge is modeled and shown in Figure 2.8. An expansion ratio of 30 was arbitrarily selected for the nozzle geometry.

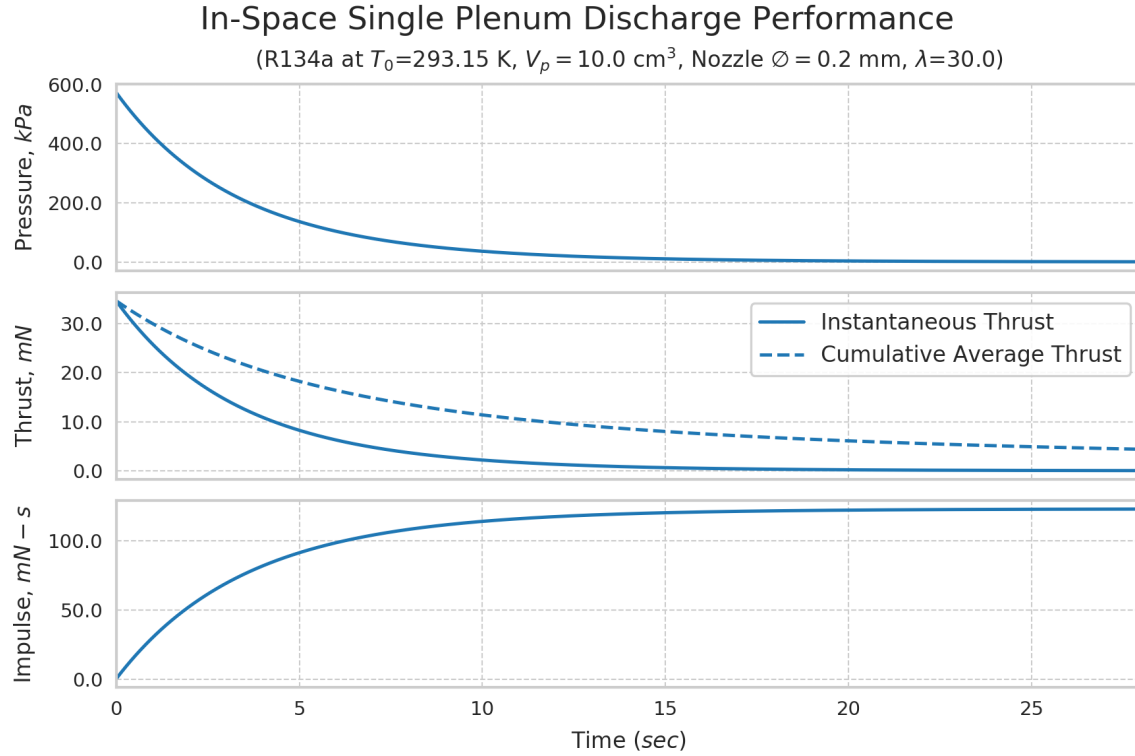


Figure 2.8: Simulation results for idealized thruster design wherein all required impulse is imparted in a single discharge. The impulse objective of 118 mN-s is met at 12.5 seconds resulting in an average thrust of 9.4 mN

The results from this simulation show that the average thrust and minimum impulse requirement can be met in a single discharge time period with the design parameters for each thruster listed in Table 2.8. With this design, the performance objective is in fact met after only 12.5 seconds, though this is not necessarily the most ideal design and would of course benefit from continued analysis beyond the scope of this project.

In-Space Design Specifications

Starting Pressure	572 kPa (82.9 psia)
Single Plenum Volume	10.0 cm 3
Nozzle Throat diameter (\emptyset)	0.2 mm
Nozzle Expansion Ratio (λ)	30

Table 2.8: Nozzle and plenum geometry to meet in-space performance requirements with one complete plenum discharge.

A group of sixteen plenums (two plenums per each of eight thrusters) at 10.3 cm^3 would require 165 cm^3 of internal volume which, while not too large for a 3U CubeSat, would warrant further exploration in the design trade space. Moreover, the design parameters listed in Table 2.8 merely represent the specifications which will exactly meet the minimum requirements and leaves no margin for error. Given the exponentially-decaying behavior of plenum-based thrust, a realistic design must consider an appropriate cutoff value at which the single discharge is considered “complete” and thus must increase the plenum volume to account for this margin. The work presented herein will proceed without considering any cutoff value and will instead attempt to observe how close to ideal performance one can achieve with the tools at hand. Considering the factors presented here and the constraints of mass and space for an actual in-space design, a realistic design would probably employ a design to achieve the net impulse requirement in multiple discharges and include additional considerations such as power requirements for holding valves open for this amount of time.

Further design consideration must also be given based on the required minimum impulse bit – the smallest unit of impulse capable of being applied by a thruster and a function of nozzle size and valve speed. The minimum impulse bit requirement will likely be determined based on the exposure time required for a single image taken by the on-board inspection cameras. In other words, the spacecraft must be capable of holding its attitude within a to-be-determined margin in order to produce clean images of the inspection target. A larger nozzle will be required for multiple plenum discharges in order to compensate for plenum recharge time, but will in turn increase the minimum impulse bit. Additionally, this idealized simulation has assumed entirely steady flow and does not take into account the time needed for the propellant to accelerate to its maximum velocity, referred to as the “rise time”. These considerations will not be explored herein since the primary focus of this work is to demonstrate the feasibility of a plenum-based propulsion system by constructing a physical prototype.

2.4.2 Total Propellant Mass for In-Space Design

Now that expected performance characteristics for an in-space propulsion system have been established, we can combine this information with the total ΔV budget outlined in Section 2.2.5 to estimate the total required propellant mass. The Tsiolkovsky Rocket Equation,

previously expressed in Equation 2.6 as a function of the nozzle exit velocity (V_e), can be reframed in terms of specific impulse (I_{sp} , the total amount of impulse delivered per unit mass of propellant mass). The transition from one form to the other takes place by equating the effective exit velocity with the product of the propellant I_{sp} and standard gravity (g_0), which is taken here to be 9.81 m/s^2 . In the form expressed in Equation 2.16, we also rewrite the final mass m_f in the denominator as the difference between the initial mass m_0 and the total propellant mass m_p used during flight.

$$\Delta V = I_{sp} g_0 \ln \frac{m_0}{m_0 - m_p} \quad (2.16)$$

I_{sp} is a measure of the efficiency of a rocket or thruster, and a higher I_{sp} is generally more desirable. Typical cold gas propulsion systems achieve an I_{sp} of 40 to 70 seconds [27] and lie on the extremely low end of efficiency, the tradeoff for which is a system with very predictable performance from an extremely simple and robust design. Based on the model results shown in Figure 2.9 which examines the time-rate of change of I_{sp} for this plenum-based architecture, we see that the system covered herein falls within this range.

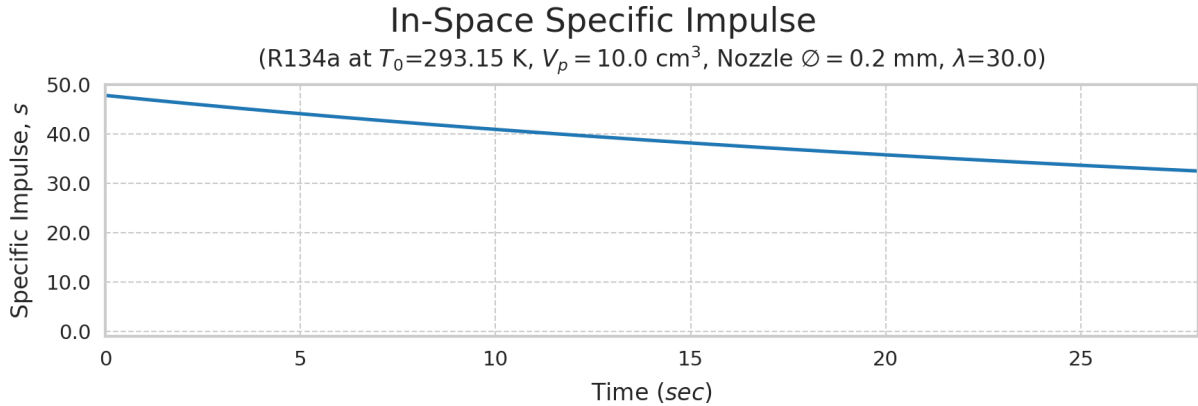


Figure 2.9: Simulation results showing the change in specific impulse (I_{sp}) for a single plenum discharge of the in-space design.

I_{sp} decreases linearly from 48 to 39 seconds resulting in a time-average I_{sp} of approximately 43.5 seconds. Rewriting Equation 2.16 to solve for the propellant mass m_p (Equation 2.17), we can directly estimate the propellant mass required to accomplish the mission objective.

$$\Delta m_p = m_0 - m_0 \exp \left(\frac{-\Delta V}{I_{sp} g_0} \right) \quad (2.17)$$

Using the system described herein, we must also take into account the thruster configuration as described in Section 2.3.3. The thruster configuration will reduce the effectiveness of the applied thrust from each individual thruster, thus the required *per-thruster* ΔV must be increased to compensate for this loss. To illustrate this, consider that in order to apply an effective 0.067 m/s of ΔV on the satellite, each thruster in a cluster of 4 configured as described must apply 0.047 m/s of ΔV for an effective total of 0.188 m/s. This results in the total mission ΔV requirement increasing by a factor of $\frac{2}{\sqrt{2}}$ to 1.259 m/s. Thus, for a 5 kg CubeSat requiring 1.259 m/s of ΔV , 15 grams of propellant would be required. Once again, this does not take into account any additional inspection maneuvers, detumbling post-ejection, or incomplete propulsive discharges.

2.4.3 On-Ground Performance Reqs. and Resultant Design

The design specifications outlined in Table 2.8 provide a good starting point for building and testing a propulsion system, but some adjustments must be made in order to effectively test it on ground. Testbed limitations imposed constraints on the prototype propulsion system which necessitated higher thrust than would be needed in-space.

Given the limitations of space available on the air bearing test bed, we desired to reach the target speed of 0.067 m/s quickly so as to leave enough room available for continued maneuvering. For a 4 ft (1.2 m) length available test section, it was desirable to have the test platform accelerate to the target speed in one-eighth of the distance, or 0.15 m. This would leave 1.05 m of linear table length available for further maneuvers, which at a speed of 0.067 m/s, would be traversed in approximately 15 seconds assuming negligible friction on the air bearing table. To meet this requirement, a net average thrust of $T_{netave} = 67$ mN must be applied for a duration of approximately 5 seconds.

The propellant supply pressure was chosen to be 790.8 kPa (100 psig when operating in standard atmosphere). This pressure was chosen to raise the average thrust and ΔV applied from a single discharge while exceeding the maximum allowable 100 psig pressure differential as specified by NASA Safety Policy and Requirements for Payloads Using the International Space Station [53]. Taking into account the thruster configuration described in 2.3.3, the performance objectives for a single thruster is broken out and listed Table 2.9.

On-Ground Performance Objectives

Propellant	CO ₂	
Parameter	Net Performance	Per Thruster
ΔV	0.067 m/s	0.047 m/s
Impulse	335 mN-s	237 mN-s
Maneuver Time	5 sec	5 sec
Average Thrust	67 mN	47 mN

Table 2.9: Performance objectives to determine nozzle and plenum design for on-ground testing.

Using the same single plenum discharge simulation as before, it was determined that the plenum volume must be 63 cm³ to achieve the 237 mN-s per-thruster impulse target. The corresponding nozzle throat diameter needed to achieve this target in 5 seconds must be 0.45 mm. Off-the-shelf tooling selection is limited to 0.1 mm increment drill bit diameters, so the throat diameter must also be limited to the same increments.

Given the space constraints on the test platform and noting that a total of 8 plenums are intended to be integrated, it is infeasible for each plenum to be 63 cm³ in volume. Accounting for the additional space required for valves, electronics, and propellant storage, the plenum volume was fixed to a maximum of 30 cm³. At this volume, and assuming perfect expansion through the nozzle, two thrusters oppositely mounted at 45° would provide 153 mN-s of impulse in a single discharge. Two complete discharges would be sufficient to reach 92% of the required velocity.

Assuming plenum discharge and recharge times are equal, the discharge time must be no greater than 1.6 sec and the average thrust for a single discharge T_{1ave} must be no less than 70 mN ($T_{1ave} = \frac{(2n-1)}{n} T_{netave}$), where n is the number of required discharges). The smallest theoretically possible nozzle throat diameter to achieve the target single-discharge average thrust within the allotted burn time is 0.54 mm. Based on tooling available off-the-shelf, the nozzle diameter was rounded up to 0.6 mm so as to be manufacturable using a standard 0.6 mm drill bit.

Section 2.4.4 covers a nozzle design optimization process which identifies an expansion

ratio which maximizes net thrust imparted during a full plenum discharge. The expansion ratio (ϵ) is defined as the ratio between the nozzle exit area and nozzle throat area which, for this nozzle, is targeted at $\epsilon = 1.17$. Table 2.10 summarizes the design choices described.

Revised On-Ground Design Specifications

Plenum Volume	30 cm ³
Starting Pressure	791 kPa (114.7 psia)
Nozzle Throat diameter (ϕ)	0.6 mm
Nozzle Expansion Ratio (λ)	1.17

Table 2.10: Nozzle and plenum geometry given the constraints and design choices described.

With these new constraints and design choices introduced, revised performance expectations are listed in Table 2.11. The expected values in this table differ from the objectives listed previously in Table 2.9 due to the constraints placed on the plenum design.

On-Ground Performance Expectations for 2x Discharges of 30 cm³ Plenum

Propellant	CO ₂		
Parameter	Net Performance	Per Discharge	Per Thruster/Discharge
ΔV	0.062 m/s	0.031 m/s	0.022 m/s
Impulse	305 mN-s	153 mN-s	108 mN-s
Maneuver Time	3.9 sec	1.3 sec	1.3 sec
Average Thrust	78 mN	117 mN	83 mN

Table 2.11: Performance expectations for a 30 cm³ plenum completing two discharges.

A single plenum discharge simulation using the specifications listed in Table 2.10 is illustrated in Figure 2.10. The differing time scales between the on-ground and in-space performances are to be expected given the requirements put in place to generate larger average thrust and achieve the net impulse requirement in a shorter time span.

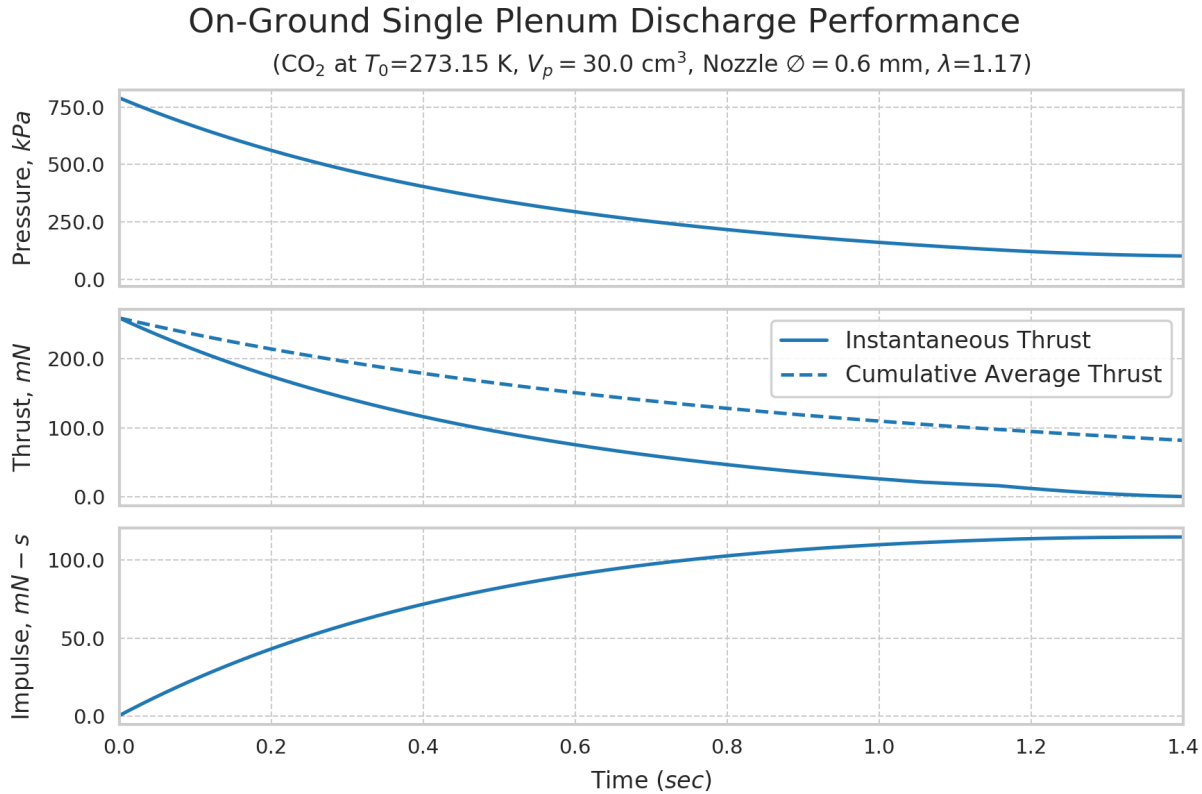


Figure 2.10: Simulation results for target thruster design. The smaller plenum necessitates multiple discharges, while the larger throat diameter makes for a larger net thrust and reduces the overall maneuver time.

2.4.4 Optimum Nozzle Geometry for On-Ground Testing

An exploration of the relationship between expansion ratio (ϵ) and total impulse imparted during a single discharge was conducted to illustrate the degree of effectiveness of expansion ratio on total impulse. This was performed for the on-ground CO₂-based system operating in atmospheric ambient conditions and using the geometry listed in Table 2.10 (not including the fixed expansion ratio, of course) Net impulse peaks very early on when $\epsilon \approx 1.17$, but this value changes for varying plenum sizes, throat diameters, and inlet pressure. The relationship between expansion ratio and net applied impulse is illustrated in Figure 2.11.

On-Ground Net Impulse & Nozzle Length vs. Expansion Ratio

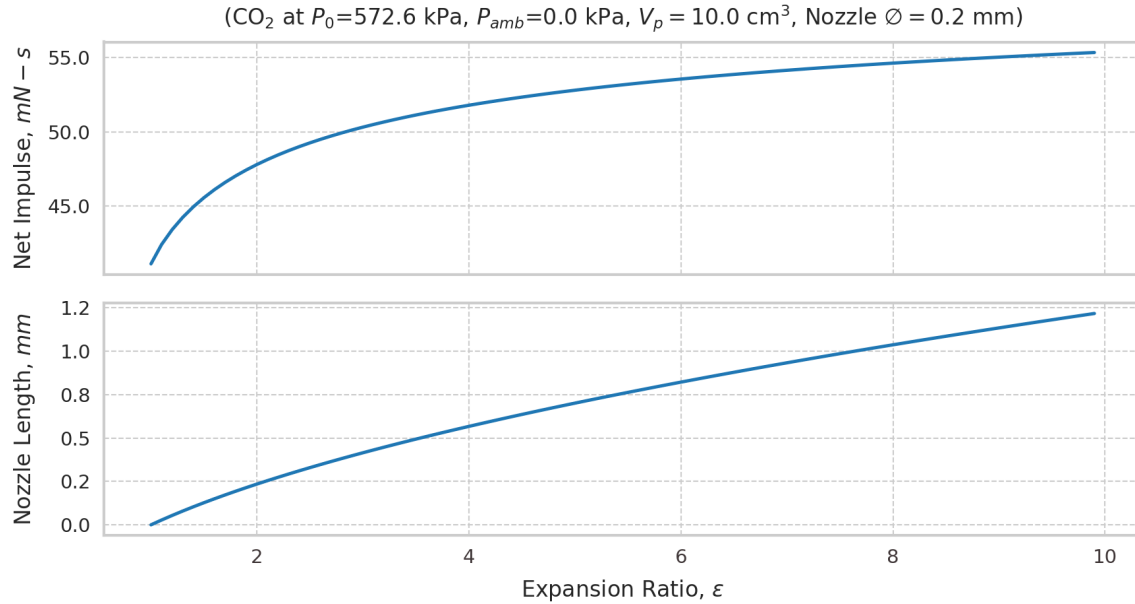


Figure 2.11: Effect of expansion ratio (ϵ) on total impulse during a single plenum discharge for on-ground propulsion system.

The same figure also illustrates how manufacturing tolerances can affect the expansion ratio by showing the relationship between ϵ and nozzle length. The nozzle is a straight-cut conical shape with 10° half-angle manufactured using a 20° conical engraving “V-bit”. Thus the drilling depth of the engraving bit will control both the nozzle length and expansion ratio. Correspondingly, the tolerance on the engraving bit drill depth will be controlled by the tolerance of the expansion ratio, which will in turn be controlled by our allowable variation in net impulse. Per Figure 2.11, having no diverging section in the nozzle ($\epsilon = 1.0$) will result in a 1.3% drop in net impulse. A similar drop in performance can also be expected when $\epsilon \approx 1.41$, which occurs at a nozzle length of 0.32 mm.

A similar exploration was performed for an R134a-based system in vacuum conditions where the propellant is assumed to be 20° C , shown in Figure 2.12. For true vacuum conditions, ideal expansion (and therefore nozzle length) would be infinite and net impulse would asymptotically approach its maximum value at infinite ϵ . This is of course not practical, and the optimal nozzle design would strike a balance between maximizing net impulse while minimizing mass.

In-Space Net Impulse & Nozzle Length vs. Expansion Ratio

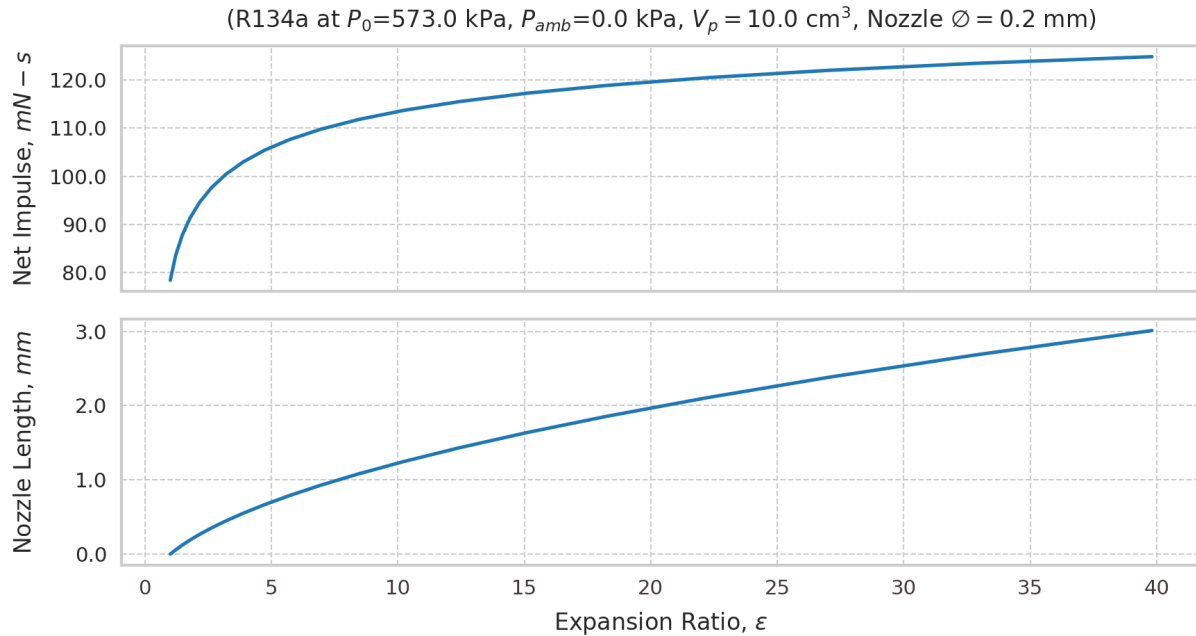


Figure 2.12: Similar impulse vs. expansion ratio exploration for in-space propulsion system in vacuum conditions.

It is of interest to note that since a larger expansion ratio is more desirable for higher inlet pressures, an incomplete plenum discharge would be more effective with a larger expansion ratio nozzle owing to the larger average inlet pressure over the discharge time.

2.5 Realistic Considerations of Performance

Additional modeling and analysis was performed after the completed CO₂-based propulsion system had been constructed and tested in an attempt to provide a more realistic model of the physical process at work. The isentropic single-plenum discharge model was augmented to account for phase changes occurring within the plenum, heat transfer through the control valve was estimated, and viscous losses were estimated for the diverging portion of the nozzle. A detailed overview of this work is presented in Appendix D and summarized herein.

Initial predictions by the isentropic model showed the plenum pressure and temperature dropping into the solid phase for CO₂, indicating that some phase change was taking place during discharge. However, the degree to which the phase change affected the overall vapor quality of the propellant was unknown. The single plenum discharge simulation was aug-

mented with real thermodynamic data for CO₂ and R134a to be used for estimating when a phase change began during a discharge process. In both cases, despite the temperature and pressure dropping steadily during a discharge, so too did the saturated vapor enthalpy, meaning the overall vapor quality remained very large (> 99%) during the two-phase portion of discharge. The rate of change in pressure was largely unchanged from the pure isentropic model, as was expected. However, the change in temperature was noticeably smaller. The lowest temperature for R134a was 10 C warmer when accounting for phase change, and 20 C warmer for CO₂.

Mass flow rate and viscosity, among other properties, are directly affected by the fluid temperature. Therefore, it was desirable to have a more accurate picture of the fluid temperature entering the nozzle. Heat transfer through the valve was estimated by calculating the Nusselt number of the flow through the valve and using this to estimate a convective heat transfer coefficient. Both substances experienced similar heating despite the valves being specified with different masses and material properties corresponding to realistic conditions. The temperature change through the valve started low and increased by as much as 20 C for R134a and 17 C for CO₂.

It was clear that by accounting for phase change and heat transfer, a seemingly more realistic estimate of flow temperature could be achieved, though unfortunately this aspect could not be experimentally verified and thus warrants future exploration. Nevertheless, this information was then used to provide an estimate of viscous drag within the nozzle by incorporating flat plate boundary layer theory into the simulation. The CO₂-based system experienced no significant reduction in nominal performance. The R134a-based system saw a steady reduction in thrust coefficient during the course of discharge, ending the discharge at approximately 20% lower than nominal. This marginally reduced the net impulse by approximately 4 mN-s since the majority of net impulse was applied early on in the discharge when the Reynolds' number was still high and viscous losses low.

2.6 Summary

Performance requirements were established for an in-space propulsion system to accomplish a hypothetical inspection task serving as a design reference mission (DRM). The DRM was

modeled using the Clohessy-Wiltshire equations which relate the relative motion between two spacecraft co-orbiting around a common third body; in this case, the ISS, our inspection CubeSat, and the Earth. We established a net ΔV requirement of 0.062 m/s and constrained the time allowed to perform this propulsive maneuver to 28 seconds, thus bounding the net impulse requirement to be a minimum of 310 mN-s and minimum average thrust requirement to a minimum of 11 mN. After considering the thruster configuration of our hypothetical propulsion system, this information was used to determine the individual requirements for a single thruster line: 110 mN-s of impulse and an average thrust of 4 mN. From this, a plenum volume and nozzle geometry design to exactly meet the requirements was derived, noting that this design did not include any margin for other maneuvers.

A similar analysis was performed for an on-ground system which will operate in atmospheric conditions on an air bearing table. This analysis also considered the space constraints of the air bearing table which it would be tested on, the tooling available for component manufacturing, and a thruster configuration for 3 DOF control. An average thrust of 64 mN must be applied over a 5 second duration in order to achieve 310 mN-s of impulse and 0.062 m/s ΔV . This objective could not be met with a single discharge since the resultant plenum size would be exceedingly large given the size of the air bearing platform. Instead, the performance requirements were revised to meet the objective with two complete plenum discharges, with each thruster required to apply 83 mN of average thrust over a duration of 1.3 seconds per discharge. The resultant design to achieve this objective consisted of a 30 cm³ plenum with a nozzle of throat diameter 0.6 mm and expansion ratio 1.17.

The crux of this chapter is a single plenum discharge simulation which was used to determine theoretical propulsive characteristics for a given plenum volume and nozzle geometry. The details of this simulation are outlined in Appendix C. This simulation utilized the principles of isentropic nozzle flow, outlined in Appendix B, to analytically estimate the time-rate of change for relevant flow properties to determine thrust and impulse.

Chapter 3

Manufacturing and Construction

This chapter outlines the manufacturing processes and tools developed in support of this project, beginning with the air bearing table development. Details regarding the selection of off-the-shelf components is also covered, as much of the propulsion system uses off-the-shelf parts in an effort to drive down cost. From there, the process surrounding the development of a 3D-printed plenum – and the challenges associated with it – is discussed. Lastly, an in-depth overview of the mathematical principles and implementation of a Kalman filter for computer vision-based tracking is provided. This last section constitutes a significant portion of this chapter since some amount of background and theoretical development is required to fully understand the rationale behind the implementation.

3.1 Air Bearing Testbed

Owing to the prohibitively high cost of testing in zero-gravity (both in Low-Earth Orbit and using a reduced gravity aircraft), a low-cost testing facility was developed in our lab at UC Davis to simulate zero gravity using a system of air bearings. When used on a sufficiently smooth and flat surface which makes up the air bearing table, the apparatus can effectively simulate zero gravity in three degrees of freedom (DOF) – two in translation and one in rotation. The apparatus is of similar mass to a 3U CubeSat and provides a modular platform to mount, test, and reconfigure a propulsion system.

3.1.1 Air Bearing Test Platform

Air bearings are a relatively low-cost and effective way to achieve low friction motion on-ground and can be used to simulate zero gravity in planar motion, rotational motion, or both. Pressurized air (or similar gas) is typically supplied between 240 and 650 kPa (20 and 80 psig) to a set of bearings which will constrict the flow between the bottom surface of the bearing and the table surface which it sits upon. This constriction will form a cushion of air on the order of 5 to 10 μm (0.2 to 0.4 $\mu\text{in.}$) thick which will support the air bearing and anything attached to it. Maximum loads are dependent on the bearing size, sustainable flow rates, supply pressure, and bearing height (which in turn is a function of the smoothness of the table surface). Air bearings have applications in high-precision manufacturing, low friction testbeds (such as for this project), and industry warehouse operations.

The air bearing test platform used for this project was designed with compactness, low-cost, and reproducibility in mind. Three 25 mm flat round air bearings from New Way are supplied with pressurized CO₂ from two 9 oz. bottles configured to allow for completely horizontal installation. The bottles themselves were originally sourced from a recreational paintball supplier and professionally modified with an anti-siphon tube to ensure that only gaseous CO₂ is consumed. A pneumatic diagram of the air bearing system designed here is shown in Figure 3.1 and a detailed description of the components used in this test platform can be found in Appendix E.4.

For comparison, consider the air bearing platforms previously used by SPHERES at NASA Ames Research Center, shown in Figure 4.8. The single large air bearing platform similarly holds two 9 oz. CO₂ bottles, albeit offset from center and inclined at an angle so as to prevent liquid CO₂ from entering the system. The advantage of this configuration lies in removing the need for aftermarket anti-siphon tubes to be installed in the bottles, though as a consequence it requires more structural components and intricate plumbing to be effective. Therefore, compactness became a design goal for our test platform owing to the limited space available on our air bearing table.

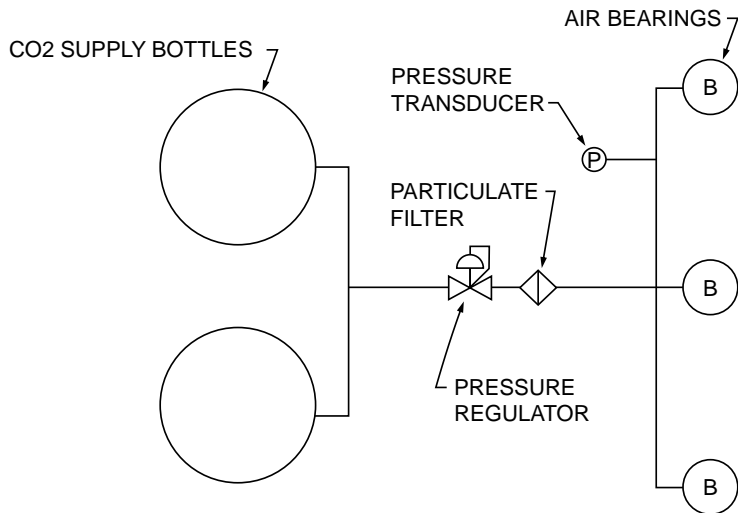


Figure 3.1: Air bearing test platform pneumatic diagram. CO₂ is stored at approximately 850 psig in two 9 oz. bottles, then brought down to 25 psig at the in-line regulator before being distributed to three 25 mm flat round air bearings.

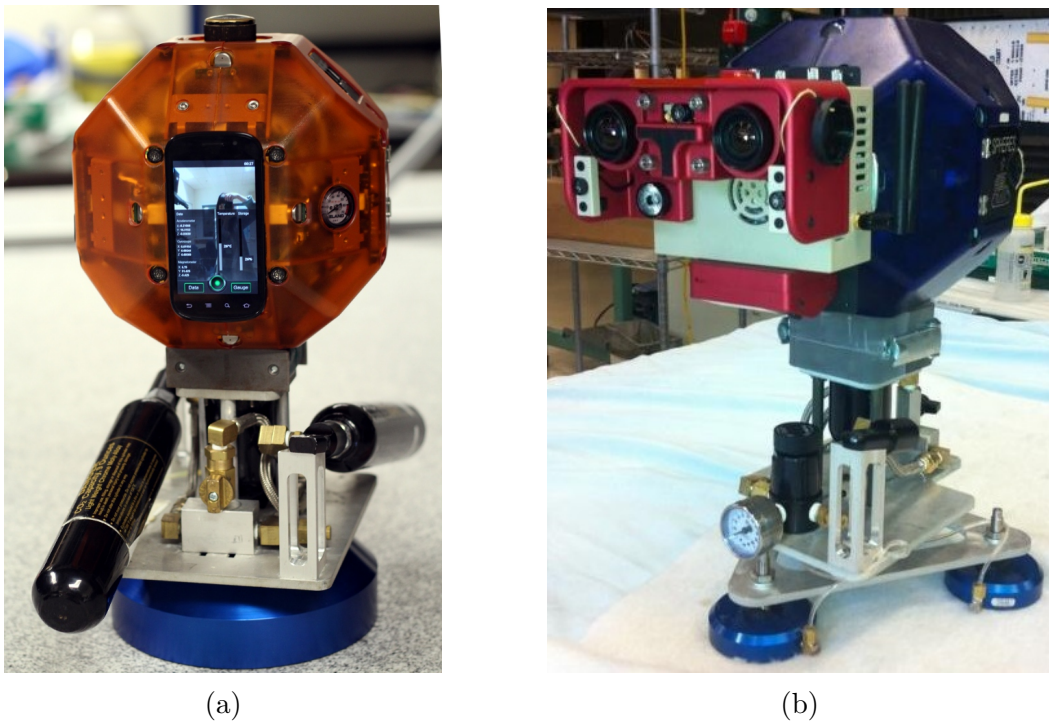


Figure 3.2: Two SPHERES air bearing test platforms used for design reference; single-bearing rear profile (view opposite of air bearing pressure regulator) [54] (a), three-bearing triangular base sans CO₂ supply [55] (b).

3.1.1.1 Revision 1

Unlike the SPHERES platform shown in Figure 3.2a which uses one single large air bearing, three small 25 mm air bearings were selected for our platform on the basis of both cost and design flexibility, configured similarly to the SPHERES platform shown in Figure 3.2b. Even as the smallest available air bearing size, their load capacity of 80 Newtons per bearing substantially exceeded the maximum expected weight of 49 Newtons of the test platform (approximately 5 kg). Based on the operational specifications of the air bearings shown in Figure 3.3 and the expected 5 kg mass of the final assembly, the platform should be capable of operating at approximately 274 kPa (25 psig) for 90 minutes. Moreover, building a base from three bearings opens the door for modifying the size of the base and provides flexibility for widening or narrowing of the platform's footprint as-needed.

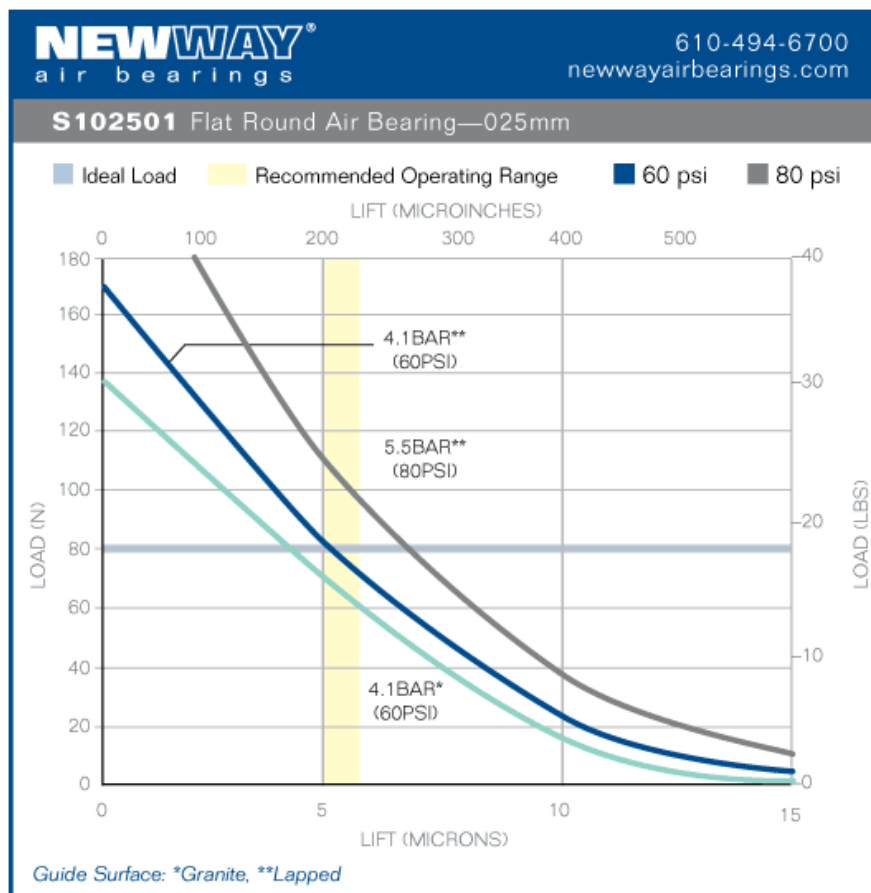


Figure 3.3: Lift-Load curve for New Way 25 mm round flat air bearing. Operating pressure was selected by assuming a 5 kg (49 N) divided evenly over three bearings, which comes out to approximately 16 N each [56].

The pneumatic design required a method to combine the two CO₂ sources via a manifold and shunt the flow directly into the regulator. The CO₂ bottles were reconfigured to sit parallel with one another with each outlet facing the other and connected to the inlets of a 2-in / 3-out brass manifold with adapters and plugs, viewable in Figure 3.4a. The fittings were epoxied in place in order to insure the components were seated at the proper angle while still providing a seal against the high pressure CO₂. The manifold outlet connects via a single flexible hose to the inlet of a Palmer's Pursuit Shop "Micro Rock" low-profile CO₂ regulator designed for recreational paintball which had an adjustable outlet pressure of 101 to 1480 kPa (0 to 200 psig). The regulator's compact cylindrical design made it simple to integrate into the rest of the system by arranging it parallel with the CO₂ supply cylinders, also viewable in Figure 3.4a.

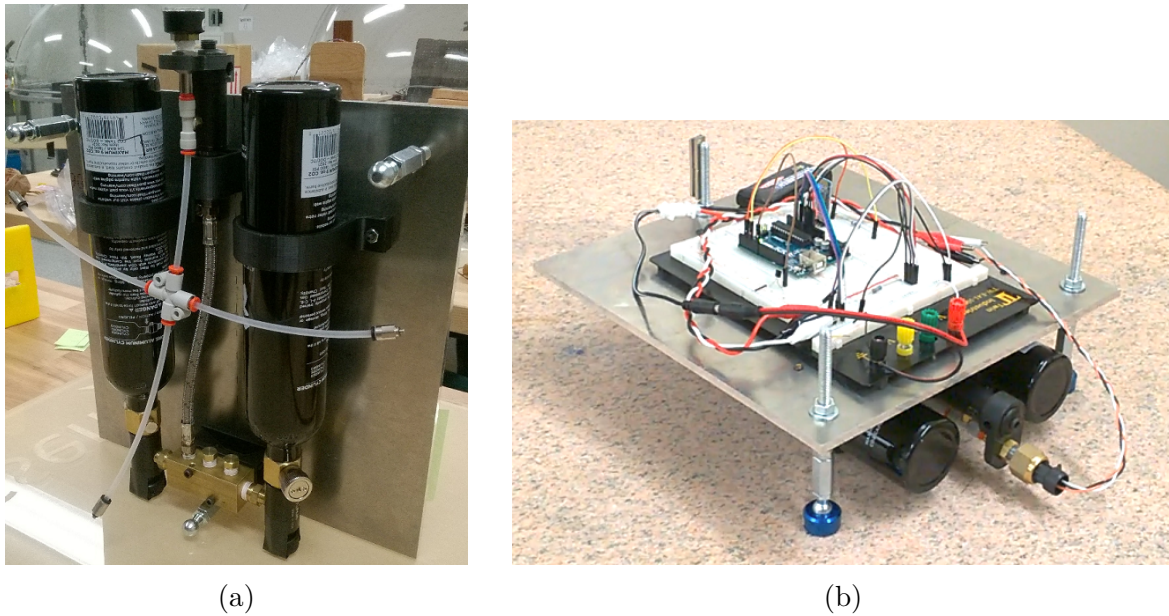


Figure 3.4: Initial test build of the air bearing test platform (Rev 1); (a) Underside showing the pneumatic layout and (b) with prototype circuitry for wireless data transmission.

The assembly was held together with a 3/16" Aluminum plate fitted with 3D-printed brackets for CO₂ bottles and tapped with holes to fasten the brackets to. The platform rested loosely on the three air bearings by means of legs assembled from 5/16"-18 threaded rods adapted to 13 mm ball studs. Larger air bearings available from New Way are capable of being secured to the ball stud, but this feature does not exist on the 25 mm air bearings used for this platform.

This platform acted as a proof-of-concept for both the air bearing method as well as wireless communicativity. A breadboard circuit was built using an Arduino Uno connected with a Bluetooth wireless antenna to relay pressure data from a single pressure transducer connected to the air bearing CO₂ supply line, shown in Figure 3.4b. A wireless device with Bluetooth connectivity could connect to the device and receive regularly-timed readings from the pressure transducer.

3.1.1.2 Revision 2

While the first revision successfully demonstrated the key components needed to support a propulsion system, it proved to be too bulky and heavy to adequately perform. Additionally, the Bluetooth connection was unreliable and difficult to interface with. Therefore, the next revision sought to mitigate these issues by turning to 3D printing for the main structure and developing a new WiFi-based communication infrastructure, the details of which are covered in Section 3.4. The motivation behind this method is consistent with the rest of the project: to allow for greater flexibility and lower cost by producing the components in-house, and to allow for easy dissemination to other institutions which wishes to construct their own platform based on this design.

The revised structure was 3D printed from Polylactic Acid (PLA) using a MakerGear M2 benchtop 3D printer and designed as two distinctly separate parts. The first part was a lower support structure which utilized a single triangular frame upon which various brackets were affixed to. This configuration allowed the pneumatic components to “hang” underneath in a manner similar to the Aluminum plate from Revision 1, although the CO₂ bottles were now held in place by Velcro straps rather than a full 3D printed bracket. The second part was a circular ring which provided a symmetric platform upon which the valves and other propulsion system components could be mounted to. As a wholly separate assembly, the propulsion system affixed to the ring structure could be easily removed from the base. This design allows for easy modularity in the event that the same air bearing system needs to be shared among multiple projects or propulsion assemblies. This version is shown in Figure 3.5 with the CAD model and build for comparison.

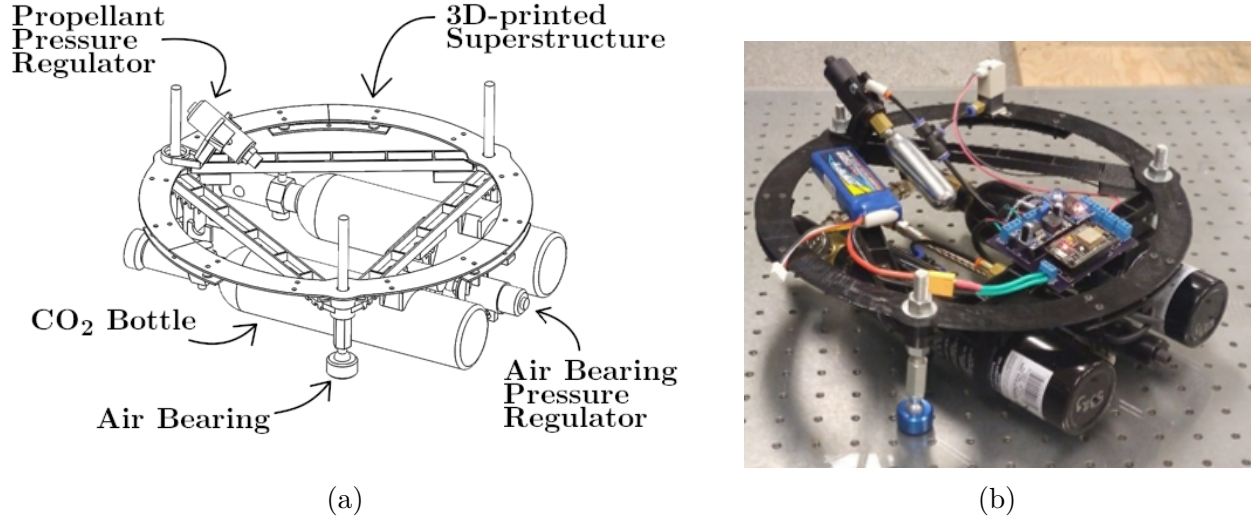


Figure 3.5: Second revision of the air bearing test platform; (a) CAD mock-up and (b) physical construction.

Revision 2 also saw a minor upgrade to the pneumatic components with the replacement of the heavy brass manifold with a simpler tee-shaped fitting. Additionally, the 1/8" NPT adapters from the ASA to the brass manifold, along with the adapter from the flexible hose to the regulator, were replaced with quick-disconnect fittings. The inclusion of quick-disconnect fittings not only allowed the assembly to be rapidly disassembled and reconfigured for testing, but also allowed complete 360° rotation of the components. This allowed the fittings to be seated into the ASA and "T"-manifold at any arbitrary angle and still allow the CO₂ bottles to sit parallel to one another, removing the need for epoxy to seal the fittings at the correct angle.

The mass of the platform was reduced by nearly 2 kg simply by replacing the Aluminum plate with the 3D printed structure. However, a significant amount of bending in the frame was observed due to the weight of the CO₂ bottles and is somewhat visible in Figure 3.5b. The bending of the frame structure, coupled with twisting due to the bottles being attached off the centerline of the beam, caused the three legs of the air bearings to splay outwards and induced warping in the propulsion ring structure. A third revision of the platform was therefore developed to mitigate these problems.

3.1.1.3 Revision 3

The transition from Revision 2 to 3 was less drastic than from Revision 1 to 2 and reused many of the same components. Nevertheless, this revision proved to be a significant improvement over the previous two. The single triangular frame present in Revision 2 was mirrored below the CO₂ bottles, and the brackets holding the three threaded rods which form the legs of the platform were modified to improve their stiffness. Two of the three leg brackets were integrated with the bottle brackets such that when the bottles were securely lashed to the frame using the same velcro straps, the combined assembly resulted in improved rigidity by taking advantage of the inherent stiffness of the aluminum CO₂ bottles. The base of the entire air bearing platform now consisted of a triangular box-frame which provided substantially improved rigidity, shown in Figure 3.6b.

The ring structure which acted as a base for the propulsion system was also mirrored and a series of brackets regularly spaced between the layers was added to stiffen the structure. Additionally, the ring components were modified to adapt to an updated configuration of the thruster lines whereby each thruster was bent 90° after the first plenum as a space-saving measure, as seen in Figure 3.6a.

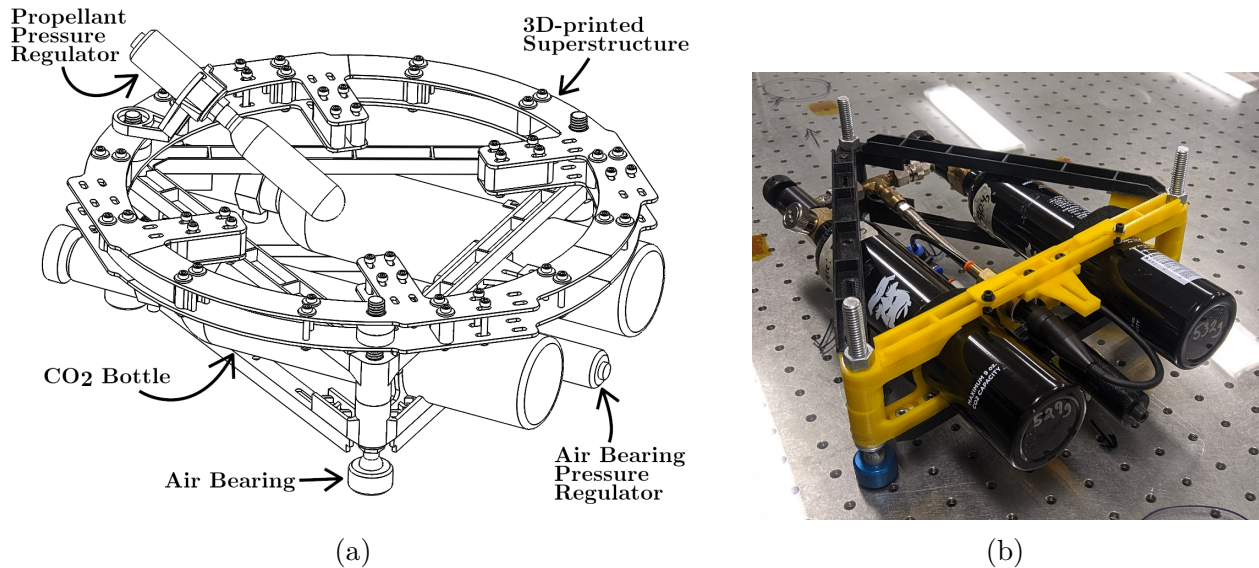


Figure 3.6: Third revision of the air bearing test platform; (a) CAD mock-up and (b) initial prototype build.

Lastly, a particulate filter was added in the low pressure line between the regulator outlet and air bearings to prevent bearing contamination. This lesson was learned only after

a noticeable degradation in bearing performance was observed and attributed to oil from the regulator being carried to the bearings and clogging the microscopic porous structure that makes up the porous carbon base of the bearings. An in-line disposable air filter was added to remove more than 99.99% of $0.1 \mu\text{m}$ particles from the incoming air stream while minimizing pressure drop to less than 7 kPa (1 psig) across it. Though the filter had to be specially adapted to connect with the 4 mm tubing used in the rest of the system, it was effective in preventing further degradation of the air bearings.

3.1.2 Air Bearing Table

The relevant terms to describe the geometric dimensioning and tolerancing used for describing the air bearing table are provided in Table 3.1.

Term	Description	Symbol	Standard
Roughness	The microscopic surface profile which largely defines the texture. Typically measured with a profilometer and expressed in terms of average (Ra) or root mean square (rms).		ISO 1302
Flatness	The macroscopic surface profile defined by deviations from an ideally flat plane which lies parallel to the surface and defined by ASME B89.3.7-2013.		ISO 1101
Levelness	The degree to which the surface approaches true horizontal as defined by perpendicularity to the local gravity vector.	N/A	N/A

Table 3.1: Definitions to describe surface quality for air bearing applications.

The surface of the air bearing table must be sufficiently smooth (i.e. possess a low roughness value) to allow the bearings to maintain a thin film of air underneath them. Additionally, the surface must be both flat and level to prevent adverse motion due to gravity. This effect can be recognized by observing the motion of the platform – any deviation from a straight-line path (assuming no propulsive force is applied) can be attributed to a slight slope in the surface. Lastly, the surface must be level so as not to introduce a systemic

bias towards one direction. This effect can be observed as a consistent tendency for the test platform to glide toward one direction.

A typical air bearing surface might be a lapped granite inspection table used in manufacturing quality control, or stainless steel optics benches. Granite inspection tables (also called surface plates) are manufactured to extremely tight flatness tolerances and are defined by three grades: Grade B, Grade A, and Grade AA. The flatness of each grade is defined in ASME B89.3.7-2013 as:

- Grade AA: $(40 + \text{diagonal (in inches)} \text{ squared}/25) \times 10^{-6}$ (unilateral)
- Grade A: Grade AA $\times 2$
- Grade B: Grade AA $\times 4$

For a 36" x 48" table, a Grade B inspection plate must have an overall flatness of less than 736 μin . ($\pm 368 \mu\text{in}$. bilateral). By comparison, an optical table from Thor Labs of similar dimension will only be able to achieve a bilateral flatness tolerance of $\pm 4000 \mu\text{in}$. [57]. Larger air bearing surfaces might be constructed using carefully poured epoxy, such as the Air Bearing Floor at NASA Johnson Space Center [58] or the Spacecraft Research Laboratory used by the Aerospace Robotics and Control research group at Caltech [59]. NASA Langley Research Center constructed a large epoxy resin-based air bearing floor for use with the Skylab T020 Experiment which employed a foot-controlled maneuvering unit (FCMU) supported on large air bearings [60]. The elevation of this floor was stated to deviate by 5000 μin . along a 1.5 meter section ($\pm 2500 \mu\text{in}$. bilateral).

Any sturdy and non-porous material can be effectively used if the surface finish is 16 nm (rms) or better [61] and if the flatness can be controlled. It is therefore possible to use regular windowpane glass (AKA “float glass”, named by virtue of the process used for manufacturing), but care must be taken to note any unevenness in the thickness since this is not a tightly controlled dimension. Uneven thickness will result in a wavy (i.e. not flat) surface that will perturb otherwise nominal linear motion, as described previously. Furthermore, the glass pane may simply conform to the surface it is placed upon, so a method for shimming the low spots must be devised so that flatness can be adjusted.

A single sheet of 36" x 48" x 1/4" windowpane glass costs on the order of \$60 USD and has a typical roughness between 0.2 and 1.3 nm Rms [62] [63] [64]. In comparison,

an identically-sized Grade B granite inspection surface can cost more than \$700 USD [65], though this will get the customer a guaranteed bilateral flatness tolerance of $\pm 200\mu\text{in}$. and a roughness on the order of 10 nm Ra [66]. Note that float glass is typically measured in terms of Rms while polished granite surfaces are typically measured in terms of Ra, making direct comparison difficult. However, Datsiou and Overend reported measuring the roughness of commercial-grade float glass at 2 nm Ra [67], which supports the use of float glass over granite (assuming the flatness issue can be resolved). The air bearing surface currently in use at UC Davis is shown in Figure 3.7.

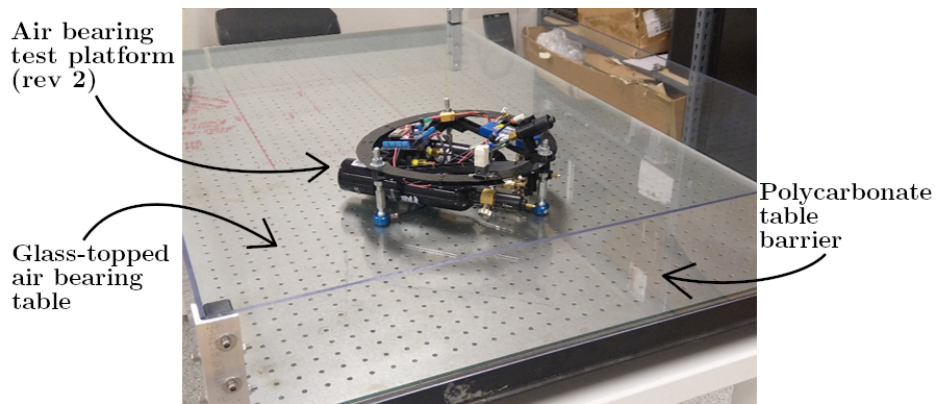


Figure 3.7: UC Davis HRVIP glass-topped air bearing table.

Levelness was controlled by placing the glass pane on an optical table with adjustable feet, although any sufficiently stiff and adjustable table could also suffice. Once the table was coarsely leveled using a standard bubble level, the test platform was placed on the glass surface and pressurized to observe unforced motion. The table was further leveled until unforced motion was minimized. At this point, a singular low spot was identified at the center of the table by noting a tendency for the platform to drift toward the center from all other points on the table. A process was developed to further flatten the surface by removing the glass pane and placing multiple increments of 1"-square pieces of 0.002"-thick Kapton tape at the previously identified low spots. This process was repeated until the air bearing platform's unforced motion was minimized across the entire table. However, it should be noted that unforced motion still occurred despite best efforts to control it, as bending of the glass over the 0.002"-thick Kapton shims was significant enough to cause deviations in linear motion.

The lessons learned from this process, as well as recommendations for future work, are covered in Chapter 5. In brief: porous carbon air bearings are capable of operating on rougher surfaces than glass (such as polished steel), and ultimately it is flatness which most strongly governs the performance of an air bearing platform. Therefore, in deciding on a surface to use for testing, greater resources should be expended in acquiring a flat surface as opposed to an extremely smooth surface. If an intermediate surface such as glass is used, one must have the means to easily adjust the height of the glass at multiple points since glass will conform to the shape of the surface it is placed upon and is not controlled in flatness during manufacturing. It is for this reason that granite is often chosen as the ideal solution: granite inspection tables are controlled in flatness during manufacturing, do not significantly warp from temperature gradients compared to metals, and are sufficiently rigid such that bending is insignificant.

3.2 Converging-Diverging Nozzle

The converging-diverging nozzle converts the energy from combustion or, in this case, high pressure gas into usable thrust. Pressure and temperature of a mostly stagnant flow are reduced and traded for increased flow velocity which, when ejected from the spacecraft, will impart an equal-but-opposite force, thus propelling the spacecraft forward. The design of a nozzle to accomplish this was detailed previously in Section 2.4, which provided general nozzle specifications such as throat diameter and expansion ratio. This section will detail how those specifications were used to inform the design and manufacturing of a real nozzle. The nozzle design and manufacturing is validated by recording the thrust and mass flow rate, both in a steady-state condition and for a single plenum discharge, covered in Section 4.2.

3.2.1 Nozzle Design Specifications

The nozzle was designed with a conical diverging section for ease of manufacturing, and integrating the nozzles into the system meant first identifying a means to integrate them with the selected valves. To accomplish this, a simple brass M5 threaded hex plug was chosen to serve as stock material from which to machine a nozzle into. The required nozzle specifications were outlined previously in Section 2.4 but will be reviewed here.

The throat length is defined by the intersection between the converging section drill depth and diverging section engraving bit depth, and the geometry of the throat can strongly influence the performance of the nozzle if not designed correctly. A longer throat provides greater opportunity for a larger boundary layer to form and choke the flow with an effectively smaller throat, thus a shorter throat section is more desirable to mitigate this effect. This section should have a length of no more than $0.4 \times$ the diameter, per the recommendations made in an article on solid rocket motor design by Charles E. Rogers [68]. This means that the throat length must not exceed 0.24 mm for a 6 mm diameter throat. A highly conservative target throat length of 0.12 mm was therefore chosen to guarantee maximal performance from this nozzle.

Further design constraints were introduced by imposing a limit on the diverging section expansion ratio which is directly controlled by the drill depth of the conical engraving bit. As discussed in Section 2.4.4, maximum impulse is applied over the course of a full plenum discharge when the expansion ratio (ϵ) is approximately 1.17. Also as discussed, the net impulse is relatively insensitive to expansion ratio over a range from $\epsilon \approx 0$ to 2, and a larger-than-nominal expansion ratio would slightly improve thrust efficiency for incomplete plenum discharges. Therefore, an expansion ratio ϵ of 1.34 was chosen as this value optimizes thrust at an inlet pressure of 515 kPa (60 psig), allowing it to operate slightly more efficiently during incomplete discharges or pulses. The resultant nozzle geometry derived from these specifications is summarized in Table 3.2 and illustrated in Figure 3.8.

Nozzle Design Specifications for On-Ground Testing

Throat diameter (ϕ)	0.6 mm
Expansion Ratio (λ)	1.34
Half-angle	10°
Length	0.26 mm

Table 3.2: Nozzle geometry to be manufactured for on-ground testing.

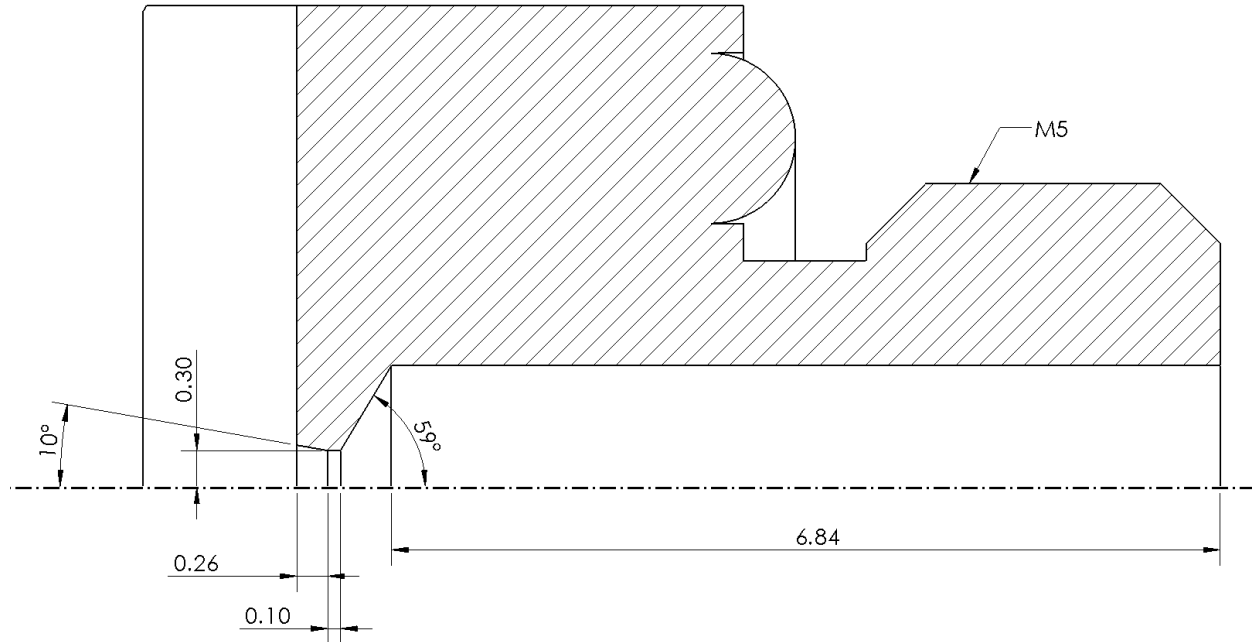


Figure 3.8: 0.6 mm throat diameter nozzle schematic (linear dimensions in millimeters). The nozzle features are machined into a COTS M5 brass hex plug.

Both the converging section drill depth and diverging section are machined in the same manner but incorporate different dimensional tolerances. The diverging section drill depth has a tolerance of ± 0.03 mm, while the converging section drill depth has a tolerance of ± 0.08 mm. Stacking these tolerances together at their respective maximum values would result in a minimum throat length of 0.01 mm which guarantees the two features will not overlap to create a throat diameter larger than 0.6 mm. Likewise, the tolerance stack at their respective minimums would yield a throat length of 0.23 mm, which will not exceed the maximum allowable throat length of 0.24 mm as outlined above. A larger tolerance was given to the drilled converging side due to the tooling utilized in that process which lacked the precision and stability of the shorter, stiffer conical engraving bit used for the diverging side.

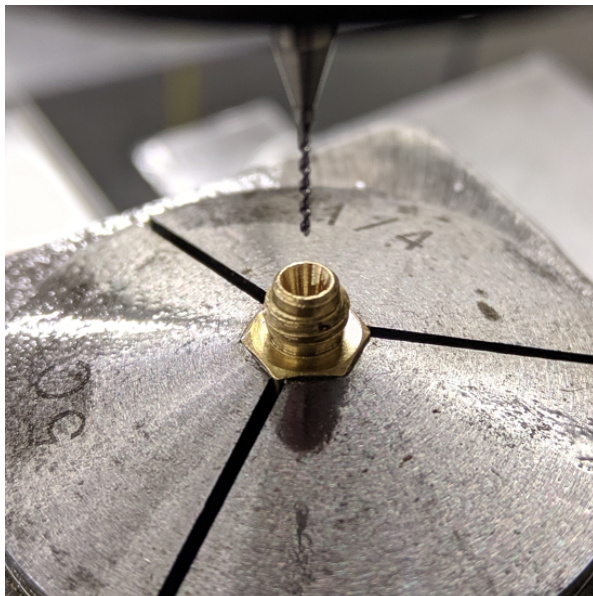
Since each feature required referencing a different datum, variations in the length of the brass hex plug stock material had to be considered. In the event an abnormally short hex plug was used as stock, the converging and diverging features could still overlap even if they were drilled to their specified depths. However, each brass plug was measured in length prior to manufacturing, and no discernable variations were found.

3.2.2 Nozzle Manufacturing Procedure

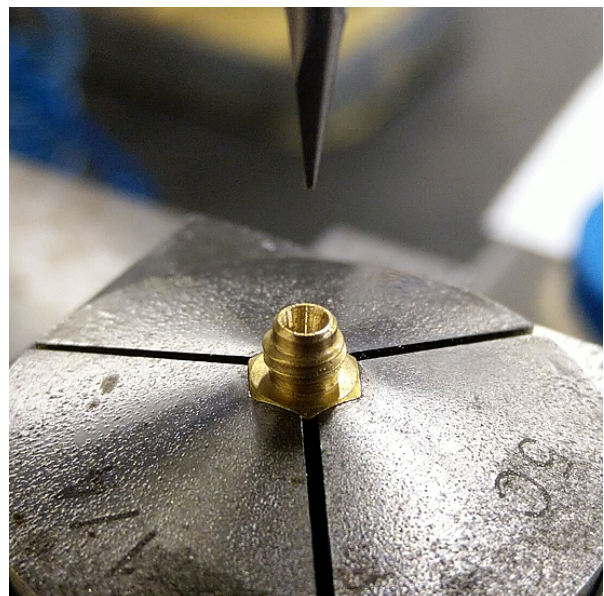
Manufacturing the nozzles consisted of a three-step process, all of which were done by manual control of a Bridgeport Series 1 vertical milling machine with 3-axis digital readout. The manufacturing steps are as follows:

1. Drill the converging section using a 2 mm drill bit with tip angle of 118°.
2. Drill the throat using a 0.6 mm micro drill bit.
3. Drill the diverging section using a 20° engraving bit with a 0.1 mm tip diameter.

The stock for the nozzle is an M5 brass hex plug which was held in place by a collet and holder, as shown in Figure 3.9.



(a)



(b)

Figure 3.9: Snapshot of the nozzle manufacturing process. (a) Drilling the throat using a $\phi = 0.6$ mm drill bit and (b) illustrating the use of a 20° engraving bit with $\phi = 0.1$ mm tip.

The collet and holder were mounted in a vice on the Bridgeport mill and the spindle was centered using a mechanical edge-finder which can repeatedly find the edge of the work to within ± 0.01 mm for the X and Y-axes. Combined with the use of calibrated digital calipers which can measure to a precision of 0.01 mm, the center of the workpiece can be located to within ± 0.02 mm. The digital readout of the Bridgeport mill could also measure to a precision of 0.01 mm, meaning the drill depth feature dimensions outlined previously could be obtained by hand, albeit with some amount of practice to maintain fine control of the

Z-axis. Validation of the manufactured nozzle was done through testing of the flow rate and thrust, as both would be adversely affected by off-nominal dimensions – especially at the throat. A snapshot of the nozzle manufacturing process

A manufacturing process plan was developed which utilized a point on the collet holder as a hard reference for zeroing the tools after a tool change. This strategy was chosen for two primary reasons: First, the brass hex plug had a limited surface to use as a consistent zero owing to the drilling process removing most of the material while drilling the converging section. Second, brass is extremely soft by nature and zeroing on a brass surface with a hardened steel tool could result in an inconsistent reference due to deformation caused by pressing the tool into the brass surface. Therefore, after the brass hex stock was placed in the vice and tightened, the distance between the top of the plug and the top corner of the collet holder was measured using the flat bottom of the edge finder and recorded. With each tool change, the new tool was zeroed at the same point on the collet holder, then the zero adjusted by the pre-measured distance, effectively making the new zero the top of the brass plug.

3.3 Plenum Chamber

3.3.1 Design Considerations

The multi-plenum concept explored in this thesis required a plenum design that was modular, scalable, and capable of being 3D printed on a commercially available 3D printer. The plenum was designed as a spherical volume of approximately 30 cm^3 capable of storing propellant at 114.7 psia, details which were outlined in Section 2.4. With a 0.6 mm nozzle, this amounts to approximately 1.5 seconds of usable thrust averaging at 90 mN and providing 130 mN-s of impulse. Three full plenum discharges would be sufficient to apply the ΔV outlined in Table 2.9 to the air bearing test platform in the required time window given the limited space available.

The plenum design utilizes an intermediate ring placed between the two hemispheres which holds a 2 mm thick, $\varnothing = 42\text{ mm}$ nitrile O-ring in place, as illustrated in Figure 3.10b. As the plenum is assembled and fastened along the circumference of the flange, this O-ring is compressed between the bottom sides of the two hemispheres to create a leak-free seal.

The O-ring sealing surface of the flange is prepared with a first pass of coarse sanding the surface to remove imperfections introduced from 3D printing, followed by a second pass with 3000-grit wet sandpaper.

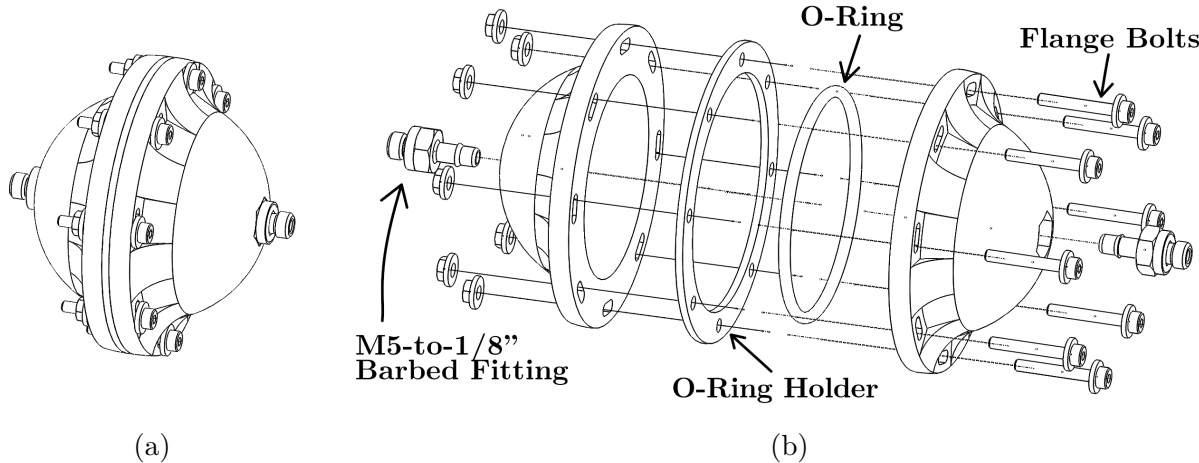


Figure 3.10: Plenum CAD design; Fully assembled (a) and broken-out (b) views.

Plenums were designed to fasten directly to the inputs and outputs of the chosen valve by using an M5-to-1/8" ID barbed fitting to serve as an adapter, illustrated in Figure 3.11. The plenums were printed with an appropriately-sized hex-shaped hole at the top to hold the fitting in place such that the threaded end was facing outward. Fittings were held in place and adhered using all-purpose epoxy which doubled as a sealant for the interior walls of the plenums.

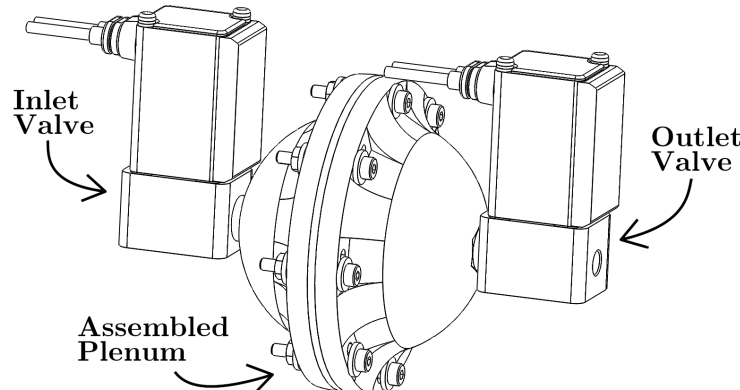


Figure 3.11: Single plenum with valves attached at each end via the M5 threaded fitting.

To allow for greater flexibility during assembly, eight slotted holes were spaced equally around the flange. The arc length of each slot was chosen so that one plenum half could line

up with slots on the other half regardless of what angle they were oriented at. This design choice was made due to the expectation that the fittings would not thread into the valves at exactly the same angle. To illustrate this, consider that the hex fitting has six sides, thus a single “clock” of the plenum on the hex fitting would rotate the entire plenum by 60° . However, since there are eight equal slots around the flange 45° apart from one another, a 60° clockwise rotation of the plenum would be effectively equivalent to a 15° clockwise rotation of the slots. This principle is illustrated in Figure 3.12.

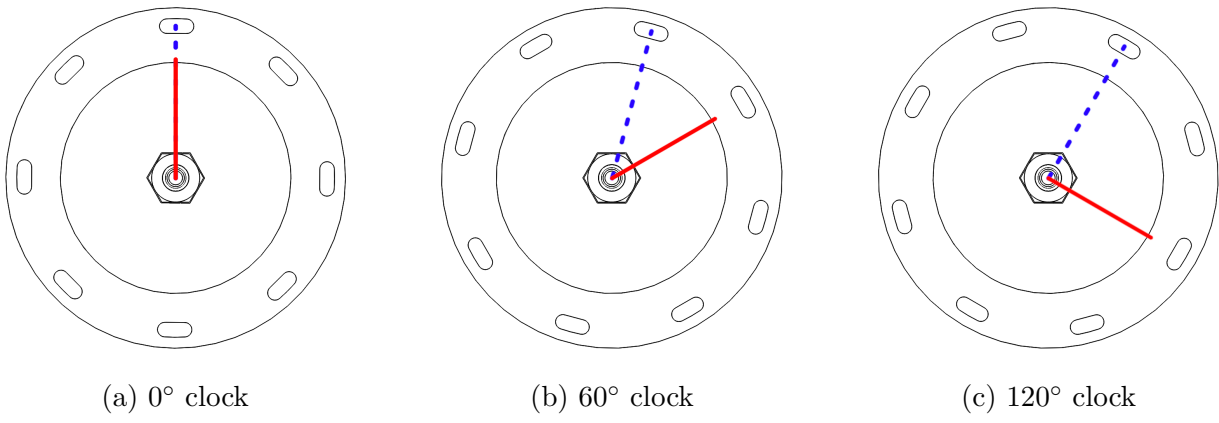


Figure 3.12: End-on illustration of a plenum half with its threaded fitting showing how a single 60° “clock” of the plenum on the fitting (solid red line) results in an effective 15° “clock” of the flange slots (dashed blue line).

When overlaid on top of one another, one can see all possible slot positions as shown in Figure 3.13a. As can be seen, the slot position repeats in 15° increments. Now consider the fact that each plenum half can be rotated independent of one another. From this we can surmise that a worst-possible orientation condition would be one where the other plenum half is rotated 7.5° such that two mating slots are offset exactly one half-clock from each other. In order to continue to guarantee a mate in this case, the slots must be sufficiently long to overlap with one another such that a single M2 screw can pass through unimpeded. With a slot length of half a plenum rotation – 7.5° center-to-center – the plenums can be aligned for any arbitrary combination of fitting angles using a finite number of 60° increment rotations of each plenum half.

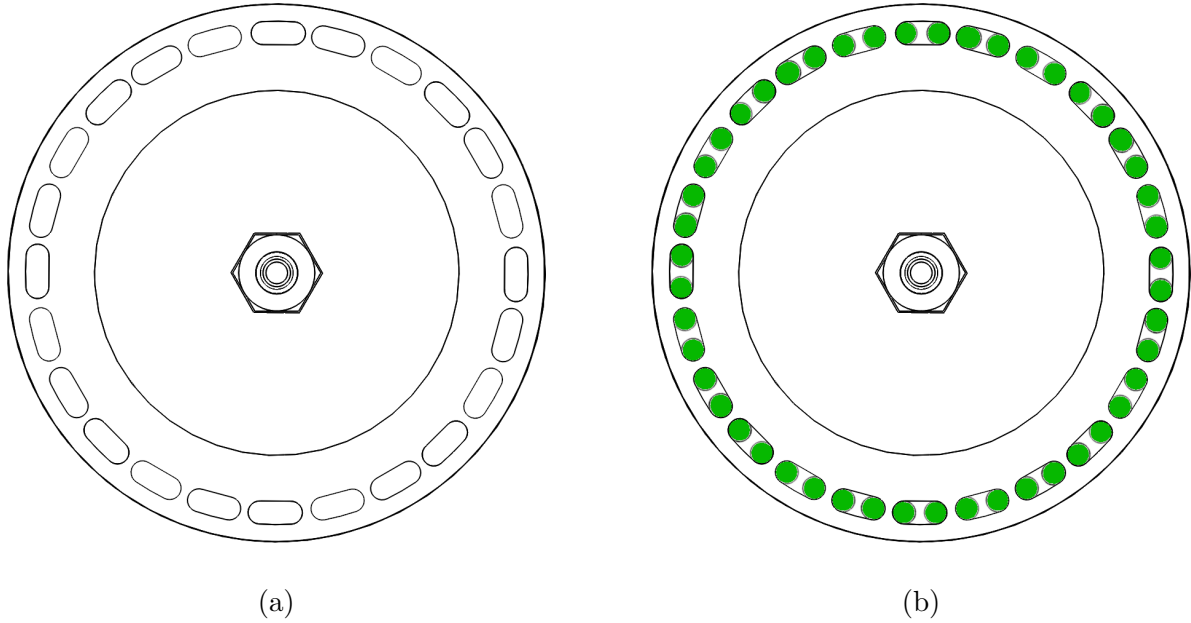


Figure 3.13: All possible slot positions for a single plenum half (a), two overlapping plenums (shaded region highlights the mating plenum slots which are offset at 7.5°) illustrating how a successful mate can be established even at the worst-possible orientation (b).

3.3.2 Assembly Process

The valves which were chosen for this system, as detailed in Section E.3, were not manufactured consistently. Specifically, the starting angle for the M5 threaded interface was different for each batch of valves, meaning the plenums could not be assembled and epoxied exactly identical to one another. However, this complication was anticipated as discussed in the previous section regarding the slots around the plenum flange. To ensure the plenums were epoxied at the correct angle relative to the barbed fitting, the entire propulsion system had to be dry-fit together with all the valves and plenums that were to be used prior to epoxying. After the system was loosely assembled, each half-plenum pair was rotated on its corresponding barbed fitting to correctly align them with their counterpart, after which they were marked and labeled. The half-plenums and their corresponding barbed fitting were then epoxied together as shown in Figure 3.14 and cured at room temperature for 24 hours before assembly.

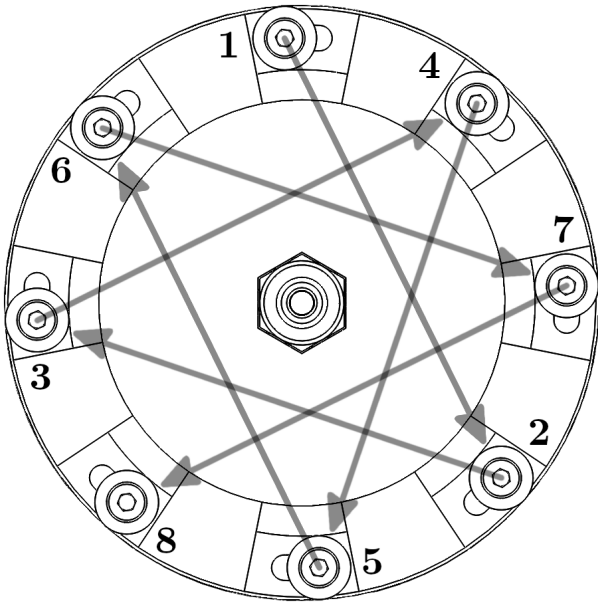


(a)

(b)

Figure 3.14: Plenum epoxy process as demonstrated with an old revision plenum, prior to the inclusion of slotted flange holes. During application (a), and while curing (b).

After curing and before assembly, the epoxied plenum was lightly sanded and cleaned, and the o-ring was coated with a thin layer of silicone grease. Plenums were oriented to their partner based on the markings applied from the dry-fit as described above and eight M2 stainless steel socket head cap screws inserted into the flange slots. The screws were finger-tightened and the loosely-assembled plenum was reintegrated into the thruster line by threading it into its corresponding valves to ensure correct alignment prior to fully tightening the flange screws. Since not all eight of the flange screws could be accessed while the plenum was installed, the accessible screws were further tightened while the plenum was at its proper orientation in order to hold the assembly in place after it was removed from the thruster line. Each of the eight flange screws required approximately 0.04 N-m of torque by assuming 25% compression on the 90 durometer $\phi = 45$ mm O-ring, as estimated by the Parker O-Ring Handbook ORD 5700, published by Parker Hannifin Corporation [69]. The flange screws were torqued in a star-like pattern to evenly distribute the preload, as shown in Figure 3.15a. Once all eight screws were tightened to the proper torque specification, the completed plenum assembly was reintegrated into the thruster line, and the line was then mounted on the propulsion ring of the air bearing platform.



(a)



(b)

Figure 3.15: Plenum tightening pattern (a), and fully assembled and integrated (b).

3.3.3 Manufacturing Challenges

Four major issues were encountered during the development of the 3D printed plenum chambers. The first issue faced relates to hex fitting, which did not sit securely in the plenum prior to epoxying and was prone to misalignment. If epoxied in this state, the plenum would not sit perpendicular to the valve. When a full thruster stack consisting of three valves and two plenums is assembled in this manner, the stack would not mount correctly to the frame of the air bearing test platform. To counteract this, a jig was produced to hold the fitting in place and align it with the plenum which then allowed reproducible quality with relative ease.

The second major issue was inconsistent manufacturing of the valves – specifically, the start angle of the threads which the fittings were to screw into. The threads started at the same angle for all valves within a single batch, but this start angle was not identical between batches. Therefore, each plenum half had to be paired with a valve prior to epoxying and the orientation properly set up to ensure that it would mate with an opposing plenum half. While this challenge was anticipated and the “clocked” slot design made specifically to overcome it (as discussed in the previous section), each plenum must still be essentially

custom-assembled for each valve (or batch of valves), and the orientation of each plenum half depended on the orientation of the other half it was mating to.

The third issue revolved around the epoxy application process which required many trials before a successful method was devised. Approximately 2.5 mL of mixed two-part part epoxy was used for each plenum, though a significant part of that amount was wasted due to the viscous and adhesive nature of epoxy. After being mixed, the epoxy was poured or “ladled” into a plenum using a wooden dowel and spread across the inside surface. Following this, the epoxy was heated using a handheld heat gun or hair dryer and rolled around the inside to evenly distribute it along the interior wall. A delicate balance of heat application was required – sufficient enough to reduce the viscosity of the uncured epoxy, but not so much as to warp the plastic plenum.

Lastly, during initial pressure testing of the plenums (covered in Section 4.1), significant leakage was found to occur along the o-ring seal. This was overcome by developing a process to consistently prepare the surface by sanding prior to assembly, and using consistent torque when tightening of the circumferential screws. Surface preparation required a heavy round of wet sanding with 3000 grit sandpaper to create a smooth, non-porous surface where the epoxy was not applied.

3.3.4 Stress Analysis

Owing to the nature of Fused Deposition Modeling (FDM) 3D printing, the plenum walls are not isotropic. Zhao et al. characterized some mechanical properties of 3D printed polylactic acid (PLA) plastics – a common material used in benchtop 3D printers [70]. Summarized results are shown in Figure 3.16 and illustrate the substantial effect of print angle on the tensile strength of 3D printed objects.

This work allowed us to more accurately model the stresses induced in the plenum structure from internal pressurization and produce a safe, robust design. Note that the yield strength of PLA (the point beyond which plastic deformation occurs) is very close to its ultimate strength, as illustrated in Figure 3.17.

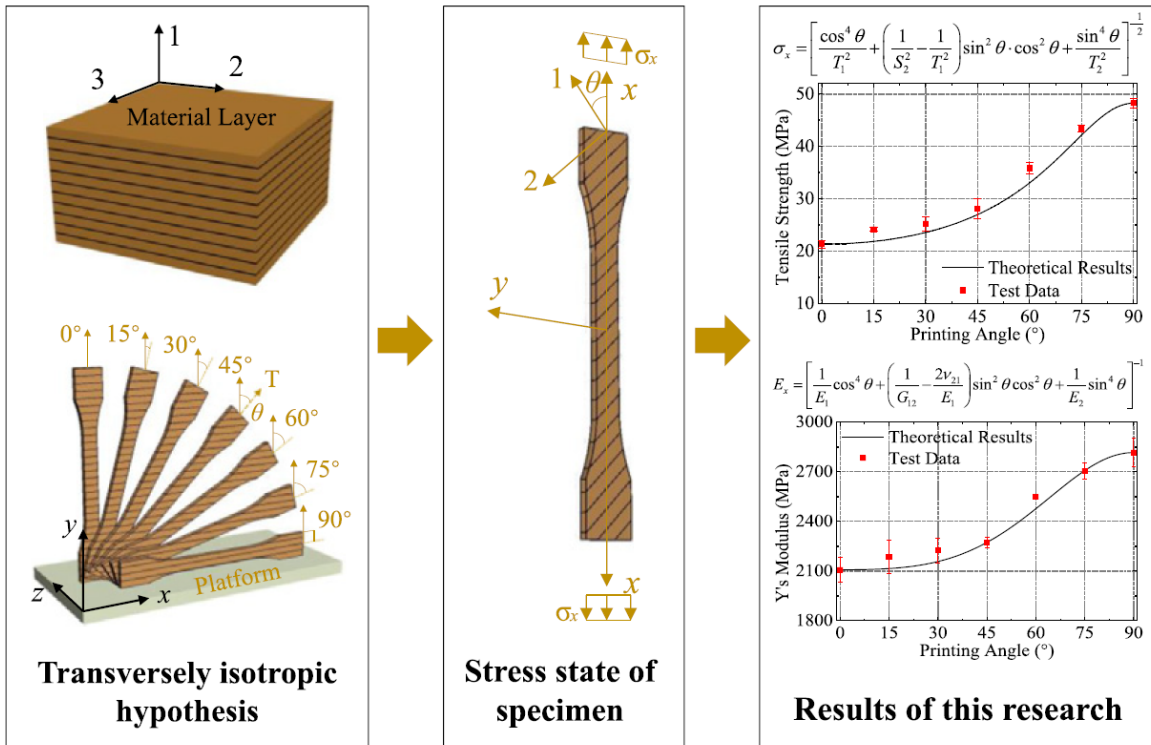


Figure 3.16: Summarized results from [70]. Tests were conducted with 0.1, 0.2, and 0.3mm layer thickness samples. Means and standard deviations are plotted for each test angle.

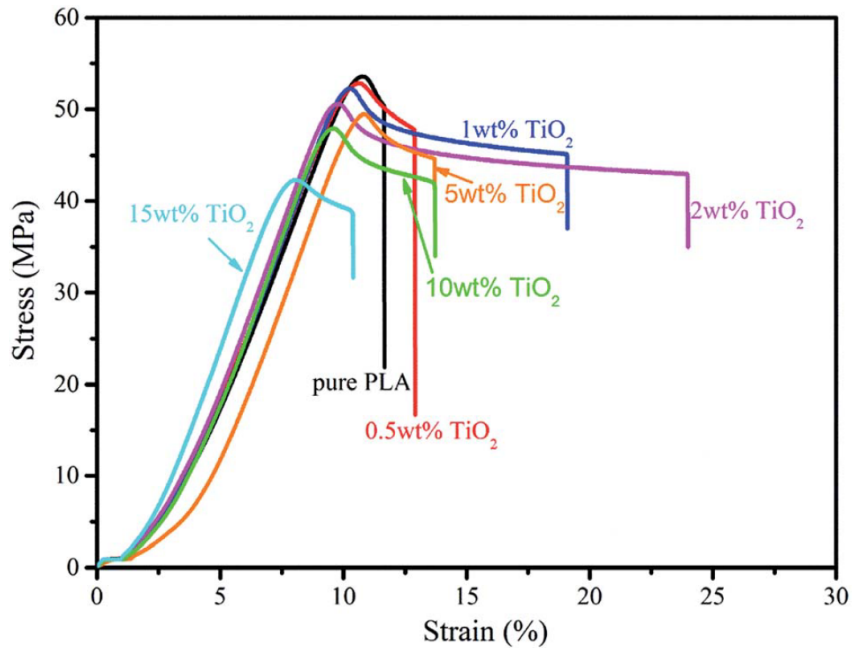


Figure 3.17: Stress-Strain curve for PLA and other plastics, from [71].

In their tests, pure PLA samples failed almost immediately after reaching their yield point. Therefore a safety factor based on the ultimate strength rather than the yield strength will make little difference in the overall strength characteristics of the plenum. Regardless, combining results from [70] and [71] could still produce a reasonable estimate for the orthotropic yield strengths of PLA. The estimated orthotropic properties of the plenum are outlined in Table 3.3. Values were obtained from the aforementioned sources, and *estimated* yield strengths are included as well.

Mechanical Property	X-axis	Y-axis	Z-axis
Ultimate Strength	48 MPa	48 MPa	21 MPa
Young's Modulus	2.8 GPa	2.8 GPa	2.1 GPa
<i>Estimated</i> Yield Strength	45 MPa	45 MPa	19 MPa

Table 3.3: Values used to define the orthotropic mechanical properties of a PLA-based 3D printed plenum.

It should be noted that [70] refers to the vertical print direction as the *Y*-axis, with the print bed defined by the *X* and *Z*-axes. However, the 3D printing community typically defines the vertical direction as the *Z*-axis, with the print bed defined by the *X* and *Y*-axes. For the sake of consistency with the print community, this section refers to the vertical direction as the *Z*-axis.

A single plenum is printed as a pair of hemispheres oriented such that their flanged sealing surfaces are in contact with the print bed. Each layer is essentially a series of nested, contiguous rings deposited down on the previous layer, decreasing in radius with each step in the *Z*-axis to eventually form a hemisphere. As noted in [70], the tensile strength in the *Z*-axis is approximately half that of the *X* and *Y*-axes (21 MPa vs. 48 MPa), so a failure in the plenum would be expected to occur in the *Z* direction.

A simple SolidWorks-based stress analysis was used to design the plenum by considering peak stress in the *Z*-axis, shown in Figure 3.18. The *Z*-axis was specifically chosen as the stress-based design constraint because, as can be inferred from the above information, it is the structurally weakest direction in FDM printing.

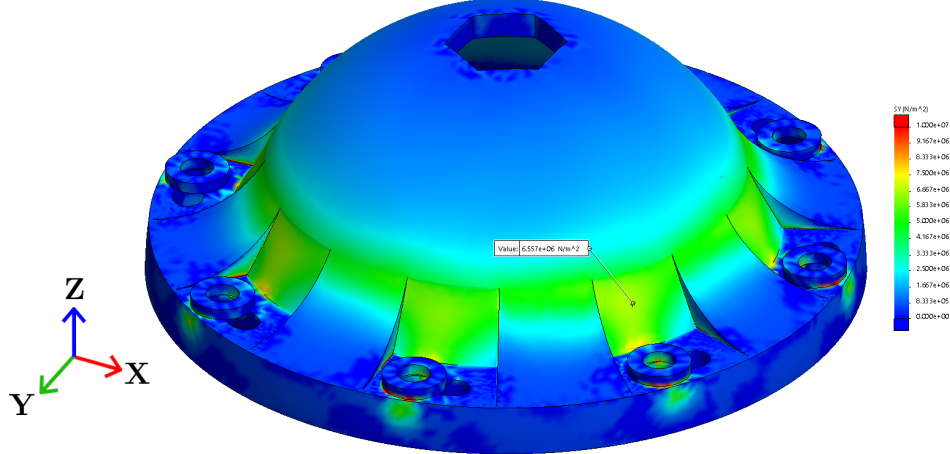


Figure 3.18: Z-Normal stress distribution over a single plenum hemisphere under 791 kPa (100 psig) internal pressure shown on a scale from a range of 0 to 10,000 kPa. The peak stress value at the flagged point is 6557 kPa.

Peak Z-normal wall stress occurs at 6557 kPa resulting a safety factor of 2.9 based on the *estimated* yield strength (3.2 based on the ultimate strength). Higher stress concentrations did appear at the corners, but the average tensile stress over the cross section at those points was overall very low – on the order of 3,000 kPa.

3.3.5 Failure Considerations

In the event of an unexpected structural failure of a plenum, a fixed amount of energy will be released via the uncontrolled expansion of gas. This analysis assumes a plenum fails under 790.8 kPa (114.7 psia, or 100 psig) of internal pressure (the design operating pressure of the plenum chambers chosen based on the maximum allowable pressure for pressure vessels stored within the habitable volume of the ISS) and the gas escapes into the atmosphere. The energy stored in a single plenum can be determined by calculating the amount of work needed to compress a column of air at STP to the pressures and densities seen within the plenum.

$$W = -P\Delta V = -P_{atm}(V_2 - V_1) \quad (3.1)$$

$$P_1 V_1^\gamma = P_2 V_2^\gamma \quad (3.2)$$

$$V_2 = V_1 \left(\frac{P_1}{P_2} \right)^{\frac{1}{\gamma}} \quad (3.3)$$

$$\begin{array}{ll}
 V_1 = 30.0\text{cm}^3 & P_1 = 790.829\text{kPa} \\
 P_2 = 101.353\text{kPa} & V_2 = 148\text{cm}^3 \\
 \boxed{W = 12.0\text{J}}
 \end{array}$$

For comparison, this is similar to the energy of a standard 3 gram paintball round with a muzzle velocity of 200 FPS (91 m/s) [72].

3.4 Propulsion System Control Board

A printed circuit board was designed and manufactured to house all of the electronics needed to control the propulsion system and relay pressure information. This control board must be capable of commanding twelve separate valves independent of one another, each operating at 12 Volts, using a NodeMCU wireless-enabled microcontroller. The L293D motor controller integrated circuit (IC) was chosen to act as valve controllers such that the microcontroller could switch a valve on or off using a 3.3 V signal to control a single channel on the L293D controller. Note that the L293D is designed to nominally operate at 5 V, but per the specifications can be triggered with a signal as low as 2.3 V, thus making it 3.3 V compatible – though this will reduce the signal voltage margin (the difference between the nominal signal voltage and the minimum required trigger voltage). An MCP23017 GPIO expansion IC was required to be used since the microcontroller did not have enough General Purpose Input/Output (GPIO) ports to control all 12 valves.

The pressure transducers selected operate at 5 V, but the chosen microcontroller's GPIO ports only operate at 3.3 V. Therefore the MCP3002 Analog-Digital Converter (ADC), which is compatible with 3.3 V logic, was chosen and a simple resistor-based voltage divider was designed into their circuit to convert the 5 V pressure signal into a 3.3 V signal before being passed through the ADC.

Power to the entire board was provided by a single 14.8V LiPo battery, and a DC-DC step-down voltage regulator used to bring the supply down to 5 V to power the microcontroller and peripheral components. Any peripherals which required a 3.3 V signal were powered by tapping off the 3.3 V pins of the microcontroller, though the microcontroller itself could be

powered by the 5 V source. The valves are designed to operate nominally at 12V but are robust enough to operate over a range of voltages. 14.8V was chosen as the design voltage since the increased voltage would result in faster response time of the valves. An 11.1V battery was also considered, but early testing showed a significant increase in valve response time. All valve, sensor, and battery connections were made using standard screw terminals soldered onto the board.

The layout of the propulsion control board was accomplished using Autodesk EagleCAD, shown in Figure 3.19a, and the board was manufactured by OSH Park (Portland, OR). The assembly process for the board is illustrated entirely in Figure 3.19, and a wiring diagram of the PCB is available in Appendix F.

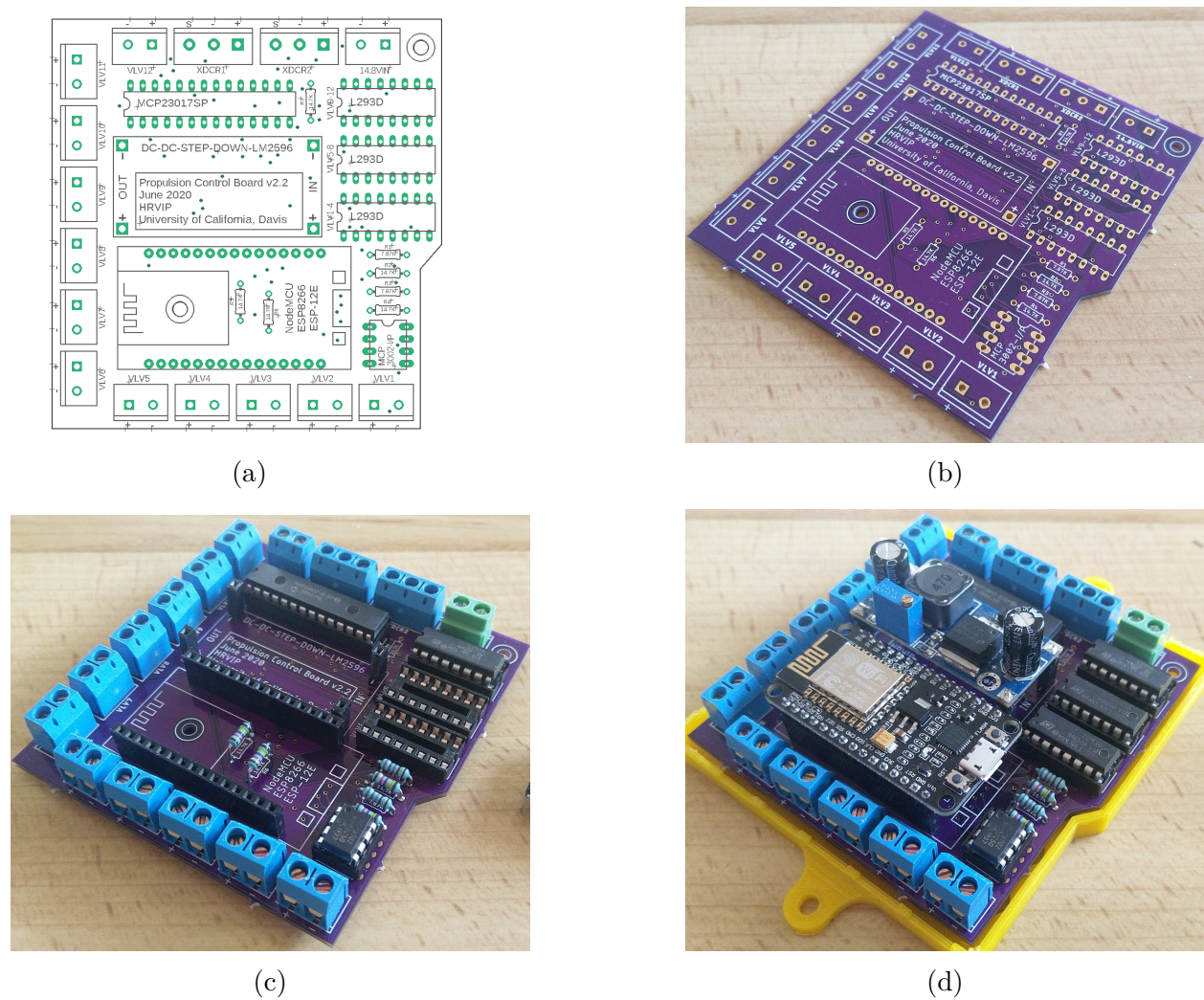


Figure 3.19: Propulsion control board schematic (a), bare board (b), with terminals soldered (c), and with all components inserted (d).

3.5 Wireless Control System

A wireless control system was developed to relay data and commands between users and the propulsion control board, and to keep the test platform physically disconnected from any stationary sources of power. Communication between the user and hardware takes place over a preconfigured Wi-Fi network with information and commands passing through a message service running on a Raspberry Pi 3+. The Arduino-based controller interprets messages broadcast over the network by the Raspberry Pi to control the valve states, and in turn relays sensor data back through to the user interface on the other end. Fig 3.20 provides a top-level illustration of the network and control architecture.

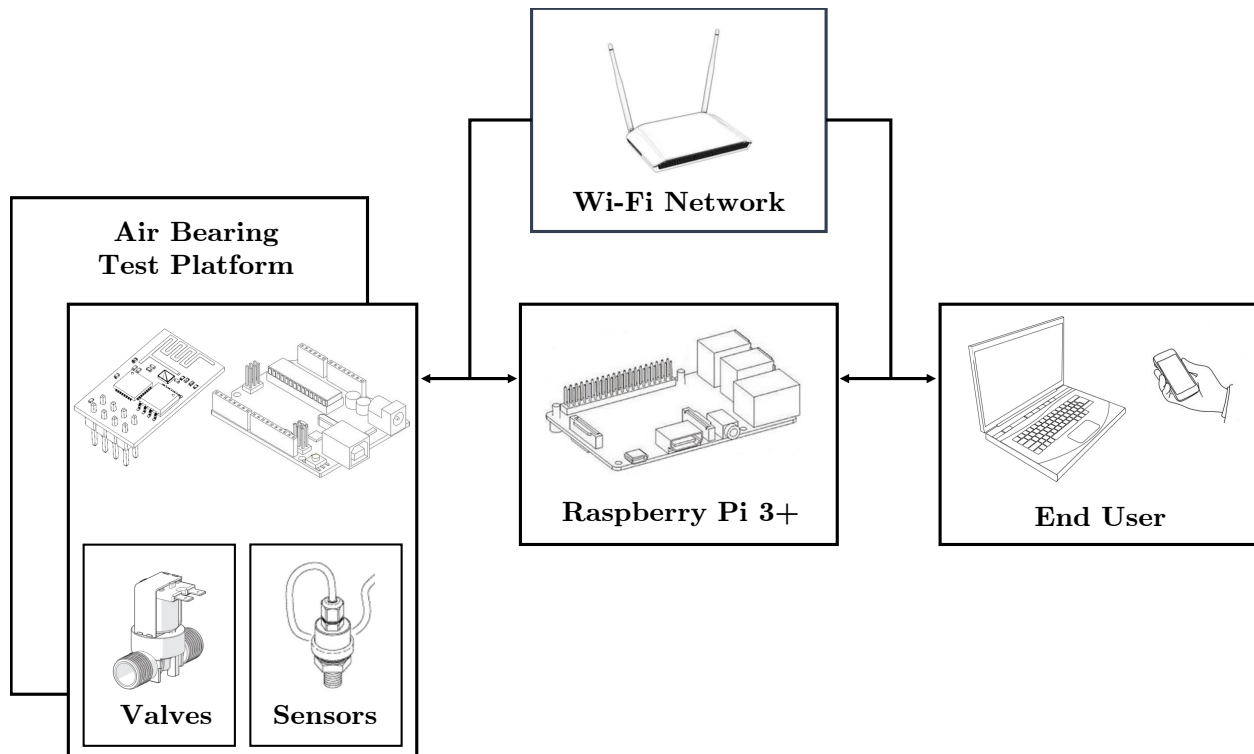


Figure 3.20: Top-level architecture diagram for wireless communication system

In addition to relaying data and commands, the Raspberry Pi can record data during a prescribed valve-open period. Data from two pressure transducers are relayed by the Arduino at 20 Hz, with each data point recorded with a timestamp into an array and saved to a file upon completion of the thruster command. This setup was also used for static thrust testing to record data from the load cell supporting the valve and nozzle.

The Raspberry Pi also runs a web server to provide a simple browser-based interface for the end user and custom-designed valve control software debugging tools. The user interface was designed with three separate control panels, each of which control the valves or valve series in various modes. The main page acts as a controller for the propulsion testbed as a whole, with touch input-based buttons used to thrust translationally or rotationally at two distinct levels: single plenum discharges (denoted by a single chevron/arrow icon), and dual plenum discharges (denoted by a dual chevron/arrow icon). Additionally, this page allows the user to refill both plenums in a single thruster line with the touch of the corresponding square-shaped icon. The second page provides toggle-based control to manually command valves to hold open while the primary display is used to input nominal directional commands, thus simulating a valve fail-open failure mode of the user's choosing. The third page acts as a "debugging" screen where valves can be individually commanded open during a press-and-hold action by the user. All three pages relay pressure measurements from the pressure transducers mounted on the air bearing test platform: one measures the air bearing supply pressure (labeled "FLOAT PSIG") while the other measures the propulsion supply pressure (labeled "PROP PSIG"). Each of these three displays are shown in Figure 3.21.

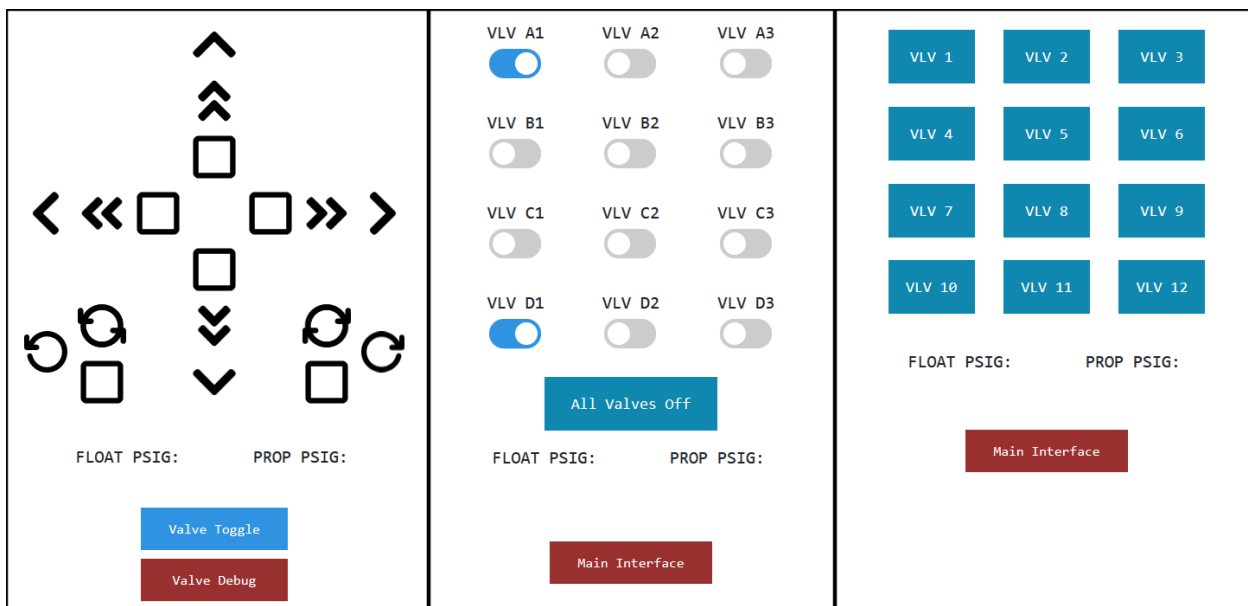


Figure 3.21: Three primary control screens of the user interface designed to control unit as a whole, hold selected valves open, and touch-toggle individually valves for debugging.

3.6 Computer Vision System

3.6.1 OpenCV and the ArUco Library

A 720 x 480 pixel camera is mounted above the air bearing test bed to record the motion of the air bearing platform. A fiducial marker is mounted to the air bearing test platform to enable object recognition and pose estimation. The fiducial marker detection library ArUco, built into the OpenCV open source computer vision library, is used to scan each frame of a recording and detect the fiducial marker. Upon detection, the relative pose between the marker and camera is estimated and saved along with a corresponding timestamp for post-processing with a Kalman filter. The foundation for this work was established by undergraduate researcher Adriana Henriquez and subsequently iterated upon to become the system used in testing.

The ArUco platform provides an easily-acquirable, easily-implementable method for fast detection of square planar markers, similar in style to common QR codes [73]. At its core, ArUco automatically generates a set of highly distinguishable square fiducial markers and combines it with a method for optimized dictionary sorting for faster recognition. The markers are designed to maximize inter-marker distance (how “alike” each marker is to one another) and the number of bit transitions (how many times a ‘0’ turns into a ‘1’, and vice-versa) as a means for reducing false positives and negatives. Finally, it employs computationally efficient methods for segmenting lines, extracting contours, removing perspective projection, extracting marker codes, and comparing the extracted code to the codes listed in the dictionary. Figure 3.22 illustrates this process for a sample board.

ArUco is made even more powerful by utilizing adaptive image scaling to reduce an image to the minimum size needed for marker detection while maintaining accuracy and robustness [74]. The initial step reduces the image size by a computed factor such that markers are of a minimum pixel count necessary for detection. This step dramatically improves the speed of the image segmentation step (essentially grouping and labeling pixels based on their similarity) by reducing the total number of pixels needing to be scanned, but will reject candidates which are too small – i.e. if a marker is too far away. In general, the code only uses a version of the image with the *lowest* resolution necessary to perform each step of the marker detection process. The end result is a detection algorithm that is capable of

operating up to $40\times$ faster than other open source contenders such as AprilTags, ArToolkit+, and Chilitags. In testing, the ArUco developers obtained an image processing speed of 720 frames per second (fps) in 1080p resolution using an Intel® Core™ i7-4700HQ processor, even when performed entirely as a single threaded operation.

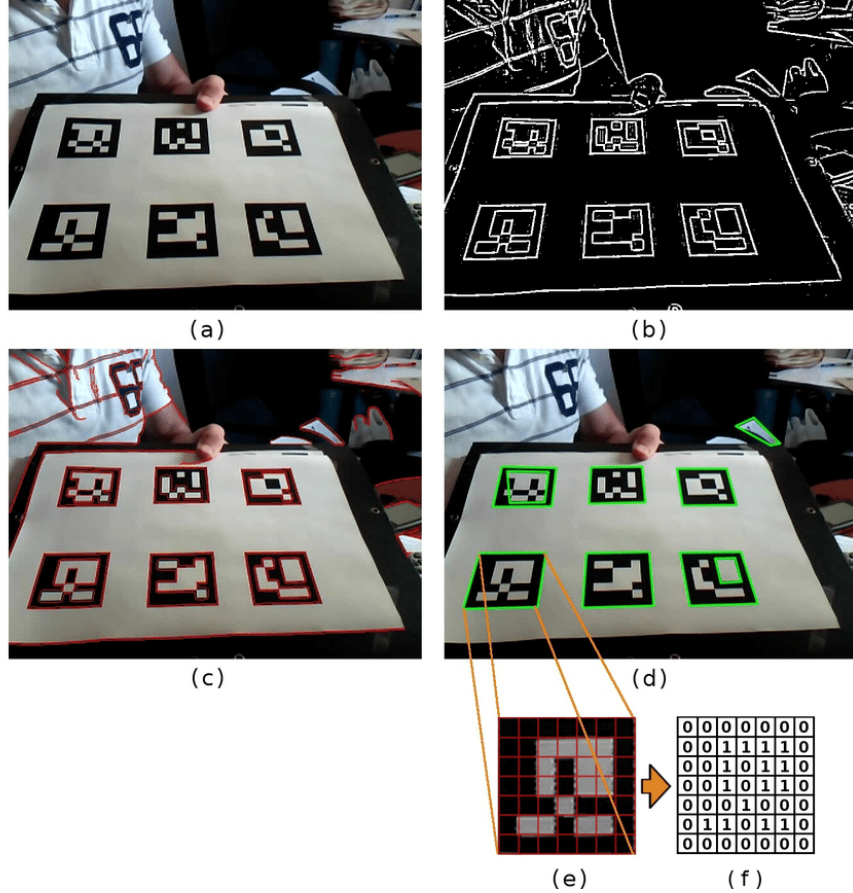


Figure 3.22: The ArUco marker detection process. (a) Original image. (b) Local thresholding used for segmentation. (c) Contour detection. (d) Polygonal approximation and removal of irrelevant contours. (e) Perspective projection correction. (f) Bit assignment for each cell within the marker.

In the air bearing platform tracking task, OpenCV is responsible for calibrating the camera and importing a video to be analyzed by the ArUco algorithm. ArUco (through OpenCV) is responsible for scanning each frame of a video and detecting a fiducial marker. If a marker is found, its relative pose (position and rotation relative to the camera) is extracted, marked with a timestamp, and exported to a list. This data is then fed into a Kalman filter in order to estimate the velocity and acceleration of the air bearing platform.

3.6.2 Kalman Filtering

Kalman filtering is a statistics-based operation that combines measurement data with a system model-based estimate to produce an *improved* estimate of the actual state of a system. The “state” referred to here is any physical property of the system that can change over time, whether it be position, orientation, temperature, or any other measurable property. A system “model” is a mathematical relationship to describe how the properties vary over time. In the world of controls, a model might take the form of a state-space matrix which relates the time-rate of change of a state (or multiple states) to their current value(s). For Kalman filtering, the model is referred to as a *state transition* matrix that relates the state (or multiple states) from one discrete time step to the next. Figure 3.23 illustrates this general process.

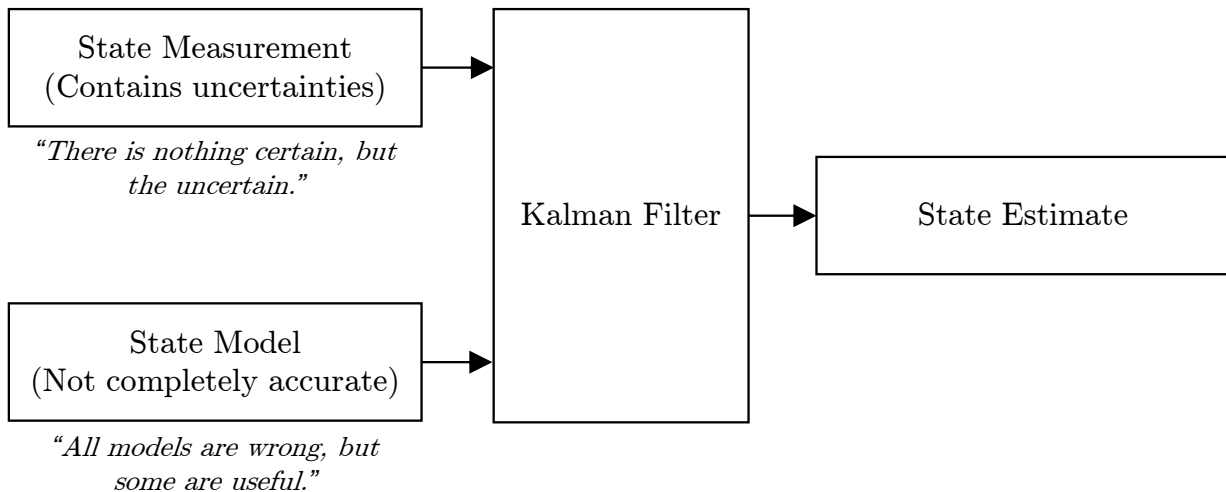


Figure 3.23: The general process of Kalman filtering to produce a state estimate from a combination of sensor data and model predictions, for each time step

Kalman filtering produces a weighted average between the state transition model prediction (which is not perfect) and sensor measurements (which are noisy and prone to error) for each data point fed to it. The advantage lies in the fact that the filter only requires data from the previous and current time steps in order to make an estimate of the current state. The filter can also be tuned to weight one input more than another based on the presumed reliability of each. For example, if the model is very crude and of low-order while the measurements are clean and consistent, then the filter can be set up to place more

weight, or more “trust”, in the measurements. On the other hand, if sensor data is noisy and prone to large variations, then a higher-order model can be used and the Kalman filter will then weight its estimations based more on the model than the measurements. What’s more, multiple sources of data can be combined to produce better estimates; a process generally referred to as *sensor fusion*.

If you are unable to directly measure a state, then that state can be estimated using other state measurements, assuming a model exists which relates the two states to one another. Indeed, this is the case for the air bearing platform tracking task at hand: we are interested in measuring velocity and acceleration of the platform as a means to measure thrust and impulse, but the computer vision system is only capable of measuring position. Position is recorded at regular intervals (based on the frame rate of the camera), and the velocity and acceleration is derived from position history by sending the position data through a Kalman filter. The model used for the state estimation is a simple kinematic relationship described by Newton’s laws of motion, explained in detail in Section 3.6.2.1.

The Kalman filtering process is iterative in nature, usually operating at a rate greater than or equal to the rate of measurements being made, and can be summarized as follows: For each time step:

- An *a priori* estimate of the state at the next time step is made using the model and the previous state estimate
- Measurements of the state are taken
- A weighting factor K is calculated based on the model prediction, the measurement(s), and assumptions about the accuracy of each
- An improved, or *a posteriori* estimate of the state is calculated from K and the *a priori* estimate

A much more in-depth description and derivation of Kalman filters has been written by Roger Labbe and is referenced heavily in this section. Figure 3.24, taken from Labbe [75], illustrates this process.

3.6.2.1 Model Development

Designing a Kalman filter first requires one to develop a series of differential equations to describe the system dynamics. For more complicated systems, these equations can often

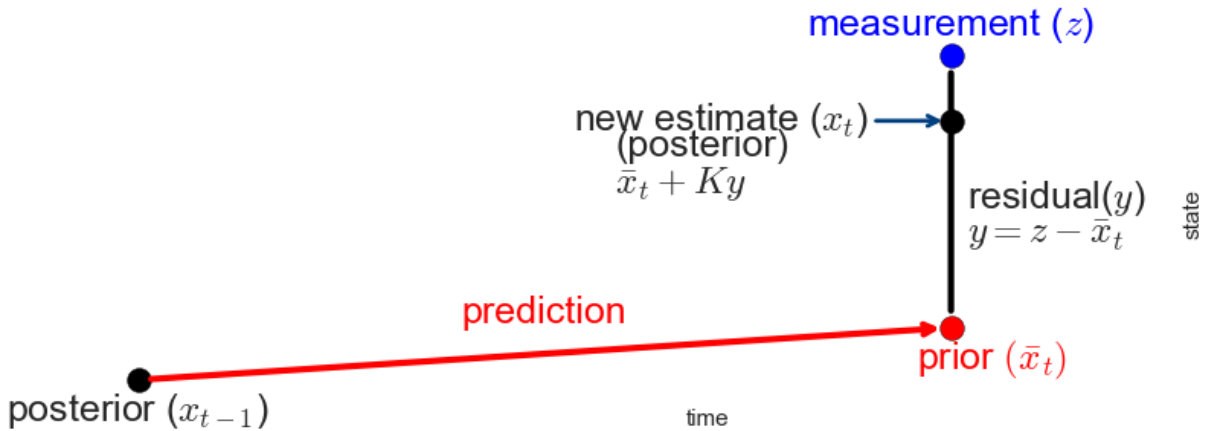


Figure 3.24: Illustration of the Kalman filtering process whereby an *a priori* state estimate is made then updated with measurements [75].

be large, non-linear, and not easily integrable. Fortunately, our satellite is a simple rigid system operating in zero gravity, so the dynamics of it are easily approximated by Newton's equations of motion. A first-order estimate of a discrete state transition is shown in Equation 3.4 for one-dimensional motion, the basis of which will be used in our *discretized continuous-time kinematic* filter:

$$\dot{x} = \frac{dx}{dt} \approx \frac{x_t - x_{t-1}}{\Delta t} \quad (3.4)$$

Rearranging this relationship to solve for x_t provides a means for predicting the new state x_t based on the previous state x_{t-1} and the velocity between the two states. Realistically, however, the velocity used in this relationship must be taken exactly from the previous state since it is only known *prior* to measuring the state at t . Collectively, this is called an *a priori* estimate: an estimate of the state at the next time step t based only on information from the previous time step $t-1$. It is the first step in a Kalman filter process, and is illustrated in Figure 3.24 by the step labeled “prediction”. The model for this state transition is shown by Equation Set 3.5:

$$x_t = \dot{x}_{t-1}\Delta t + x_{t-1} \quad (3.5a)$$

$$\dot{x}_t = \dot{x}_{t-1} \quad (3.5b)$$

This model is referred to as a “constant velocity” model (made apparent by Equation 3.5b), and can be used with some success for simple tracking and estimation tasks. However,

seeing as the goal of this project is to attempt to measure thrust (acceleration), a relationship between position, velocity, and acceleration must be included in the model. The elegance of Kalman filtering becomes more apparent when we consider that we can observe “hidden”, or *inferred* values – values which are mathematically related to the measured value(s) but are not directly measured themselves. With one additional integration of Equation Set 3.5 with respect time, we develop a system model which now contains the “hidden” value of acceleration. Equation Set 3.6 now relates the state at $n = 1$ to the state at $n = 0$, including acceleration components.

$$x_t = \frac{1}{2}\ddot{x}_{t-1}\Delta t^2 + \dot{x}_{t-1}\Delta t + x_{t-1} \quad (3.6a)$$

$$\dot{x}_t = \ddot{x}_{t-1}\Delta t + \dot{x}_{t-1} \quad (3.6b)$$

$$\ddot{x}_t = \ddot{x}_{t-1} \quad (3.6c)$$

Given Equation 3.6c, Equation Set 3.6 describes what would be called a “constant acceleration” model. This process could theoretically continue indefinitely, since with each integration we are effectively adding a higher order to our model.

It should also be noted that even though the models assume some parameter is constant between states – whether it be velocity or acceleration – this is of course rarely the case in any real dynamic system. A pulsing thruster will produce time-variant acceleration, a changing orbit altitude will produce varying velocities, and so on. Recall that the model is only used to predict the next state using the previous estimated state as a starting point. Specifically, it will use the *Kalman estimate* of the previous state to estimate the next step, meaning these parameters will almost certainly vary between steps regardless of our assumptions of constant velocity or acceleration. Once again we are reminded that “*all models are wrong, but some are useful*”. The model does not have to be perfect – it just needs to be good enough to provide a reasonable estimate of the state at the next time step. Naturally, the definition of “reasonable” is subjective and depends on the details of the particular application.

Equation Set 3.6 can also be represented as a *state transition matrix*, shown in Matrix Equation 3.7. The canonical representation of this relationship is shown in Equation 3.8.

$$\begin{bmatrix} x_k \\ \dot{x}_k \\ \ddot{x}_k \end{bmatrix} = \begin{bmatrix} 1 & \Delta t & \frac{1}{2}\Delta t^2 \\ 0 & 1 & \Delta t \\ 0 & 0 & 1 \end{bmatrix} \begin{bmatrix} x_{k-1} \\ \dot{x}_{k-1} \\ \ddot{x}_{k-1} \end{bmatrix} \quad (3.7)$$

$$\mathbf{x}_k = \mathbf{F}\mathbf{x}_{k-1} \quad (3.8)$$

The model portion of the Kalman filtering process is used to produce an *a priori* estimate of the system – a *prediction* of the state prior to measurement. To differentiate between the *a priori* and *a posteriori* estimates, the symbol $\bar{\mathbf{x}}$ is used to denote the *a priori* estimate, while the symbol $\hat{\mathbf{x}}$ is used to denote the *a posteriori* estimate. Therefore, Equation 3.8 would describe an *a priori* estimate as follows:

$$\bar{\mathbf{x}}_k = \mathbf{F}\hat{\mathbf{x}}_{k-1} \quad (3.9)$$

Note that the *a priori* estimate at t ($\bar{\mathbf{x}}_t$) is based on the *a posteriori* estimate at $t - 1$ ($\hat{\mathbf{x}}_{t-1}$). In other words, the corrected estimate from the previous time step (the *a posteriori* from $t - 1$) is used to predict the state at the next time step (the *a priori* at t).

3.6.2.2 Measurement and Process Variance

In addition to designing the state model, the designer must also consider how *accurate* the model and measurements are. Accuracy is reflected in the *variance* (σ^2) term for what is assumed to be a Gaussian distribution of noise (or model deviance from reality) in the state model. A better sensor will produce more accurate results and will therefore have less variance. Likewise, a poor model will yield poor predictions and will therefore have greater variance.

Sensor variance can be acquired by taking multiple samples and observing the distribution of values. Determining the process model variance, on the other hand, can be quite demanding. In practice, this is often performed iteratively by running collected data through many variations of a Kalman filter until a suitable process model variance is arrived at.

Process noise can be approximated by assuming all lower-order terms have zero noise associated with them. Only the highest-order process term will have noise associated – that is, the process term that changes most rapidly between states for each variable. This approach is valid by virtue of the fact that numerical differentiation of real data generally results in very noisy derivatives. Therefore, information derived from higher derivatives is weighted less in the estimation. For a state transition modeled by Equation 3.7, the associated process noise would be modeled by Equation 3.10.

$$\mathbf{F} = \begin{bmatrix} 1 & \Delta t & \frac{1}{2}\Delta t^2 \\ 0 & 1 & \Delta t \\ 0 & 0 & 1 \end{bmatrix} \quad \mathbf{Q} = \begin{bmatrix} 0 & 0 & 0 \\ 0 & 0 & 0 \\ 0 & 0 & \sigma^2 \end{bmatrix} \quad (3.10)$$

An exhaustive body of work is available which describes the formulation of process variance noise based on numerous methods. For this project, a process variance matrix was generated using the *Q_discrete_white_noise* package in the *filterpy* Python library. This library automatically generates a discrete white noise model for a given matrix dimension and variance which, while perhaps not the most accurate model of noise, provides an acceptable starting point with which to iterate from.

3.7 Summary

This chapter introduced the reader to the development of the propulsion system hardware and corresponding support hardware. Information was provided on the processes involved for manufacturing the nozzles and plenums, and additional details covering some of the challenges faced during this process were provided. It was shown that nozzles with features as small as 0.4 mm were capable of being manufactured with tolerances as small as 0.03 mm. Furthermore, we have demonstrated that it is viable to utilize benchtop 3D printing processes to manufacture custom-sized pressure vessels, and that careful anticipation of upstream uncertainties can be successfully designed against. Lastly, the reader was introduced to the wireless control interface and data acquisition setup using a computer vision system, followed by the development of a Kalman filter algorithm for post-processing the acquired data. With the details of the propulsion hardware and support hardware outlined, we can now proceed to the testing phase of this project, covered in the next chapter.

Chapter 4

Thruster Characterization and Full System Testing

The propulsion system design and manufacturing was validated by first individually testing the subcomponents then the assembly as a whole. Plenum design was validated through proof testing whereby the plenums were held above their design pressure for a period of time and checked for leaks. Nozzle design was validated with a combination of steady-state thrust and steady-state mass flow rate measurements at varying inlet pressures. The thrust and mass flow rate measured at these pressure set points were compared to theoretical values for the same conditions. Following the steady-state results, the time-rate of change thrust was measured for a single plenum discharge and compared to the theoretical model. Lastly, the entire propulsion system was assembled and integrated onto the air bearing platform, after which a test battery of maneuvers was performed for varying combinations of intentional valve failures. Platform motion during the valve failure modes was recorded by the computer vision system and processed through a Kalman filter to extract the velocity and acceleration states. Results from these measurements were compared to the performance objectives from Section 2.4.3 which originally informed the thruster design.

4.1 Characterization of 3D Printed Plenum Chambers

Plenum design validation was performed by direct pressurization to a proof pressure of 1480 kPa (200 psig). Testing was completed using a specially designed closed hemisphere such that the plenum assembly only had one singular connection point. A short piece of nylon

tubing was epoxied to the connection port on the other hemisphere, allowing the plenum to connect directly to the pressure regulator, seen in Figure 4.1a.



Figure 4.1: Plenum pressure testing configuration (a), and aftermath of a failed test (b).

Water, being largely incompressible, was used for proof testing to minimize the amount of stored energy that would be released in the event of failure. The plenum assembly was housed in a secondary PVC container during testing to contain any water or debris in the event of a failure. Figure 4.2 illustrates the setup for this test.

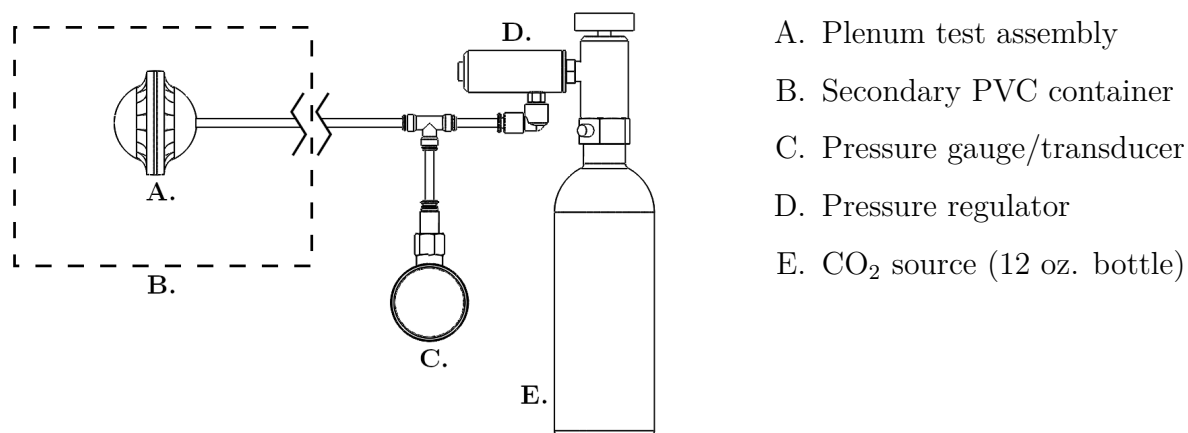


Figure 4.2: Plenum pressure test configuration with test hardware labeled.

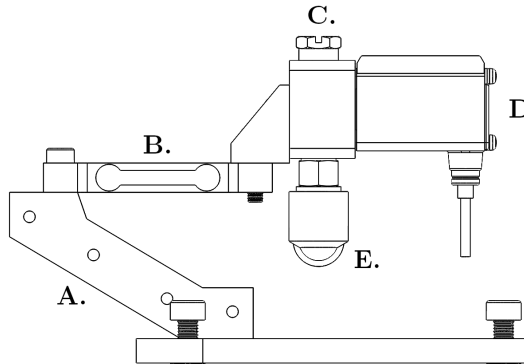
Three plenums tested in this fashion were subjected to the proof pressure and held for five minutes. Any visible signs of leakage were recorded and marked on the plenum for closer inspection. Of the three, only one displayed minor leaking at the interface between the tube and plenum structure. Close inspection of the interface revealed that the epoxy did not set evenly, which allowed a small channel to form for water to escape. Since this failure occurred due to improper assembly and did not reflect a failure of the plenum structure itself, the plenums were deemed safe to use for CO₂ at 791 kPa (100 psig).

A single plenum catastrophically failed at approximately 722 kPa (90 psig) while undergoing pressure testing, shown in Figure 4.1b. The point of failure was at the point of highest stress concentrations for a plenum under pressure, as seen in Figure 3.18. The failure behavior reflected that which was expected during the design phase whereby the structure separated along the Z-axis, separating the plenum structure between layers of the 3D printed structure. It was noted that this failure was due to an unseen error in the printing process whereby a single layer was not deposited cleanly or consistently, resulting in significantly reduced structural integrity. The plenum design was therefore left unchanged, future prints were carefully examined, and each plenum was cycled multiple times during proof testing prior to integration.

4.2 Characterization of Nozzle Design

4.2.1 Steady-State Thrust and Mass Flow Rate

Steady-state testing was performed with a 3D-printed test stand upon which a 200 gram-max load cell was mounted and connected to an HX711 load cell amplifier to measure thrust. A single valve with a hex-plug nozzle was attached to the load cell and oriented vertically, below which hung the electrical and pneumatic connections, shown in Figure 4.3. Data from the load cell and supply-line pressure transducers was collected by a microcontroller and passed into a database via the wireless communications system described previously in Section 3.5. For thrust testing, three trials were conducted at five pressure set points: 239, 377, 515, 653, 791 kPa (20, 40, 60, 80, and 100 psig), though the results will show that the pressure did not remain constant during the trials.



- A. 3D printed test stand
- B. 200 gram-max load cell
- C. Hex-plug nozzle
- D. Solenoid control valve
- E. CO₂ inlet fitting

Figure 4.3: Steady-state thrust test stand with adjustable base.

The trial-averaged pressure and thrust over the duration of a valve open-and-close cycle at each set point is shown in Figure 4.4 with shaded regions representing the standard deviation about the mean for each trial. The median standard deviations for the pressure and thrust measurements were ± 3.03 kPa and ± 0.72 mN, respectively. Thrust time was set such that the estimated propellant consumption was equal for each trial, resulting in increasing thrust time as the pressure set point was decreased.

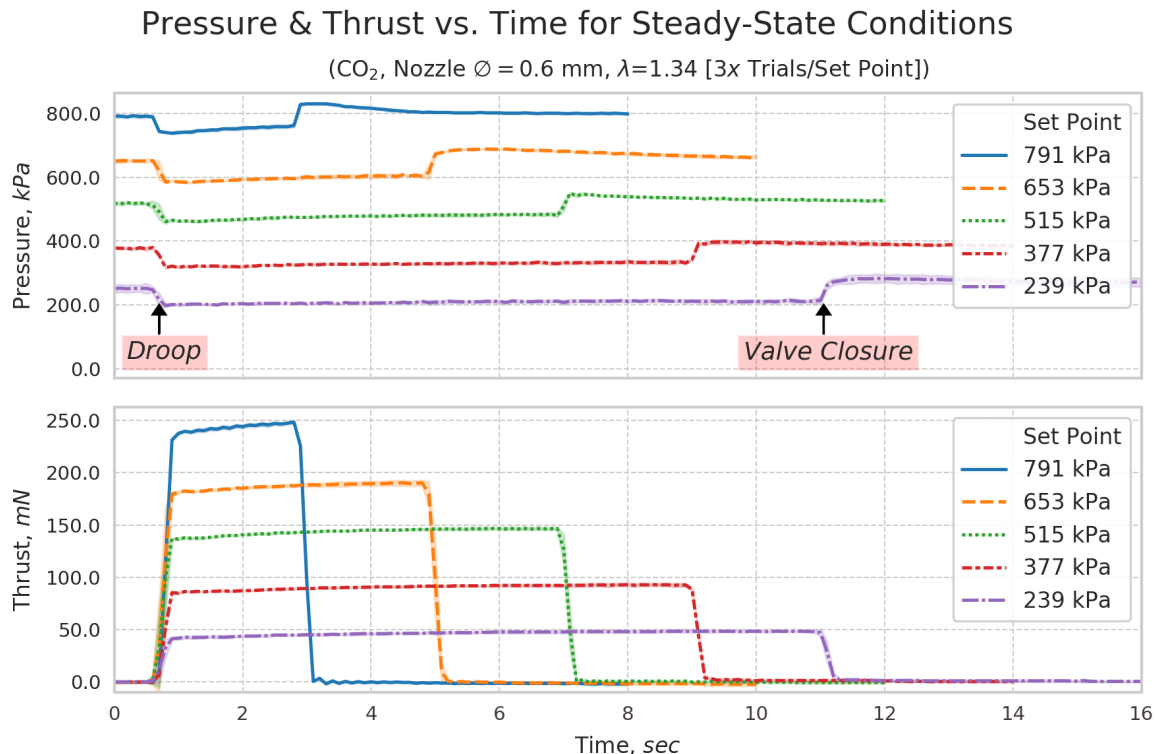


Figure 4.4: Inlet pressure and resultant thrust for fixed pressure set points.

The measured pressure dropped when the valve was opened for each test, indicating that the regulator struggled to maintain pressure while demands were placed on the pneumatic system – a phenomenon known as “droop”. Because of this droop, the outlet pressure drops between 35 to 70 kPa and the thruster slightly underperforms as a result. Additionally, a sharp rise in pressure occurred at the end of each discharge when the valve closed, possibly due to delayed reaction in the valve, which slowly returned to the setpoint in 3-5 seconds. This return action did not occur at lower pressures where frictional forces within the regulator dominate over the lower piston spring and pressure forces. Measured thrust is directly compared with measured inlet pressure in Figure 4.5 and compared with the ideal thrust modeled using isentropic relationships and assuming inviscid flow.

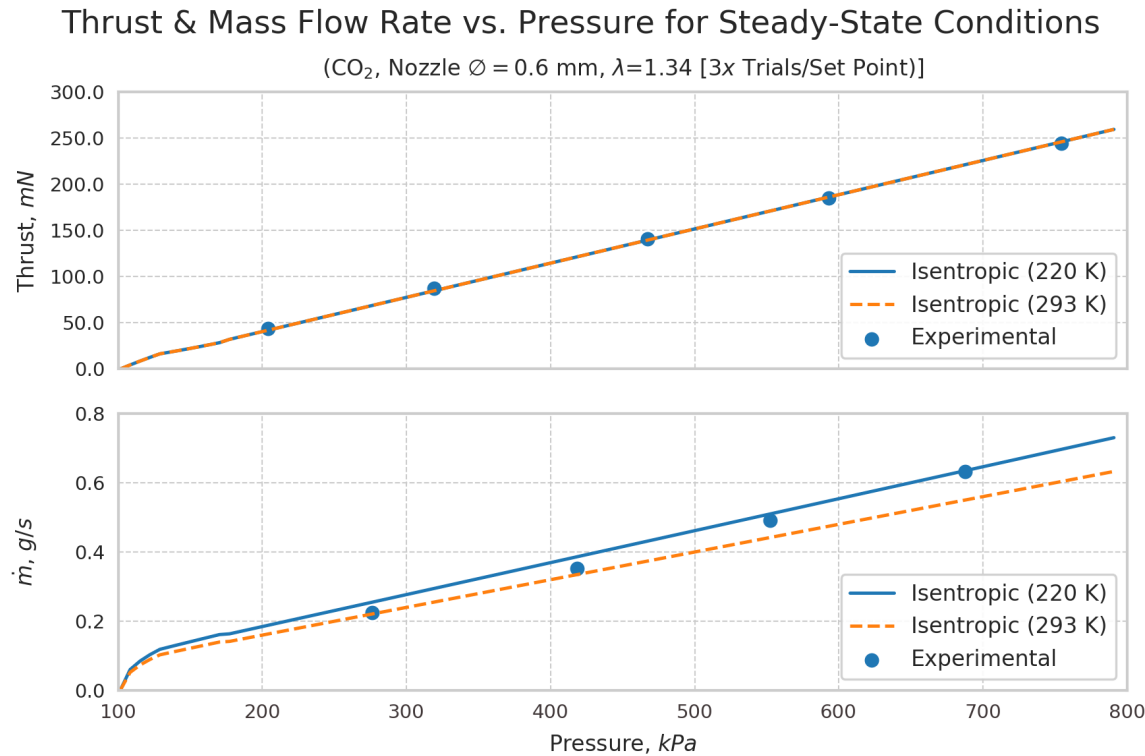


Figure 4.5: Thrust and mass flow rate at measured pressures compared to their respective isentropic models.

Mass flow rate measurement trials were conducted at four slightly higher pressure set points: 274, 412, 550, and 687 kPa (25, 45, 65, and 85 psig). Mass flow rate was determined by measuring the change in mass (Δm) of the CO_2 supply before and after commanding the thruster valve open for a prescribed time set by the user via the interface. Required

valve-open time was estimated from the isentropic mass flow rate calculated at each pressure set point to ensure that the total change in mass was sufficiently large relative to the scale's precision in order to minimize measurement error. A measurement error of no more than $\pm 2.5\%$ was desired, thus the required minimum Δm per test was determined based on Equation 4.1 for a measurement uncertainty (δm) of ± 0.02 grams.

$$\Delta m \geq \frac{\sqrt{2}\delta m}{0.025} \quad (4.1)$$

Per Equation 4.1, at least 1.13 g of CO₂ was required to be expelled per trial to keep the error bound within $\pm 2.5\%$. For each mass flow rate trial, the system was depressurized and the regulator + CO₂ source assembly removed and measured alone. Each time this occurred, some amount of gas equal to the volume of the system escaped, after which the system was repressured before another test was performed. To compensate for this lost gas, the system volume was estimated by pressurizing and depressurizing it several times and measuring the corresponding mass difference in the CO₂ cartridge + regulator assembly. Knowing the system pressure, temperature of the surrounding environment, and measuring the average change in mass between pressurization-depressurization cycles, the volume of the system was calculated, and the corresponding mass subtracted from the results of the mass flow rate test.

Results shown in Fig 4.5 show good agreement between isentropic and experimental values, although the overall measured mass flow rate seems to be higher than predicted. This could indicate that the throat diameter of the nozzle is slightly larger than 0.6 mm. The measured flow rate as a function of pressure departs somewhat from the isentropic results which seems to correlate with a decrease in predicted gas temperature. This departure is expected since the isentropic results assume a constant gas temperature, whereas the CO₂ gas temperature varies considerably throughout the actual test procedure. CO₂ in the line begins at approximately room temperature, while CO₂ coming from the regulator is extremely cold (approximately -50° C) due to Joule-Thomson expansion (throttling) at the regulator orifice. As supply pressure increases, so too does the rate of cold CO₂ entering the line. As such, this predicted decrease in temperature corresponds to a proportional increase in density and therefore mass flow rate.

4.2.2 Single Plenum Discharge

A single plenum was placed in line between two pressure transducers, which in turn were set between two valves used to emulate the final intended configuration (Figure 4.6). The upstream valve was used to prime the plenum and the downstream valve (with attached nozzle) used for discharging, or “firing”, the system. The purpose of this test was to compare the time-rate of change of pressure and thrust for a single plenum discharge to that of the isentropic solution and observe what losses are incurred. While not included in Figure 4.6, the valve is mounted on the same thrust test stand for the steady-state thrust testing setup, and pressure and thrust data are collected in an identical manner.

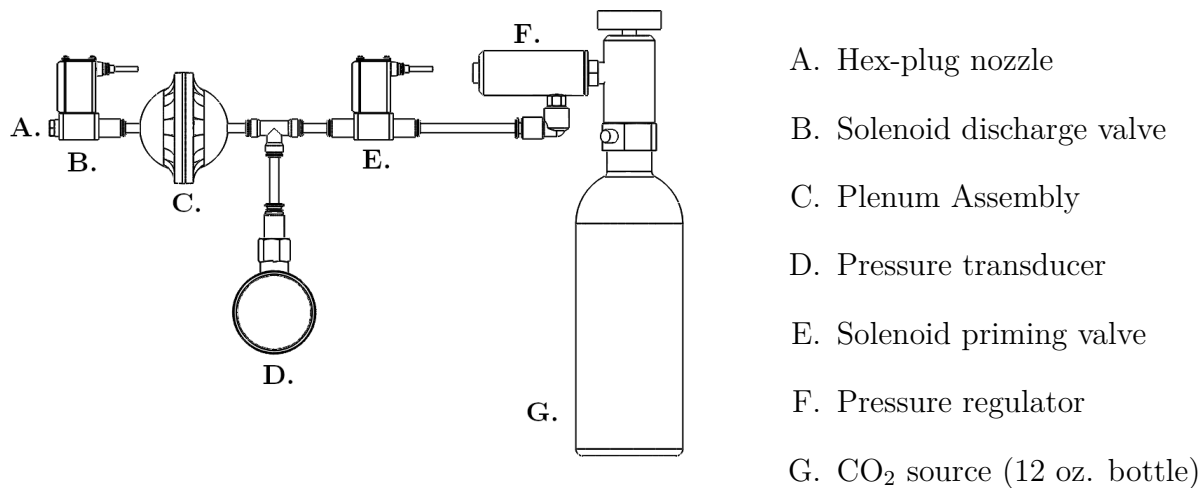


Figure 4.6: Single plenum discharge characterization configuration.

Test results are shown in Figure 4.7. The experimental results are compared to the isentropic solution for a similarly pressurized 30 cm^3 plenum with a 0.6 mm nozzle. Sampling rate is capped at approximately 12 Hz due to limitations in the data recording hardware. While this is sufficiently fast to characterize the long-period characteristics, it is only marginally fast enough to capture the initial thrust curve when the flow is in the process of developing, as can be seen in the first second of the results. Furthermore, pressure measurements were taken on the supply-side of the valve and therefore differ from the pressure at the nozzle inlet. Nevertheless, the results demonstrated good agreement between simulated and real performance after the initial startup.

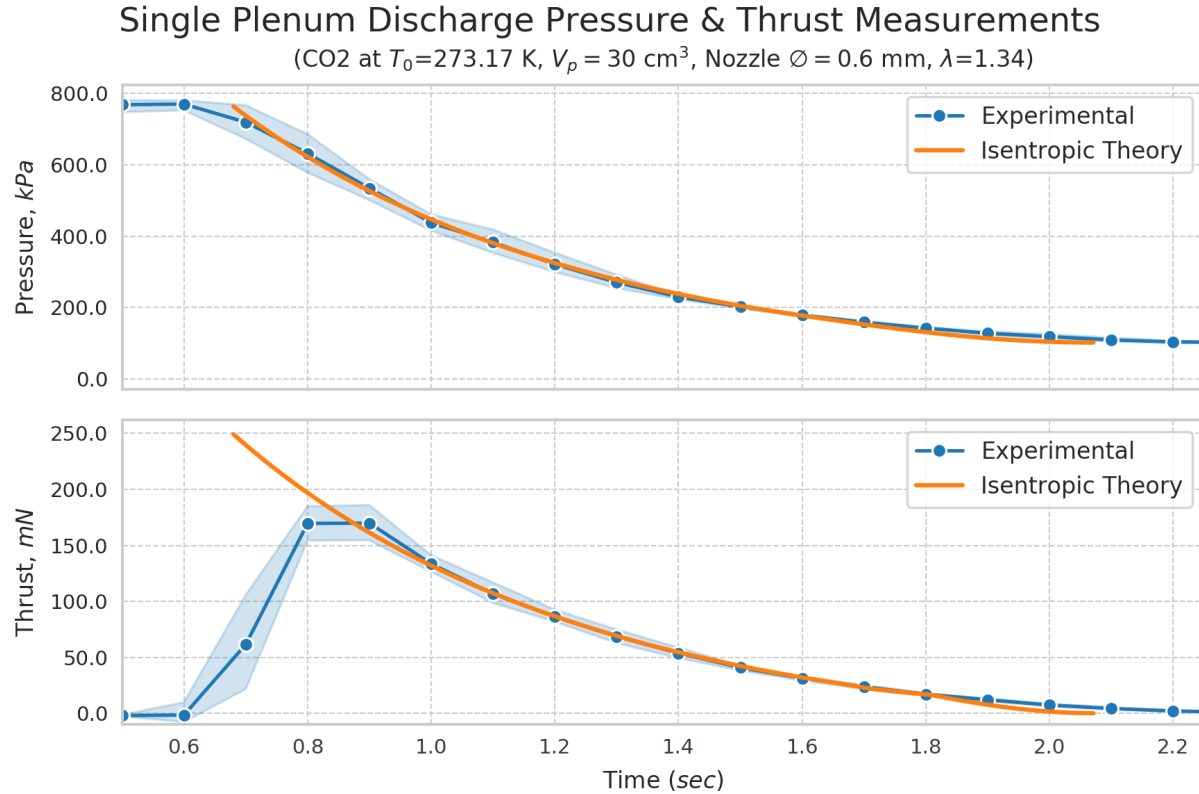


Figure 4.7: Single plenum discharge compared to isentropic model.

4.3 Full-Scale Two-Stage Thruster Testing

The full propulsion assembly consisting of 8x 30 cm^3 plenums and 12x solenoid valves was mounted onto the air bearing test platform. A series of tests were conducted to measure the real-world performance of the CO₂-based propulsion system in both nominal and off-nominal conditions. Nominal performance was gauged by executing a consecutive series of plenum discharges to perform pure translational maneuvers. Since the most critical off-nominal case is that of a jet fail-on (see Section 1.1), off-nominal performance (i.e. valve fail-opens) was gauged by manually commanding different combinations of valves to be held open while a translational or rotational maneuver was performed. Each maneuver was recorded by the computer vision system and post-processed through the Kalman filter to extract total displacement, velocity, and acceleration (both translational and rotational). The mass of the air bearing test platform was measured before and after each test battery which, when combined with acceleration data, is used to estimate the net thrust on the system.

4.3.1 Valve Designations

An illustration of the fully assembled propulsion system mounted onto the air bearing platform is shown in Figure 4.8a. This layout is consistent with the layout shown in Figure 2.7, which defined the “forward” direction of the air bearing platform as the +X-axis. For this configuration, simultaneous plenum discharges from thrusters A and D would produce forward motion. Likewise, simultaneous plenum discharges from thrusters A and C would produce clockwise rotation about the +Z-axis.

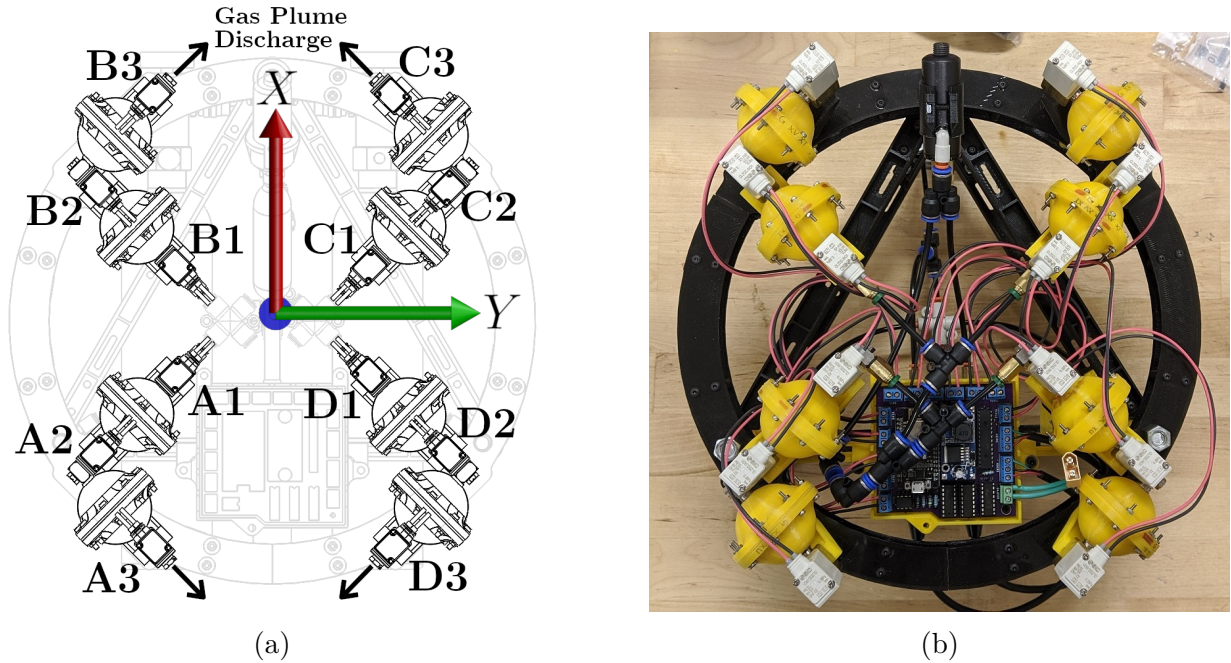


Figure 4.8: Valve layout and designations used for full test platform assembly (a); completed prototype assembly (b).

Specific designations for valves are shortened to their thruster identifying letter (A - D) followed by the valve number (1 - 3) in the thruster line. For example, valve 1 in thruster A is designated ‘A1’, valve 3 in thruster D is designated ‘D3’, and so on. Valve combinations are designated by concatenating the two specific valve labels with a ‘+’ sign. For example, the designation for the first and second valves in thruster line A would be ‘A1+A2’, valve A1 paired with valve D3 would be ‘A1+D3’, and so on.

Failure modes are identified by the valves which are intentionally failed open during the given test. For example, valve A2 failing would be labeled simply as an ‘A2 failure mode’. Similarly, valves A2 and D2 failing open would be referred to as an ‘A2+D2 failure mode’.

mode'. Once again, all failure modes are assumed to be of the fail-open type, so no special designation will be given to differentiate between fail-open versus fail-closed. A valve fail-close mode, while inconvenient, will still allow partial control of some degrees of freedom and in turn allow the satellite to be removed from the proximity of the inspection target.

4.3.2 Nominal Performance

Validation of the plenum-based thruster design was performed by executing two consecutive plenum discharges from thrusters A and D to produce pure translational motion. The position of the air bearing platform was tracked and resultant information pulled from this data. Translational velocity and acceleration are inferred from position using the Kalman filter, and knowing the mass of the platform allows us to estimate the net thrust acting on the platform. Rotational motion was not used for evaluating nominal performance due to the fact that no rotational requirements were specified for the design reference mission.

The final velocity after two complete discharges was compared to the target performance objective listed in Table 2.11. Figure 4.9 demonstrates the overhead view of the motion capture process used in the computer vision system and illustrates the motion of the test platform as it undergoes translation from left-to-right. An ArUco marker was affixed to the platform at the approximate center of mass and is highlighted in the figure showing how position and rotation are recorded.

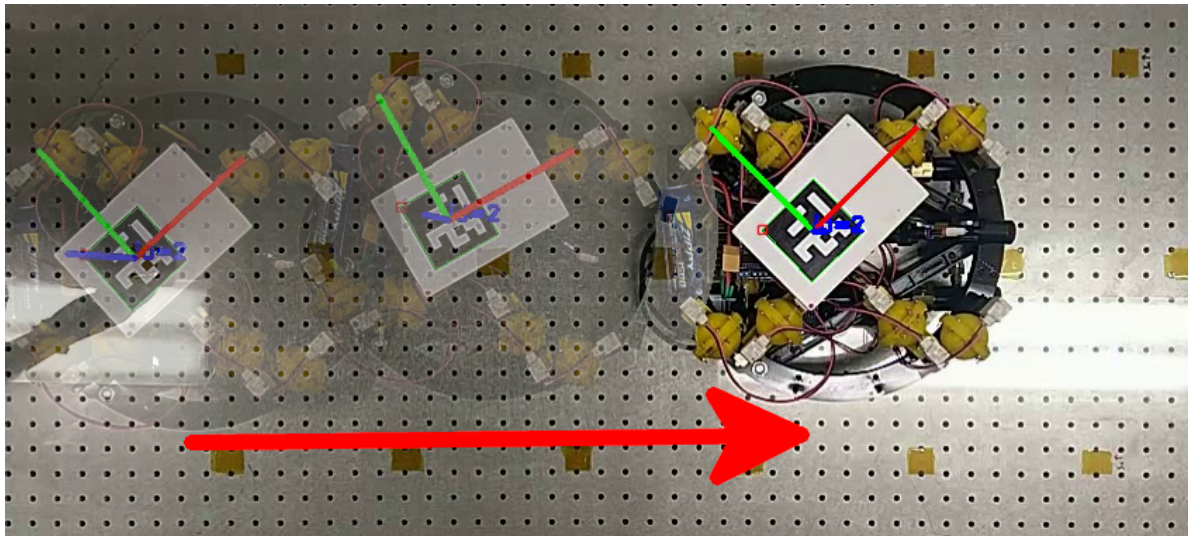


Figure 4.9: Illustration of pure translation-type motion moving left-to-right. Some rotation is induced by imperfections in the air bearing table.

Each test was recorded in this manner and the subsequent data was pulled from the computer vision system and fed into the Kalman filter to produce estimates on the time-rates of change of position, velocity, and acceleration for both translational motion and rotation. All recorded data for a single test was zeroed by the data's initial values and the X and Y displacements were added in quadrature ($\sqrt{X^2 + Y^2}$) to determine the total displacement. For each test type, the displacement (d), velocity (\dot{d}), and acceleration (\ddot{d}) is shown alongside rotation, as seen in Figure 4.10.

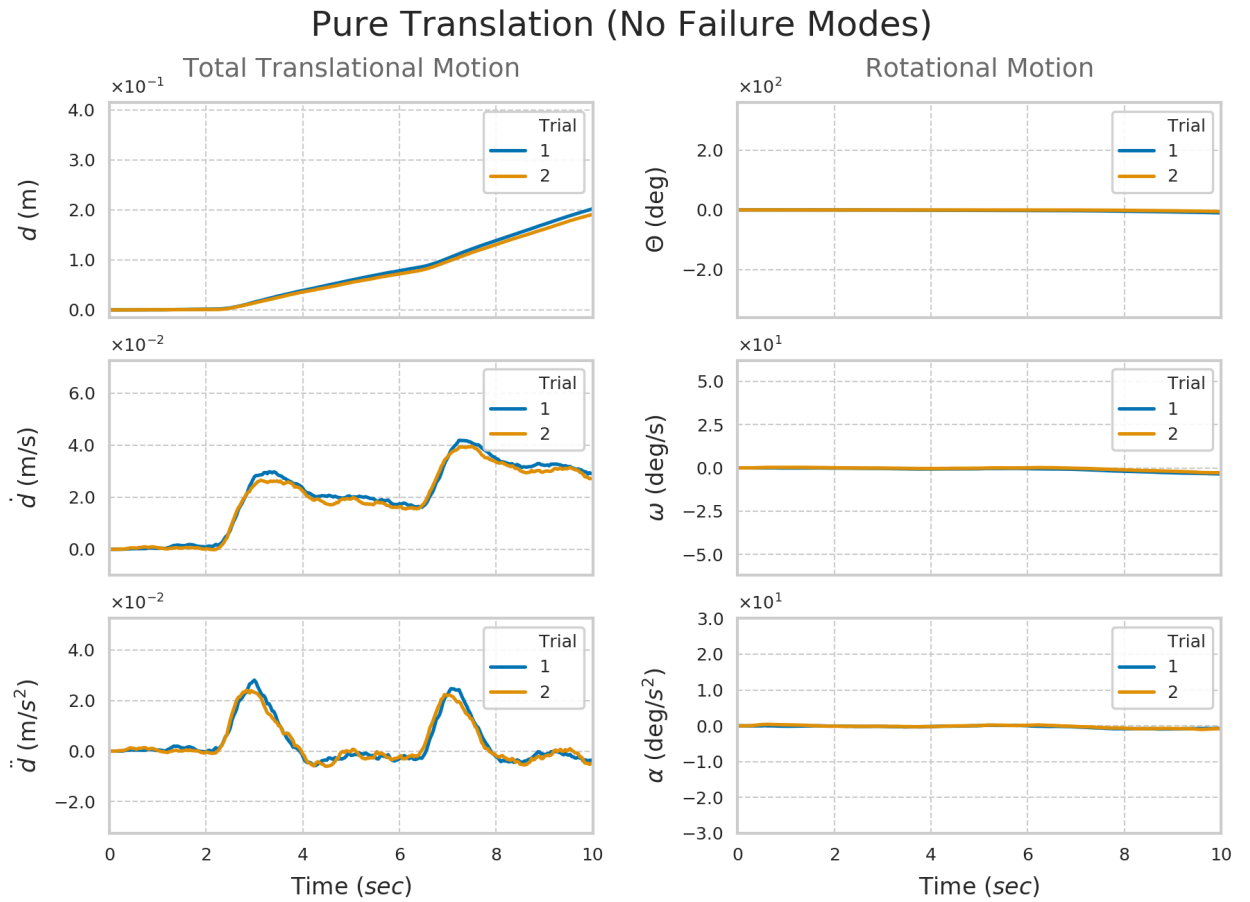


Figure 4.10: Results from executing two consecutive plenum discharges to produce pure translational motion.

Plenum discharges are clearly identifiable in the test results. The first discharge occurred at approximately $T = 2.25$ sec, followed by a second discharge at approximately $T = 6.5$ sec. The final velocity of the test platform was approximately $v = 0.04$ m/s – only about 66% of the target velocity objective of 0.062 m/s.

The discrepancy can potentially be explained by systemic errors in the air bearing testbed, noting how frictional forces are visibly at work in the linear velocity (\dot{d}) and acceleration (\ddot{d}) data. By strictly measuring the peak ΔV immediately before and after the thrust, we estimate that the final velocity *barring kinetic friction* in the testbed is closer to 0.053 m/s, bringing us to within 15% of the objective velocity. Additionally, despite our best efforts to flatten the air bearing table, there were still deviations in the surface profile which were significant enough to alter the movement of the platform. In effect, the platform may have had to expend some energy traveling ‘uphill’, thus losing speed due to gravitational losses.

To illustrate how much ΔV is possible for surface variations as large as 0.1 mm (4000 $\mu\text{in.}$, consistent with the optical table used in this experiment), consider the lossless transfer of potential to kinetic energy (Equation 4.2) for an object elevated by this amount and beginning at rest.

$$\frac{1}{2}m\Delta V^2 = mg\Delta h \quad (4.2)$$

For $\Delta h = 1 \times 10^{-4}$ m and $g = 9.81$ m/s, a final velocity of 0.044 m/s is expected – a significant fraction of our own target velocity of 0.062 m/s.

Nominal performance also assumes zero deviations from the ideal design and layout of the propulsion system. Realistically, even on a perfectly flat air bearing table, some adverse motion may occur due to imperfectly oriented thrusters. Adverse thrust and moments can be calculated using the relationships expressed in Equation 2.14 and by estimating the maximum thruster orientation deviation ($\delta\Theta$) based on the mounting screw allowance for any single propulsion stack. This scenario is expressed in Equation 4.3 for thrusters ‘A’ and ‘D’ mounted with an angular deviation of $\delta\Theta = \pm 2^\circ$ in each thruster (i.e. $\Theta_A = 133^\circ$ and $\Theta_D = -137^\circ$). For brevity, *sin* and *cos* are written as *s* and *c*, respectively.

$$\begin{bmatrix} T_X \\ T_Y \\ M_Z \end{bmatrix} = \begin{bmatrix} c(133^\circ) & c(45^\circ) & c(-45^\circ) & c(-137^\circ) \\ -s(133^\circ) & -s(45^\circ) & -s(-45^\circ) & -s(-137^\circ) \\ 0.18s(268^\circ) & 0.18s(180^\circ) & 0.18s(-90^\circ) & 0.18s(-272^\circ) \end{bmatrix} \begin{bmatrix} T_A \\ T_B \\ T_C \\ T_D \end{bmatrix} \quad (4.3)$$

For an attempted pure translational maneuver using thrusters A and D, a net average discharge thrust of 117 mN as listed in Table 2.9 would produce approximately 3.5 mN of

thrust perpendicular to the desired direction of travel and a negligible moment on the test platform. This would result in a lateral acceleration of 0.7 mm/s^2 for a 5kg mass while effectively applying no adverse moment due to the magnitude of angular deviation for each thruster being equal and thus equal-and-oppositely affecting the moment.

4.3.3 Valve Failure Test Outline

The objective of this test is to observe how the motion of the air bearing test platform is affected by a valve failing open during the execution of a translational and rotational maneuver. Valve failures of this type are expected to be observed as deviations from straight-line paths for a translation maneuver or induced translation during a rotation maneuver.

With twelve valves, many hundreds of valve failure combinations theoretically exist for this experimental configuration, necessitating the development of a strategy to reduce the number of required tests while still representing all the different possible valve fail-open failure modes. By identifying points of symmetry both in motion and in function, the list of all possible valve combinations can be reduced to a significantly smaller number. For example, an A2 failure mode is functionally equivalent to B2, C2, D2 failure modes since all are expected to produce the same thrust, impulse, and combination of motion: adverse rotation during translation, or adverse translation during rotation. From this we conclude that only an A2 failure mode needs be tested: once while executing a translation and once while executing a rotation. Similarly, an A2+D2 failure mode would be expected to produce the same kind of motion as A2+B2, B2+C2, and C2+D2 failure modes, so only the A2+D2 failure mode needs to be tested.

All one- or two-fault failure modes which affect only a single thruster line are tested in both translation and rotation due to the fact that the same thruster line may be used to perform both maneuvers. Two-fault failure modes are only tested in the relevant direction which they nominally affect. For example, an A2+D2 failure mode during a rotation maneuver using valves A2 and C2 would affect the rotation in a manner identical to a single A2 failure mode in rotation, so the A2+D2 failure mode is only tested in translation.

Lastly, any one-fault failure mode of valve 1 is not tested since, by design, valve 2 segments off the propulsive end of the thruster such that a failure of only valve 1 will not affect performance. Any two-fault failure mode which involves any valve 1 can therefore effectively

be treated as a one-fault failure mode of whichever other valve has failed along with V1. The only exception to this is a two-fault failure mode occurring in a single thruster line. The battery of tests which will cover all valve combinations is tabulated in Table 4.1 along with a brief summary of the expected effects on the overall motion of the air bearing platform.

Failure Mode	Maneuver	Expected Effect on Motion
A2	Translation	Moderate adverse rotation
A2	Rotation	Moderate adverse translation
A3	Translation	Small adverse rotation
A3	Rotation	Small adverse translation
A1+A2	Translation	Large adverse rotation
A1+A2	Rotation	Large adverse translation
A1+A3	Translation	Large adverse rotation
A1+A3	Rotation	Large adverse translation
A2+A3	Translation	Large adverse rotation
A2+A3	Rotation	Large adverse translation
A2+D2	Translation	Increased linear acceleration
A2+D3	Translation	Moderate adverse rotation
A3+D3	Translation	Reduced net linear acceleration
A2+C2	Rotation	Increased angular acceleration
A2+C3	Rotation	Moderate adverse translation
A3+C3	Rotation	Reduced net angular acceleration

Table 4.1: Summary of conducted tests and expected resultant motion of the air bearing platform.

4.3.4 One-Fault Failure Modes

A one-fault failure mode can only occur in one thruster line at any given time, thus only three distinct failure modes are possible. Of those three, only two are potentially capable of affecting thruster performance. Each of the two modes can occur for pure translation and pure rotation, thus requiring four tests total.

4.3.4.1 A2 Failure Mode - Translation

An A2 failure mode effectively doubled the total plenum volume for a single thruster line by removing the barrier between the first and second stage plenums. This failure mode was expected to result in increased net impulse over the duration of a single plenum discharge, resulting in higher time-averaged thrust and net impulse compared to a typical single plenum discharge. A commanded translation using this thruster therefore resulted in some adverse rotation in addition to the nominal translation, which can be seen in Figure 4.11.

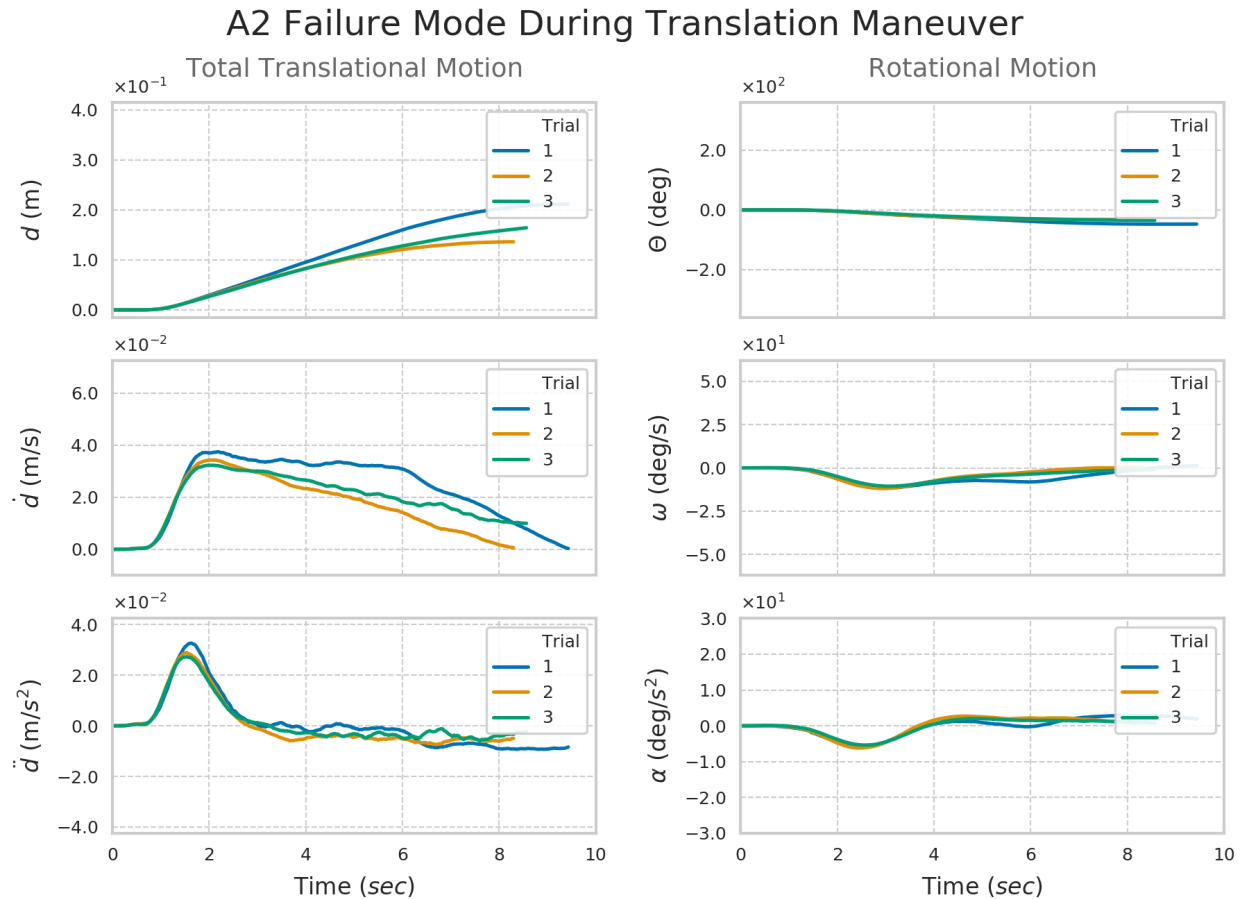


Figure 4.11: Recorded displacement and resultant estimated states for an A2 failure mode during translation maneuvers.

4.3.4.2 A2 Failure Mode - Rotation

As before, an A2 failure mode effectively doubled the total plenum volume for a single thruster line. A commanded rotation using this thruster therefore resulted in the addition of some adverse translation in addition to the nominal rotation, visible in Figure 4.12.

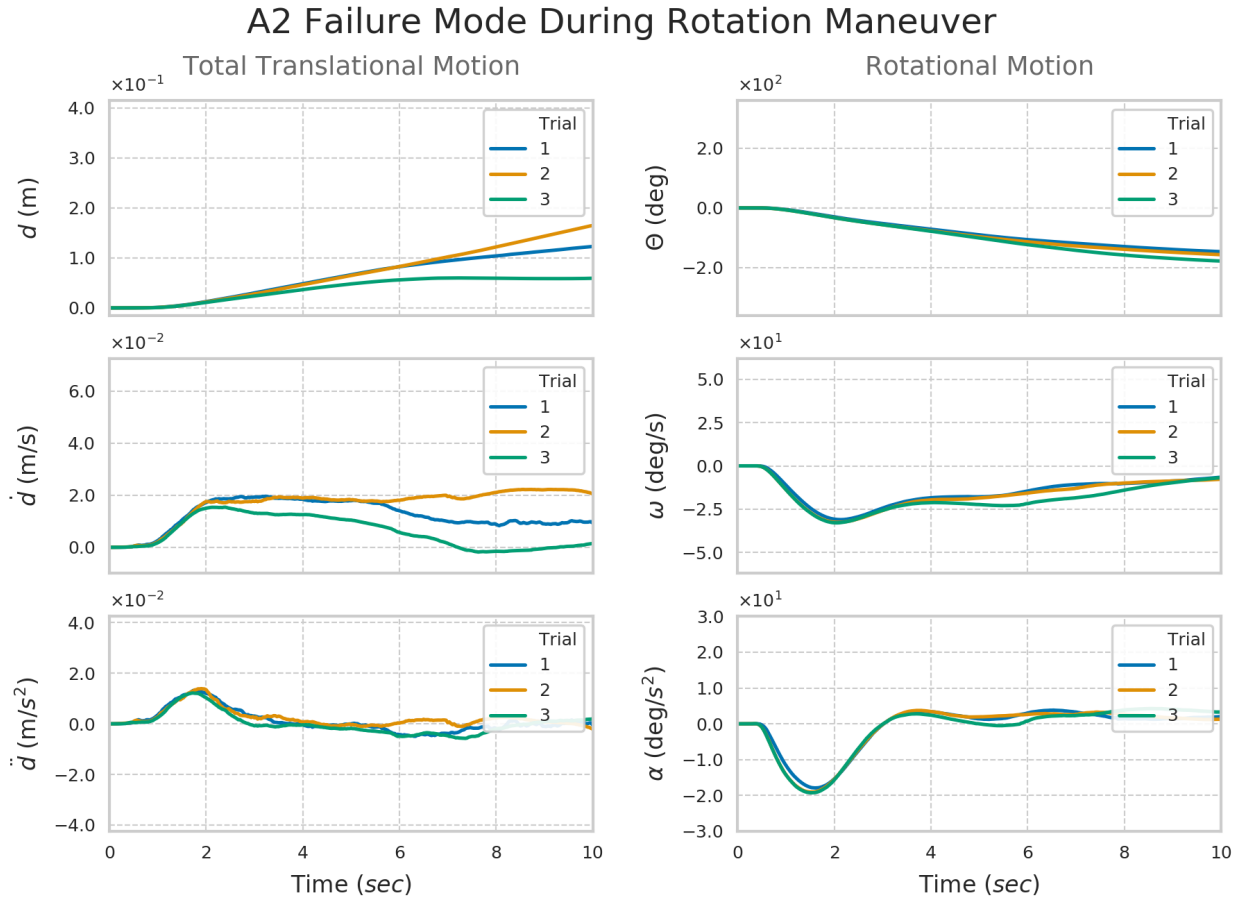


Figure 4.12: Recorded displacement and resultant estimated states for an A2 failure mode during rotation maneuvers.

4.3.4.3 A3 Failure Mode - Translation

An A3 failure mode would prevent the stage 2 plenum in the thruster from being primed, requiring the use of valve 2 to control the thruster. Due to the additional plenum volume and line length that the propellant gas must feed through before exiting, this failure mode was expected to result in a slight startup delay and reduction of effective thrust. Thus, a commanded translation using this thruster resulted in the addition of a slight rotation that was quickly nulled out. This phenomenon was very inconsequential overall and cannot be easily seen in the data shown in Figure 4.13.

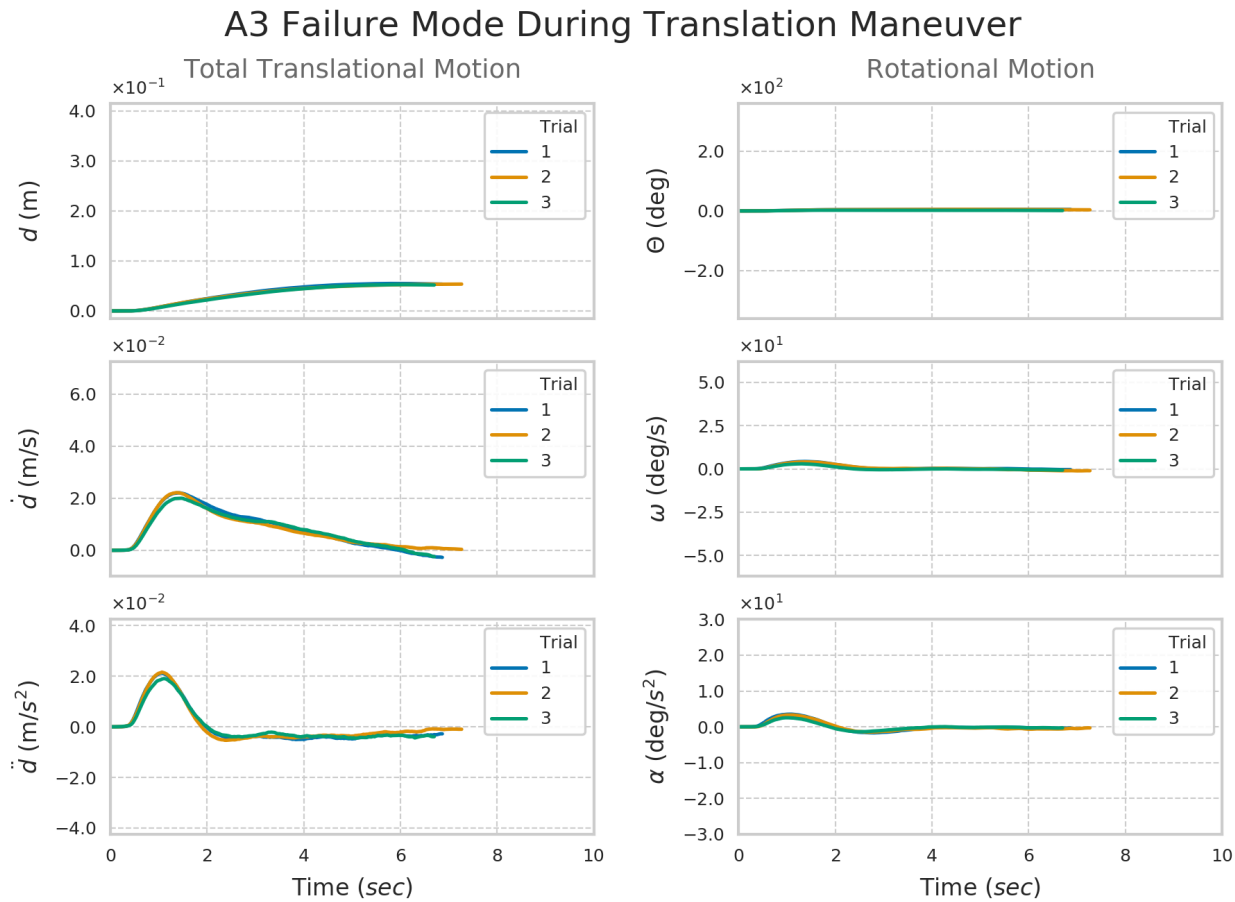


Figure 4.13: Recorded displacement and resultant estimated states for an A3 failure mode during translation maneuvers.

4.3.4.4 A3 Failure Mode - Rotation

Similar to the translation test, a commanded rotation using this thruster resulted in the addition of a slight translation caused by the delayed startup and reduced effectiveness. While this delayed startup is visible for an A3 failure mode in translation, it is not visible in the rotation data shown in Figure 4.14.

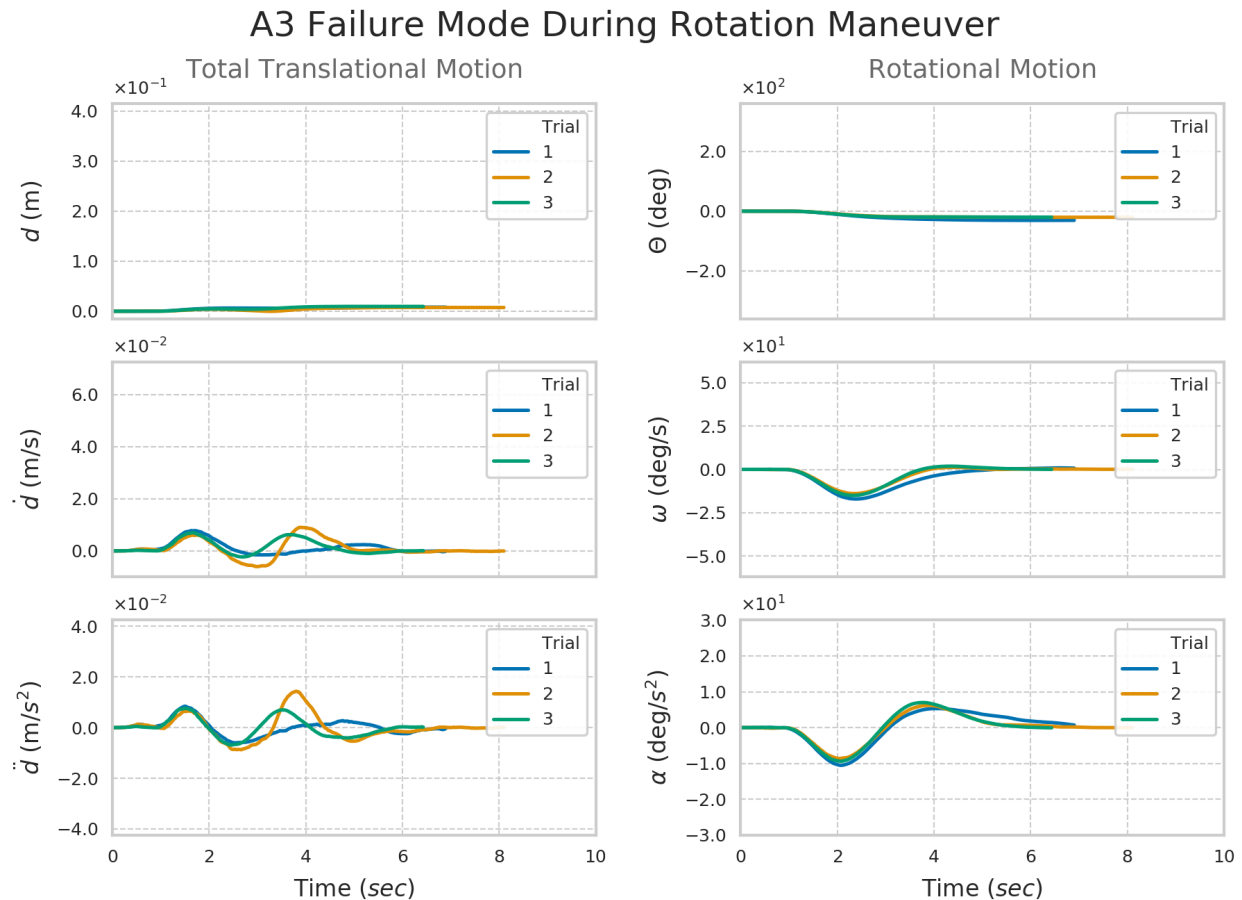


Figure 4.14: Recorded displacement and resultant estimated states for an A3 failure mode during rotation maneuvers.

4.3.5 Two-Fault Failure Modes, Single Thruster Line

For a single thruster consisting of three valves, there exist only three possible combinations of two-fault valve failure combinations. Each failure combination can occur during either translation or rotation, meaning a total of six different tests must be performed.

4.3.5.1 A1+A2 Failure Mode - Translation

An A1+A2 failure mode will expose the nozzle inlet directly to the propellant supply and result in constant maximum thrust when valve 3 is commanded open. A commanded translation using this thruster will result in the addition of large adverse rotation caused by the constant maximum thrust. Figure 4.15 shows the large adverse motion both in translation and rotation caused by this failure.

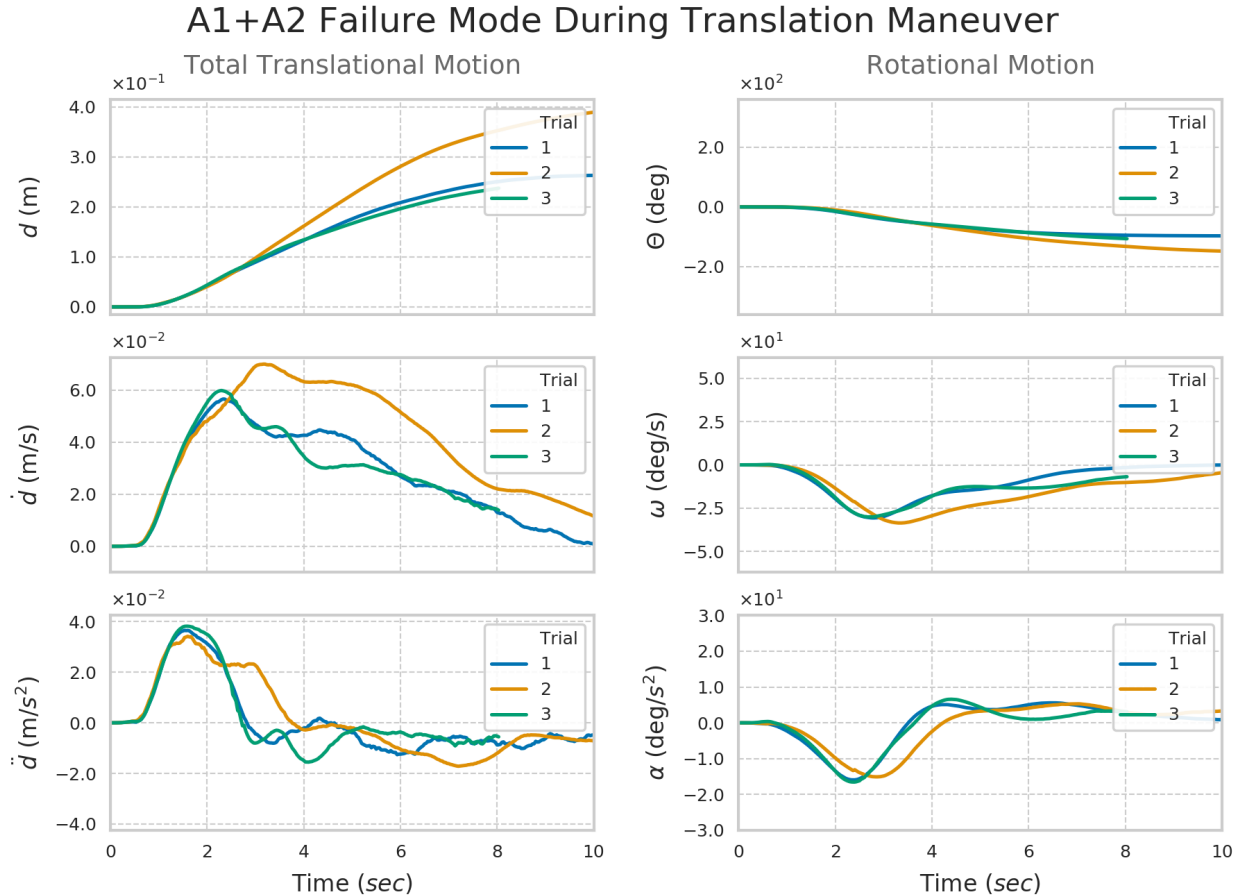


Figure 4.15: Recorded displacement and resultant estimated states for an A1+A2 failure mode during translation maneuvers.

4.3.5.2 A1+A2 Failure Mode - Rotation

A commanded rotation using thrusters A+C resulted in the addition of a large adverse translation caused by the constant maximum thrust. Despite commanding a different maneuver, the results in Figure 4.16 are very similar to those of an A1+A2 failure during translation.

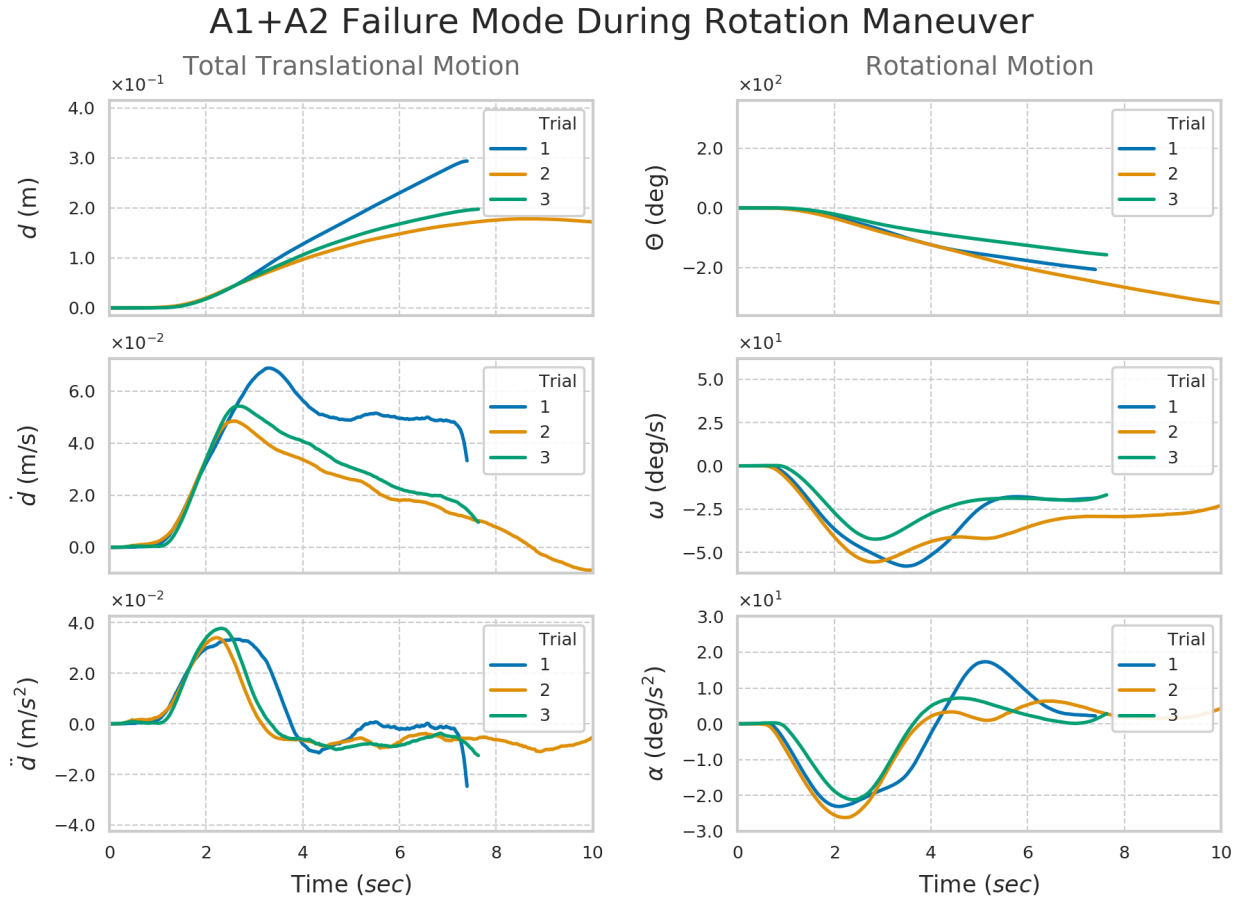


Figure 4.16: Recorded displacement and resultant estimated states for an A1+A2 failure mode during rotation maneuvers.

4.3.5.3 A1+A3 Failure Mode - Translation

An A1+A3 failure mode will prevent the stage 2 plenum from priming and will expose valve 2 directly to the propellant supply, resulting in constant thrust when valve 2 is commanded open. This will result in slightly delayed startup as the propellant must travel through the stage 2 plenum before reaching the nozzle but the overall motion will quickly be dominated by the constant thrust from this thruster. A commanded translation using this thruster would result in the addition of a large rotation. Only two trials were conducted before propellant was depleted during testing, but the recorded motion still demonstrated similar behavior as the A1+A2 translation failure. A very slight startup delay is visible in the angular acceleration (α) curve in Figure 4.17 as the platform first undergoes counter-clockwise rotation before quickly changing directions.

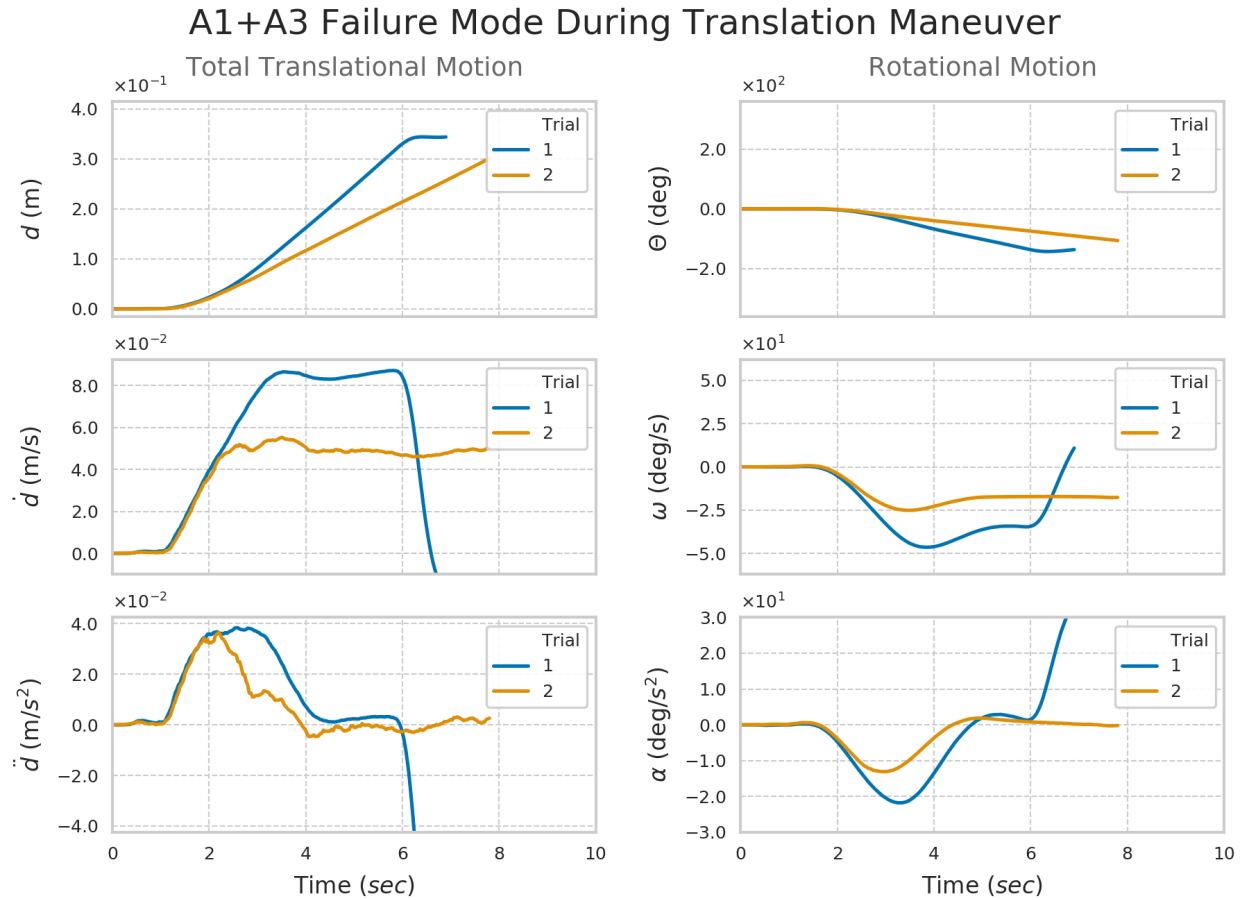


Figure 4.17: Recorded displacement and resultant estimated states for an A1+A3 failure mode during translation maneuvers. Fuel was depleted prior to conducting a third trial and a bearing crash occurred in Trial 1, indicated by the sudden deceleration at $t = 6$ sec.

4.3.5.4 A1+A3 Failure Mode - Rotation

A commanded rotation using thrusters A+C resulted in the addition of a large translation just as before. Figure 4.18 shows the behavior of this failure mode and is similar to others of its class, though no startup delay is observable in the translational motion data.

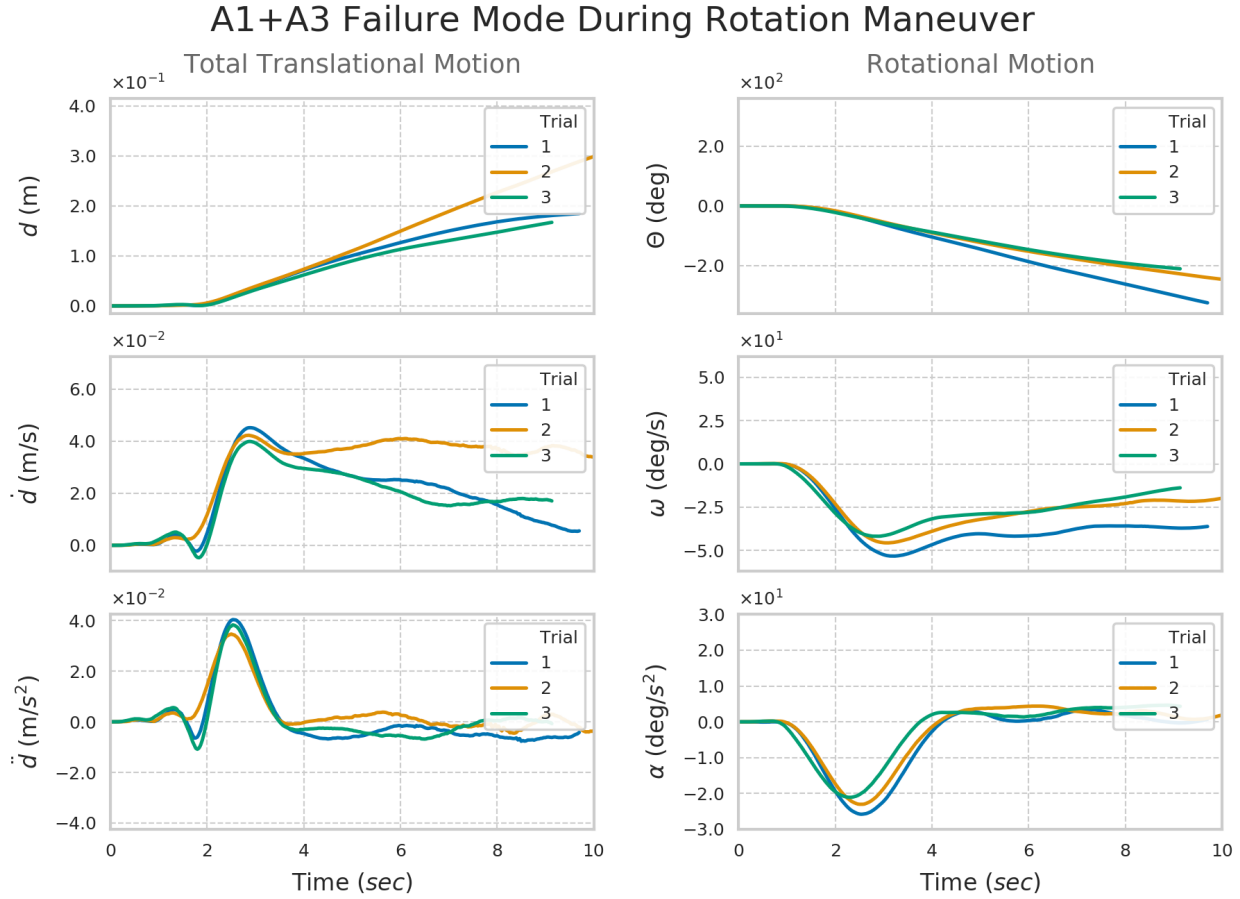


Figure 4.18: Recorded displacement and resultant estimated states for an A1+A3 failure mode during rotation maneuvers.

4.3.5.5 A2+A3 Failure Mode - Translation

An A2+A3 failure mode will prevent both the stage 1 and stage 2 plenums from being primed and, similar to the A1+A2 and A1+A3 failure modes, result in constant thrust when valve 1 is commanded open. As with the A1+A3 failure mode, this mode resulted in delayed startup as the propellant must travel through P1+P2 before reaching the nozzle. A commanded translation using this thruster resulted in the addition of a slight rotation caused by the delayed startup, similar to V1+V3 but greater in magnitude. This delay is subtle but noticeable in the angular rotation and acceleration shown Figure 4.19 at approximately $t = 2$ sec, when the platform's rotational direction reverses.

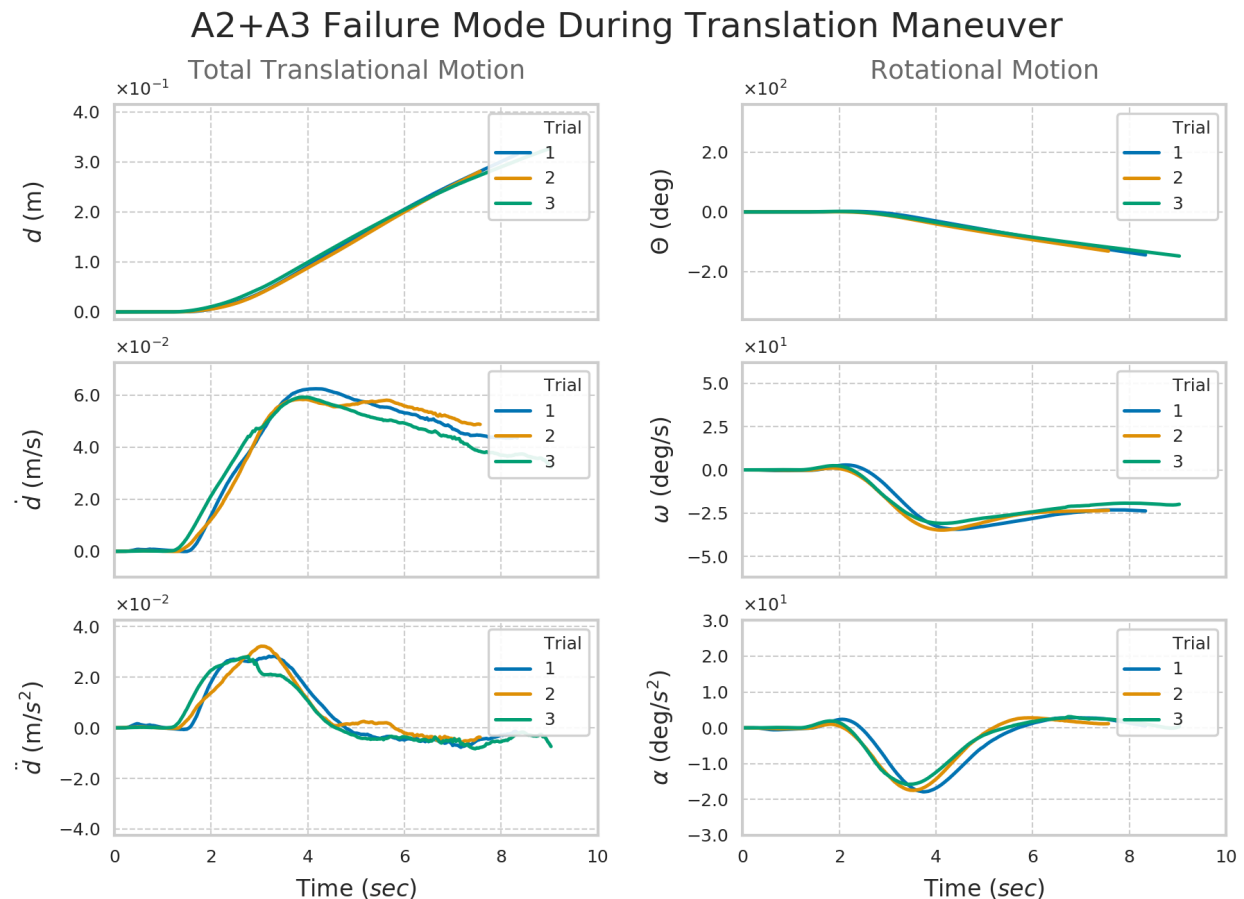


Figure 4.19: Recorded displacement and resultant estimated states for an A2+A3 failure mode during translation maneuvers.

4.3.5.6 A2+A3 Failure Mode - Rotation

A commanded rotation using this thruster resulted in the addition of a large translation similar to A1+A3. The delayed startup is not noticeable since, unlike the translational mode of motion, both thrusters apply a torque in the same direction.

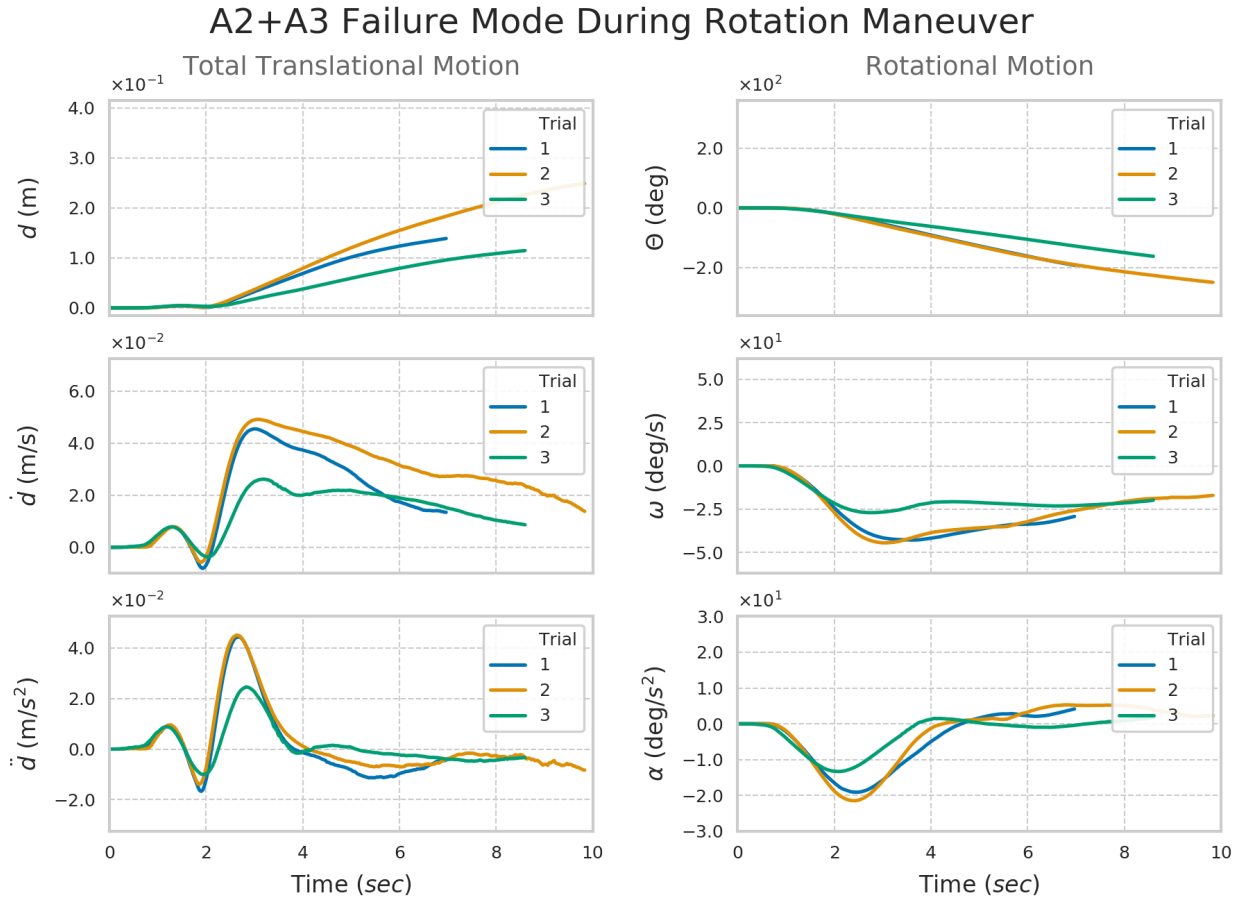


Figure 4.20: Recorded displacement and resultant estimated states for an A2+A3 failure mode during rotation maneuvers.

4.3.6 Two-Fault Failure Modes, Adjacent Thruster Lines

Three combinations of failure modes exist for two thrusters in a two-fault failure mode, as this thruster pairing warrants excluding any analysis that involves a failure of the first valve. Furthermore, only translational motion caused by the tandem use of the thrusters A and D are tested since the use of either of these thrusters with any other will produce results identical to those seen in one-fault modes.

4.3.6.1 A2+D2 Failure Mode - Translation

An A2+D2 failure mode will not result in any adverse rotation since the failure was symmetric. However, the time-average thrust and net impulse applied for the duration of a nominal single plenum discharge increased since the effective plenum volume doubled for both thrusters. At the end of the discharge time, the net average thrust applied to the platform was predicted to be 196 mN with a net impulse of 255 mN-s, resulting in an expected ΔV of 0.051 m/s. The results shown in Figure 4.21 indicate that the valves were held open longer than what would be typical for a single plenum discharge, as gauged by the width of the acceleration curve and total velocity at the end.

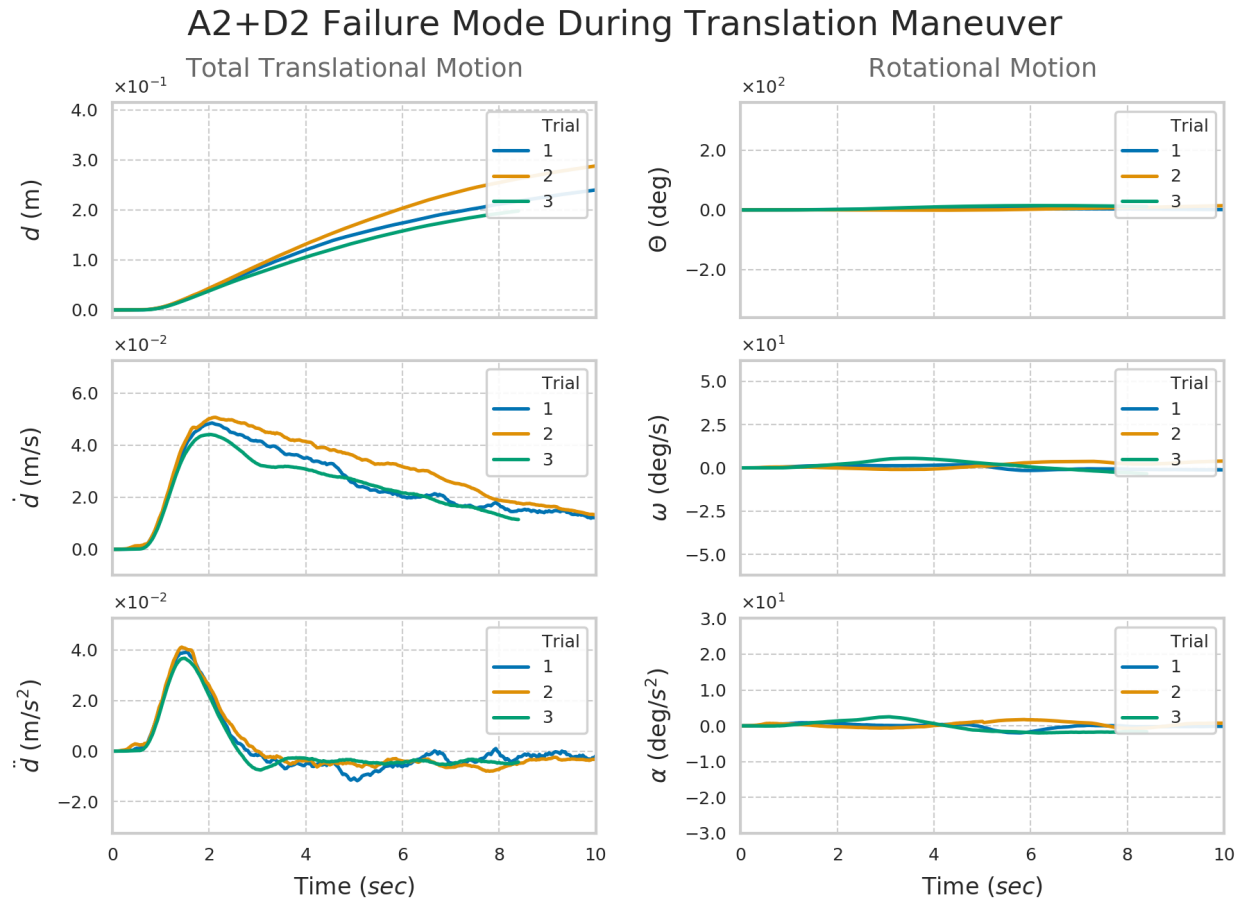


Figure 4.21: Recorded displacement and resultant estimated states for an A2+D2 failure mode during translation maneuvers.

4.3.6.2 A2+D3 Failure Mode - Translation

As previously explored, an A2 failure mode increased the average thrust and net impulse in thruster A while a D3 failure mode will slightly delay startup and reduce the overall thrust in thruster D. A commanded translation combined the effects of both failure modes to produce greater adverse rotation than either would produce on their own, though the resultant rotational velocity and acceleration is more similar to that of an A2 failure mode than an A3 failure mode. Figure 4.22 shows the resultant motion of this failure mode.

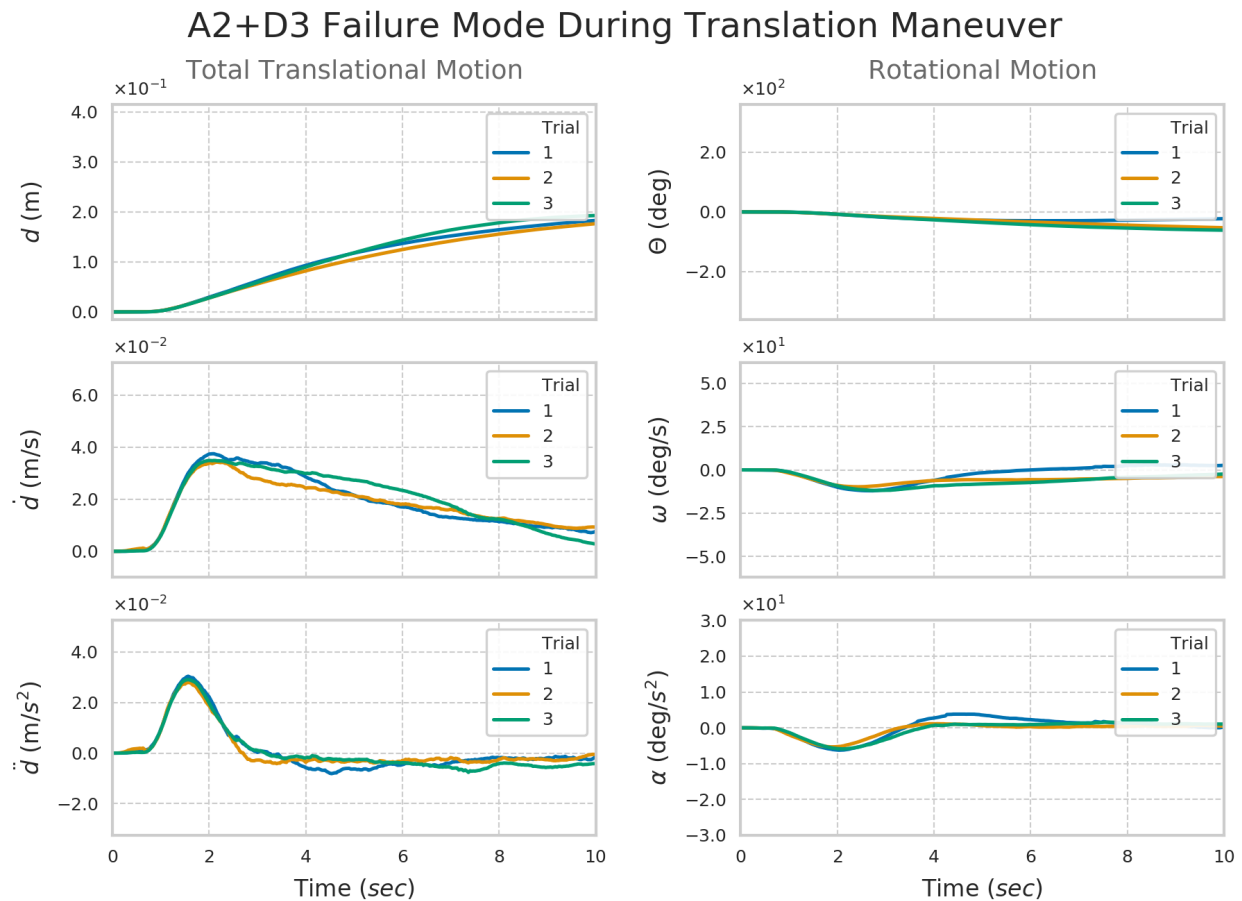


Figure 4.22: Recorded displacement and resultant estimated states for an A2+D3 failure mode during translation maneuvers.

4.3.6.3 A3+D3 Failure Mode - Translation

An A3+D3 failure mode did not result in any adverse rotation since the failure was symmetric. Both thrusters experienced identical startup delay and reduced performance as can be seen in Figure 4.23. By comparison, the initial ΔV from a single plenum discharge observed in Figure 4.9 is 0.025 to 0.030 m/s, whereas the results from this test indicate a reduction in ΔV by nearly 0.010 m/s.

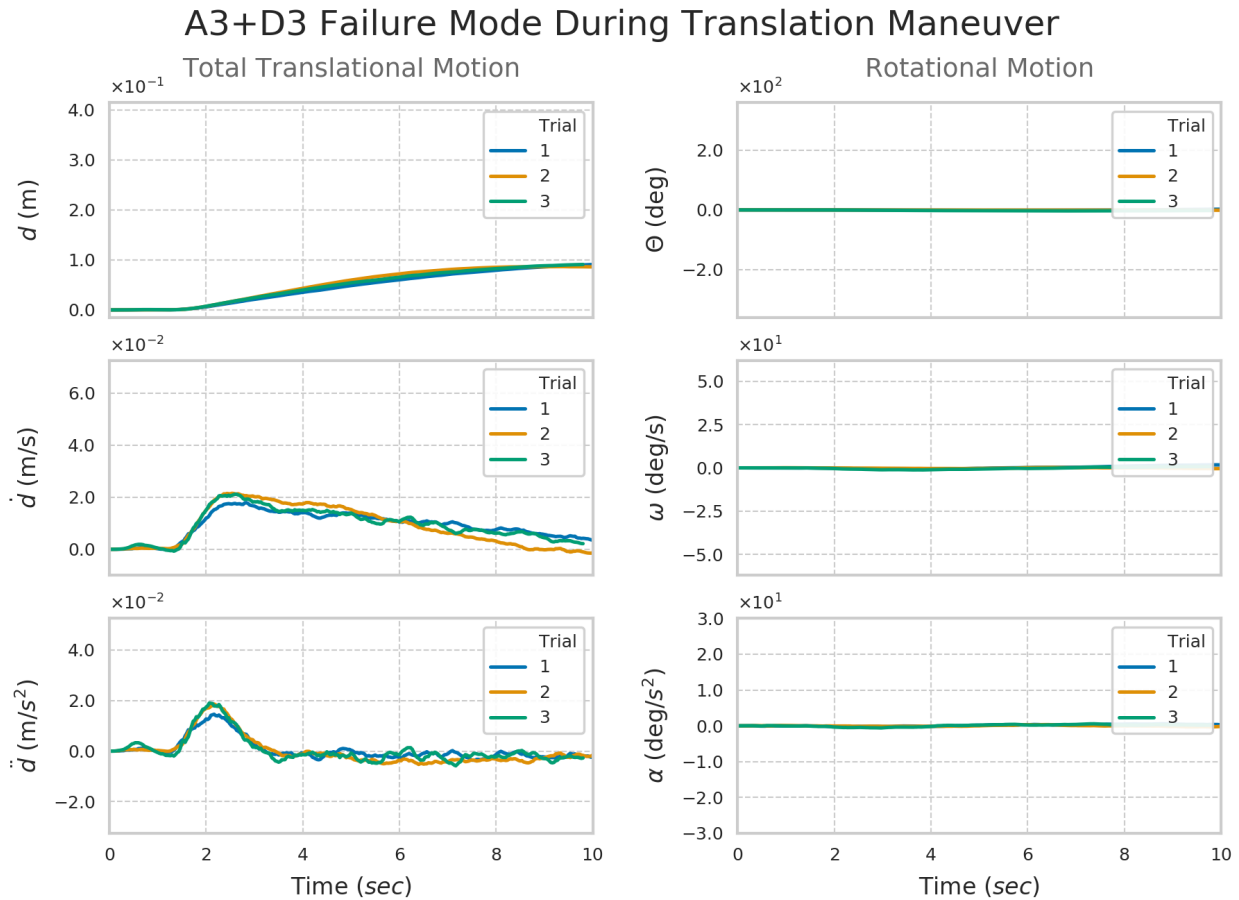


Figure 4.23: Recorded displacement and resultant estimated states for an A3+D3 failure mode during translation maneuvers.

4.3.7 Two-Fault Failure Modes, Opposite Thruster Lines

As before, three combinations of failure modes exist for two thrusters in a two-fault failure mode. Similarly, thruster pairings warrant excluding any analysis that involves a failure of the first valve since this would reduce to a single-fault failure mode. Only rotational motion caused by the tandem use of the thrusters A and C are tested.

4.3.7.1 A2+C2 Failure Mode - Rotation

Two opposite thrusters experiencing a failure of valve 2 did not result in any adverse translation since the failure was symmetric. Like the A2+D2 failure mode, the average thrust and net impulse applied for the duration of a nominal single plenum discharge increased since the effective plenum volume doubled for both thrusters. This resulted in an effectively larger rotational acceleration as seen in Figure 4.24.

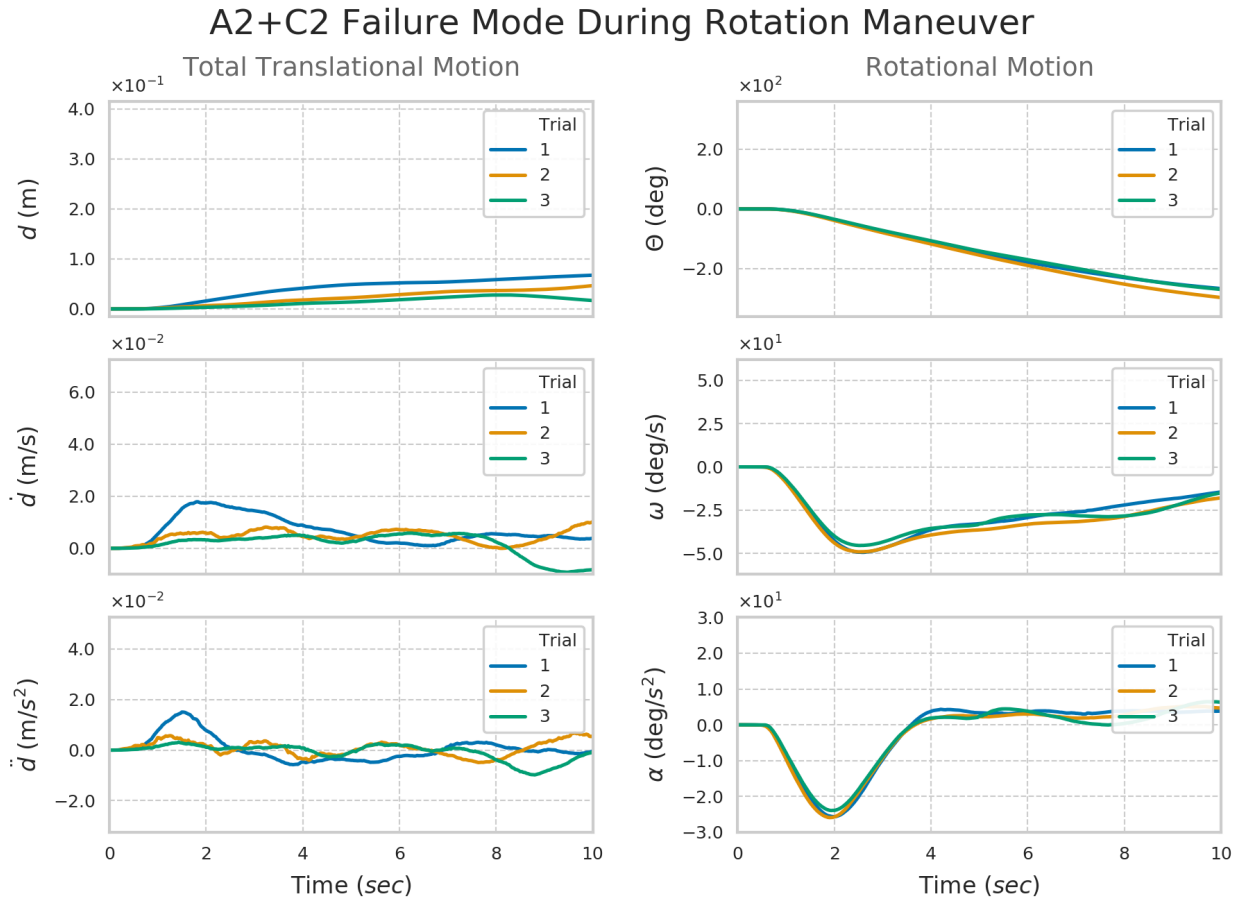


Figure 4.24: Recorded displacement and resultant estimated states for an A2+C2 failure mode during rotation maneuvers.

4.3.7.2 A2+C3 Failure Mode - Rotation

As explored earlier, an A2 failure mode increased the average thrust and net impulse in thruster A while a C3 failure mode reduced the performance of thruster C. A commanded rotation combined the effects of both failure modes to produce greater adverse translation than either would produce on their own, though the results are most similar to an A2 failure mode in rotation. Comparison of Figure 4.24 to Figure 4.12 shows almost no difference in the magnitude of adverse translational velocity or acceleration.

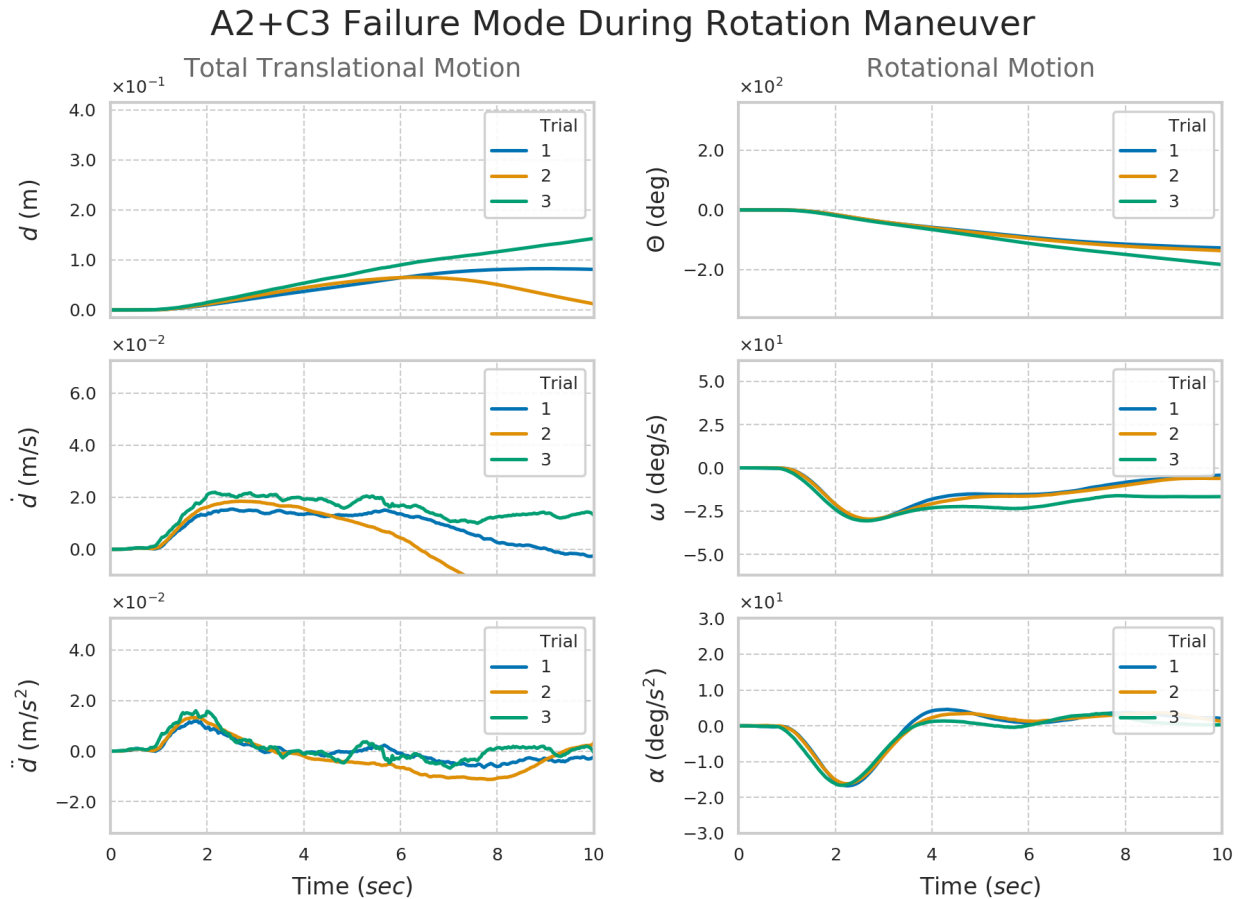


Figure 4.25: Recorded displacement and resultant estimated states for an A2+C3 failure mode during rotation maneuvers.

4.3.7.3 A3+C3 Failure Mode - Rotation

A valve 3 fail-open in two opposite thrusters did not result in any adverse translation since the failure was symmetric. Both thrusters experienced identical startup delay and reduced performance resulting in no asynchronous thruster timing, thus having no sizable adverse translational motion in Figure 4.26.

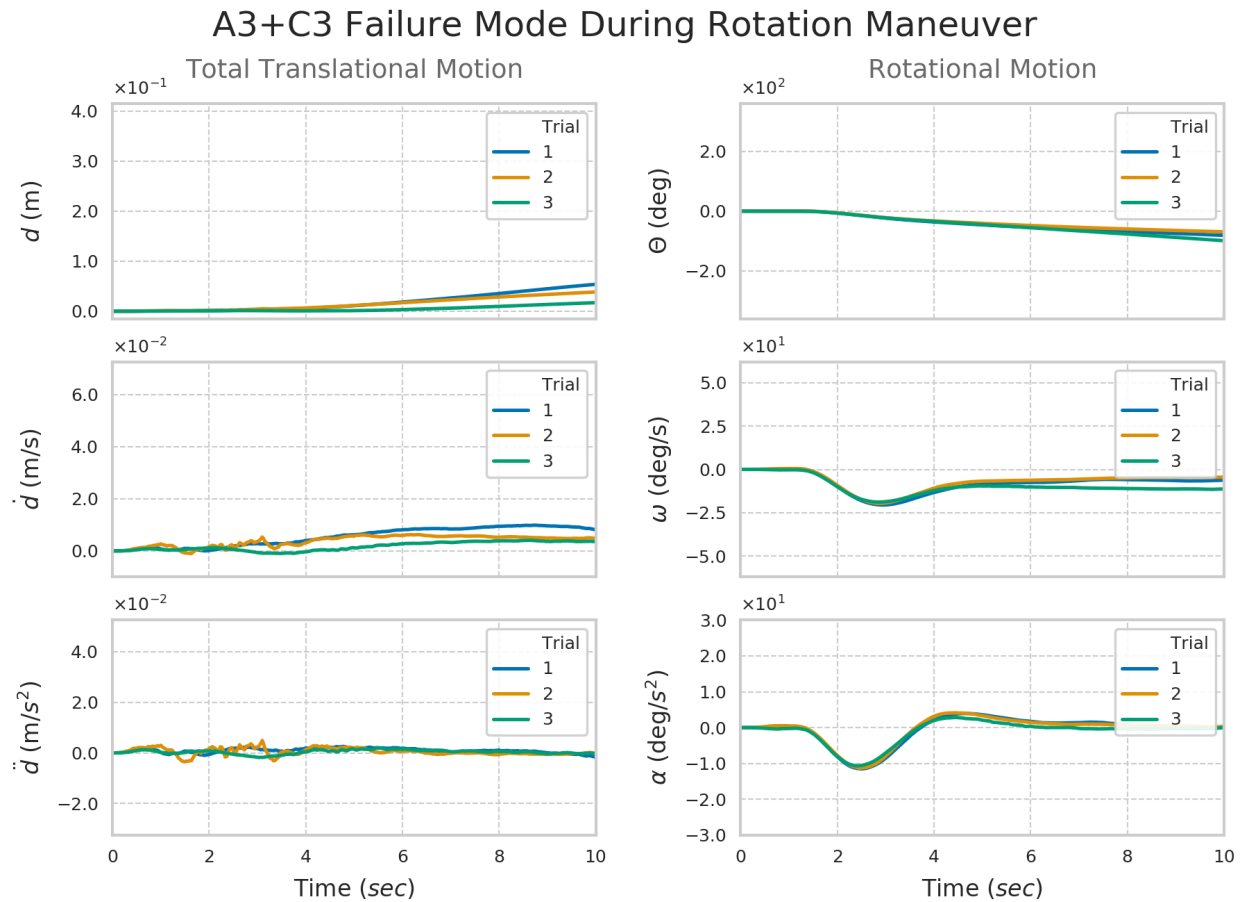


Figure 4.26: Recorded displacement and resultant estimated states for an A3+C3 failure mode during rotation maneuvers.

4.4 Summary of Results

4.4.1 Air Bearing Test Platform

Based on the operational performance curves provided by the manufacturer, the 25 mm air bearings supplied with CO₂ at 207 kPa (30 psig) were expected to operate for approximately 1.5 hours with a 5 kg load. In reality, inconsistencies in the glass-topped air bearing table required the operational pressure to be increased to 345 kPa (50 psig) and maximum run time was cut down to approximately 45 minutes. Significant time was spent attempting to flatten the glass-topped table by adding 0.1 mm Kapton shims under observed low points of the table, identified by observing drift direction of the air bearing platform. Theoretically, a height deviation of 0.1 mm (consistent with the optics table used to support the glass surface) can impart up to 0.044 m/s of ΔV , although this coarse approximation does not account for friction and variable slope. Cleanliness of the surface was found to be important in preventing the air bearings from catching on microscopic contaminants and imparting a large torque on the platform, inducing rotation where none would otherwise occur. Repeated cleaning of the surface with lint-free alcohol wipes greatly reduced the rate of this occurrence and increased the overall performance of the air bearings.

The bearings themselves were found to be highly susceptible to performance degradation caused by oils and chemical contaminants. Porous carbon air bearing performance is not largely affected by physical damage (scrapes, scratches, etc.), but any oils from skin or lubricants in the supply lines can quickly clog the porous graphite matrix and reduce the effectiveness of the air bearing. A disposable Grade 50 in-line filter (which removes 99.99% of 0.01 micron contaminants) was added to the pneumatic system at the pressure regulator outlet, after which no more performance degradation appeared to occur.

Since the pressure regulator used in the air bearing platform was of the same manufacturer as the regulator used for the propulsion system, the same flow rate limitations applied. Operating the platform at 345 kPa quickly caused the regulator to develop condensate on the surface due to evaporation and Joule-Thomson expansion of the CO₂. Test sessions were limited to 10 minutes of continuous operation to prevent the formation of ice on the surface of the regulator, and the regulator was wiped dry to prevent water droplets from depositing contaminants on the air bearing surface.

4.4.2 Thruster Design and Characterization

3D printing the plenums proved to be an effective method for designing a custom propellant supply volume once the variety of small challenges were overcome. Polylactic Acid (PLA) is not as strong compared to other material options, but it is well-characterized by both the engineering and hobbyist communities and has highly predictable behavior. Coupled with an inexpensive epoxy to seal the plenum and wet sanding the o-ring surface, the 3D-printed plenum demonstrated reliable and repeatable manufacturability. Most of the challenges with this approach were in keeping the 3D printer operating consistently, rather than with the design of the plenums themselves.

4.4.3 Wireless Communications Interface

The Raspberry Pi-based data and command relay successfully passed commands and data to-and-from an HTTP-based web server used to host a browser-based user interface. This setup utilized entirely open-sourced web server and message broker software implemented on an inexpensive Raspberry Pi 3+ with Raspberry Pi OS hardware platform. The user interface effectively relayed the appropriate information and provided the means to perform all the necessary tests. The user interface was not optimized to operate on mobile devices with screen resolution less than 1080×1920 pixels and resulted in some controllability challenges for older mobile devices.

4.4.4 Nozzle Design

At the operational supply pressure of 791 kPa (100 psig) or less, the nozzles effectively provided the thrust and net impulse necessary to operate the propulsion system on the air bearing test platform. The mass flow rate was measured to be slightly higher than expected which indicated the throat diameter was slightly larger than 0.6 mm. No tolerance was specified on the tooling used to manufacture the nozzles, and no method was available to directly measure the throat diameter or area. However, more important to note is the inconsistent supply pressure from the pressure regulator during steady-state testing. The supply pressure dropped with each valve discharge, indicating that the regulator chosen for this application was not designed for such high flow rate applications. Fortunately the pressure could be easily recorded and the resulting thrust and mass flow rate results adjusted

accordingly. Nozzle manufacturability was not challenging once the appropriate methods were established. Rigid workpiece jigs and precision measuring equipment used to center the tool and measure the feature drill depths were readily available to students by the university's machine shop, making the nozzle manufacturing process repeatable and efficient. Performance did not measurably differ between nozzles manufactured in this manner.

4.4.5 Full-scale Propulsion System Testing

Two single-fault failure modes in a single thruster were tested during translational and rotational maneuvers. An A2 failure mode resulted in increased time-averaged thrust and net impulse since this failure mode effectively doubled the available propellant volume for a single thruster. An A3 failure mode resulted in a slight delay in thruster startup time since the propellant stored in P1 needed to travel through P2 before exiting the nozzle, though this effect was hardly noticeable. Between the two failure modes, an A2 failure produced greater adverse velocity and acceleration during both translational and rotational maneuvers.

Three different effects occurred for the three two-fault failure modes which could occur in a single thruster for translational and rotational maneuvers. Regardless of the valve failure combination, any attempt to control with this thruster resulted in asymmetric thrust which quickly spiraled the platform out of control. Of the three modes, only an A2+A3 failure mode in translation caused any noticeable reversion of motion whereby the platform would begin rotating one direction before accelerating in the opposite direction due to the delayed onset of thrust from thruster A.

Three combinations of two valves failing open were tested for two-fault failure modes in adjacent thrusters (those used for translational motion). No adverse rotation was expected or observed for an A2+A3 failure mode, and both thrusters experienced an expected increase in average thrust and net impulse. An A2+D3 failure mode resulted in adverse clockwise rotation caused by the combined valve 2 failure mode in thruster A producing greater average thrust and valve 3 failure mode in thruster B delaying startup. As with the A2+D2 failure, no adverse rotation was expected or observed for an A3+D3 failure, but both thrusters experienced delayed startup and reduced performance.

Three failure modes were tested for two-fault failure modes in adjacent thrusters (those used for rotational motion). An A2+C2 failure mode resulted in no adverse translation since

the failure mode was symmetric, but both thrusters experienced increased average thrust and net impulse resulting in a large rotational velocity. An A2+C3 failure mode resulted in adverse translation caused by the combined valve 2 failure mode in thruster A producing greater average thrust and valve 3 failure mode in thruster C delaying startup. Like the A2+C2 failure mode, the A3+C3 failure mode resulted in no adverse translation, but both thrusters experienced delayed startup and reduced performance.

4.4.6 Computer Vision and Kalman Filter

The ArUco-based computer vision system operated extremely well and proved to be an effective approach for motion tracking using entirely open-sourced software. However, notable differences in quality were observed when performing live object tracking compared to post-processing due to a combination of lower-quality cameras and computational performance limits of the Raspberry Pi. Ultimately it was decided that post-processing would be a more effective approach, and each test was therefore recorded with a higher-quality camera at 720p vertical resolution. Additionally, the OpenCV-based ArUco method for tracking includes a number of refining and recognition algorithms which are disabled by default to increase object tracking speed. As the tests were being analyzed in post, it was found that tracking quality was greatly improved after enabling the Corner Refine Subpixel method in the OpenCV ArUco marker recognition algorithm. The only persistent issue was related to lighting in the testing area, specifically reflection of overhead lighting off the glass-topped surface, which can be observed in Figure 4.9. The ArUco algorithm seemed to be incapable of recognizing the marker when it passed across the threshold of the light's reflection, though it picked the marker up again once the marker was completely inside the light reflection zone. This would seem to indicate that it might be possible to adjust the settings of the ArUco algorithm to compensate for this adverse lighting condition, though the interim solution was to simply turn the light off.

The Kalman filter which implemented a constant-acceleration model was sufficient for extracting velocity and acceleration data from the position data provided by the computer vision system. As expected, some time was needed to refine the covariance matrices of the model and measurements and strike a balance between smooth data and meaningful results.

Chapter 5

Conclusion and Recommendations

This chapter will summarize the lessons learned during the development of the propulsion system and corresponding testbed with the intent of guiding future developers. A brief discussion of the challenges associated with each system will be followed by recommendations for how to develop a better system. The recommendations are focused on the hardware aspects of the system since the software proved to be the least troublesome aspect of this project. Finally, this report will be closed out with concluding remarks for each of the major systems ultimately leading to discussion of possible future options for continued development of a cold gas propulsion system for the actual inspection CubeSat.

5.1 Lessons Learned and Future Recommendations

5.1.1 CubeSat Propulsion System

Much of the target performance of the propulsion system will be based on the valves chosen for the system. The choice of valve – in terms of both performance and geometry – will greatly affect the physical configuration of the propulsion system. Furthermore, consideration will need to be made for how the valves will interface with the propulsion system and what sort of mating brackets and face seal requirements will need to be made. For example, The Aerospace Company’s MEPSI propulsion system utilized Lee Co. microvalves which were bracketed directly to the SLA-printed propulsion manifold [32], and pressure sealing was achieved using a simple gasket-based face seal.

It is advised that future work on the propulsion system be focused primarily on the design

and configuration of a manifold to support two-fault tolerance with the expectation that only 2 or 3 SLA-based prints will be made. This will require the integration of a minimum of 12 microvalves (of the designer’s choice), at least 1 pressure transducer, at least 1 temperature transducer, and possibly a heating element. A carefully-designed manifold could potentially utilize waste heat from the control electronics to increase the gas temperature and improve specific impulse. Physical prototyping to gauge size and fit could still be performed with an FDM-based 3D printer, but this model would not be suitable for testing propulsion system performance.

5.1.2 3D Printing

A fused deposition modeling (FDM) 3D printer can be an effective asset in quickly prototyping and manufacturing customized parts for an air bearing system, and indeed it was extremely beneficial in reducing the weight of the air bearing platform. However, a 3D printer must be constantly cleaned and maintained in order to maintain reasonable turnaround times and consistency in part quality. More importantly, anyone using the machine must be trained not only on how to use it but also how to maintain it, thus requiring extensive documentation on the specific printer used. A regular cleaning schedule should be maintained and calibration prints should be performed at regular intervals to check for bed levelness and nozzle cleanliness. Filament cleanliness must also be maintained since dust, dirt, and any other small particulate can settle on the filament and cause extrusion issues when it gets drawn into the printer’s extruder. To mitigate the possibility of similar future issues, a living document has been initialized for use by UC Davis HRVIP lab personnel to reference both during training and troubleshooting (see Appendix G). Lab personnel and users of the lab 3D printer are encouraged to study this document and, more importantly, add their own knowledge and experience to it when they encounter issues with the printer.

5.1.3 Air Bearing Table

In developing an air bearing testbed, the majority of time and financial resources should be spent on the surface itself as it was found that commercially-available float glass was only as effective as the surface which it was placed on. Surface deviations by as little as 0.1 mm are enough to cause significant adverse motion which cannot be overcome by nominal operation

of the cold gas propulsion system tested here. Either significant time will need to be spent on shimming the glass from the surface which it is placed on, or significant financial resources must be spent in acquiring a granite inspection surface. Fortunately, even the lowest-quality granite inspection surface (Grade B) is nearly an order of magnitude flatter than an optics table and can cost under \$1,000 USD for a modestly-sized 36” x 48” surface. If glass is to be the surface of choice, the development of a method for quantitatively measuring the surface deviations and modeling them accordingly is recommended, perhaps by using the very same air bearing platform and computer vision system discussed herein.

5.1.4 Air Bearing Platform

Second only to the table itself, the largest factor seeming to affect the performance of the air bearing platform was the rigidity of the structure which supported all the accessory items. Air bearings themselves are quite durable to physical impact and scratches, but any contact with oil – whether it be from a person’s skin or lubrication from pneumatic components upstream – can quickly deteriorate the performance. Individual bearing performance is determined by observing the consistency of motion of that bearing over time and across the surface of the testbed. Ideally, they should move with little friction and very little acceleration should be noted in free motion. When acting with a group of bearings, differences in performance between each bearing are observed as adverse rotations in the platform caused by increased drag on one bearing versus the others. A single, large air bearing could ameliorate issues with adverse rotations, but the up-front cost is nearly proportional to the diameter of the bearing and would require a larger air supply source to accommodate the larger under-bearing surface. It is advised that operators of air bearings wear gloves when handling the bearings and clean the porous graphite surface with isopropyl alcohol wipes before and after each use. A more effective strategy would be to house the air bearing table in a clean room or clean tent that is regularly purged with filtered air.

The initial design of the air bearing platform for this project sought to keep the center of gravity as low as possible to prevent tipping. The CO₂ supply bottles were therefore placed in a completely horizontal orientation and thus required specially-installed anti-siphon tubes to prevent liquid CO₂ from entering the air bearing supply lines. Tipping was later found to be a non-issue since the total height of the platform with propulsion system was less than

expected, and the velocities which were tested at were significantly smaller than what would be necessary to tip the assembly over. A “full” CO₂ bottle is only approximately 30% liquid, so the bottle only needs to be angled appropriately to prevent liquid from entering the line. Removing the requirement for anti-siphon tubes to be installed in CO₂ bottles means one is no longer restricted to using specially-modified bottles. This removes the risk of another user accidentally attempting to use a non-modified bottle and can decrease the turnaround time if operating the platform continuously by having multiple, generic CO₂ bottles on standby.

5.2 Conclusion

The isentropic and inviscid model is a good predictor of cold gas propulsion performance and requires minimal effort to implement. The greater challenge lies in predicting the state properties of the propellant if using a two-phase source since large temperature fluctuations can occur. It is of interest to note that the isentropic model completely decouples temperature from net thrust, which is instead governed only by momentum exchange and pressure gradients. Nozzle geometry and supply pressure dictate the Mach number throughout the nozzle, so for fixed geometry and fixed supply pressure the Mach number will also remain fixed. What is changing with temperature is the local speed of sound which for a fixed Mach number results in changing fluid velocity. Thus, higher temperatures result in higher exit velocities and lower mass flow rates, which theoretically results in unchanging momentum exchange across the operational range of temperatures. This phenomenon was observed in testing as thrust was found to be consistent with the isentropic model despite an increase in mass flow rate due to decreased propellant temperature.

Air bearings were found to be an effective means for providing a near-frictionless platform with which to use for zero-gravity analogs, and their use in such applications are well documented. The actual operational parameters, however, are much more difficult to predict and are governed by a highly non-linear relationship between supply pressure, platform weight, and table build quality. Ultimately it was found that table build quality seemed to play the most important role in effectively operating an air bearing-based space zero-gravity simulator. Thin glass bends easily, and deviations from flatness will still occur even if it is placed on a level surface. Thicker glass may mitigate these issues to some degree, but since

plate glass is not manufactured to any flatness tolerance, there is no way to be certain that these issues will not still occur. Lastly, without a means to accurately measure the amount of deflection, it is difficult to determine the exact shape the surface takes. As such, most of the time spent developing a testbed will in fact be spent on simple trial-and-error: determining through qualitative observation where the low points are, then incrementally shimming the surface until deviations are reduced.

Small nozzles for cold gas propulsion can be manufactured consistently using equipment typically found in university machine shops so long as positional measurement precision can achieve 0.01 mm. It may even be possible to completely skip manufacturing the diverging section and instead just use a straight drilled hole when operating at 100 psig since the flow pressure quickly drops after the throat. This of course depends on the penalty to net impulse one is willing to accept and will be a less feasible option if operating at higher pressures. Higher operational pressures will require stronger and more robust valves which will in turn drive cost up. For low-thrust applications such as this project, low-cost and easily available valves are typically limited to 125 to 150 psig depending on the desired flow rate.

Overall, it was found that developing a propulsion system actually meant that most effort was expended on developing the systems with which it would be tested on. The isentropic model is a good starting-off point as experimental results are in good agreement with the model. The largest challenges surrounded the air bearing testbed which, despite the results acquired from testing, could still be greatly improved either through a more refined shimming procedure or complete replacement with a granite surface. While not completely frictionless, air bearings do provide a relatively inexpensive foundation upon which to build a test platform, but there is certainly going to be a lower limit to the magnitude of thrust that is testable on such a system.

Insofar as operations of the actual inspection satellite are concerned, a ΔV of 0.062 m/s is very easily achievable with a plenum-based two-fault tolerant system. Only minor performance drops are expected to be incurred for single-valve failures which prevent the outward-facing plenums from being pressurized (such as an A3 failure mode). The most critical failure modes are two-fault failure modes which occur in the same thruster line and result in constant thrust and significantly increased net impulse. The largest challenge for

future development is predicted to be the integration of a larger number of valves in such a small volume, but this could potentially be overcome with the use of SLA-based 3D printing technology and aviation-grade microvalves. Depending on power constraints of the satellite, an intelligent valve-opening schedule may be devised in order to charge the plenums with propellant in a reasonable amount of time. When sizing the propulsion system, it is expected that the majority of propellant will be spent on deorbiting the satellite post-mission. It therefore may be worth considering the development of a dedicated high- I_{sp} branch of the propulsion system such as a warm gas system specifically for this leg of the mission, or developing methods for satellite recovery post-mission if fuel is a premium commodity as might be the case for deep-space manned missions.

Appendix A

Hohmann Transfer Review

A Hohmann transfer is a method of transferring a spacecraft or satellite from one circular orbit to another by means of an intermediate elliptical “transfer” orbit. The method is used equally for raising or lowering an orbit and requires two separate burns of the spacecraft’s propulsion in order to accomplish. The ΔV (velocity change) required to modify the orbit can be calculated from the *vis-viva* (Latin for “living force”) equation, shown here as Equation A.1, which in turn can be derived by total specific energy for an object in orbit.

$$v^2 = GM \left(\frac{2}{r} - \frac{1}{a} \right) \quad (\text{A.1})$$

The *vis-viva* equation applies the conservation of energy to orbital motion such that, for any given circular or elliptical orbit, the relative velocity (v) can be determined simply by knowing the distance (r) between the orbiting object and central body. The mass of the orbiting body (such as a spacecraft or satellite) is assumed to be negligible, and as such the equation is parameterized by the Gravitational Constant (G), mass of the central body (M), and the semi-major axis of the orbit (a).

Figure A.1 illustrates the process of reducing an object’s altitude by means of a Hohmann transfer, which requires two separate burns to complete. The orbital motion is in a counter-clockwise direction and is entirely planar. The total ΔV for a Hohmann transfer is determined by first identifying the amount of ΔV required to modify a current circular orbit (notated in Figure A.1 as A) so that it becomes elliptical (noted in the same figure as B). For this we use Equation A.1 to first identify the velocity at a point for an object on orbital

path A, then identify the velocity at the same point for an object on orbital path B. The difference in these two calculated velocities is the ΔV required to modify our orbit from one path to the other. This maneuver is marked in Figure A.1 as ΔV_1 and, for the case of reducing altitude, is in the direction opposite of the orbital motion so as to slow the object down and bring the orbital path closer to the central body.

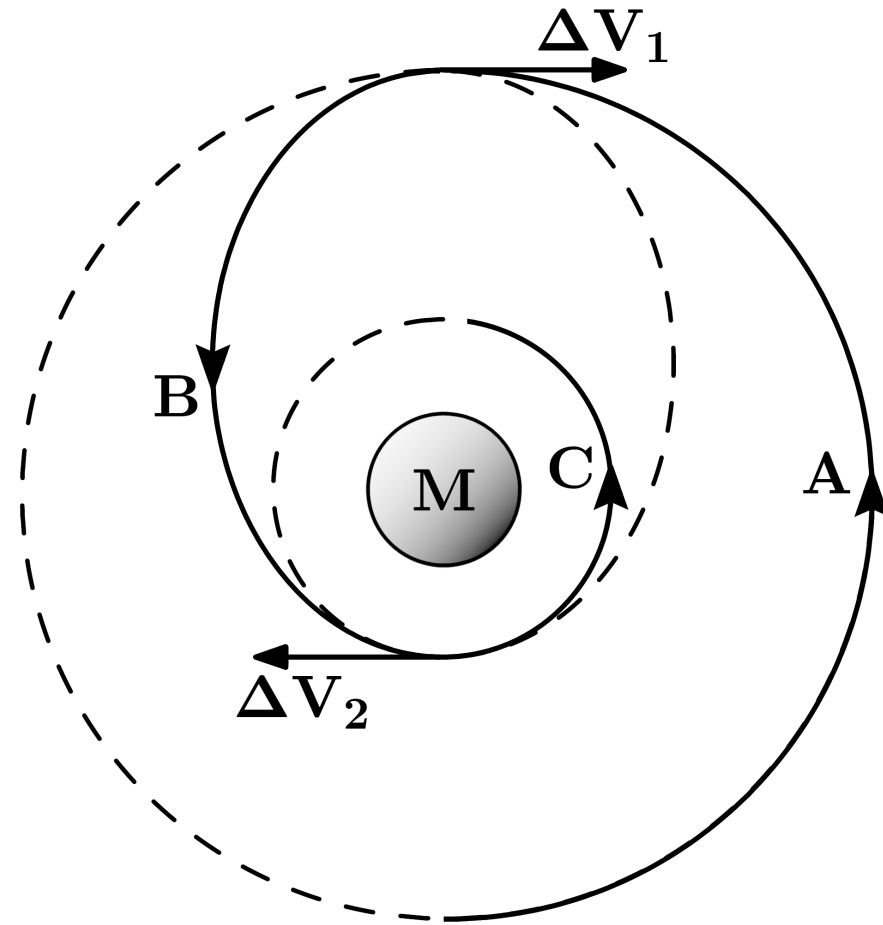


Figure A.1: Depiction of a Hohmann transfer used to reduce the altitude of an object by transferring it from circular orbit A to circular orbit C by means of elliptical orbit B and two separate propulsive burns.

Following this maneuver, the object is at its apogee (highest point) on elliptical orbit B and is left to follow this path until it reaches the point opposite of where the initial burn took place – its perigee (lowest point). The second ΔV maneuver then takes place at perigee

and is marked in Figure A.1 as ΔV_2 and, as before, is in the direction opposite of the orbital motion. Once again, determination of the ΔV required to modify the orbit from this point is done so using Equation A.1, first to determine the current velocity in the elliptical path B and again to determine the velocity at the same point for a circular orbit path C. This maneuver serves to reduce the size of the elliptical orbit such that it becomes circular once more with an altitude equal to the perigee of the transfer orbit set by ΔV_1 .

The total ΔV to reduce the radius of a circular orbit is the sum of ΔV_1 and ΔV_2 . Note that for this process, all burns are assumed to be “impulsive burns” – that is, instantaneous (or otherwise extremely short compared to the total orbital period). Modified Hohmann transfers are possible using extended burns, but are out of scope for this work and thus will not be covered.

Appendix B

Isentropic Nozzle Flow Review

A Python-based analysis program was developed in support of this work to explore the design tradeoffs between plenum size, storage pressure, and nozzle design. This program assumes the gas used as propellant is ideal and inviscid, and that the plenum discharge process is isentropic. A review of the isentropic relationships is presented here.

$$\frac{A}{A^*} = \left(\frac{\gamma+1}{2}\right)^{-\frac{\gamma+1}{2(\gamma-1)}} \frac{\left(1 + \frac{\gamma-1}{2}M^2\right)^{\frac{\gamma+1}{2(\gamma-1)}}}{M} \quad (\text{B.1})$$

$$\dot{m} = \frac{Ap_t}{\sqrt{T_t}} \sqrt{\frac{\gamma}{R}} M \left(1 + \frac{\gamma-1}{2}M^2\right)^{-\frac{\gamma+1}{2(\gamma-1)}} \quad (\text{B.2})$$

$$\frac{p}{p_t} = \left(1 + \frac{\gamma-1}{2}M^2\right)^{\frac{-\gamma}{\gamma-1}} \quad (\text{B.3})$$

$$\frac{T}{T_t} = \left(1 + \frac{\gamma-1}{2}M^2\right)^{-1} \quad (\text{B.4})$$

$$a = \sqrt{\gamma RT} \quad (\text{B.5})$$

$$M = \frac{v}{a} \quad (\text{B.6})$$

$$\text{Thrust}_{axial} = \left[\frac{1 + \cos \Theta}{2} \right] \dot{m} v_{exit} + A_{exit} (p_{exit} - p_{amb}) \quad (\text{B.7})$$

For a given nozzle geometry, the exit Mach number can be solved for using iterative methods to determine the roots of Equation B.1. To set this up, the following relationships are introduced:

$$P = \frac{(k + 1)}{2} \quad (\text{B.8})$$

$$L = \frac{(k - 1)}{2} \quad (\text{B.9})$$

$$W = \frac{k}{(k - 1)} \quad (\text{B.10})$$

$$Q = \frac{(k + 1)}{(k - 1)} = \frac{P}{L} \quad (\text{B.11})$$

$$S = \left(\frac{A}{A^*} \right)^2 \quad (\text{B.12})$$

$$X = M^2 \quad (\text{B.13})$$

Equation B.1 is then rewritten in a suitable form, shown below:

$$0 = (1 + LX)^Q - SX(P^Q) \quad (\text{B.14})$$

The *SciPy* Python library is a wrapper around the FORTRAN-based MINPACK library of subroutines for solving systems of non-linear equations. This library contains the *fsolve*

function which is used two find the two roots of Equation B.14. The two roots correspond to the *critical* Mach numbers, and each correspond to the nozzle exit Mach number for either a fully subsonic choked flow ($M_{crit_{sub}}$) or fully supersonic flow ($M_{crit_{sup}}$). This relationship is shown for three separate gasses in Figure B.1.

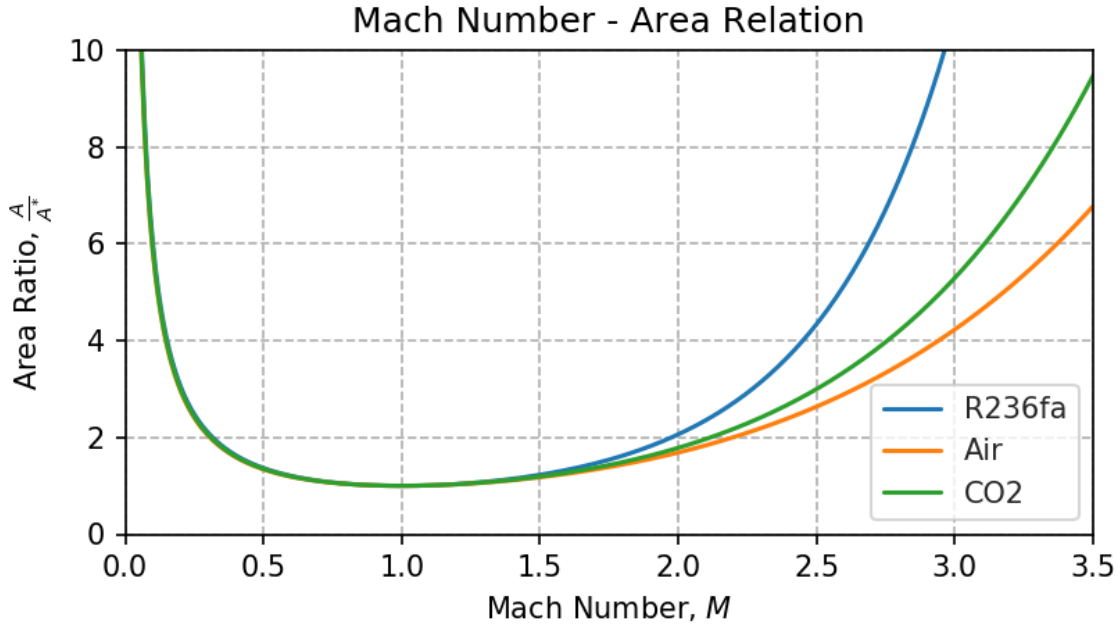


Figure B.1: Mach Number - Area relationship defined by Equation B.1 for three gasses

For a given nozzle geometry (and therefore given area ratio), the corresponding subsonic and supersonic critical Mach numbers can be combined with Equation B.3 to find the sub- and supersonic critical pressure ratios, PR_{sub} and PR_{sup} , respectively. A pressure ratio below the subsonic critical value ($PR < PR_{sub}$) will result in entirely subsonic flow through the nozzle.

At exactly the subsonic critical pressure ratio ($PR = PR_{sub}$), the throat will be sonic but the diverging section will remain entirely subsonic. Likewise, at exactly the supersonic critical pressure ratio ($PR = PR_{sup}$), the diverging section will be entirely supersonic. Furthermore, the exit pressure of the flow will be equal to the ambient pressure and no shocks will occur.

Any pressure ratio in between these two values ($PR_{sub} < PR < PR_{sup}$) will result in partially supersonic flow in the diverging section with a normal shock occurring at some point in the post-throat flow. This could take the form of a normal shock inside the nozzle or, if the pressure ratio is sufficiently high, a weak shock immediately outside the exit. In

either case, the exit pressure will be less than ambient and the resultant flow considered to be *overexpanded*.

A pressure ratio above the supersonic critical value ($PR > PR_{sup}$) will still result in continuous supersonic flow through the diverging section of the nozzle, but the exit pressure will be greater than ambient and the resultant flow considered to be *underexpanded*. The pressure distribution along the length of a converging-diverging nozzle is illustrated in Figure F.1.

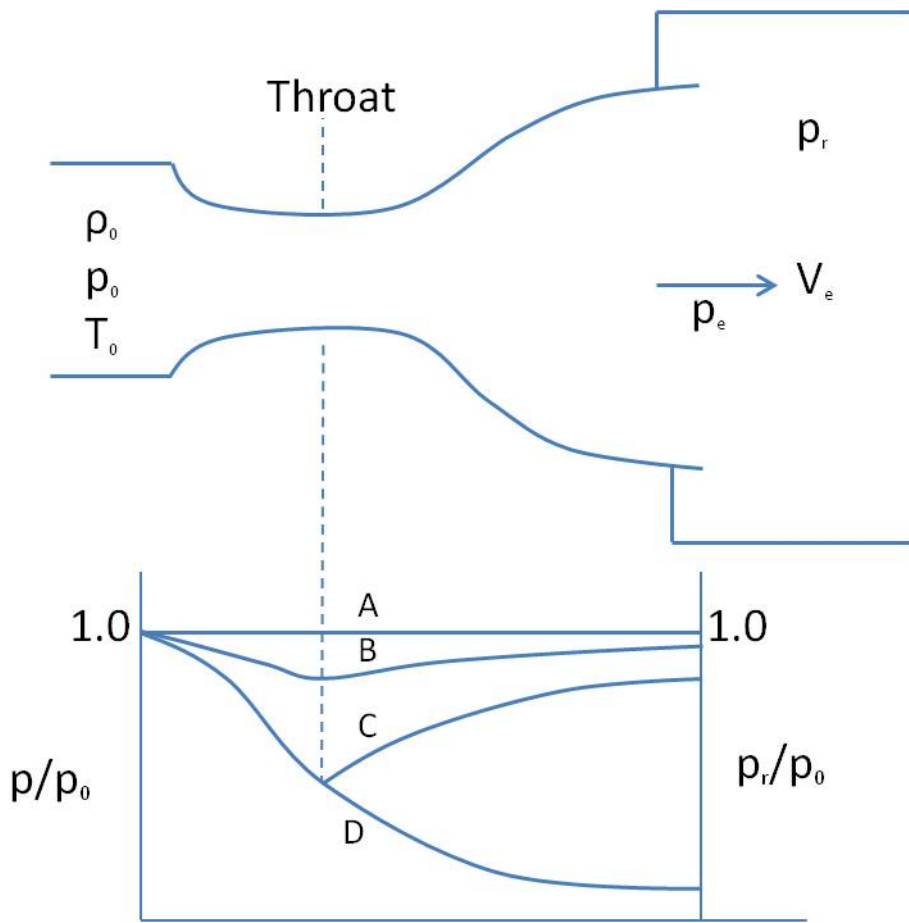


Figure B.2: Pressure ratio distribution along the length of a converging-diverging (De Laval) nozzle. The subsonic and supersonic solutions to Equation B.1 are labeled as lines C and D, respectively [76].

Further investigation will reveal that, for fully supersonic flow in the diverging section, the Mach number at any given station along the nozzle length is independent of the pressure ratio. This observation will be illustrated in Section C once a nozzle simulation is performed and all the state variables observed over a range of inlet pressures.

Appendix C

Single Plenum Discharge Simulation

C.1 Simulation Development

The time-rate of change of plenum pressure is modeled by discretizing the mass flow rate (Equation B.2) and calculating it at sufficiently small time steps. At each time step, the pressure ratio is used to determine whether the diverging section flow is entirely supersonic, entirely subsonic, or somewhere in between (shock), as discussed in B. Simulation results are validated experimentally in Section 4.2.2. An appropriately-sized time step is determined by exploring the effect of time step on simulation results and comparing it to experimental results.

For a given nozzle geometry, plenum (total) pressure and temperature, and gas constants, a mass flow rate is calculated. A forward difference finite approximation method is used for the mass reduction calculation, meaning the flow rate is assumed constant for the finite time period. Given the mass flow rate and time step, a determinable amount of gas is subtracted from the total plenum gas mass at each time step. This reduction in mass corresponds to a reduction in density and gas temperature.

For this model, the gas flow is treated as undergoing a *polytropic* process, and the reservoir walls adiabatic. Because of this assumption, the reservoir temperature is predicted to drop quickly as the remaining gas does work on the departing gas. The model predicts that the reservoir temperature would drop below the phase change temperature and a mixed-phase gas would enter the nozzle. However, this is unlikely to occur as there is expected to be significant heat transfer between the brass body of the nozzle and the incoming air flow.

$$\dot{m}_i = \frac{A^* p_{t_i}}{\sqrt{T_{t_i}}} \sqrt{\frac{\gamma}{R}} \left(1 + \frac{\gamma - 1}{2}\right)^{-\frac{\gamma+1}{2(\gamma-1)}} \approx \frac{m_{i+1} - m_i}{\Delta t} \quad (\text{C.1})$$

Equation B.2 is evaluated at the throat and a finite difference approximation made for \dot{m} , subsequently reducing to Equation C.1. Rearranging for m_{i+1} , the total mass in the plenum is calculated at each time step:

$$m_{i+1} \approx \dot{m}_i \Delta t + m_i \quad (\text{C.2})$$

With the mass known and the plenum volume fixed, a new density can be calculated.

$$\rho_{i+1} \approx \frac{m_{i+1}}{V_{plenum}} \quad (\text{C.3})$$

As stated before, the isentropic model dictates a change in gas temperature governed by the relation shown in Equation C.4.

$$T_{i+1} = T_i \left(\frac{P_{i+1}}{P_i} \right)^{\frac{\gamma-1}{\gamma}} \quad (\text{C.4})$$

The new plenum pressure can be calculated assuming an ideal gas as shown in Equation C.5 and using Equation C.4 to determine the total temperature at time $t + 1$.

$$p_{t_{i+1}} = \rho_{i+1} R T_{t_{i+1}} \quad (\text{C.5})$$

The script starts with known initial conditions (plenum pressure, temperature, volume) and marches forward in time, tracking the total mass of gas remaining in the plenum. At each time step, the mass flow rate \dot{m} (and additional thermodynamic properties) is calculated from the gas properties, pressure, temperature, and nozzle geometry. A corresponding amount of propellant is subtracted from the remaining gas by assuming a constant \dot{m} for the time period, and the plenum gas density is recalculated. The newly calculated density is then used to determine a new pressure and temperature based on the following isentropic relations, derived from Equations C.4 and C.5:

$$P_{i+1} = P_i \left(\frac{\rho_{i+1}}{\rho_i} \right)^\gamma \quad (\text{C.6})$$

$$T_{i+1} = T_i \left(\frac{\rho_{i+1}}{\rho_i} \right)^{\gamma-1} \quad (\text{C.7})$$

This process is repeated until one of the following conditions are met:

- Plenum pressure has reached ambient pressure
- Plenum $\frac{\Delta P}{\Delta t}$ drops below 0.01%/sec
- Simulated thrusting time exceeds the maneuver time determined in Section 2.4

A similar solution can be reached analytically if the plenum discharge is treated as an unsteady thruster pulse beginning immediately after the thruster valve has been closed. In this situation, the reaction chamber pressure is unsteady and governed by the mass flow rate through the nozzle. If we assume the nozzle stays choked, we can continue to use the mass flow rate equation described by Equation B.2. Likewise, if we assume constant temperature, a solution emerges wherein pressure decays exponentially. This solution, originally presented by Professor Jerry M. Seitzman at Georgia Tech College of Engineering [77], is recreated here:

$$P_0(t) = P_{0_{max}} \exp -f(\gamma) \frac{\sqrt{RT_0} A_t}{V_{plenum}} t \quad (\text{C.8a})$$

$$f(\gamma) = \sqrt{\gamma} \left(\frac{\gamma + 1}{2} \right)^{-\frac{\gamma+1}{2(\gamma-1)}} \quad (\text{C.8b})$$

C.2 Selection of Appropriate Simulation Time Step

Rounding errors can become problematic and produce inaccurate results if the selected time step is too large. Likewise, setting the end condition too large will result in below-actual estimates for net impulse and required discharge time.

A convergence study was performed for both an on-ground CO₂-based system and an in-space R134a-based system to identify what time step would be sufficient for each. The results for both in-space and on-ground situations are illustrated in Figures C.1 and C.2, respectively. The chosen time step was heavily dependent on the nozzle geometry, which in

turn affected the mass flow rate. For the in-space R134a system, the nozzle throat diameter and corresponding mass flow rate was significantly smaller, given the requirements and constraints discussed in the previous section. This in turn necessitated a larger time step to perform the simulations efficiently. In contrast, on-ground CO₂-based system required a much smaller time step in order to produce accurate results, owing to the much larger nozzle throat diameter and corresponding mass flow rate.

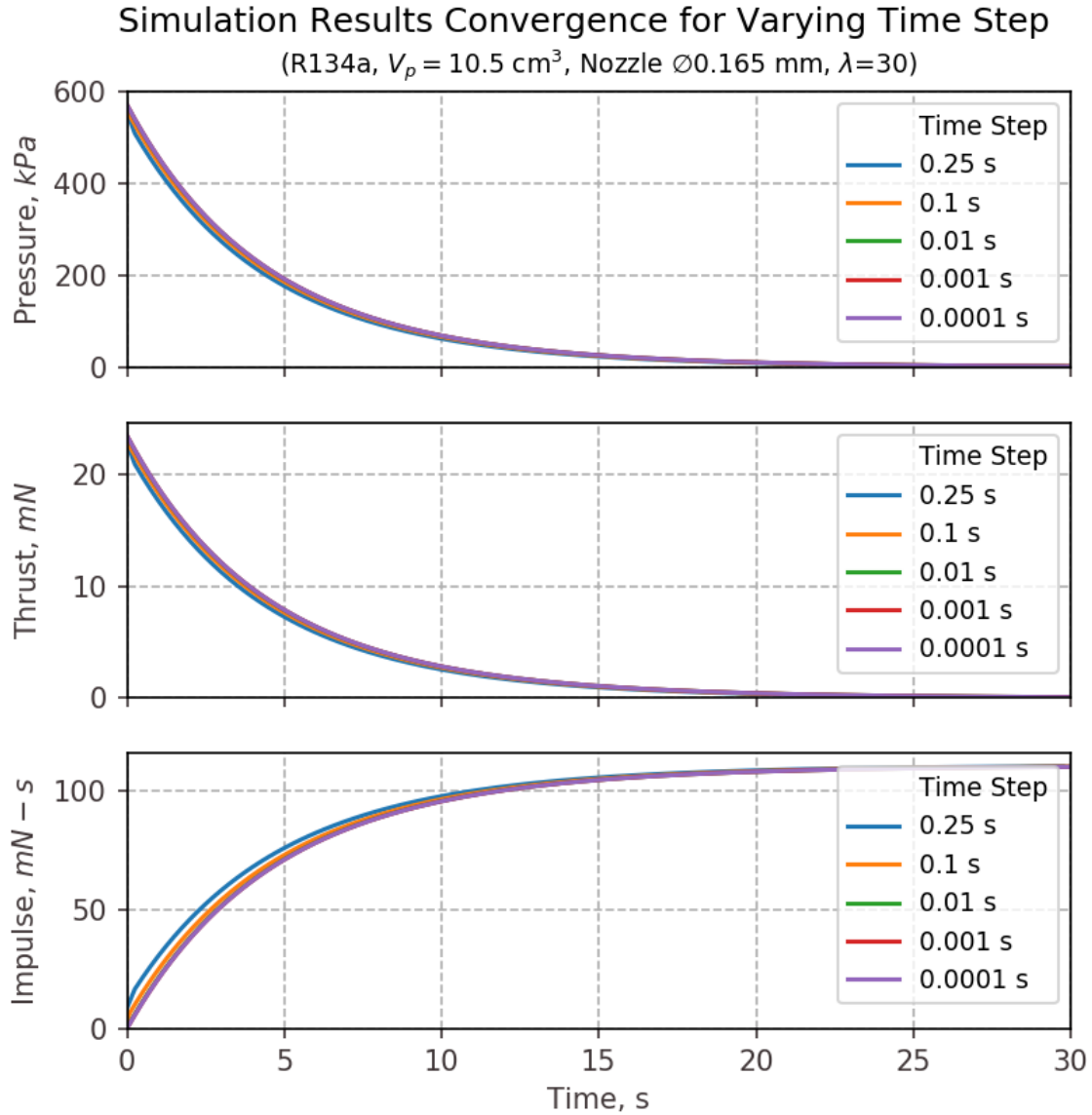


Figure C.1: Convergence study for an in-space R134a-based system described in Section 2.4.

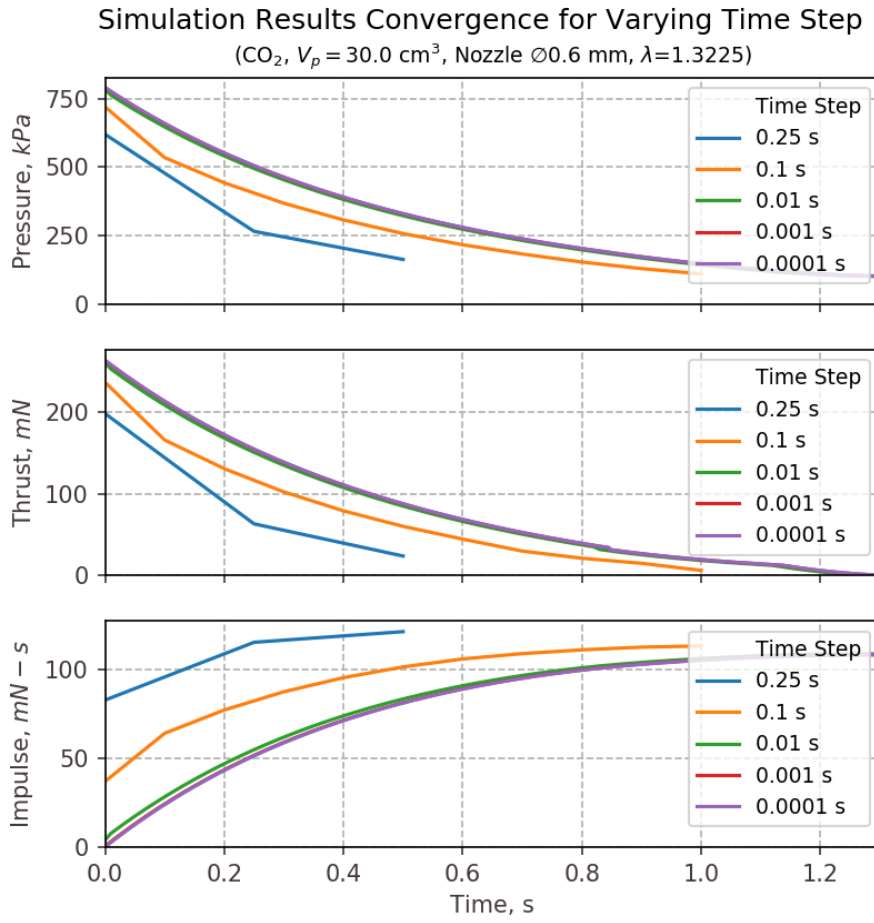


Figure C.2: Convergence study for an on-ground CO₂-based system described in Section 2.4.

As can be seen for an in-space, R134a-based system, results are similar for each time step. Bear in mind however the time scale of the simulation – nearly 30 seconds – compared to that in the CO₂ based system. Closer inspection reveals the results converge satisfactorily for a time step of 0.01 seconds. For an on-ground, CO₂-based system, results converge after a time step of 0.001 seconds is used.

Based on these results, a function was empirically derived to determine an appropriate fixed time step for the simulation based on the nozzle geometry and starting pressure ratio. Higher pressure ratios (P_0/P_{amb}) and larger nozzle throat areas (A^*) will require a smaller time step, whereas larger plenum volumes will contribute to smaller changes in pressure and thrust over time, necessitating a larger time step.

$$\Delta t = f(P_{amb}, P_0, A^*, V_{plenum}) = 15.28V_{plenum} \left(\frac{P_{T_0} - P_{amb}}{P_{T_0}^2 d^{*2}} \right) \text{ sec} \quad (\text{C.9})$$

A sample listing of the resultant time steps calculated from Equation C.9 are listed below in Table C.1. This listing demonstrates how modifying the individual parameters in Equation C.9 results in a varying time step, specifically showing the “weight” that each parameter carries when calculating a time step. Furthermore, the benefits of this approach are illustrated by showing the order of magnitude difference between the time steps calculated for in-space versus on-ground simulations.

Empirically Derived Simulation Time Steps

d^*	P_{T_0}	P_{amb}	V_{plenum}	Δt
In-Space Conditions				
0.165 mm	571.6 kPa	0 kPa	10.5 cm^3	0.010 sec
0.233 mm	571.6 kPa	0 kPa	10.5 cm^3	0.005 sec
0.165 mm	285.8 kPa	0 kPa	10.5 cm^3	0.021 sec
0.165 mm	571.6 kPa	0 kPa	21.0 cm^3	0.020 sec
On-Ground Conditions				
0.600 mm	790.8 kPa	101.3 kPa	30.0 cm^3	0.001 sec
0.400 mm	790.8 kPa	101.3 kPa	30.0 cm^3	0.003 sec
0.600 mm	446.1 kPa	101.3 kPa	30.0 cm^3	0.002 sec
0.600 mm	790.8 kPa	101.3 kPa	60.0 cm^3	0.003 sec

Table C.1: A sample listing of time steps calculated from Equation C.9 based on the convergence results from Figures C.1 and C.2. Parameters which are varied from their design value are bolded.

As the characteristic discharge time for an in-space system is significantly longer than an on-ground system (roughly 30 seconds versus 1.3 seconds, respectively), so too must the time step be adjusted accordingly. The resultant effect of this process is holding the number of data points relatively constant between simulation parameters.

Appendix D

Realistic Considerations of Performance

The performance estimates made in the previous section were contingent on a model that assumes isentropic and inviscid flow throughout the entire nozzle. A better picture of performance could be obtained by estimating any viscous losses within the nozzle which would reduce the overall thrust effectiveness. To do so would first require an estimation of the Reynolds Number – a nondimensional parameter used to identify how laminar or turbulent a flow is – at the throat. Viscosity is also heavily dependent on fluid temperature, so a reasonable estimation of the temperature must also be made and thus requires the implementation of a higher fidelity thermal model. This section will briefly discuss the implementation of a model which takes into account the phase change of CO₂ inside the plenum. The phase of the propellant inside the nozzle was not addressed due to the additional spacial relationship involved, and as such this exploration only serves to provide superficial insight into the matter. Further work into the matter would require the development of a higher fidelity nozzle flow simulation which, at present, is out of scope for this project.

D.1 Limitations of Isentropic Model

The isentropic model assumes the flow through the nozzle is adiabatic, inviscid, and entirely single phase. While it is already suspected that a phase change occurs through the nozzle, the extent of such a phase change can only be properly determined with an extensive 2D (or greater) simulation of flow through the nozzle. Such a simulation would need to track

the internal energy and density at every point along the nozzle to identify when a phase change begins to occur mid-flow. Without completely rebuilding the discharge simulation from the ground up, the extent of a phase change occurrence can still be explored by looking at the time-rate of change of pressure and temperature within the plenum, assuming an isentropic process between time steps for the fixed volume. As seen in Figure D.1, the isentropic model becomes invalid once the plenum pressure and temperature crosses into the solid phase region, thus necessitating further model refinement to track the properties in a phase coexistence region.

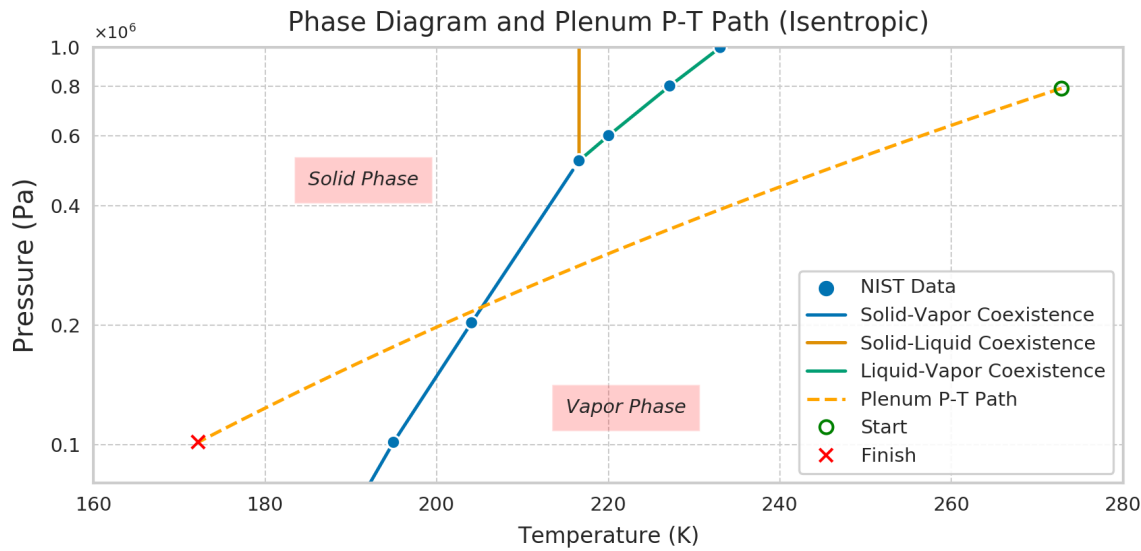


Figure D.1: Plenum pressure and temperature over the course of a single plenum discharge modeled as entirely isentropic, illustrating how the isentropic model does not account for phase change.

To determine the extent to which phase changes occurs, the single plenum discharge simulation was augmented to track the internal energy of the flow for the duration of a single discharge. At each step, the change in total energy inside a control volume drawn around the plenum was calculated from the enthalpy and mass flow rate. For a fixed plenum volume and known mass flow rate, and by using the enthalpy of the gas in the previous time step, the specific internal energy of the gas in the plenum can be determined for each time step and used with the density to determine the phase. This density-energy ($\rho-u$) path was plotted along with the known phase boundaries for CO₂, and an algorithm written to

ascertain when the path crosses from the “vapor” region into the “solid-vapor coexistence” region.

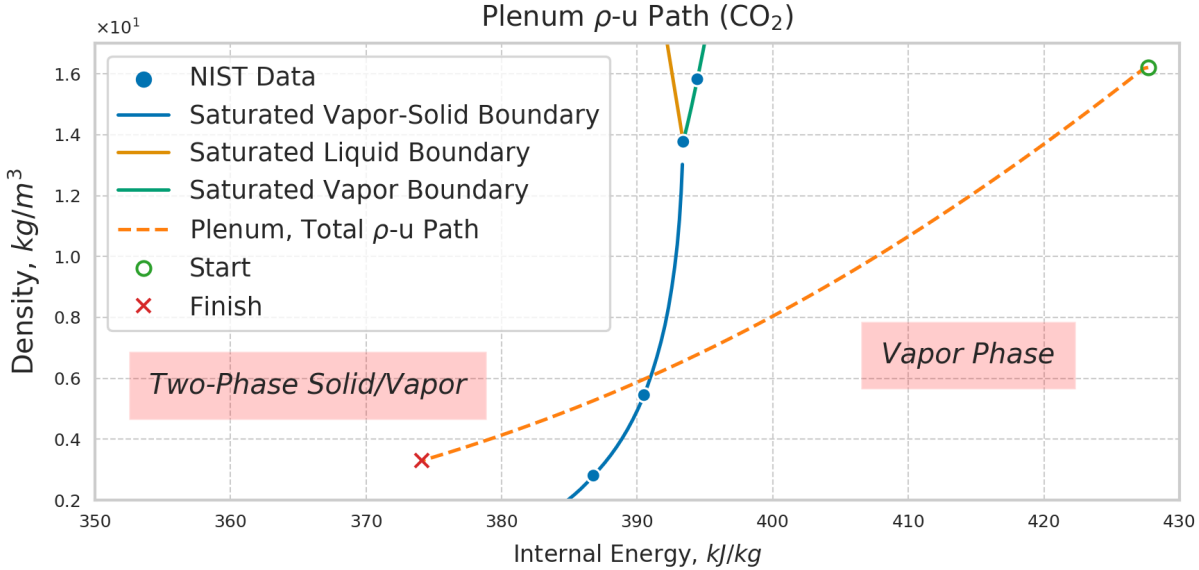


Figure D.2: Density-energy plot of CO_2 illustrating the path it takes as a plenum discharges, showing when a phase change begins to take place as the path crosses into the phase coexistence region.

The phase is monitored with simple boolean logic: if the ρ - u curve lies within the “vapor” region, then the energy balance equation is applied, some mass is removed from the control volume, and a new pressure and temperature is calculated from the known density and internal energy. Otherwise, if the ρ - u curve enters the “solid-vapor coexistence” region, the pressure is allowed to continue to decrease as before, and the temperature is fixed to the phase-change temperature for each given pressure. Using this method, the simulation is re-run and pressure-temperature tracked as before with the results plotted in Figure D.3.

Despite the seemingly large time spent in the two-phase region, the enthalpy inside the plenum drops only marginally faster than the saturated vapor enthalpy for CO_2 at the same pressure and temperature. As a consequence of this, the vapor quality inside the plenum remains above 99.9% for the entire duration. This realization yields an interesting conclusion, one that was corroborated by testing in Section 4.2: that the isentropic model can continue to successfully predict performance even when the gas transitions into the two-phase region as long as the vapor quality remains near 100%. A similar analysis was performed for R134a

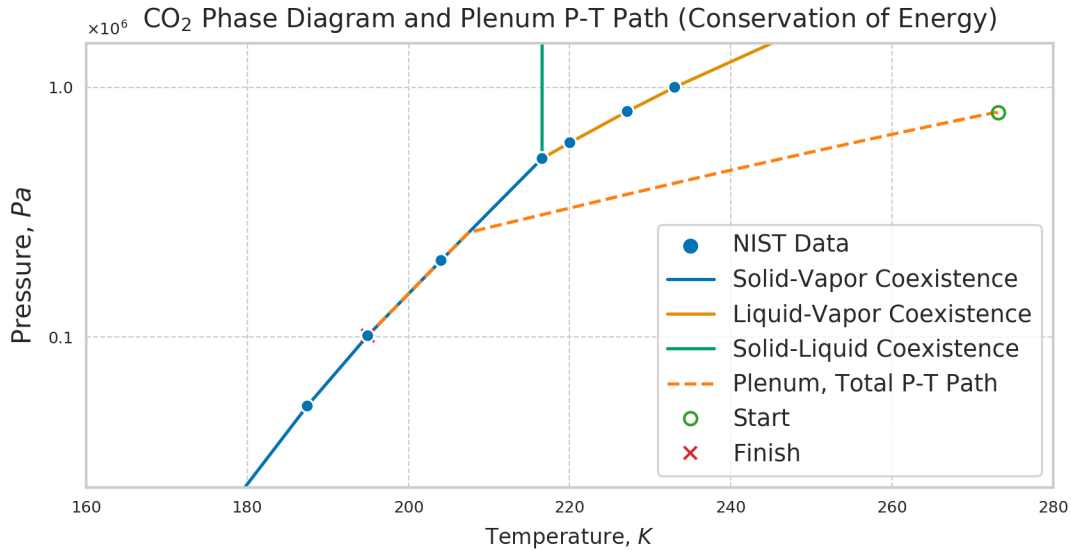


Figure D.3: Plenum pressure and temperature over the course of a single plenum discharge modeled using conservation of energy and by tracking when a phase change occurs.

and the resulting behavior was largely identical, thus it is not shown here.

D.2 Heat Transfer Through Valve

Owing to the low temperatures reached by the CO₂ during a discharge and the large mass associated with the solid brass valve base, a heat transfer model was developed to estimate the amount of propellant heating as it passed through the valve. The model could not be validated due to the short time period associated with a discharge compared to the large time scales required for thermocouple responses. Nevertheless, the model can at least provide a sense of scale for how much heat might be added to the flow from the valve, thus delaying the onset of a phase transition.

A control volume analysis was performed on the valve, and a seven-step algorithm was developed to estimate the temperature change of the flow through the nozzle.

1. Upstream pressure, temperature, and viscosity are calculated from the stagnation properties within the plenum. The velocity is determined using the subsonic Mach number-area relation for an inlet of 2 mm.
2. The upstream Reynolds number (Re), specific heat capacity (C_p), coefficient of conductive heat transfer (k), and Prandtl number (Pr) are calculated or otherwise acquired for the upstream conditions.

3. These parameters are used to calculate the Nusselt number of the flow using the Gnielinski correlation [78].
4. The convective heat transfer coefficient (h_c) is calculated from the definition of the Nusselt number, the conductive heat transfer coefficient, and the valve geometry.
5. Heat rate is then estimated from h_c , nozzle geometry, and the temperature difference between the wall and upstream flow.
6. The corresponding change in enthalpy of the propellant is then calculated from the heat rate.
7. From this, the change in propellant temperature is estimated along with the corresponding wall temperature drop.

Since the mass flow rate is controlled downstream by the nozzle (assuming choked flow), the first time step requires us to first determine the initial mass flow rate pre-temperature change before updating it with the now-warmer propellant flow. Continuing forward, the mass flow rate from the previous time step is used as the \dot{m} for the next time step when calculating the heating rate. The Gnielinski correlation, which is based on empirical data, is dependent on the friction factor and Prandtl number and is valid for turbulent pipe flow of $Re > 4000$, of which the vast majority of the flow takes place. The correlation used for this analysis is presented as follows:

$$Nu = \frac{(f/8)(Re - 1000)Pr}{1 + 12.7\sqrt{f/8}(Pr^{(2/3)} - 1)} \left[1 + \left(\frac{d}{L} \right)^{(2/3)} \right] K \quad (\text{D.1})$$

where

$$K = \left(\frac{T_{fluid}}{T_{wall}} \right)^{0.45} \quad (\text{D.2})$$

In this formulation, f is the Darcy friction factor. As the valve was not a straight tube, the correlation may not be exactly applicable, and such a determination would warrant experimental testing. The Prandtl number is calculated from the upstream viscosity but remains fair constant through the duration of the discharge, averaging out at approximately 0.781 ± 0.011 . For the short portion of flow wherein the Reynolds number goes below 4000,

the Nusselt number is defined by a simple linear relationship with the mass flow rate. This latter portion of the flow, however, contributes very little to the overall thrust, so its accuracy is not crucial to this exercise. Flow through the valve is treated as Rayleigh flow and the corresponding downstream flow components are calculated accordingly. Note that the simulation time was adjusted for R134a to focus more graphing space on the beginning of the discharge.

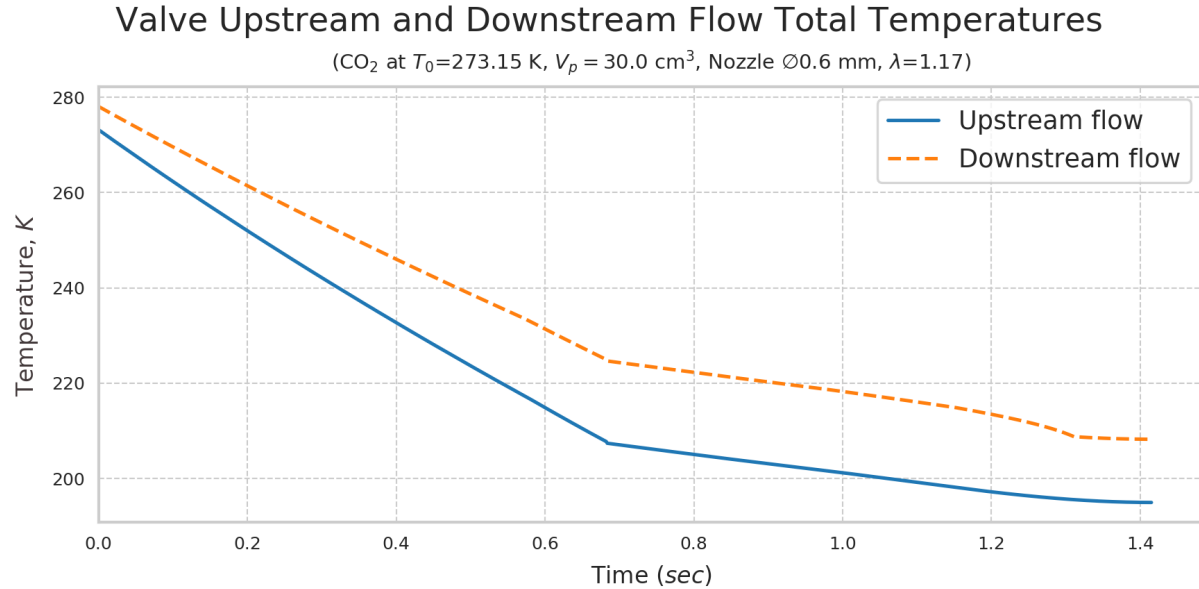


Figure D.4: Total CO_2 flow temperatures upstream and downstream of the valve illustrating the marginal effect of heat transfer on the flow temperature itself.

Ultimately, the flow through the valve was raised a maximum of 18 K. The valve temperature itself dropped less than 0.1 K and was therefore not shown. While seemingly extraordinarily small, consider that a total propellant mass of approximately 0.6 grams was utilized compared to the approximately 70 gram brass body and as such did not result in any significant drop in valve temperature.

A similar analysis was performed for R134a and assuming a valve mass of 1.5 grams and polymer-based construction (consistent with specifications provided by microfluidic valve manufacturers). In both cases, the temperature rise through the valve was, naturally, greater as the propellant temperature reduced during discharge. Likewise, the drop in valve temperature was insignificant compared to the rise in propellant temperature.

Valve Upstream and Downstream Flow Total Temperatures

(R134a at $T_0=293.15$ K, $V_p = 11.2 \text{ cm}^3$, Nozzle $\varnothing 0.212$ mm, $\lambda=30.0$)

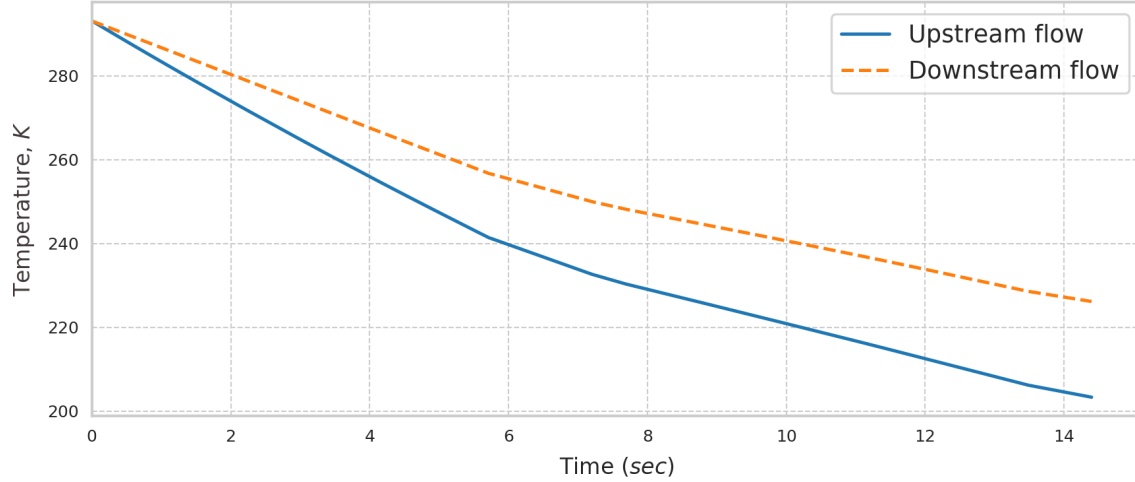


Figure D.5: Total R134a flow temperatures upstream and downstream of the valve illustrating the marginal effect of heat transfer on the flow temperature itself.

D.3 Throat Reynolds Number During Discharge

The time-rate of change of the Reynolds number at the throat was calculated over the course of a single plenum discharge for both the in-space and on-ground design cases in order to gain insight in the flow conditions at the throat. As before, the in-space design assumes R134a at 20° Celsius as propellant and uses the corresponding geometry presented in Table 2.8. Likewise, the on-ground design assumes CO₂ at 0° Celsius as propellant and uses the geometry listed in Table 2.10. Figure D.6 presents the results of this analysis for both the in-space and on-ground designs. Note that the scales of both time and Reynolds number are extremely dissimilar due to the varying nature of the propellants, nozzle geometry, and ambient pressure, and thus are not plotted together on the same graph. As expected, the value of the Reynolds number drops as chamber pressure (and therefore throat velocity and density) decreases. For the in-space design, the Reynolds number indicates that the flow through the throat is entirely turbulent throughout most of the discharge, dropping below 4000 and transitioning to laminar only after the supply pressure has dropped by about 92% at approximately 8 seconds into the discharge. For the on-ground design, the flow remains turbulent even after transitioning into the entirely subsonic regime and only dropping below 4000 in the last fraction of a second.

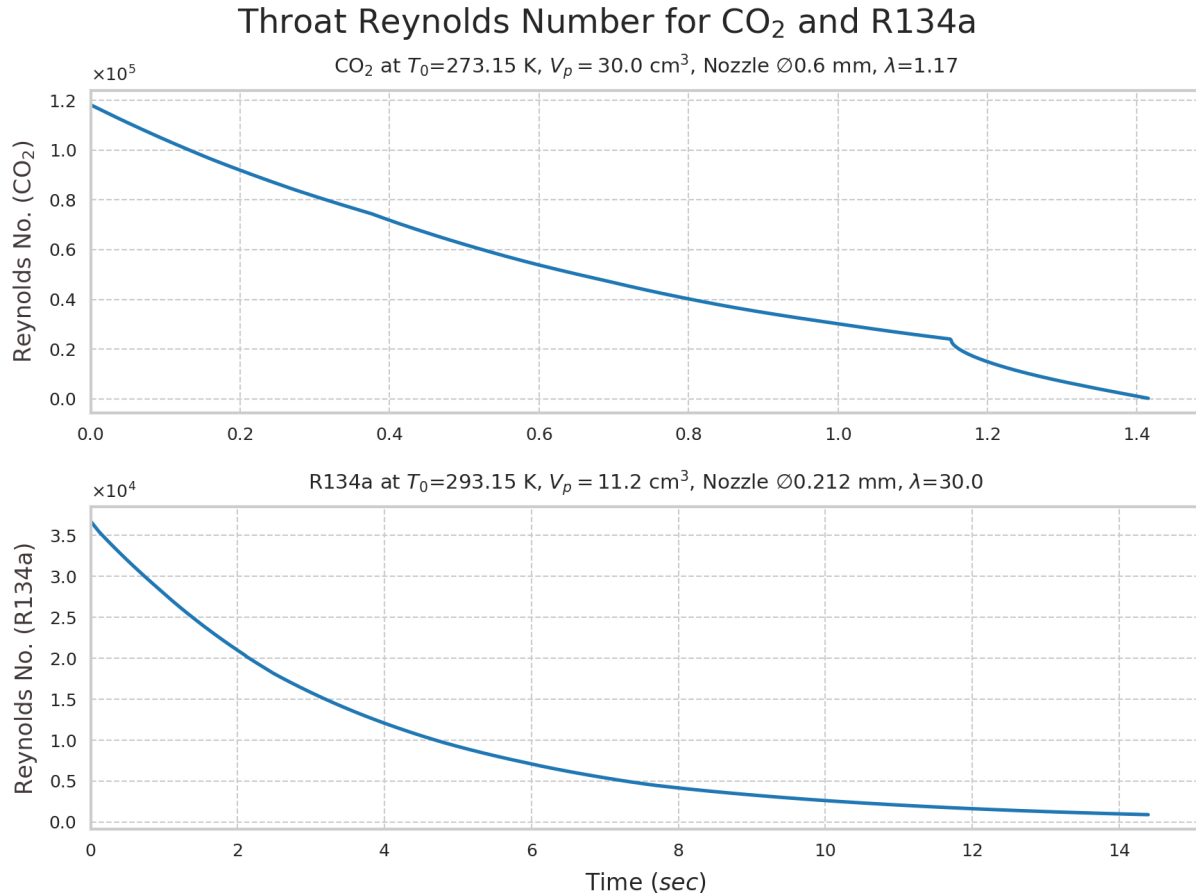


Figure D.6: Comparison of the throat Reynolds number for CO₂ and R134a.

D.4 Estimating Viscous Losses

For cold gas propulsion nozzles, departures from ideal thrust are primarily caused by viscous losses in the boundary layer formed within the nozzle interior. Estimating the magnitude of these losses can be accomplished by modeling the viscous losses along the interior nozzle wall using skin friction relations for laminar flow over a flat plate [79]. To estimate the losses, we begin by reframing the performance in terms of a nondimensional thrust coefficient: thrust normalized by the product of stagnation pressure and throat area (Equation D.3).

$$C_f = \frac{F_t}{P_0 A_{th}} \quad (\text{D.3})$$

Viscous losses are then defined as contributing to a reduction in thrust coefficient, and are therefore also nondimensional. Due to the nature of a plenum-based design, the thrust

coefficient will vary over the course of a pressure in the same manner as thrust, impulse, and Reynolds number. Therefore we must also consider the time-rate of change of thrust coefficient as well as the time-rate of change of viscous losses. Summarizing the equations presented in [79], the following integral was numerically computed at each time step of the simulation to calculate the viscous losses along the length of the nozzle:

$$C_{F_v} = \frac{0.664 f_0}{\sqrt{Re_{th} \tan \alpha}} \int_1^{A_e/A_{th}} f_1 f_2 d \left(\frac{A}{A_{th}} \right) \quad (\text{D.4})$$

where

$$f_0 = \gamma \left(\frac{\frac{\mu_w}{\mu_{th}} \frac{\rho_{th}}{\rho_0} \sqrt{\frac{T_{th}}{T_0}}}{2 \frac{T_w}{T_0}} \right)^{1/2}$$

$$f_1 = \left(\sqrt{\frac{A}{A_{th}}} - 1 \right)^{-1/2}$$

$$f_2 = M^{1.5} \left(\frac{T}{T_0} \right)^{\frac{5\gamma-3}{4(\gamma-1)}}$$

The solution presented in Equation D.4 is evaluated at the local geometric area ratio and is independent of the influence of boundary layer thickness. This approximation presented a solution for viscous drag ‘uncoupled’ from the effect of boundary layer thickness on the free stream flow conditions and is generally suitable for high Reynolds’ number and low expansion ratio nozzles. Figure D.7 illustrates the results of this calculation by showing the change in thrust coefficient (C_f) and corresponding coefficient of viscous losses (C_{f_v}) for the on-ground CO₂-based system. It is evident that, except for the far end of the discharge time when useful thrust is all but absent, the viscous losses in the nozzle are exceedingly small owing to the short nozzle length and large Reynolds number.

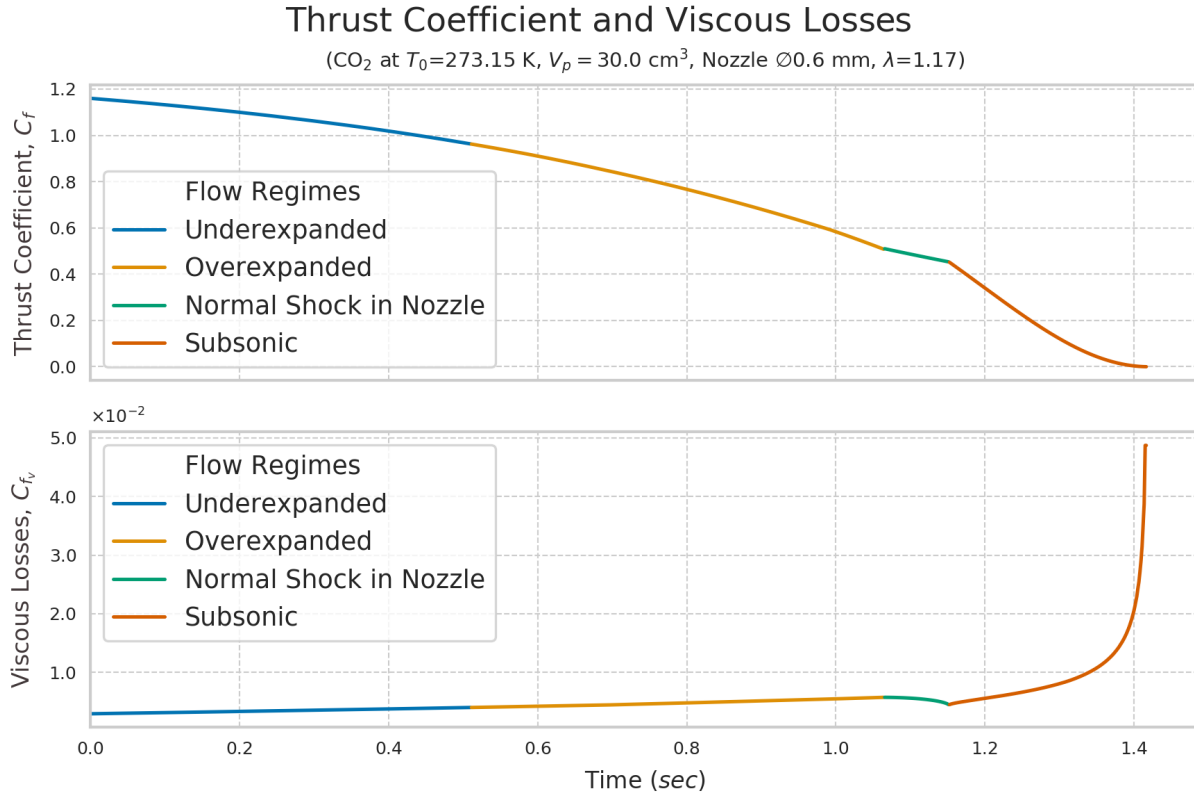


Figure D.7: Thrust coefficient and estimated viscous losses for CO_2 -based nozzle used in on-ground testing.

A similar analysis was performed for the hypothetical R134a-based nozzle, shown in Figure D.8. Note that because the nozzle is operating in vacuum environment, the thrust coefficient as defined by Equation D.3 remains constant throughout the entire discharge due to thrust being proportional to absolute pressure (as opposed to gauge pressure in an atmosphere). Furthermore, no significant difference was found between the coupled and uncoupled results for either setup.

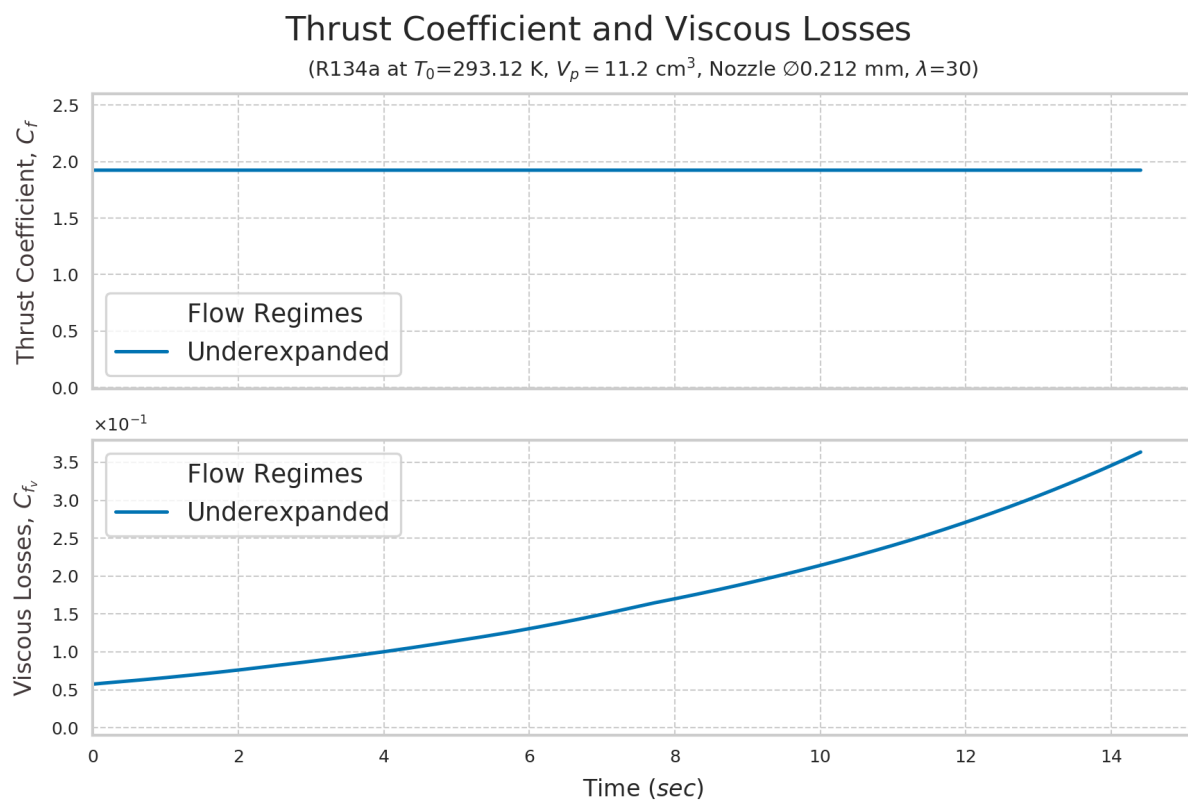


Figure D.8: Thrust coefficient and estimated viscous losses for a hypothetical R134a-based nozzle to be used in space.

Appendix E

Off-The-Shelf Component Selection

E.1 Pneumatic Component Selection

The motivation behind selecting as many off-the-shelf components as possible was born partially to promote replicability of the air bearing platform, but also out of frustration in finding a sizable lack of information available on valves and other components used for propulsion systems. This was important as it seemed to establish a financial barrier to entry for developing a propulsion system, especially one that is merely in the initial prototyping phase when funding is minimal. To that end, this section will seek to outline the requirements and chosen components for the air bearing platform and propulsion system, and conclude with a summary of the components including their cost and source.

E.2 Regulator Selection

Knowing that the prototype propulsion system would operate using CO₂ at or near 100 psig, the first task was finding a suitable CO₂ regulator. The ideal regulator would have a small form factor and be capable of supplying CO₂ over 100 psig at the outlet. Furthermore, the regulator must be capable of being adapted to use with 9 oz. CO₂ bottles which typically are fitted with a standard Air Supply Adapter (ASA) to adapt the G1/2"-14 output of the CO₂ bottles to 1/8" NPT.

Commercial markets which primarily use inexpensive and compact CO₂ regulators include the paintball, aquarium, home beer brewing, and home carbonated beverage industries. However, the typical operating pressures for all of these industries save for paintball

was typically no more than 30 psig, meaning most regulators available for these markets were unsuitable for the propulsion system (though they would suffice for an air bearing platform). Moreover, the low pressure regulators which might have been usable for the air bearing platform were not able to be adapted to the 1/8" NPT output of the ASA due to a lack of appropriate fittings. Most of these regulators were designed to be used with small 12 or 16 gram CO₂ cartridges for which threaded adapters do not appear to exist. Though the possibility to manufacture an adapter in-house does exist, recall that one of the goals of this project is to promote replicability. To that end, this solution was only considered in the event that no other off-the-shelf solution could be found.

In the paintball industry, both CO₂ and high pressure air (HPA) are used as propellant for equipment, but in both cases the regulators seemed to be built into the marking equipment itself and were unavailable for individual purchase. Given the restraints on regulator selection summarized above, one choice stood out as an acceptable solution: the "Micro Rock" regulator manufactured by Palmer's Pursuit Shop out of North Highlands, CA. This regulator is made to use with CO₂-based paintball equipment and features a piston-style design which allows for adjustable output up to 200 psig. The piston-style regulator, illustrated in Figure E.1a, benefits from a robust and simple configuration that is easy to manufacture and easily configurable based on the desired range of output. However, compared to a diaphragm-style regulator which is illustrated in Figure E.1b, the piston-style regulator suffers from hysteresis due to frictional forces between the piston and cylinder wall, and is often incapable of meeting high-flow demands. Considering the intermittent and low-flow use cases we expect to use these with, the selection of a piston-style regulator was ultimately deemed not to be concerning.

E.3 Valve Selection

Propulsion engineering has often been described as little more than high-tech plumbing, and with good reason. The engineer must be cognizant of pressure differentials and flow rates and must therefore select suitable components to meet or exceed the demands of the system. The driving factor behind valve selection for this project was the expected flow rate at the nozzle, which for a 0.6 mm throat diameter and 100 psig CO₂ supply pressure (the expected

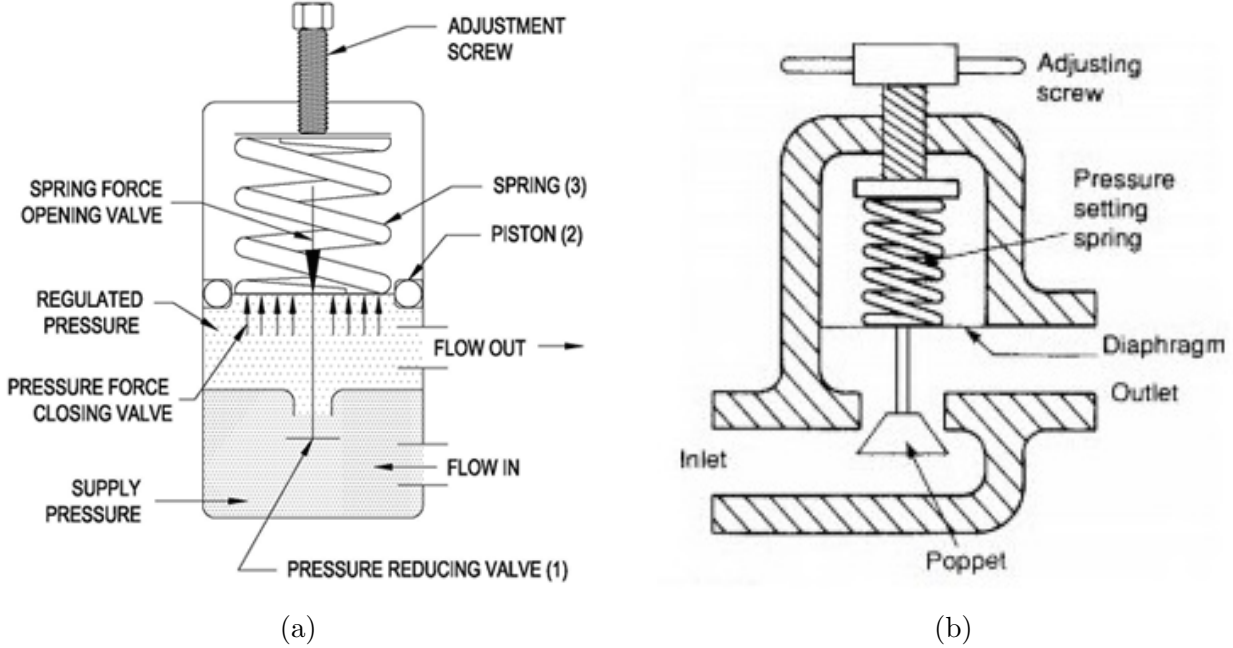


Figure E.1: Regulator style comparison, piston [80] (a), and diaphragm [81] (b).

use case for on-ground testing) corresponds to a maximum flow rate of 0.65 g/s (equivalent to 5.1 SCFH). Therefore, any valve selected must be capable of handling at least that much, plus a sizable margin to account for line losses. A survey of solenoid valves was completed and considerable care was taken to ensure that the selected valve would be suitable for this application given that a total of twelve valves would be required for a four-thruster, two fault-tolerant system. Microfluidic valve manufacturers such as Lee Co., Marotta Controls Inc., or Parker Fluidics have all had their products used in the CubeSat projects covered in Chapter 1, but these suppliers specialize in high tolerance aerospace-grade components thus driving the cost prohibitively high. Finding a suitable low-cost valve proved difficult, but ultimately two suppliers were found to carry products which were adequately priced, tabulated in Table E.1.

The Clippard EV-2-12 “Mouse” Valve, despite its physically smaller size and lower mass compared to its SMC counterpart, proved to possess too small of a flow coefficient to be suitable for a 0.6 mm nozzle, but only just. Therefore, the SMC VDW-12GZ1D valve was chosen as it possessed the necessary fluid and electrical characteristics, and M5 threaded inlet/outlet ports used to attach 4 mm outer diameter (OD) push-to-connect fittings for

Mfgr.	Model No.	Mass (g)	Orifice Dia. (mm)	Flow Coeff. (Cv)	Flow Rate [CO ₂ @ 20°C] (SCFM)	Price (\$USD)
Clippard	EV-2-12	77	0.7	0.013	0.60 @ 100 psig	30.01
SMC	VDW-12GZ1D	80	1.0	0.040	1.72 @ 100 psig	21.02
Converging-Diverging Nozzle			0.6	0.017	0.65 @ 100 psig	N/A

Table E.1: Sample valve selection and flow rate comparison to 0.6 mm C-D nozzle.

easy configuration of the pneumatic supply lines. This interface also allowed us to integrate M5 threaded barbed fittings into the plenums such that they could screw directly into the valve ports. The plenum design and manufacturing is outlined in detail in Section 3.3. Since this valve is made for on-ground industrial applications, it of course would not be suitable for spaceflight applications. Nevertheless, the cost is nearly an order of magnitude lower than a comparable product from the aforementioned microfluidic valve manufacturers, making it an attractive solution for on-ground prototypes and projects with limited funding.

E.4 Fittings and Adapters

Perhaps the most frustrating aspect of designing the pneumatic assembly was determining how to connect the components in a reliable and safe manner without using an excessive number of fittings. Every fitting provides an opportunity for leaks, so considerable effort was made to limit the number of parts which in turn would limit the amount of time spent attempting to seal the threads and ensure a leak-free assembly. For the high pressure side, brass and stainless steel adapters – most specifically designed for use in the paintball industry – were utilized. The selection of fittings was bound by the components purchased, such as the Micro Rock regulator with its 1/8” MNPT inlet or the ASA with its 1/8” FNPT outlet. A summary of components used on the higher pressure side is listed in Table E.2.

Connecting pneumatic components together on the low pressure side of the regulator

Qty.	Item	Inlet	Outlet
2x	9 oz. CO ₂ bottle	N/A	G1/2"-14 (Male)
2x	Airstream Adapter (ASA)	G1/2"-14 (Female)	1/8" FNPT
3x	8mm Quick Connect Disconnect Set	1/8" MNPT	1/8" FNPT
1x	MNPT Brass Tee	1/8" MNPT (2x)	1/8" MNPT
1x	6" Stainless Braided Hose Line	1/8" MNPT	1/8" MNPT
1x	FNPT Brass Coupler	1/8" FNPT	1/8" FNPT

Table E.2: Fitting types used to assemble the high-pressure side of the air bearing platform's pneumatics, listed here for ease of reproducibility.

was a much simpler task. The Micro Rock regulator output was a simple #10-32 threaded hole which allowed for inexpensive push-to-connect fittings to be used. The low pressure side exclusively used 4 mm nylon hose which was malleable enough to be bent and shaped with a heat gun to conform to the geometrical configuration of the air bearing platform. From the regulator, the #10-32 outlet was adapted to a 5/32" push-to-connect fitting which took advantage of the fact that design tolerances allowed 4 mm tubing to be used with 5/32" receptacles. After passing through a particulate filter, an array of tubing and push-to-connect fittings was then used to split the air flow to the three bearings and a pressure transducer. Each bearing required a single M3 to 4 mm push-to-connect adapter, and the transducer required a 5/32" to 1/8 FNPT adapter. All of the pneumatic components used in the low pressure assembly are listed below in Table E.3.

Qty.	Item	Inlet(s)	Outlet(s)
1x	#10-32 to 5/32" PTC Elbow	#10-32 (Male)	5/32" PTC Receptacle
1x	Grade 50 In-Line Filter	1/4" Stub (4 mm adapted)	1/4" Stub (4 mm adapted)
1x	4 mm PTC Cross	4 mm PTC Receptacles	4 mm PTC Receptacles
1x	4 mm PTC Wye	4 mm PTC Receptacles	4 mm PTC Receptacles
3x	M3 to 4 mm PTC	4 mm PTC Receptacle	M3 (Male)
1 m	4 mm OD Nylon Tube compatible with Push-to-Connect (PTC) fittings		

Table E.3: Fitting types used to assemble the low-pressure side of the air bearing platform's pneumatics, listed here for ease of reproducibility.

Appendix F

PCB Wiring Diagram

A printed circuit board (PCB) was designed and manufactured to house all the necessary electronics in a compact and reliable manner. The central microcontroller is a NodeMCU with code written in Arduino. Three L293D motor controllers act as valve controllers, while an MCP23017 acts as a general purpose input/output (GPIO) expander to allow the NodeMCU to control all 12 valves. Pressure transducer input is digitized using an MCP3002 10-bit analog-to-digital converter (ADC). Power is brought down to 5 Volts using an LM2596-based adjustable power supply module, which steps down the voltage from a battery-supplied 14.8 Volts. To allow the 5 Volt-based pressure transducers to operate correctly with the 3.3 Volt-based MCP-series of chips (as well as the NodeMCU), a simple resistor-based voltage divider was integrated between each transducer and the input to the ADC. Two pull-down resistors were integrated into the signal lines to enable SPI-based communication between the NodeMCU and the MCP23017 GPIO expander. One pull-up resistor was placed on the *RESET* pin of the MCP23017 as this pin would reset the GPIO expander if grounded. A detailed wiring diagram is reproduced here for reference.

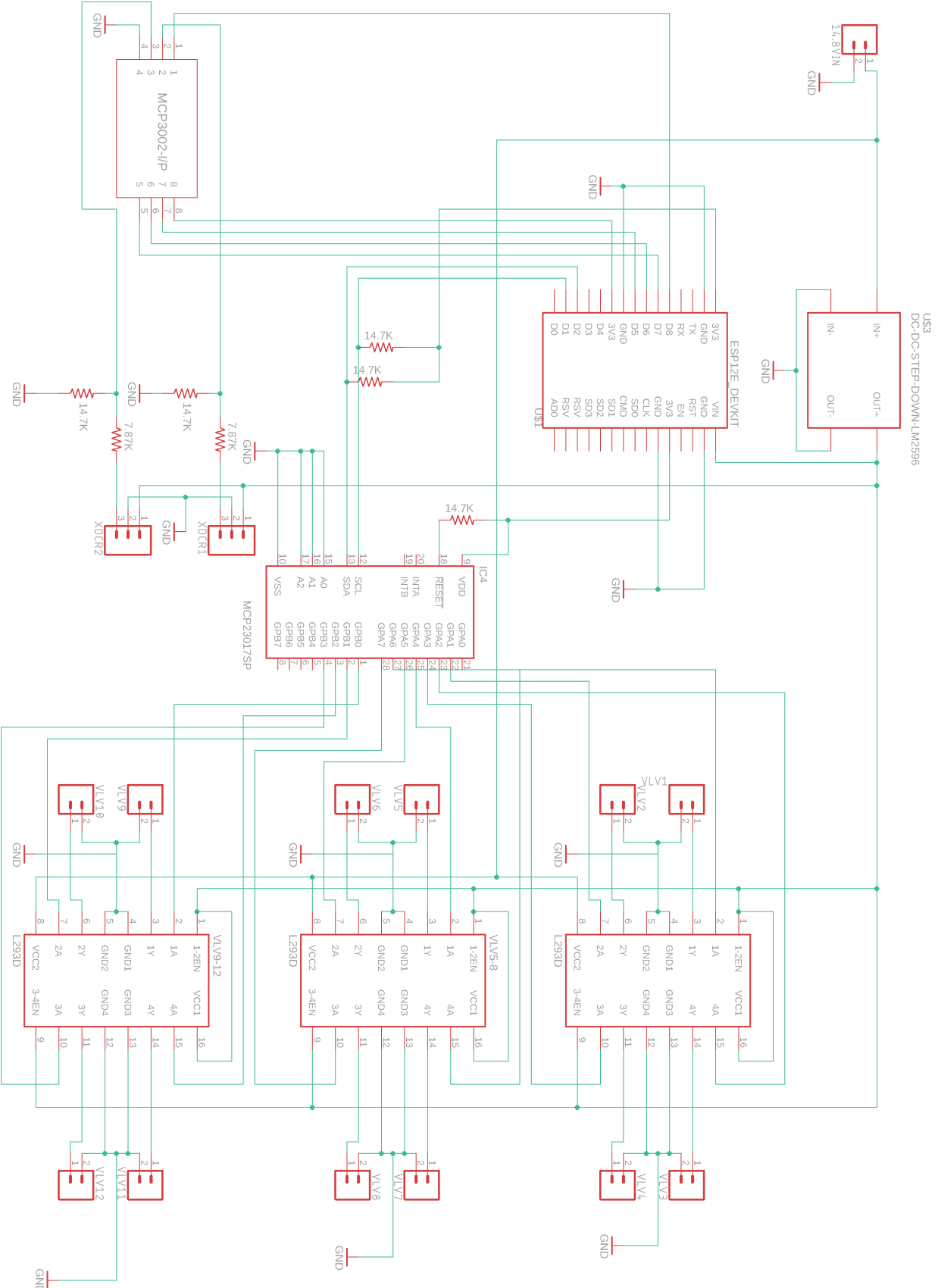


Figure F.1: Wiring diagram for propulsion system control board.

Appendix G

Online Resources

The following is a list of URLs which are homes to online resources pertaining to various aspects of this project.

UC Davis HRVIP 3D printing lessons learned:

<https://github.com/HRVIP/3D-printer>

Repository for 1D isentropic simulation code:

<https://github.com/jwdays/nozzleDesign>

Repository for computer vision and Kalman filter code:

<https://github.com/jwdays/ComputerVision>

Repository for air bearing testbed files and assembly notes:

<https://github.com/jwdays/ABTestbed>

REFERENCES

- [1] P. Dempsey, “Inspection Considerations from the ISS Program.” [Online]. Available: https://www.nasa.gov/sites/default/files/files/P_Dempsey-Inspection_Considerations_from_the_ISS_Program.pdf
- [2] C. Lorenzen and S. M. Stitch, “Low-Risk Spacecraft-Inspection CubeSat,” Logan, UT, 2016. [Online]. Available: <https://digitalcommons.usu.edu/smallsat/2016/Poster1/7/>
- [3] S. Arestie, E. G. Lightsey, and B. Hudson, “Development of A Modular, Cold Gas Propulsion System for Small Satellite Applications,” *Journal of Small Satellites*, vol. 1, no. 2, pp. 63–74, 2012.
- [4] J. W. Thomas, “STS-27R OV-104 Orbiter TPS damage review team, volume 1,” 1989, NASA Document ID 19890010807.
- [5] W. Harwood, “Legendary commander tells story of shuttle’s close call,” story written for CBS News Space Place and used with permission. [Online]. Available: <https://spaceflightnow.com/shuttle/sts119/090327sts27/>
- [6] NASA, “Partially melted aluminum mounting plate for the l-band antenna due to thermal protection tile loss in STS-27,” 1986. [Online]. Available: http://cbsnews.cbs.com/network/news/space/119/119graphics/fd13/27_land3.jpg
- [7] “Removing the Gap Fillers: A Spacewalking First,” 08 2005. [Online]. Available: https://www.nasa.gov/returntoflight/crew/EVA_gapfiller.html
- [8] C. Camarda, “Space Shuttle Return-to-Flight Following the Columbia Tragedy,” 03 2014.
- [9] NASA, “STS-114 Remote Manipulator System (RMS) robot arm flexes above Earth,” 2005. [Online]. Available: <https://spaceflight.nasa.gov/gallery/images/shuttle/sts-114/html/s114e5330.html>

- [10] A. Kauderer, “Ammonia Leak Outside Station; Crew in No Danger,” NASA, Tech. Rep., May 2013. [Online]. Available: https://www.nasa.gov/mission_pages/station/expeditions/expedition35/e35_050913.html
- [11] K. Dismukes, “AERCam Sprint,” 04 2003. [Online]. Available: <https://spaceflight.nasa.gov/station/assembly/sprint/>
- [12] S. Fredrickson, S. Duran, and J. Mitchell, “Mini AERCam inspection robot for human space missions,” in *Space 2004 Conference and Exhibit*, 2004, p. 5843.
- [13] D. Hinkley, “A Novel Cold Gas Propulsion System for Nanosatellites and Picosatellites,” in *Big Business*, Logan, UT, 2008, p. 10. [Online]. Available: <https://digitalcommons.usu.edu/smallsat/2008/all2008/44/>
- [14] “Seeker,” 2019. [Online]. Available: <https://sites.utexas.edu/tsl/seeker/>
- [15] R. Pendley, “Project X - Seeker,” Apr. 2019. [Online]. Available: <https://roundupreads.jsc.nasa.gov/pages.ashx/1130/Project%20X%20Seeker>
- [16] P. Walton, J. Cannon, B. Damitz, T. Downs, D. Glick, J. Holtom, N. Kohls, A. Laraway, I. Matheson, J. Redding *et al.*, “Passive CubeSats for remote inspection of space vehicles,” *Journal of Applied Remote Sensing*, vol. 13, no. 3, p. 032505, 2019.
- [17] E. A. Hanlon, M. E. Lange, B. P. Keegan, E. A. Culton, M. J. Corbett, J. G. Roser, C. P. Safbom, B. A. Wenger, and J. S. Kang, “Amods: Autonomous mobile on-orbit diagnostic system,” in *2016 IEEE Aerospace Conference*. IEEE, 2016, pp. 1–10.
- [18] R. Carvalho, *Nano-satellites : space and ground technologies, operations and economics*. Hoboken, NJ: Wiley, 2020, ISBN: 978-1-119-04203-7.
- [19] D. Gibbon, M. Paul, P. Smith, and R. McLellan, “The use of liquefied gases in small satellite propulsion systems,” in *37th Joint Propulsion Conference and Exhibit*. Salt Lake City, UT, U.S.A.: American Institute of Aeronautics and Astronautics, 2001. [Online]. Available: <http://arc.aiaa.org/doi/10.2514/6.2001-3246>

- [20] S. Mauthe, F. Pranajaya, and D. R. E. Zee, “The Design and Test of a Compact Propulsion System for CanX Nanosatellite Formation Flying.” Logan, UT: AIAA/Utah State University, 2005, p. 12.
- [21] NASA, “Cubesat Proximity Operations Demonstration (CPOD),” NASA, vol. 2, May 2013. [Online]. Available: https://www.nasa.gov/sites/default/files/atoms/files/factsheet_cpod_19_july2018-508.pdf
- [22] NASA Jet Propulsion Laboratory, “Mars Cube One (MarCO),” Oct. 2018. [Online]. Available: <https://www.jpl.nasa.gov/cubesat/missions/marco.php>
- [23] “Deploying Small Satellites From ISS,” 2015. [Online]. Available: https://www.nasa.gov/mission_pages/station/research/benefits/cubesat
- [24] K. Rainey, “Deploying Small Satellites from the ISS,” 2015, nASA. [Online]. Available: https://www.nasa.gov/mission_pages/station/research/benefits/cubesat
- [25] E. Kulu, “Nanosats Database | Constellations, companies, technologies and more,” 2019. [Online]. Available: <https://www.nanosats.eu/>
- [26] VACCO Industries, “Our MarCO CubeSat Propulsion System Featured in Chemical & Engineering News,” Aug. 2016. [Online]. Available: <https://www.cubesat-propulsion.com/marco-cubesat-propulsion-system/>.
- [27] “State of the Art of Small Spacecraft Technology,” NASA Ames Research Center, Mountain View, CA, Tech. Rep., 2019. [Online]. Available: <https://www.nasa.gov/smallsat-institute/sst-soa>
- [28] S. Mauthe, “Overview of the canx-2 nanosatellite propulsion system,” Aug. 2005, presentaiton. [Online]. Available: digitalcommons.usu.edu/cgi/viewcontent.cgi?filename=0&article=1641&context=smallsat&type=additional
- [29] D. Gibbon, J. Ward, and N. Kay, “The design, development and testing of a propulsion system for the snap-1 nanosatellite,” 2000.

- [30] D. Schmuland, R. Massee, and C. Sota, “Hydrazine propulsion module for CubeSats,” 2011, Aerojet Rocketdyne.
- [31] D. Schmuland, C. Carpenter, R. Massee, and J. Overly, “New insights into additive manufacturing processes: enabling low-cost, high-impulse propulsion systems,” 2013.
- [32] D. Hinkley, “A Novel Cold Gas Propulsion System for Nanosatellites and Picosatellites,” 2008, Presentation. [Online]. Available: <https://pdfs.semanticscholar.org/434c/3c24948271d41c3012034e1bd44bec17abee.pdf>
- [33] Carbon, “NASA Seeker Robot x The Technology House, Powered By Carbon,” 2019. [Online]. Available: <https://carbon3d.com/resources/nasa-seeker-x-tth-powered-by-carbon/>
- [34] S. Conkle, “The Near Tragedy of Gemini 8: How Neil Armstrong’s First Space Mission Was Almost His Last,” 2019.
- [35] “14 C.F.R. § 417.409,” in *Code of Federal Regulations*, 2010.
- [36] M. Mizukami, T. J. Barber, and R. S. Baker, “Mars Science Laboratory Cruise Propulsion Maneuvering Operations,” Pasadena, CA: Jet Propulsion Laboratory, National Aeronautics and Space Administration, Tech. Rep., 2013.
- [37] D. Owen, “Apollo Spacecraft Propulsion Systems Design Philosophies,” in *AIAA SPACE 2010 Conference & Exposition*, 2010, p. 8813.
- [38] J. G. Thibodaux, “Apollo spacecraft propulsion systems,” *SAE Transactions*, pp. 2328–2337, 1969.
- [39] D. M. Bates, P. Meakin, R. M. Weitl, E. K. Wang, and A. Y. Lee, “Fault protection design and testing for the Cassini spacecraft in a “mixed” thruster configuration,” in *AIAA Guidance, Navigation, and Control (GNC) Conference*, 2013, p. 4632.
- [40] VACCO Industries, “JPL MarCO Micro CubeSat Propulsion System,” Mar. 2018. [Online]. Available: <https://www.cubesat-propulsion.com/jpl-marco-micro-propulsion-system/>

- [41] “NASA Extravehicular Mobility Unit (EMU) LSS/SSA Data Book,” 2017. [Online]. Available: <https://www.lpi.usra.edu/lunar/constellation/NASA-EMU-Data-Book-JSC-E-DAA-TN55224.pdf>
- [42] R. Frost, “What does getting “human-rated” mean in regards to NASA vehicles?” Feb. 2017. [Online]. Available: <https://qr.ae/pNowjo>
- [43] L. Fesq, N. Dennehy *et al.*, “Fault management handbook, nasa technical handbook,” NASA-HDBK-1002, Apr. 2012, https://www.nasa.gov/pdf/636372/main_NASA-HDBK.pdf, Tech. Rep., 2011.
- [44] A. France-Presse, “International Space Station,” 2019. [Online]. Available: <https://phys.org/news/2019-08-docking-aborted-russia-humanoid-robot.html>
- [45] W. Clohessy and R. Wiltshire, “Terminal guidance system for satellite rendezvous,” *Journal of the Aerospace Sciences*, vol. 27, no. 9, pp. 653–658, 1960.
- [46] E. Mamajek, A. Prsa, G. Torres, P. Harmanec, M. Asplund, P. Bennett, N. Capitaine, J. Christensen-Dalsgaard, E. Depagne, W. Folkner *et al.*, “IAU 2015 Resolution B3 on Recommended Nominal Conversion Constants for Selected Solar and Planetary Properties,” 2015.
- [47] C. Peat, “ISS - Orbit,” <https://www.heavens-above.com/orbit.aspx?satid=25544>, accessed: 2018-09-28.
- [48] J. Ries, R. Eanes, C. Shum, and M. Watkins, “Progress in the determination of the gravitational coefficient of the earth,” *Geophysical research letters*, vol. 19, no. 6, pp. 529–531, 1992.
- [49] “Iadc Space Debris Mitigation Guidelines,” United Nations Office for Outer Space Affairs, Vienna, Austria, Tech. Rep., 2007.
- [50] D. L. Oltrogge and K. Leveque, “An Evaluation of Cube Sat Orbital Decay.” Logan, UT: 25th Annual AIAA/USU Conference on Small Satellites, 2011.

- [51] H. Klinkrad, J. Alarcon, and N. Sánchez-Ortiz, “Collision Avoidance for Operational ESA Satellites,” *European Space Agency, (Special Publication) ESA SP*, vol. 587, p. 509, 07 2005.
- [52] “NSTS 1700.7B - Safety Policy and Requirements for Payloads Using the Space Transportation System,” 12 2003. [Online]. Available: https://snebulos.mit.edu/projects/reference/NASA-Generic/NSTS_1700-7B.pdf
- [53] “NSTS 1700.7B ISS ADDENDUM - Safety Policy and Requirements for Payloads Using the International Space Station,” 12 2003. [Online]. Available: https://snebulos.mit.edu/projects/reference/NASA-Generic/NSTS_1700-7B.pdf
- [54] F. Ion, “The Nexus S as attached to a SPHERES satellite at NASA Ames,” 2013. [Online]. Available: <https://arstechnica.com/gadgets/2013/03/how-nasa-got-an-android-handset-ready-to-go-into-space/>
- [55] B. E. Tweddle, T. P. Setterfield, A. Saenz-Otero, and D. W. Miller, “An Open Research Facility for Vision-Based Navigation Onboard the International Space Station,” *Journal of Field Robotics*, vol. 33, no. 2, pp. 157–186, 2016.
- [56] N. W. A. Bearings, “S102501 Flat Round Air Bearing 25 mm Lift-Load Curve,” 2017. [Online]. Available: https://www.newwayairbearings.com/wp-content/uploads/2017/07/air_bearing_flat_round_025mm_curve_lift-load_new_way_S102501_en.pdf
- [57] “Optical Tables, 210 mm (8.3”) Thick.” [Online]. Available: https://www.thorlabs.com/newgroupage9.cfm?objectgroup_id=7091
- [58] “Air Bearing Floor.” [Online]. Available: https://www.nasa.gov/centers/johnson/engineering/integrated_environments/air_bearing_floor/index.html
- [59] “Our New Spacecraft Research Laboratory,” 10 2017, caltech. [Online]. Available: <http://aerospacerobotics.caltech.edu/>
- [60] “Development of a Large Support Surface for an Air-Bearing Type Zero-Gravity Simulator.” [Online]. Available: <https://ntrs.nasa.gov/archive/nasa/casi.ntrs.nasa.gov/19760019162.pdf>

- [61] *Air Bearing Application and Design Guide*, New Way Air Bearings, 2006. [Online]. Available: https://www.newwayairbearings.com/sites/default/files/new_way_application_and_design_guide_%20Rev_E_2006-01-18.pdf
- [62] K. R. Jensen, P. Fojan, R. L. Jensen, and L. Gurevich, “Surface Characterization of Coated and Uncoated Float Glass,” in *International Summer PhD school on Application of SPM*. River Publishers, 2013.
- [63] B. W. Yates and A. M. Duffy, “Statistical analysis of the metrological properties of float glass,” in *Advances in X-Ray/EUV Optics and Components III*, vol. 7077. International Society for Optics and Photonics, 2008, p. 70770D.
- [64] H. Arribart and D. Abriou, “Ten years of atomic force microscopy in glass research,” *Ceramics-Silikáty*, vol. 44, no. 4, pp. 121–128, 2000.
- [65] “Grade B Toolroom Granite Inspection Surface Plate,” 2020. [Online]. Available: <https://www.mscdirect.com/product/details/00150078>
- [66] Y. D. Filatov, V. Yashchuk, A. Y. Filatov, U. Heisel, M. Storchak, and G. Monteil, “Assessment of surface roughness and reflectance of nonmetallic products upon diamond abrasive finishing,” *Journal of Superhard Materials*, vol. 31, no. 5, p. 338, 2009.
- [67] K. C. Datsiou and M. Overend, “Evaluation of artificial ageing methods for glass,” in *Challenging Glass Conference Proceedings*, vol. 5, 2016, pp. 581–592.
- [68] C. E. Rogers, “Departures from Ideal Performance for Conical Nozzles and Bell Nozzles, Straight-Cut Throats and Rounded Throats,” *High Power Rocketry*, vol. 35, no. 8, p. 31, 2004. [Online]. Available: <http://rasaero.com/dloads/Departures%20from%20Ideal%20Performance.pdf>
- [69] *Parker O-ring Handbook*, 2018, parker Hannifin Corporation. [Online]. Available: <https://www.parker.com/Literature/O-Ring%20Division%20Literature/ORD%205700.pdf>
- [70] Y. Zhao, Y. Chen, and Y. Zhou, “Novel mechanical models of tensile strength and elastic property of FDM AM PLA materials: Experimental and theoretical analyses,” *Materials & Design*, vol. 181, p. 108089, 2019.

- [71] H. Zhang, J. Huang, L. Yang, R. Chen, W. Zou, X. Lin, and J. Qu, “Preparation, characterization and properties of PLA/TiO₂ nanocomposites based on a novel vane extruder,” *RSC Advances*, vol. 5, no. 6, pp. 4639–4647, 2015.
- [72] L. Eppley and J. Araniego, “Airsoft and Paintball Kinetic Energies.” [Online]. Available: <http://www.floridaairsoft.com/features/avspb.htm>
- [73] S. Garrido-Jurado, R. Muñoz-Salinas, F. J. Madrid-Cuevas, and M. J. Marín-Jiménez, “Automatic generation and detection of highly reliable fiducial markers under occlusion,” *Pattern Recognition*, vol. 47, no. 6, pp. 2280–2292, 2014.
- [74] F. J. Romero-Ramirez, R. Muñoz-Salinas, and R. Medina-Carnicer, “Speeded up detection of squared fiducial markers,” *Image and vision Computing*, vol. 76, pp. 38–47, 2018.
- [75] R. Labbe, “Kalman and bayesian filters in python,” 2015. [Online]. Available: <https://github.com/rlabbe/Kalman-and-Bayesian-Filters-in-Python>
- [76] “A supersonic nozzle,” 2007, Krishnaexp at Wikimedia Commons. [Online]. Available: https://commons.wikimedia.org/wiki/File:Fig,_A_supersonic_nozzle.jpeg
- [77] J. M. Seitzman, “Thruster Pulsing,” 2017, aE6450 Rocket Propulsion.
- [78] V. Gnielinski, “On heat transfer in tubes,” *International Journal of Heat and Mass Transfer*, vol. 63, pp. 134–140, 2013.
- [79] E. W. Spisz, P. F. Brinich, and J. R. Jack, “Thrust coefficients of low-thrust nozzles,” National Aeronautics and Space Administration, Cleveland, OH, Lewis Research Center, Tech. Rep., 1965.
- [80] “Piston Regulators,” IEEE GlobalSpec. [Online]. Available: https://www.globalspec.com/learnmore/flow_control_fluid_transfer/valves/air_pressure_regulators
- [81] “Air Compressors, Air Treatment and Pressure Regulation,” 2015. [Online]. Available: <http://machineryequipmentonline.com/hydraulics-and-pneumatics/air-compressors-air-treatment-and-pressure-regulationrelief-valves/>